Investigation of thermal and structural integrity of modules and ladders of Silicon Tracking System of the CBM experiment

Dissertation
der Mathematisch-Naturwissenschaftlichen Fakultät
der Eberhard Karls Universität Tübingen
zur Erlangung des Grades eines
Doktors der Naturwissenschaften
(Dr. rer. nat)

vorgelegt von

Shaifali Mehta
aus Tosham, India

Tübingen
2024

Gedruckt mit Genehmigung der Mathematisch-Naturwissenschaftlichen Fakultät
der Eberhard Karls Universität Tübingen.

Tag der mündlichen Qualifikation: 10.2024
Dekan: Prof. Dr. Thilo Stehle
1. Berichterstatter: Prof. Dr. Hans Rudolf Schmidt
2. Berichterstatter: Prof. Dr. Peter Senger

Betreuer: Dr. Ulrich Frankenfeld

Datum der Disputation: 2024

Dedicated to...

...my family

Abstract

The Compressed Baryonic Matter (CBM) at the Facility for Antiproton and Ion Research (FAIR) is a fixed target experiment designed to investigate the properties of strongly interacting matter in the region of high net-baryon density. The Silicon Tracking System (STS) is the core detector of the CBM experiment and aims to track and measure the momentum of the charged particles. The STS detector comprises of 876 double sided silicon micro-strip sensors connected via micro cables to the Front-End Boards (FEBs) which are kept outside the detector acceptance of 2.5° to 25°. These sensors are mounted on 106 carbon fiber ladders which includes standard ladders and central ladders with an opening for the beam-pipe. For good particle tracking accuracy in the CBM, the silicon sensors must be mounted on the ladders with extremely high precision, minimizing misalignment and optimizing the spatial resolution of the detector.

The experimental operating conditions of STS present challenges to the electronics due to a highly variable thermal environment. A significant portion of the thesis focuses on the thermal studies of the STS components. This involves a detailed investigation of the requirements for thermal interface materials (TIMs) between the FEBs and the cooling shelves. The study includes optimization techniques for adhesive application and thermal testing to ensure the effectiveness of the TIMs. To ensure the reliable functioning of FEBs under significant temperature variations, thermal cycling tests were conducted, and potential failure scenarios have been analyzed.

The main focus of the thesis is the understanding of the structural integrity of the STS detector. It is investigated how the STS ladders, essential for supporting the silicon sensors, are put together and how they perform. The design and quality assurance processes for carbon fiber ladders are examined, followed by a step-by-step description of the ladder assembly procedure. The evolution of the ladder assembly procedures, from initial prototypes to fully functional ladders with the required mounting precision are highlighted. The developed procedure is designed to be iterative and easily adaptable for producing 106 STS ladders.

The final section of the thesis addresses the vibration challenges encountered by the STS ladders due to air cooling, which is essential for maintaining the sensor performance. It describes the experimental setups used to measure the eigenfrequencies and vibrations on the sensor surface

under airflow conditions. The study uses a perforated tube to direct airflow onto the sensor surfaces and highlights the performance differences between the standard and central ladders. Through the analysis of vibration magnitude, the impact of airflow on the stability of the silicon sensors once they are mounted on the ladders, is evaluated. These findings underline the significance of effective vibration control to maintain sensor stability.

This thesis provides a comprehensive understanding of both thermal management and structural integrity of the STS. Through extensive testing of TIM and thermal cycling of the FEBs, the last step of the module assembly process has been optimized, resulting in a reliable TIM now used in the series production of the modules. Along this work, significant progress has been made in developing the ladder assembly procedure, which is now being implemented for all the ladders, with series production already underway. The central ladder assembly procedure has been optimized and validated with a prototype ladder. The vibration measurements have established the boundary conditions for airflow through the perforated tube, ensuring the mechanical integrity and necessary cooling to prevent thermal runaway.

Zusammenfassung

Das Compressed Baryonic Matter (CBM) Experiment an der Anlage für Antiprotonen- und Ionenforschung (FAIR) hat zum Ziel, die Eigenschaften von stark wechselwirkender Materie im Bereich hoher Baryondichte zu untersuchen. Das Silicon Tracking System (STS) ist der zentrale Detektor des CBM-Experiments, der dazu dient, die Spuren und den Impuls geladenen Teilchen zu vermessen. Der STS-Detektor besteht aus 876 doppelseitigen Silizium-Mikrostreifensensoren, die über Mikrokabel mit den Front-End-Boards (FEBs) verbunden sind, die sich außerhalb des Detektorakzeptanzbereichs in der Peripherie befinden von 2,5° bis 25°. Diese Sensoren sind auf 106 Kohlefaserstrukturen (Leitern) montiert, die neben Standardleiter auch zentrale Leiter mit einer Öffnung für das Strahlrohr umfassen. Für eine präzise Vermessung der Teilchenspuren im CBM-Experiment müssen die Siliziumsensoren mit extrem hoher Präzision auf den Leitern montiert werden, um Fehlausrichtungen zu minimieren und die räumliche Auflösung des Detektors zu optimieren.

Die experimentellen Betriebsbedingungen des STS stellen aufgrund extremer und schwankender Temperaturen eine Herausforderung für die Elektronik dar. Ein wesentlicher Teil dieser Arbeit konzentriert sich auf die thermischen Studien der STS-Komponenten. Dies umfasst eine detaillierte Untersuchung der Anforderungen an thermische Schnittstellenmaterialien (TIMs) zwischen den FEBs und den Kühlfinnen. Die Studie beinhaltet Optimierungstechniken für die Klebstoffanwendung und thermische Tests, um die Wirksamkeit der TIMs sicherzustellen. Um die zuverlässige Funktion der FEBs unter extremen und schwankenden Temperaturen zu gewährleisten, wurden thermische Tests durchgeführt und potenzielle Ausfallszenarien analysiert.

Der Hauptfokus dieser Arbeit liegt auf dem Verständnis der strukturellen Integrität des STS-Detektors. Es wird untersucht, wie die STS-Leitern, die für die Befestigung der Siliziumsensoren unerlässlich sind, zusammengebaut werden und wie sie funktionieren. Die Design- und Qualitätssicherungsprozesse für Kohlefaserleiter werden untersucht, gefolgt von einer Schritt-für-Schritt-Beschreibung des Montageverfahrens der Leiter. Die Entwicklung des Leiterzusammenbaus, von den ersten Prototypen bis hin zu voll funktionsfähigen Leitern mit der erforderlichen Montagepräzision, wird erläutert. Das entwickelte Verfahren ist darauf ausgelegt, iterativ zu sein und sich leicht an die Produktion von 106 STS-Leitern anzupassen.

Der letzte Abschnitt dieser Arbeit befasst sich mit den durch die für den Sensorbetrieb unerlässliche Luftkühlung verursachten Vibrationen der STS-Leitern. Es werden die experimentellen Aufbauten beschrieben, die zur Messung der Eigenfrequenzen und der Schwingungen aufgrund des Luftstroms auf der Sensoroberfläche verwendet werden. Die Studie verwendet ein perforiertes Rohr, um den Luftstrom auf die Sensoroberflächen zu lenken, und zeigt die Unterschiede zwischen den Standard- und Zentralleitern auf. Durch die Analyse der Schwingungsamplitude wird der Einfluss des Luftstroms auf die Stabilität der Siliziumsensoren auf den Leitern bewertet. Diese Ergebnisse unterstreichen die Bedeutung eines effektiven Schwingungsmanagements zur Aufrechterhaltung der Sensorstabilität.

Diese Arbeit bietet ein umfassendes Verständnis sowohl des thermischen Managements als auch der strukturellen Integrität des STS. Durch umfangreiche Tests der TIMs und thermische Tests der FEBs wurde der letzte Schritt des Modulmontageprozesses optimiert, welcher nun in der Serienproduktion der Module verwendet wird, was zu einem zuverlässigen TIM geführt hat. Im Laufe dieser Arbeit wurden bedeutende Fortschritte bei der Entwicklung des Leiterbauverfahrens erzielt, das nun für alle Leiter der bereits laufenden Serienproduktion angewendet wird. Das Montageverfahren für zentrale Leiter wurde optimiert und mit einem Prototyp validiert. Die Vibrationsmessungen haben die Rahmenbedingungen für die Luftstromkühlung durch perforierte Rohre festgelegt, wodurch die mechanische Integrität und die notwendige Kühlung für die elektrische Stabilität der Sensoren gewährleistet werden.

Contents

1 Introduction **1**

1.1 Understanding of nuclear matter 1

1.2 Silicon detectors in high energy physics 4

1.3 Compressed Baryonic Matter experiment 9

1.4 The Silicon Tracking System 11

1.5 Scope of the thesis 15

2 Thermal studies of STS components **16**

2.1 Introduction to STS module assembly 17

2.2 Requirements of TIM between FEBs and cooling shelf 19

2.2.1 Optimization of TIM between FEB and cooling shelf 21

2.3 Survey of thermally conductive adhesives 24

2.3.1 Thermal tests 25

2.3.2 Mechanical stability test 28

2.3.3 Results and outlook 33

2.4 Characterisation of adhesive to be used as TIM 36

2.4.1 Optimisation of glue pattern 37

2.4.2 Gluing tool for the glue application 41

2.4.3 IV measurement of the glued samples 42

2.4.4 Quality assurance of surfaces 44

2.4.5 Possible solution for surface optimization 47
2.4.6 Results of TIM characterization 52
2.4.7 Failure scenario for TIM 54
2.5 Testing the thermal reliability of FEBs glued on cooling shelves 56
2.5.1 Passive cycle 59
2.5.2 Active cycle 60
2.5.3 Power cycling 62
2.5.4 Results and conclusion 64

3 Ladder Assembly for STS **71**
3.1 Motivation for ladder assembly 71
3.1.1 Specifications of STS ladder 72
3.1.2 Performance requirements of STS ladder 74
3.2 Design of carbon fiber ladder 75
3.3 Quality assurance of bare ladders 77
3.4 Components of Ladder Assembly 80
3.5 Ladder Assembly procedure 83
3.5.1 Ladder preparation and integration 83
3.5.2 Mounting of L-legs on the ladder 84
3.5.3 Positioning of sensors on the ladders 86
3.5.4 Optical survey of silicon sensor positions 88
3.6 Evolution of ladder assembly procedure 90
3.6.1 Assembly of (prototype) half ladder 90
3.6.2 Functional standard ladder for mini-STS(mSTS) 91
3.6.3 Standard full ladder 93
3.6.4 Central ladder 98

4 Vibration measurement **102**

4.1 Introduction to the cooling concept . . . 102

4.1.1 Electronics cooling . . . 105

4.1.2 Sensor cooling . . . 105

4.1.3 Consequence of air cooling on silicon sensors . . . 107

4.1.4 Impact of Vibrations on detector performance . . . 108

4.2 Eigenfrequency measurement for STS ladder . . . 110

4.2.1 Experimental set-up description . . . 112

4.2.2 Displacement measurement using capacitive sensor . . . 114

4.3 Vibration measurement under air flow . . . 117

4.3.1 Experimental set-up description . . . 118

4.3.2 Approach to measure sensor vibration . . . 119

4.3.3 Optimization of the setup . . . 123

4.3.4 Measurement of vibration signal and analysis technique . . . 124

4.4 Experimental Findings: Airflow Measurement Using Perforated Tube . . . 127

4.4.1 Standard ladder . . . 129

4.4.2 Central ladder . . . 132

5 Summary **134**

Appendix **137**

A.1 Gluing procedure for FEB to the cooling shelf . . . 137

A.1.1 Calculations for the glue pattern . . . 141

A.2 Acquisition of data using Laser Doppler Vibrometer . . . 142

List of figure **166**

List of tables **168**

Chapter 1

Introduction

1.1 Understanding of nuclear matter

Particle physics explores the universe's fundamental building blocks and the forces that govern their interactions. The theoretical framework for this exploration is provided by the Standard Model of Particle Physics which describes the fundamental particles and their interactions. This model categorizes the known elementary particles into two primary groups: Fermions and Bosons.

Fermions obey Fermi-Dirac statistics and comprises of quarks and leptons divided into three generations. The first generation consists of up and down quarks, which combine to form the baryonic matter in the universe, including protons and neutrons. Heavier particles in the second and third generations, such as charm and strange quarks, and top and bottom quarks, typically decay into more stable forms from the first generation. Bosons, on the other hand, are the force carriers and obey Bose-Einstein statistics. They mediate the fundamental forces of nature: the electromagnetic force via photons, the weak force via W and Z bosons, and the strong force via gluons. The Higgs boson is responsible for giving mass to other particles through the Higgs mechanism.

The strong nuclear force, integral to holding quarks together within particles, is governed by the principles of Quantum Chromodynamics (QCD). These interactions are mediated by gluons, and their dynamics are mapped out in the QCD phase diagram. This diagram, as shown in Fig. 1.1, outlines the transitions between various states of matter under different conditions of

temperature (T[1]) and baryon chemical potential (μ_B[2]).

At low temperatures and chemical potentials, quarks and gluons are confined within hadrons, forming the hadronic phase of matter, where the strong nuclear force keeps quarks tightly bound within hadrons. As the temperature rises or under extremely high energy densities, such as those achieved in heavy ion collisions, the hadronic matter transitions into a quark-gluon plasma (QGP). In the QGP phase, quarks and gluons are no longer confined within hadrons but exist freely, similar to the conditions of the universe microseconds after the Big Bang [6].

For very low μ_B, where the numbers of particles and anti-particles are approximately equal, the theoretical predictions from QCD, especially through lattice calculations, suggest a smooth crossover from hadronic to quark-gluon states at temperatures around 155 MeV [7]. However, for higher values of μ_B (and low T), calculations indicate the existence of a critical endpoint, beyond which a first-order phase transition into the partonic matter is expected [8]. Moreover, the diagram suggests a quarkyonic phase at large μ_B and moderate T, these conditions could exist within the cores of neutron stars, where such extreme baryon densities are present.

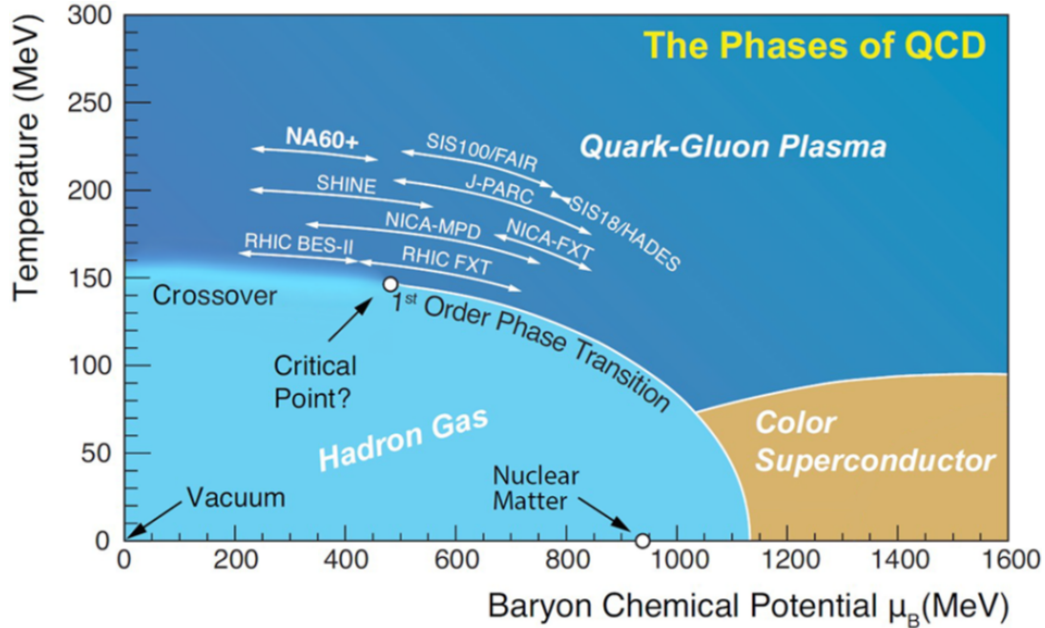

Figure 1.1: Schematic of the phase diagram of strongly interacting matter, in the Temperature and Baryon chemical potential region [1].

[1] T in this context relates to the energy density of the matter, with higher temperatures leading to a state where quarks and gluons can become deconfined from their hadronic states.

[2] μ_B is a measure of the difference in energy when adding a baryon or an antibaryon to the system, with high values corresponding to baryon-rich environments like those in neutron stars.

Experimentally, the study of hot and dense nuclear matter is conducted by colliding heavy nuclei, generating conditions suitable for exploring the QCD phase diagram across different temperatures and density regimes. The experiments at the Relativistic Heavy Ion Collider (RHIC) and the Large Hadron Collider (LHC), have extensively explored the high-temperature regime of the phase diagram where the baryon chemical potential (μ_{B}) is nearly zero. This exploration helps to study the de-confined QCD matter [4].

However, the region of the phase diagram with finite μ_{B} remains less explored, where theoretical models predict a critical endpoint and potentially a first-order phase transition. To address this gap, several heavy ion collision experiments have been designed and are ongoing. The STAR collaboration at RHIC has performed the Beam Energy Scan (BES), examining Au-Au collisions with energy ranges from 39 to 7.7 GeV [9]. To achieve the high precision measurements and increase statistics (one order of magnitude in collider mode and two orders of magnitude in fixed target mode), the second phase of BES program was extended to include energies below $\sqrt{\mathrm{S_{NN}}}$ = 7.7 GeV down to 3 GeV [10]. Other experiments like NA61/SHINE at CERN-SPS [11], and NICA at JINR [12] are also aiming to explore the regime of high μ_{B}.

The properties of dense nuclear matter can be studied by examining the experimental observables that include the production of (multi-)strange hyperons and hyper-nuclei, the flow patterns of identified particles, fluctuations in conserved quantities on an event-by-event basis, the emission of di-leptons, and particles that contain charm quarks. However, the ability of the experiments to study such phenomena is often constrained by detector limitations and luminosity constraints that limit the observations to more abundantly produced particles. To measure these rare observables, high statistical accuracy and significant interaction rates are required. The CBM experiment at FAIR aims to be operated at the highest interaction rates (10 MHz) in the high μ_{B} region. The rate capabilities of existing and planned heavy-ion experiments are presented in Fig. 1.2.

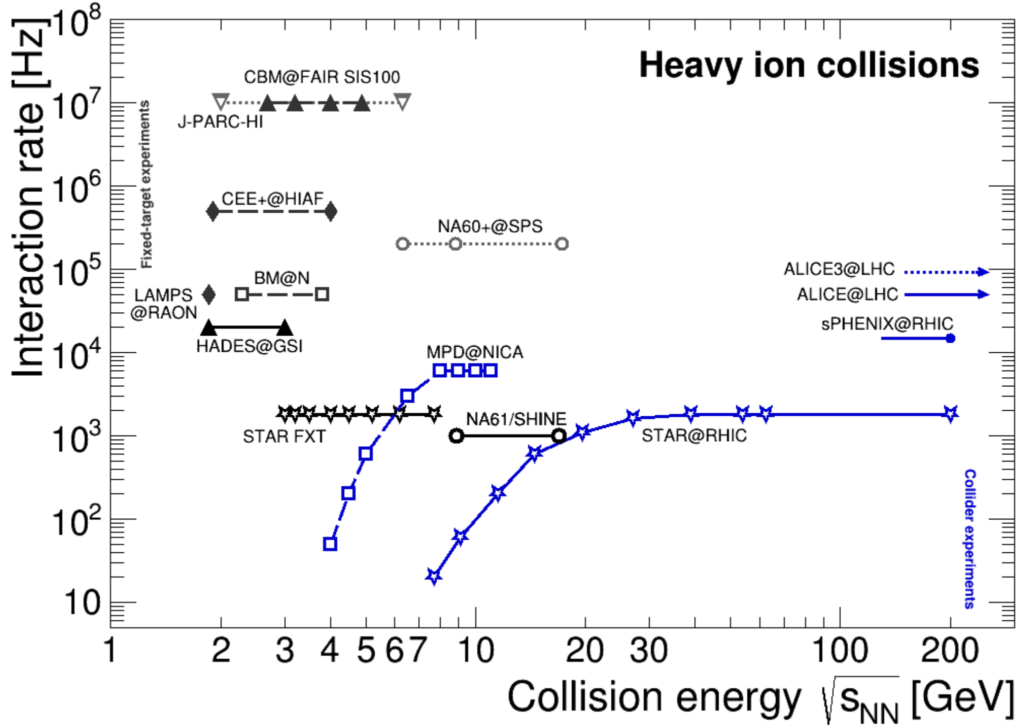

Figure 1.2: Comparison of interaction rate as a function of center-of-mass energy for the existing and planned heavy-ion experiments [13, 2].

1.2 Silicon detectors in high energy physics

To experimentally probe the validity of the Standard Model and unveil the mysteries of particle physics, particle detectors are essential. These detectors are designed to capture the properties of particles produced in high-energy physics experiments. Various types of detectors are integrated into experimental setups to extract the data that challenges the theoretical predictions.

Detectors can be broadly categorized based on their operating principles and the type of materials used. These categories include ionization detectors, scintillation detectors, gaseous detectors, and solid-state detectors, each tailored for specific purposes. Ionization detectors, such as proportional counters and ionization chambers, measure the particles by detecting the ionization produced in the medium. Scintillation detectors use materials that emit light (scintillate) when excited by ionizing radiation. Gaseous detectors operate on the principle of gas ionization, which monitors the ionization of gases caused by passing particles, which allows the detectors to reconstruct the particle's trajectory and measure its energy [15].

Semiconductor detectors, which are made from solid-state materials like silicon or germanium, operate by detecting the charge carriers (electron and hole pairs) produced when ionizing ra-

diation interacts with the semiconductor material. This interaction provides high-resolution detection of particle energy [16]. Among various detector technologies, silicon detectors have emerged as a fundamental technology used for particle tracking due to their high precision, robustness, and adaptability.

In scenarios where determining the trajectory, momentum, and origin of particles is crucial, the role of these detectors is irreplaceable [20]. In experiments like the CMS and ATLAS, those conducted at the LHC, silicon detectors are essential for identifying and reconstructing the paths of short-lived particles like the Higgs boson [18]. The ability of silicon detectors to provide high spatial resolution and recently timing resolution significantly contributes to the understanding of particle physics. The evolution of silicon detector technology can be observed through the expansion in the number of readout channels relative to the silicon area used in these detectors. Over the past four decades, there has been a substantial increase in the number of readout channels, which enhances the ability to capture and analyze data from particle collisions more thoroughly and with greater granularity, as shown in the Fig. 1.3.

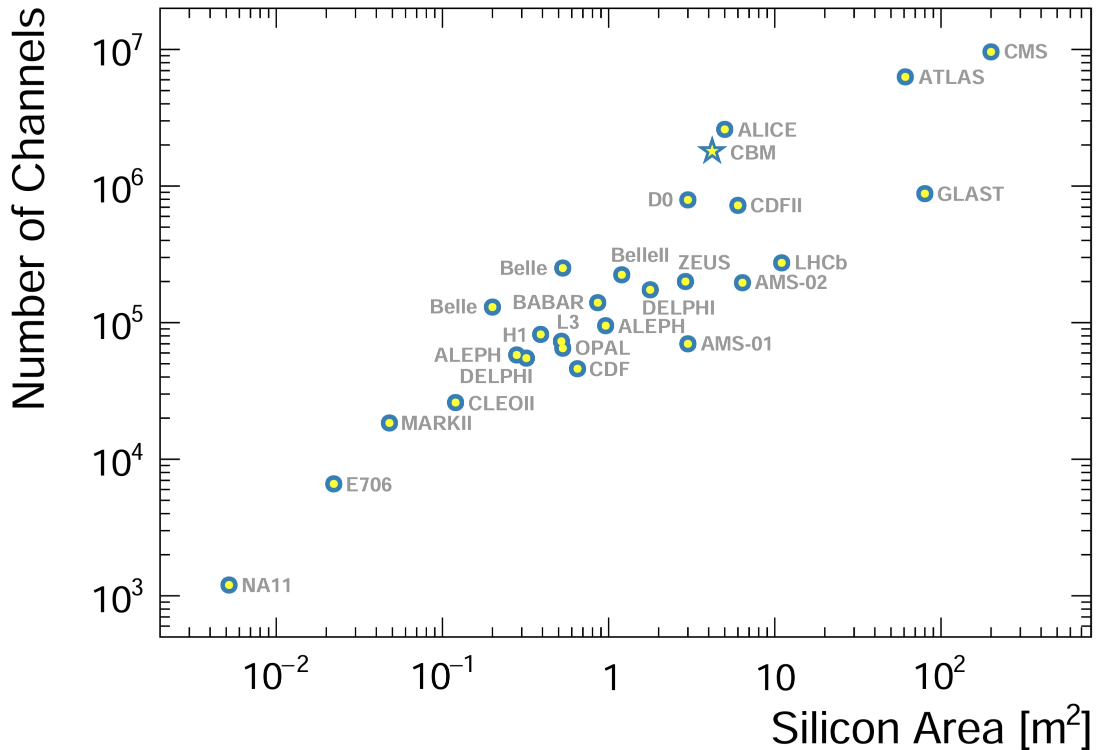

Figure 1.3: Increase in the number of read-out channels with the change in the area of the strip in silicon for different experiments has been shown. The different experiments are shown with circle and CBM experiment, focus of the thesis has been shown with star (Figure is taken from [19]).

Silicon detectors use different types of silicon sensor technology starting from 1989 till date, which includes silicon strips, pads, and pixels, which are integral to modern particle detectors. These technologies are integral to modern particle detectors due to their precision in tracking particle trajectories. Starting with basic silicon strip detectors, advancements have led to the development of silicon pads and pixels, each offering improvements in granularity and detection efficiency [17]. While the silicon sensors are at the forefront of detecting and tracking particles due to their high spatial resolution and sensitivity, support structures are needed for these silicon elements that are equally crucial for the efficiency of the tracking system. These support structures, often referred to as ladders or staves, are designed to provide mechanical stability, ensure optimal thermal management, and facilitate the integration of electronic components, all of which are essential for maintaining the silicon detectors performance over prolonged periods under the harsh conditions of high-energy physics experiments. The choice of materials, the engineering design of these supports, and their capability to minimize material interaction with passing particles, thereby minimizing the background noise and enhancing the signal-to-noise ratio, are paramount.

The choice between ladders or staves to be used as support structures depends on the design requirements of the experiment, desired granularity, mechanical stability, thermal management, and overall detector performance. Staves are integrated assemblies that combine mechanical support, thermal management, and electrical readout systems. They are preferred in scenarios requiring high granularity and precision, such as in experiments ATLAS ITk[3] and ALICE ITS[4] at the LHC, where conditions include high radiation, intense heat, and the need for rapid data processing. Staves efficiently manage these challenges by incorporating advanced cooling and electronics directly into their structure.

Ladders are relatively simple structures used in particle tracking experiments. They are preferred in the experiments for their ease of construction and integration. The integration of cooling and electronics into the detector support is less critical for ladders, allowing for easier implementation and management. They are particularly useful in various experimental setups, such as fixed-target experiments, detector endcaps or configurations requiring specific geometrical arrangements. For example, the CBM experiment at FAIR uses ladders to provide robust and straightforward mechanical support in an environment characterized by high particle fluxes

[3]Inner Tracker of ATLAS (A Toroidal LHC Apparatus) Experiment

[4]Inner Tracking System of ALICE (A Large Ion Collider Experiment)

and the need for precise tracking of particle trajectories. Also, the STAR[5] experiment uses ladders in its SSD to enhance tracking capabilities within the TPC[6].

The importance of staves and ladders across these experiments highlights the diverse engineering and design solutions required to meet the varied objectives of different experiments. Whether optimizing for precision in high-luminosity collider experiments or for durability in fixed-target environments, the development of support structures exemplifies the specialized approaches needed to advance our understanding of support system. This thesis will focus on the integration and importance of support structure in STS of the CBM experiment.

[5] Solenoidal Tracker at RHIC

[6] Time Projection Chamber

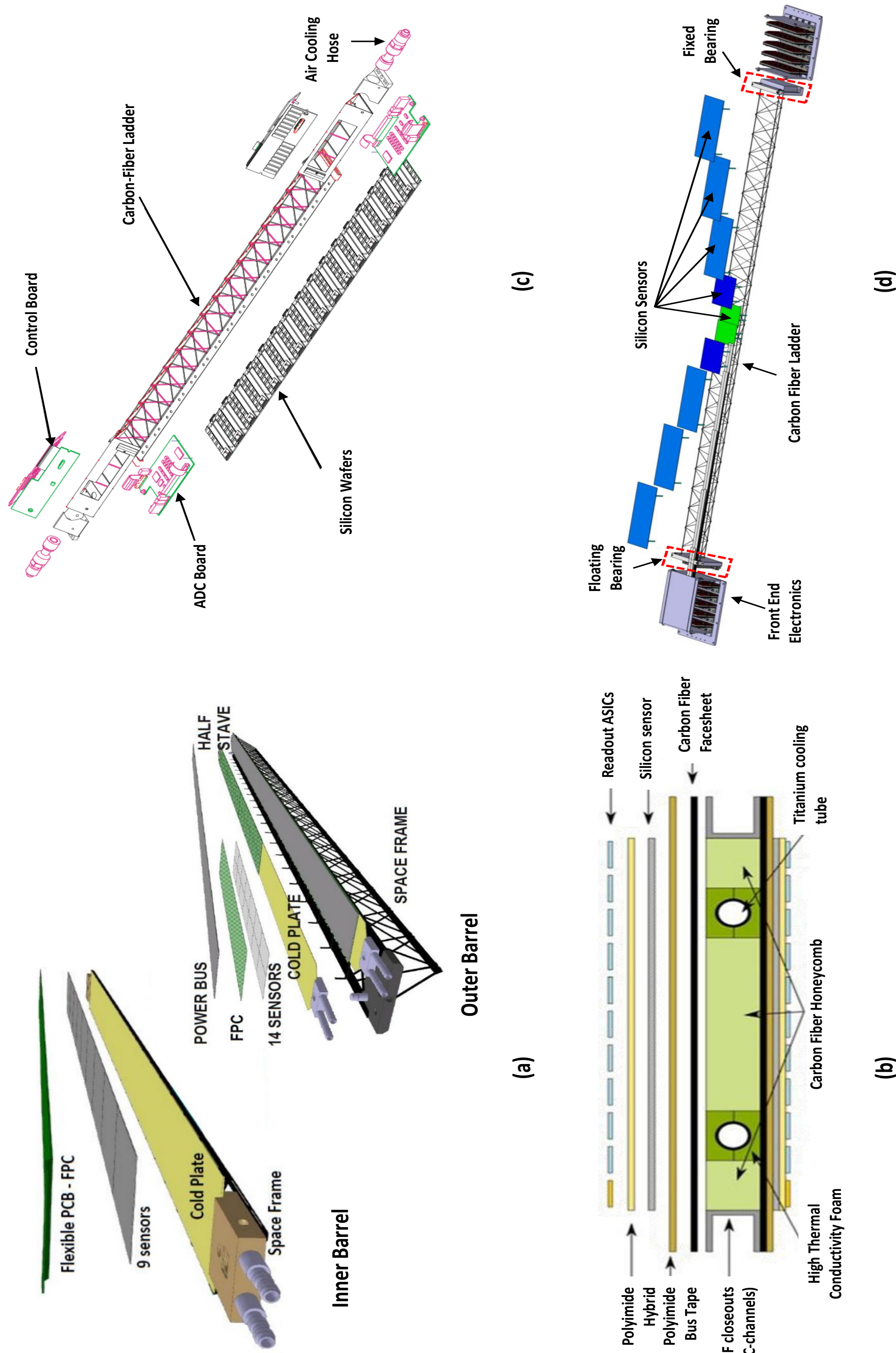

Figure 1.4: Schematic diagrams showing the support structures for different detector systems. (a) shows the staves in inner and outer barrel of ALICE ITS, [22] [23] (b) details the stave design of ATLAS ITk [24], (c) outlines the ladder configuration of STAR SSD, [21] and (d) presents the integration of silicon sensors on the carbon fiber ladder for CBM STS.

1.3 Compressed Baryonic Matter experiment

The Facility for Antiproton and Ion Research (FAIR) [53], located in Darmstadt, Germany, is an international accelerator facility designed to deliver heavy ion beams of high intensity through SIS100[7] accelerator ring (see Fig. 1.5). The research framework of FAIR is structured around four pillars: APPA (Atomic, Plasma Physics, and Applications), CBM (Compressed Baryonic Matter), NuSTAR (Nuclear Structure, Astrophysics, and Reactions), and PANDA (antiProton ANnihilation at DArmstadt), each dedicated to different areas of physics research.

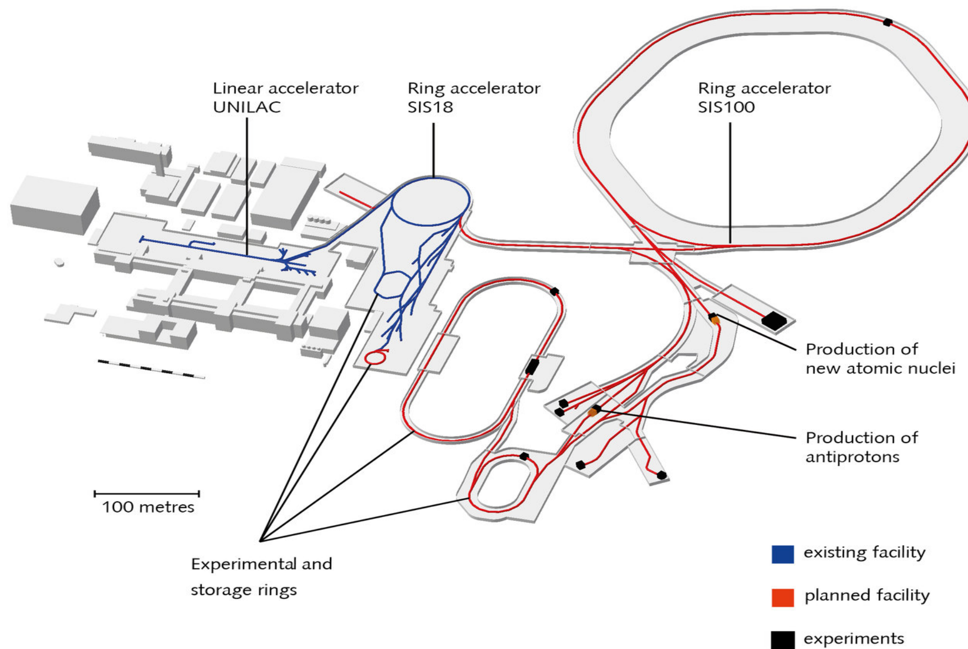

Figure 1.5: Overview of the FAIR experiment facility [53], where blue and red lines shows the existing and planned facilities. SIS100 will provide beam to the CBM experiment.

The SIS100 accelerator will deliver proton beams with energies up to 29 GeV and gold ion beams with energies up to 11 AGeV. This energy range is suitable for exploring the QCD phase diagram, where the critical endpoint (CEP) is theoretically predicted to be located [14]. One of the key features of the CBM experiment is its ability to handle high interaction rates, achieving up to 10^7 Au+Au collisions per second. This is made possible by the slow extraction process from the synchrotrons, which ensures a continuous beam structure with uniformly distributed beam particles over time.

Achieving a high collision rate places challenging requirements on both detector technologies and

[7] SchwerIonenSynchrotron, GSI, Germany

computational capabilities. To handle these rates, detectors must be both fast and radiation-resistant, equipped with free-streaming front-end electronics for high speed data acquisition. The high-speed data acquisition systems, coupled with high-performance computing resources, are essential for online event selection, using four-dimensional (space+time) event reconstruction [28].

CBM is a high precision, fixed target experiment, as shown in the Fig. 1.6 aiming to achieve interaction rates ranging from 100 kHz to 10 MHz. This is achieved by the detector's data acquisition system, which relies on self-triggering, time-stamped front-end electronics [27]. The angular acceptance of the detector is between 2.5° to 25° for all detector systems, to cover the mid and forward rapidity region over the energy range. The integration of high-intensity beams with a high-rate detector system in the CBM experiment provides an opportunity to conduct precise measurements of rare particles like dileptons, multi-strange hyperons, and hypernuclei. Equipped with a forward detector geometry, the CBM setup is specifically designed to maximize the detection and analysis efficiency of the rare particles. The overall physics program of CBM is outlined in [25] [26]. A brief description of sub-detectors of CBM is described below:

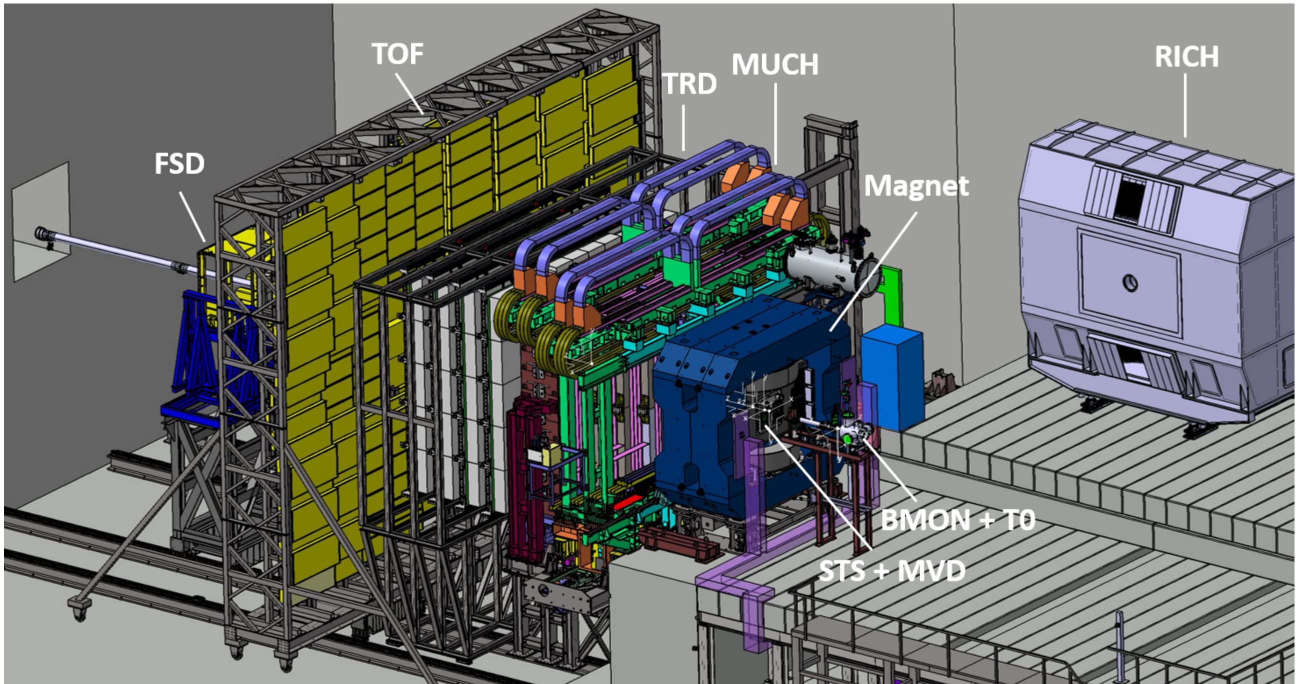

Figure 1.6: The experimental setup of CBM experiment at FAIR [29], with STS and MVD located inside the dipole magnet.

- Beam monitor, or T0 (BMON) detector ensures the quality of the beam by monitoring its position and time structure and to determine the start time of the reaction [30].
- Micro-Vertex detector (MVD) provides high spatial resolution necessary for identifying the vertices of particle decays, thereby allows to study the short-lived exotic particles, such as charmed mesons [31].
- Silicon Tracking System (STS) for tracking the charged particles and measuring their momentum [32]. STS along with MVD in the front, is kept inside a dipole magnet [33]. More details about STS are explained in Sec 1.4.
- Muon Chambers System (MuCh) for dimuon identification using RPCs[8] and GEMs[9] [34].
- Ring Imaging Cherenkov detector (RICH) to perform identification of di-electrons using Cherenkov radiation [35].
- Transition Radiation Detector (TRD) to perform pion suppression enhancing light particle identification [36].
- Time of Flight (TOF) wall for hadron identification using Multi-gap Resistive Plate Chambers (MRPCs) [37].
- Forward Spectator detector (FSD) will determine the collision centrality and reaction plane orientation [38].

1.4 The Silicon Tracking System

The Silicon Tracking System [32] [39] is the core tracking detector of the CBM experiment located inside a 1 Tm superconducting dipole magnet. The main role of STS is to provide track reconstruction efficiency ($>$ 95 %) and measure the momentum of charged particles ($<$ 2%) produced during the beam-target interaction. Since the momentum resolution is dominated by multiple scattering of the detector material, therefore, the material budget of STS components is kept as low as possible. STS comprises of 8 tracking layers, referred to as stations, covering the physics aperture of $2.5^\circ \leq \theta \leq 25^\circ$. These stations, as shown in Fig. 1.7, are positioned between 30 cm and 100 cm downstream of the target. To achieve a low material budget, the

[8] Resistive Plate Chambers

[9] Gas Electron Multipliers

front-end electronics and the readout electronics are placed out of the physics acceptance, in the detector's periphery.

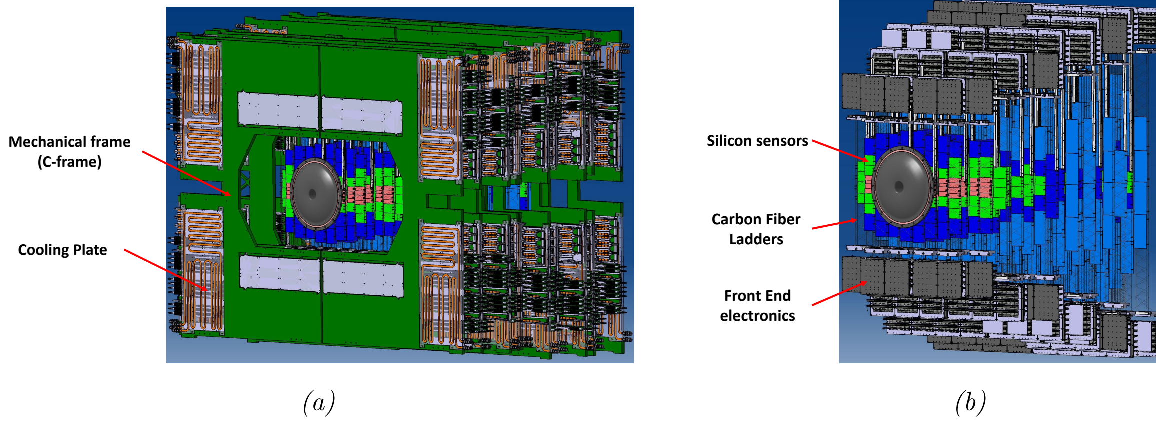

(a) (b)

Figure 1.7: (a) STS tracking stations with C-frames equipped with the cooling plate are shown. (b) Conceptual design of STS with silicon sensors (in blue, green, and red color) mounted on the ladders, assembled on the mechanical C-frames. The Front-End Electronics is located outside the periphery of the detector [40].

Within the acceptance region of the detector, 876 double-sided silicon micro-strip sensors from Hamamatsu Photonics KK will be installed. These sensors are 320 μm thick, as shown in Fig. 1.8 (a), and come in four different variants. A sensor features 2048 strips, with a stereo angle of 7.5°on the p-side strips and perpendicular n-side strips, to minimize the possibility of ghost hits during the particle tracking. Each sensor after the delivery has been electrically and optically inspected and assigned with the quality grades depending on the sensor's performance[10] [41].

Each sensor, 320 μm thick as shown in Fig. 1.8 (a), is connected to two Front-end Boards (FEBs) via 32 ultra-lightweight aluminum polyamide micro-cables, making it the functional building block of the STS, referred to as a detector module (Fig. 1.8 (b)). These micro-cables, which can be up to 50 cm long, are covered with a shielding layer to reduce electromagnetic interference and noise levels. Each FEB contains eight SMX ASICs[11]. The sensors contribute 0.34 % X_0 to the total material budget of the station, while the micro cables add up to a maximum of 1 % X_0 per station. By optimizing the design and components of STS, it allows for 5-D tracking in the STS [27].

[10] The details regarding the quality grades have been summarised in an internal Technical note and depending on the sensor's performance they are assigned the positions in the sensor geometry.

[11] Application-Specific Integrated Circuits

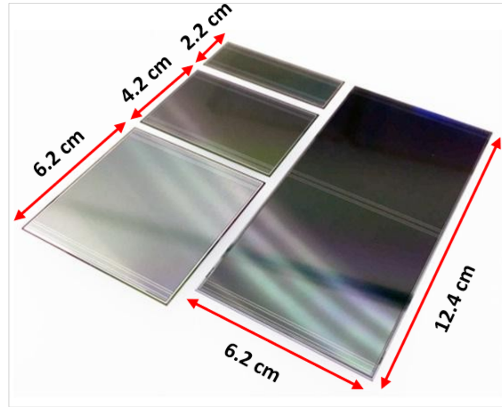

(a)

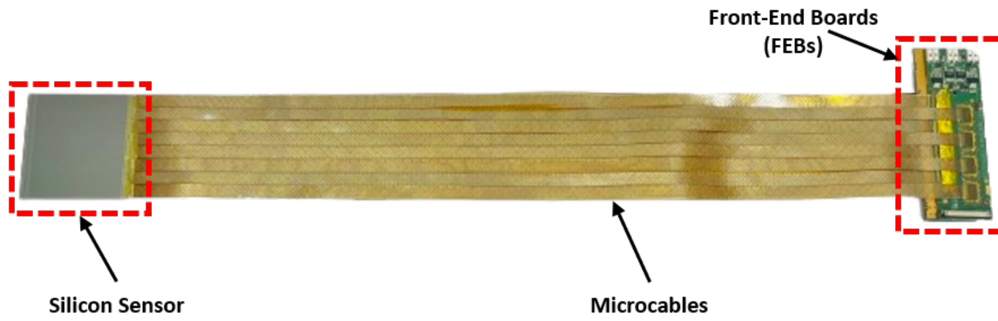

(b)

Figure 1.8: (a) Variants of Silicon sensors with width of sensor equals 6.2 cm and length varies from 2.2 cm, 4.2 cm, 6.2 cm and 12.4 cm distributed over the stations. (b) STS module after connecting to its components. The module afterwards is covered with the shielding layer and the FEBs are glued to the cooling shelves.

Ensuring the optimal functionality of the detector requires careful positioning of the sensors within the detector geometry. To achieve this, the silicon sensor modules are mounted on 106 carbon-fiber support structures, known as ladders (see Fig. 1.4 (d)), with alignment accuracy within the range of $\pm 100\,\mu$m. The precision mounting of the modules on the ladder is optically inspected to acquire the input for the track-based alignment used for the particle reconstruction. More details about the precision mounting of sensors on the ladders will be covered in the next chapter. After the assembly of ladders with the modules, these ladders are shifted onto a C-shaped aluminum-type ladder holding structure, referred to as the C-frame, which in turn forms a station of STS. Each C-frame can accommodate up to four ladders (see Fig. 1.9), arranged according to the STS geometry requirements.

The STS is housed within a CF-foam enclosure providing thermal insulation and a central section for the vacuum beam pipe. In addition to the components within the detector's acceptance region, the peripheral electronics dissipate approximately 40 kW of heat, primarily from the front-end electronics. To manage this heat, NOVEC coolant capable of removing up to 50 kW of dissipated heat will be used inside the detector box.

Given the high radiation environment, the detector must withstand an energy deposition equivalent to a neutron fluence of 10^{13} n_{eq}/cm^2 within 10 years of operation at SIS100. To mitigate radiation-induced effects and prevent reverse annealing, the sensors will operate at 10°C, with excess heat dissipated through convective gas flow. For regions close to the beam pipe, excess heat will be removed using perforated tubes that blow cold air directly onto the sensor surface. Although direct air exposure could induce sensor vibrations, this impact has been cross-checked and addressed in this thesis.

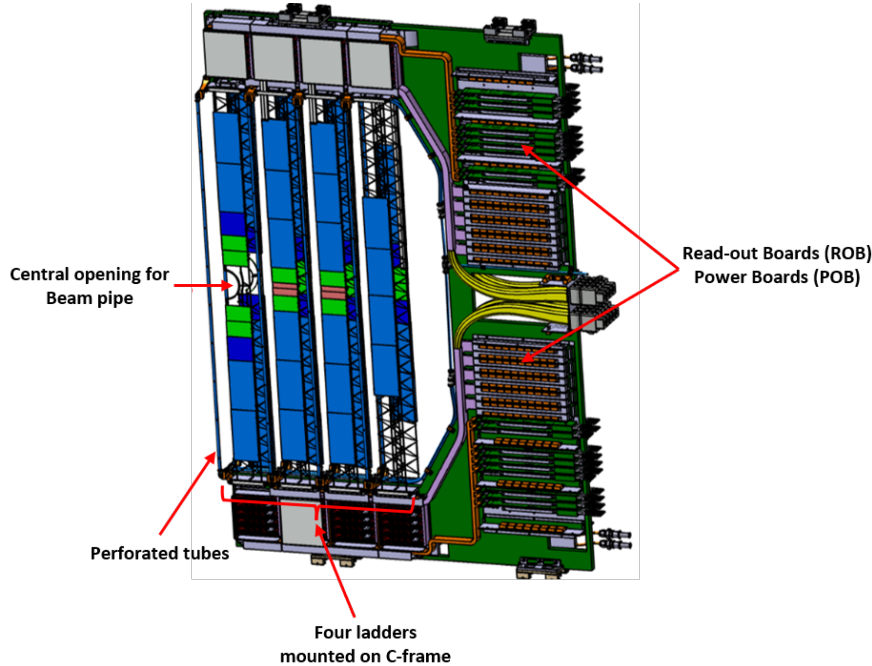

Figure 1.9: Illustration of the conceptual design for the C-frame, which shows four mounted ladders in the front. On the right side of the C-frame, the read-out and power electronics are integrated, allowing for efficient signal processing and power distribution. A perforated tube, running along the entire length of the central ladders, is positioned to channel cold air directly onto the sensor surfaces.

1.5 Scope of the thesis

The main role of the Silicon Tracking System (STS) in the CBM experiment is to track the momentum of charged particles. As a tracking detector, the STS aims to maximize particle tracking by optimally assembling the sensors. Silicon sensors, being key components, must be placed with high precision on support structures to ensure accurate tracking. To minimize the multiple scattering of particles, the detector components with low material budget are selected.

The objective of this thesis is to optimize the stability of sensors on ultra-light carbon fiber ladders, ensuring precise mounting to enable accurate reconstruction of particle tracks. Additionally, the stability of the components under the extreme operating conditions of the detector has been tested and summarised. The thesis is structured into five chapters, focusing on the assembly and performance of the sensors after assembling on the ladders and the testing of Thermal Interface Materials (TIM) required for module functionality in extreme conditions.

Chapter 2 focuses on the testing of TIMs used between the FEBs and cooling shelves under extreme temperature conditions of STS. It also covers the thermal cycling of modules to identify failure scenarios and establish boundary limits for the STS operating temperature conditions.

Chapter 3 addresses the experimental challenges faced during the precision mounting of modules on the ladder, following a well-defined assembly procedure and advanced optical metrology procedure. The goal is to optimize the process to ensure reproducible results within the defined precision for all ladders.

Chapter 4 focuses on the stability of the ladder after the integration, focusing on the impact of excess cooling required for sensors close to the beam pipe, which may cause vibrations. This chapter covers the measurement and analysis of the effects of cooling on sensor stability and the resulting vibrations on sensor surfaces.

Chapter 5 provides a summary and outlook based on the learning gained from this work. By enhancing sensor stability and ensuring precise assembly and operation, this work improves the capability to accurately track charged particles under the challenging conditions of the STS.

Chapter 2

Thermal studies of STS components

The STS consists of 876 detector modules that are configured to form 8 tracking stations. One of the main challenges in STS is to achieve a momentum resolution of $< 2\%$. A low material budget is mandatory, thus the STS has been designed in such a way that sensors are mounted within the acceptance region (2.5 to 25 degrees) while the heavier electronics is positioned outside of the detector acceptance. The electronics mainly include front-end electronics boards (FEBs), power boards (POBs), and readout boards (ROBs). The FEBs alone dissipate approximately 12.5 kW across 3.5 m^3 detector volume. These FEB boxes are connected to cooling plates which use 3M^{TM}NOVEC^{TM} 649 [66] as a cooling liquid, thereby reaching temperatures as low as -40 °C, if needed.

The FEB boxes are designed to operate as an efficient heat bridge, channeling the power dissipation from FEEs to the cooling plates. This heat transfer involves an intricate combination of thermal interface materials (TIMs), as well as thermal vias on 16-layer PCB boards, different adhesives used during module production, and aluminum heat bridges such as cooling T-shelves. The major components that produce heat on the FEBs are STS-MUCH-XYTER (SMX) Application-Specific Integrated Circuit (ASICs) and the Low-Dropout (LDO) regulators, contributing nearly 10 W of heat per FEB. Therefore, it is imperative to verify the FEB's capability to withstand the imposed temperature range during operation. Before directly examining the complexities of the FEBs, it is crucial to establish an understanding of the various components of a module, as well as the intricate process of module fabrication.

2.1 Introduction to STS module assembly

The sensor modules for the STS consist of three main components: a double-sided double metal silicon microstrip sensor, signal transmission micro cables of the different lengths according to the position in a station, and two types of front-end-boards (FEBs) to read out p- and n- side, as shown in Fig. 2.1. The assembly process of STS modules is a comprehensive procedure that involves testing components, positioning or fixing them at the right position with precision and thorough documentation at each stage, noting any encountered issues. The assembly procedure is divided into several steps which include:

- Two layers of micro-cables with 64 lines each, are TAB (Tape Automated Bonding) bonded to the ASICs, followed by the connectivity tests. The compound object of micro-cable and ASIC is referred to as chip-cable.
- Chip cables are die-and-wire bonded to the FEB followed by functionality tests of wire bonded ASICs. The ASICs are then protected with the glob top and covered with a small shielding layer which is soldered to the FEB.
- The other side of the chip cable is TAB bonded to the sensor and connectivity tests are performed. The cable is later fixed to the edge of the sensor using glue to provide pull relief.
- Once the module is assembled and carefully tested at each step, the FEBs are attached to the cooling shelves. This is done using a thermally conducting but electrically isolating, Thermal interface material (TIM) to ensure efficient cooling and to prevent any electrical connections between FEB and the cooling shelf. This will be discussed in detail in this chapter.
- The last step of module assembly is the fixation of shielding layers on both sides of the module to reduce the noise level and prevent shorting between the stack of micro-cables.

Since the sensors are delicate, therefore they need to be dealt with care. During the assembly of STS modules, different adhesives at various steps of the assembly are used for strong, durable yet flexible bonding. Any misalignment during the assembly process could lead to unusability and the damage of modules. Therefore, it is important to characterize the properties of the material. There are several factors to be considered while using any glue such as electric

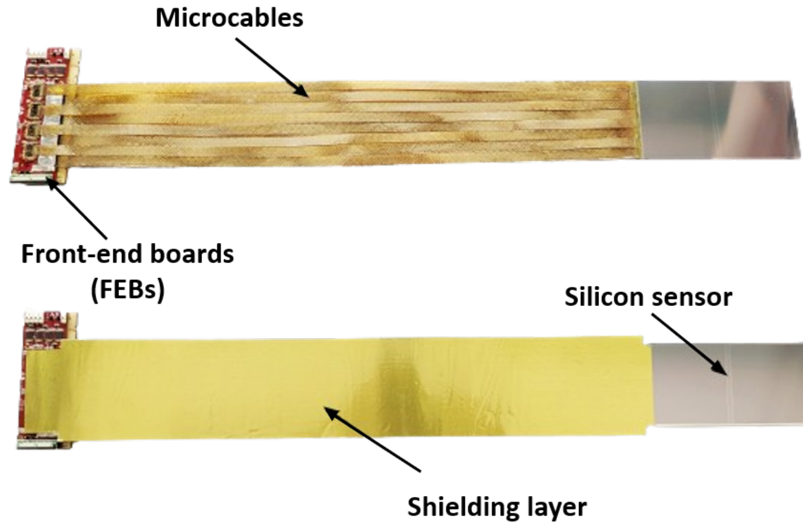

Figure 2.1: Image of an STS module (top) before and (bottom) after connecting the shielding layers of the microcables ([59]).

insulation, thermal conductivity, viscosity, operating conditions, radiation hardness, and many more. The studies have been performed to test for the properties of glues used in module assembly and have been summarised in [67].

The adhesives used during the building of a module will be partly in the acceptance region while some adhesives will be used in the area outside the acceptance where electronics are placed. Given the requirement for electronics to be cooled down at lower temperatures, it is imperative to assess the functionality of the adhesives within the electronics proximity to ascertain the potential risk of any failures. This includes TIM implementation between FEBs and cooling shelf as well as between cooling plate and FEB box. Applying any TIM after the module is assembled already is challenging since it involves a lot of risks for the module to go out of usage. Additionally, a well-defined procedure is needed to ensure the proper cooling of the major heat-generating components, namely the ASICs and LDOs. This chapter will focus on the optimization of TIM planned to be used between the FEBs and cooling shelves and Graphit sheets were decided to be used as the TIM between FEB box and the cooling plate.

2.2 Requirements of TIM between FEBs and cooling shelf

Each FEB is equipped with 2 rows of readout ASICs, with 4 ASICs in each row (see Fig. 2.2 (left)) and is used to read out one side of a sensor, consisting of 1024 channels. Two FEBs are needed to read out one module and each FEB box can have a maximum of ten FEBS, required to read out the half ladder with 5 modules stacked together. This suggests that from the overall heat dissipated within the enclosing box of STS, FEBs are one of the largest contributors. To address this concern, it becomes critically important to implement a strategy for managing this heat. The approach to cool down the FEBs involves their integration with a cooling shelf, made of aluminum due to its good thermal conductivity properties [68]. Both the FEBs of each module will be attached to this cooling shelf. Given the constraints of the FEB box dimensions, asymmetric T-shaped cooling shelves were chosen. This design ensures ample space is available on both sides of the shelf to accommodate the FEBs, with one side extended to screw the cooling shelf into the FEB box (Fig. 2.2 (right)).

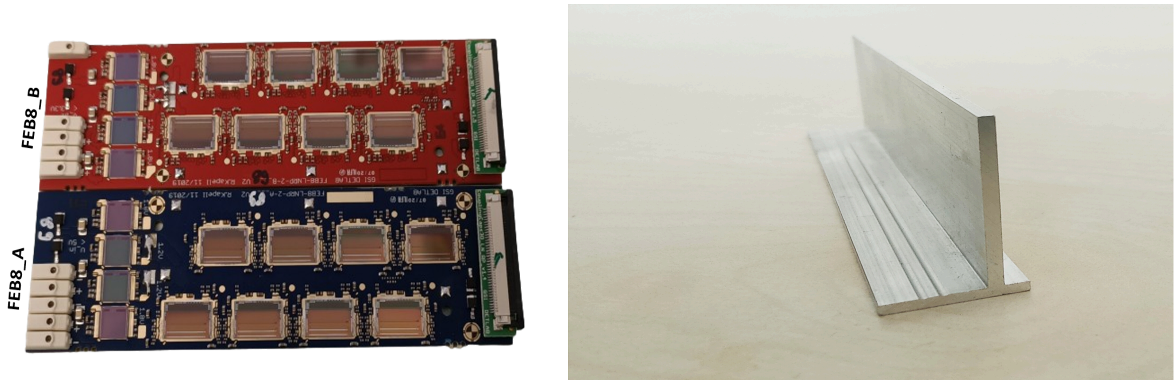

Figure 2.2: (Left) Image of FEB8_A *(Blue) and* FEB8_B *(red) that connects the p-side and n-side of the sensor, (Right) Image of an asymmetric T-shaped cooling shelf, having length equal to that of FEBs.*

At the same time, the back planes of the FEB (copper) and the shelf (aluminum) cannot be directly connected due to both being metals; a direct connection would result in a short circuit, potentially damaging the FEBs. Therefore, to achieve the close proximity between FEB and the cooling shelf and facilitate the efficient heat transfer, a good thermal interface is needed. However, to accomplish this goal, there are several requirements to be met while choosing the interface which are mentioned below:

- **Radiation hardness:** Due to the high radiation exposure during STS operation, the TIM must be radiation-hard. This is fundamental to ensure reliable electronics operation even after prolonged exposure.

- **Thermal Conductivity:** When two materials are glued together, it becomes important to choose an interface that enables effective heat transfer between them. An interface with high thermal conductivity (> 1 W/mK) is preferred to ensure that the heat is efficiently conducted between the glued materials, promoting optimal thermal management and preventing overheating.

- **Coefficient of Thermal Expansion (CTE):** The chosen TIM should be able to compensate for any thermal stresses that may arise due to the mismatched CTE between copper and aluminum. The interface should be able to accommodate temperature-induced changes, either by closely matching the CTE of both materials or by acting as an elastic medium.

- **High dielectric strength:** Since the FEBs and cooling shelves are both conducting surfaces, the interface material acts as an insulating layer that separates the two surfaces. Therefore, the interface should have high dielectric strength to prevent the electric breakdown and discharge between the two surfaces.

- **Room temperature curing:** The curing of the interface at room temperature plays an important role in the final assembly stages, particularly when fixing the FEBs to the cooling shelf. At this stage, the sensor has already been connected with the FEBs via micro-cables. Hence, selecting an interface that cures at room temperature is favorable. This approach eliminates the need to expose the sensor and micro-cables to high temperatures, thereby simplifying their handling.

- **Viscosity:** It is an important property of TIM that ensures the formation of a consistent layer between two surfaces, enhancing heat transfer efficiency. Materials with low viscosity can improve thermal conductivity but may not maintain their shape. On the other hand, materials with high viscosity may not be able to fill gaps and voids. Thus, selecting an optimal viscosity is important for maximizing heat dissipation, easy handling, and ensuring good connection between the surfaces.

- **Permanent joint:** For the surfaces to remain in place and maintain their performance over time, a permanent joint provided by the interface is essential. This requires treatment

of surfaces, i.e., they need to be clean and free from dirt. The bonding surfaces especially aluminum, should be rough enough to allow the interface to adhere firmly but not so rough to create voids or air bubbles. Therefore, the interface chosen should be able to provide firm bonding between the surfaces and withstand the thermal and mechanical stress that might occur during the operation.

- **Operating temperature:** The selected TIM must be able to maintain its thermal and mechanical properties under both realistic and worst-case scenarios. The operating temperature of STS electronics is expected to be around -10 °C when the temperature of the coolant can go as low as -40 °C. So, the material should handle temperatures till -40 °C.

The list of requirements described above illustrates that selecting an appropriate thermal interface is essential for effective heat transfer between the FEBs and the cooling shelf. Based on the outlined properties, it's crucial to choose the right interface, as it must be effective not only under regular operating conditions but also in worst-case scenarios. Also, equal consideration should be given to the practicality of the chosen interface from a module assembly perspective, ensuring alignment of the interface material within the overall module structure.

2.2.1 Optimization of TIM between FEB and cooling shelf

To dissipate the heat generated by the FEBs, they are attached to the cooling shelf. The thickness of the cooling shelves significantly influences the heat conduction from the FEBs. Though a thicker aluminum shelf can absorb and distribute heat more effectively, the thickness is limited by the gap between the two FEBs. The size of the gap between the two FEBs is determined by the length of the micro-cables. Using the STS geometry, the optimal gap size was determined to be approximately 3 mm between two FEBs.

The focus in optimizing this 3 mm gap is to maximize the cooling shelf's thickness for enhanced heat dissipation while minimizing the thickness of the TIM required to attach the FEB to the cooling shelf. Therefore, it was decided to keep the cooling shelf thickness at 2.7 mm with 0.15 mm thickness for the interface on each side of the shelf, as shown in Fig. 2.3.

It is also important to understand that when two solid surfaces, such as aluminum (cooling shelf) and copper (FEBs), come into contact, their surfaces are not perfectly smooth and they only touch at specific points on their interface. This actual contact area is usually much smaller, often less than 2 % of the expected contact area [69]. In regions where there's no direct contact

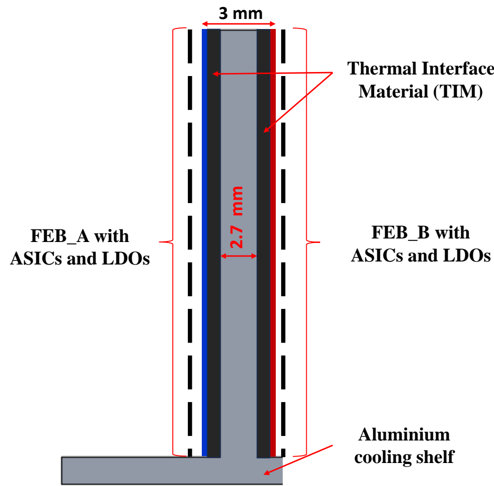

Figure 2.3: Sketch showing the spacing between two FEBs (shown in blue and red), where the gap is filled with the cooling shelf and TIM.

between the two surfaces, a small gap exists. This gap can be filled with a third substance, which could be air, gases, liquids, grease, or even tiny solid particles. The thickness of this gap can vary from as little as 0.5 μm for very smooth surfaces to about 60 to 80 μm for very rough surfaces.

Heat transfer across such surfaces involves conduction through the actual contact area and conduction through the interface in the non-contact area. In cases of elevated temperatures or vacuum conditions, radiation heat transfer through open spaces can also be significant. This emphasizes the importance of selecting a thermal interface that fits well within the 0.15 mm gap, ensuring complete surface coverage and optimal operating temperatures and prevents overheating. TIMs with high thermal conductivity are designed to offer a lower thermal resistance path for an efficient heat transfer path with thickness varying from 25 μm to around 250 μm. The various thermal interface options available are as follows:

- **Thermal adhesives:** They are viscous, gel-like materials that stick components together and allow heat to pass through. They create a durable, semi-permanent bond between the components, making them suitable for long-lasting applications. However, it can be challenging to rework once they are cured.

- **Thermal grease or paste:** Thermal grease is a semi-liquid or paste-like substance used to improve heat transfer. While it enhances heat dissipation by filling gaps, it offers less adhesive strength compared to the adhesives. This flexibility can be advantageous

during the disassembly or maintenance, but it might dry out over time and need periodic reapplication.

- **Thermal pads:** These pads are placed between a PCB and heat sink to distribute heat evenly. They are easy to apply and can be electrically or non-electrically conductive, with an adhesive bond or without. However, they may not eliminate all microscopic air gaps, and there may be degradation over time.

- **Thermally conducting adhesive film:** These films are die-cut into complex shapes to bond specific parts while retaining conductivity. They offer consistent application and performance due to an even distribution of conductive material, are machine-automobile, and have no risk of overflow. Thickness can be adjusted, but they may not fill certain roles such as heat sinks, and there may be microscopic air gaps.

In the context of the STS module requirements, the two most viable options are thermal adhesives and thermal pads. While thermal adhesives demand a certain level of precision during application, they offer better performance characteristics. On the other hand, thermal pads are user-friendly and necessitate minimal research and development efforts. Initially, the gel-type silicone thermal interface material GCS-060-S [70] was selected for its flexibility and ease of adhesion to surfaces. Additionally, 1 mm thick thermal pads were chosen for their flexibility, despite exceeding the target thickness. However, during assembly, the pads compressed under pressure, simplifying module handling.

The modules were assembled using the thermal pads and were mounted on a ladder, which was later placed vertically onto a C-frame. Over the span of a few months, it was observed that the vertical mounting caused the thermal pads to detach from the FEBs, contradicting the intended purpose of using thermal interfaces.

To address this issue, two solutions were proposed. The first involved clamping the FEBs after applying thermal pads, but this was not feasible due to design constraints. Therefore, a second solution was chosen, i.e., replacing the thermal pads with adhesives. Considering the requirements outlined earlier, various thermal adhesives, previously used in different experiments [71, 72] were examined. Multiple options were evaluated to determine the most suitable adhesives for the thermal interface between FEBs and the cooling shelf of the STS system.

2.3 Survey of thermally conductive adhesives

After a thorough analysis of the prerequisites for the TIM, we have identified three adhesives that fall within the specified boundary conditions. The chosen adhesives are - Stycast 2850 FT with 23 LV catalyst [73], Dowsil SE 4445 [74], Bergquist EA1805 [75] - each exhibiting varying levels of viscosity. The summary of the main properties of adhesives has been compiled in Table 2.1.

Table 2.1: Summary of the important properties of the selected adhesives.

Product	**Thermal conductivity (W/m.K)**	**Dielectric Strength (kV/mm)**	**Operating temperature (°C)**	**Viscosity (Pa.s)**	**Curing at 25 °C (hrs)**	**Hardness (Shore D)**	**Thermal Expansion (ppm)**	**Radiation hardness (n_{eq}/cm^2)**
Stycast **2850 FT (+23LV)**	1.02	14.8	-65....+105	5.6	16-24	92	39.4	8 x 10^{15}
Dowsil **SE4445**	1.34	5.0	-45....+150	15	24+	-	-	10^{21}
Bergquist **EA1805**	1.80	10.0	-40....+125	60.0	10	90	-	-

Amongst the three adhesive candidates, Stycast is classified as the low-viscosity glue, Dowsil as the medium-viscosity adhesive, and Bergquist stands out as a high-viscosity adhesive. For adhesives ranging from low to medium viscosity, using a glue dispenser is advised to maintain optimal viscosity during application. Choosing adhesives with lower viscosities offers the benefit of providing sufficient adjustment time for components, such as FEBs and cooling shelves, before the curing process. However, maintaining precise control over viscosity can be challenging. In contrast, Bergquist's clay-like viscosity negates the necessity for a dispenser, and potentially simplifies handling and accelerates the process.

One of the main considerations when using adhesives lies in achieving the thinnest possible application to prevent voids that might obstruct the conduction of heat generated by electronics. Additionally, the adhesive's ability to provide good mechanical and thermal strength is crucial, given the permanent nature of the bond. However, characterizing TIMs poses significant challenges due to two main factors: TIM materials are very soft, and the sample thickness is very small. Therefore, to determine the best-suited adhesive among the three candidates, extensive characterization tests have been performed to evaluate their properties.

2.3.1 Thermal tests

During the detector operation, adhesive joints are frequently exposed to a range of conditions that could potentially impact their performance. Given that these materials can undergo differential expansion or contraction during temperature fluctuations, there is a significant risk of weakening the adhesive bond over a prolonged duration. Therefore, it becomes imperative to study adhesive materials under an extreme temperature range to ensure optimal device performance and longevity. This is achieved by exposing adhesive joints to changes in temperature, referred to as thermal cycling.

The main goal is to see how the different types of adhesive materials react to the ups and downs of temperature, and how they interact with the materials they're sticking together. The CTE mismatch between aluminum and copper poses a significant challenge, as differing expansion rates can lead to mechanical stress and potential failure of the adhesive bond. This helps to understand which adhesive works best as the interface between the aluminum and copper. Although the thermal conductivity of all the components is known separately, it becomes challenging to predict the thermal conductivity of the combination since heat propagation through the FEBs to cooling shelves is sequential. To address this question, it is important to assess the effectiveness of three distinct candidate adhesives under similar temperature scenarios and also to identify the mechanism that could potentially lead to adhesive failures.

2.3.1.1 Test setup for thermal cycling

The purpose of the thermal cycling was to replicate the operating temperature scenarios and investigate the potential failures amongst the glue candidates. Given that each FEB dissipates around 11 W of power during the nominal operating scenario, it was important to evaluate if the glue could handle the differences in thermal expansion coefficients between the FEB's back-plane and the cooling shelf when operated at nominal power dissipation.

To test the same, thermal dummy FEBs were designed to mimic the thermal behavior of the real FEBs while minimizing the complexity of the read-out electronics. This was done by depositing copper meanders on the Printed circuit boards (PCBs) as the heat producing elements instead of using ASICs and LDOs, allowing them to replicate their different power densities. It must be noted the rest of the PCB structure, most importantly thermal vias, are identical to the real FEB PCB.

To perform thermal cycling, test samples were prepared where two thermal dummy FEBs were glued to both sides of a cooling shelf, as can be seen in Fig. 2.4. After attaching the FEBs to the cooling shelf, the cooling shelf was screwed to a cooling block. This cooling block mimics the cooling plate that will be used in the final system where coolant will pass through. These cooling blocks were mounted in a Binder MK chamber [76], where FEBs were thermally cycled. Subsequently, the FEBs were powered using a power supply, and an Arduino microprocessor was used to ensure precise monitoring of the DS-18 temperature sensors.

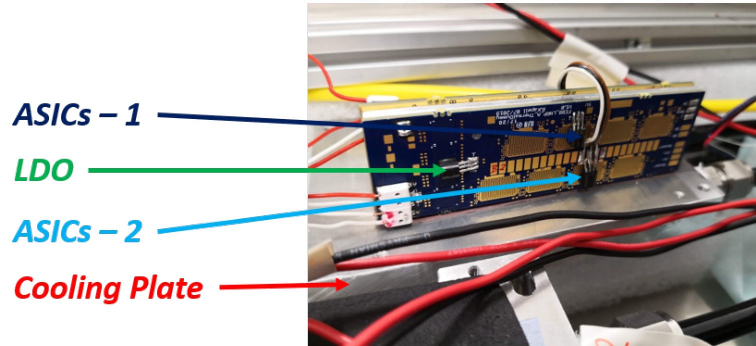

Figure 2.4: Thermal dummy FEBs with DS-18 temperature sensors glued on the copper meanders. Three sensors have been positioned: two to monitor the temperature of individual ASIC rows, and the third to measure the temperature of the LDO regulators. FEBs were glued to the cooling shelf with different glue candidates (Dow-corning in this image) and finally mounted on to a cooling plate.

Given that the operating temperature for the STS electronics might go as low as -10 °C, it was planned to perform the thermal cycling within a temperature range of +40 °C to -15 °C, with the cooling plate maintained at these temperatures. While the final STS system will use NOVEC coolant for cooling the plates, an alternative coolant, Kryo 51 [64], was used for the thermal cycling activities. A total of 25 thermal cycles were conducted within the specified temperature range. During each cycle, the setup was held stable at extreme temperatures for 2 hours as shown in Fig. 2.5.

The plot highlights that LDOs are hotter compared to ASICs. This is attributed to the voltage drop in the LDOs, leading to power dissipation and subsequent heat generation. This observation makes LDOs the critical component to be considered during thermal cycling. Additionally, the temperature difference between the rows of ASICs is comparable. To understand how well the interfaces can handle the stress induced by 25 temperature cycles, the difference in temperature between the cooling block and the LDO regulator has been calculated. This helped to get an understanding of how the temperatures change during the cycling and how they vary for the different interfaces.

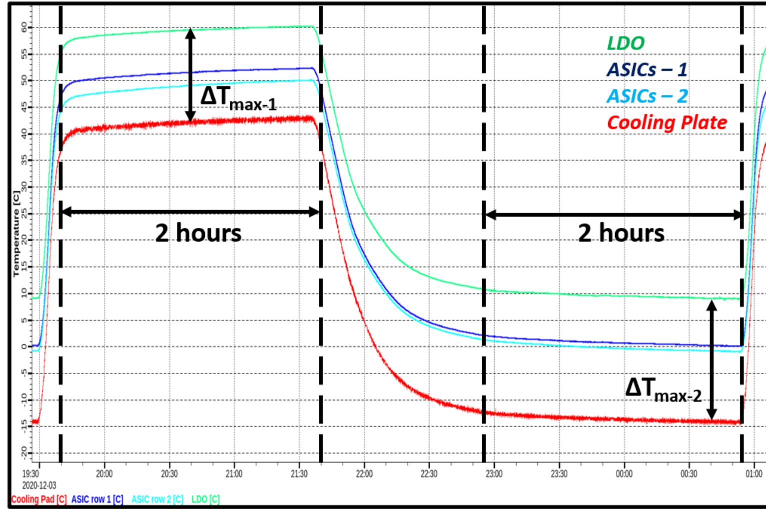

Figure 2.5: Plot showing single thermal cycle from +40 °C to -15 °C for one thermal dummy FEB where different colors represent the temperature variation in ASICs, LDOs with respect to the cooling block.

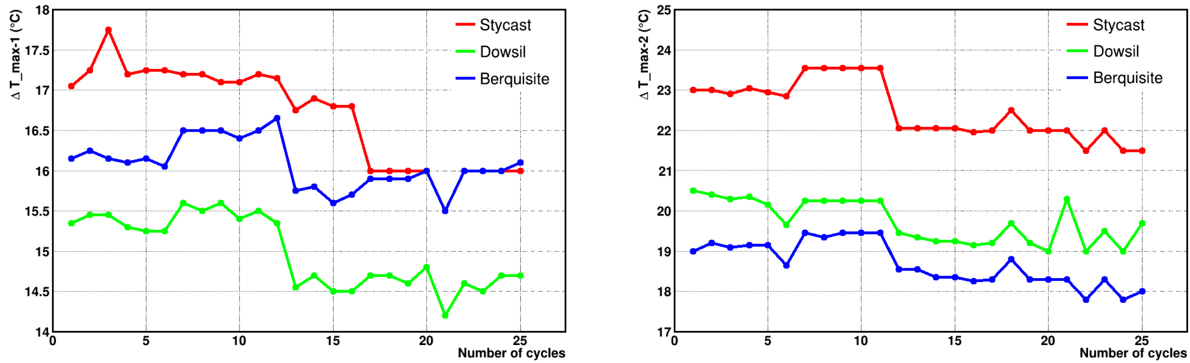

Figure 2.6: Plot showing the variation of temperature with 25 cycles for different glues.

The plots presented in Fig. 2.6 demonstrate the temperature differences observed in three interfaces. These temperature differences were calculated as ΔT (= $T_{LDO} - T_{Coolingblock}$), plotted on the y-axis, and the x-axis indicating the number of thermal cycles. In the left plot, $\Delta T_{max\text{-}1}$ represents the temperature difference at high temperatures between the LDO regulators and the cooling plate, while $\Delta T_{max\text{-}2}$ represents the temperature difference observed at lower temperatures (see Fig. 2.5).

From the depicted trends in the plots, it becomes apparent that all examined adhesive samples showed almost negligible deterioration after 25 cycles. As a result, the thermal cycling analyses conducted did not provide significant differentiation among the different adhesives in terms of identifying the best-suited TIM to be used between FEBs and the cooling shelf.

Given that thermal cycling alone was not enough to identify a suitable interface, the next crucial step was to subject these adhesive candidates to mechanical stability. These tests intend to check the adhesive's ability to withstand mechanical stresses and ensure the long-term structural integrity of the glued FEBs. By combining thermal and mechanical assessments, we aim to identify the optimal TIM that not only has good thermal conductivity but also meets the mechanical requirements. Once the glue candidate is shortlisted, more rigorous tests will be conducted using actual FEBs instead of thermal dummy boards.

2.3.2 Mechanical stability test

To evaluate the mechanical strength of an adhesive between two substrates, a lap shear test is performed [65]. This test allows for measuring the shear strength of the adhesive when bonded between aluminum and copper. Additionally, it allows for an examination of the mode of failure, offering insights into the suitability of the adhesive for applications subjected to mechanical stresses.

All materials exhibit distinct coefficients of thermal expansion and they undergo differential expansion and contraction in response to temperature fluctuations, potentially compromising the integrity of the adhesive bond over time. Various operational factors, such as thermal stress, radiation exposure, application method, vibration, and gravitational forces, can also affect these adhesive joints. Therefore, conducting lap shear tests helps ascertain whether a given adhesive can withstand these forces when adhering to the metals.

Moreover, to achieve a robust bond between the two surfaces requires effective wetting of the adhesive on both substrates. Wettability, denoting the adhesive's capacity to spread across a solid surface, plays a crucial role in ensuring maximum coverage with minimal voids. The concept of adhesive wetting is based on the work function ($\mathrm{W_a}$), described by the equation:

$$\mathrm{W_a} = \gamma_{\mathrm{lv}} + (1 - \cos\theta) \tag{2.1}$$

where, γ_{lv} is surface energy at solid liquid interface, θ is equilibrium contact angle. The contact angles vary as per the roughness of surfaces, where $\theta > 90\ ^{\circ}\mathrm{C}$ degrades wettability, while $\theta < 90\ ^{\circ}\mathrm{C}$ indicates favorable wetting. In the case of $\theta = 0\ ^{\circ}\mathrm{C}$, complete wetting occurs, resulting in full surface coverage, as can be seen in Fig. 2.7.

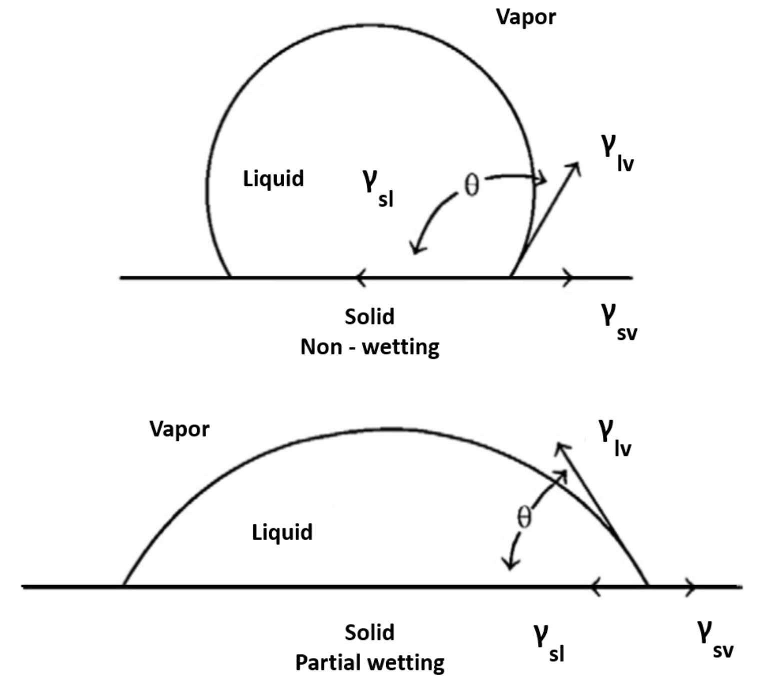

Figure 2.7: Wettability of adhesives with respect to contact angle [77].

2.3.2.1 Testing procedure

To examine the mechanical strength of the chosen adhesives, eight samples were prepared for each adhesive. These samples consisted of aluminum and copper-clad FR4 sheets resembling the surfaces of the cooling shelf and FEB with comparable thickness, measuring 5×10 cm^2, with an overlap of 5×5 cm^2 as shown in Fig. 2.8.

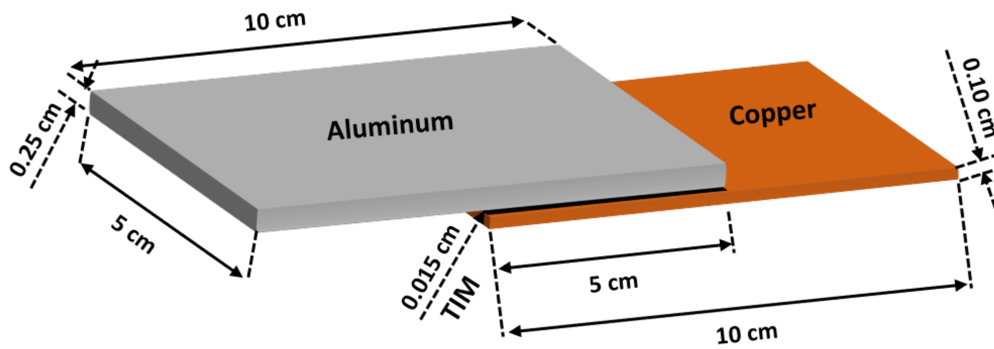

Figure 2.8: Side view of the sample for lap shear test: Aluminum and copper with overlapping region covered by different adhesives aiming for a thickness of 0.015 cm.

After the preparation of the samples, a curing process was carried out at room temperature according to the provided data sheets. The samples were divided into two sets of four objects each: one set for shear testing after the curing of glue, and another for first the thermal cycling of samples followed by shear testing. The thermal cycling involved performing 10 cycles in a climatic chamber, ranging from -40 to +40 $^{\circ}$C, and each extreme temperature was maintained for 1 hour. The purpose of thermal cycling was to investigate how temperature variations might affect the mechanical stability of the bond.

The lap shear test was conducted to observe the extension in the samples and determine the applied load required to achieve the extension. The test was performed using an Instron 5940 machine [78], based on the principle of mechanical testing through controlled application of force. The samples were clamped vertically between the grips and pulled at 180° at a constant rate (see Fig. 2.9). The pulling force was gradually increased until the adhesive joint failed. By measuring the applied force and monitoring the extension of the samples, it was possible to precisely quantify the mechanical properties of the adhesive bonds.

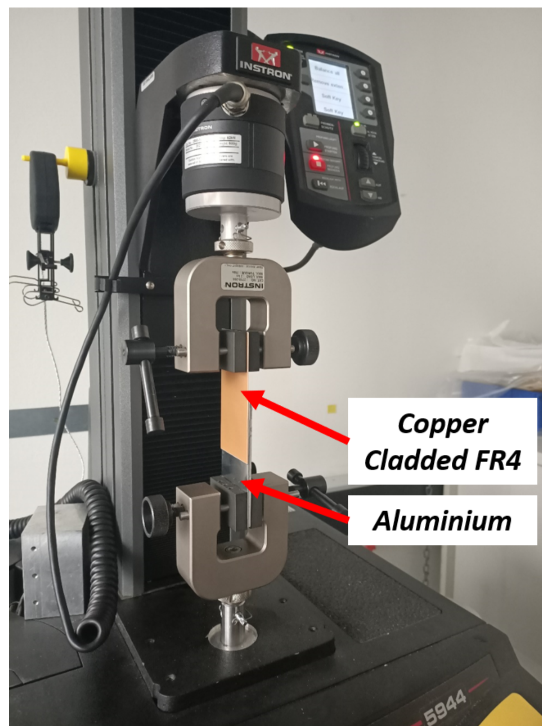

Figure 2.9: Front-view of Instron 5940 testing machine to perform the lap shear test. At the bottom grip, the aluminum sheet is clamped and the copper sheet is fixed on the top grip which is pulled at 180° until the surfaces are separated or maximum limit of the software is reached.

To summarize the lap shear strength test, two key parameters were considered (see Fig. 2.10):

1. **Load required for a 0.1 mm extension:** This parameter represents the amount of force that can cause a slight extension in the adhesive bond. In practical applications, this could be due to factors such as the movement of micro-cables during the assembly of a module or mounting modules to the ladder. Essentially, it tells that how well the adhesive bond can handle minor stresses without failing.

2. **Maximum break-off load:** This parameter indicates the maximum force that can be endured by the adhesive bond before the failure. It helps to determine the adhesive's strength and its ability to withstand extreme forces.

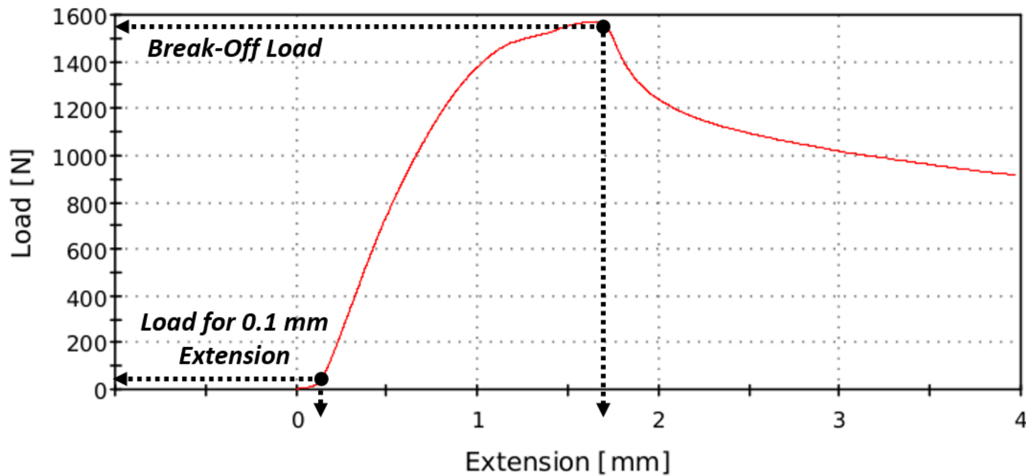

Figure 2.10: Graph representing a single stycast sample before the thermal cycling, showing load plotted against the sample extension.

Both parameters were measured for all the samples, including both freshly bonded specimens and those that experienced thermal cycling. Also, it is important to highlight that the samples were initially prepared with a surface area of 5×5 cm^2, which is different from the final objects having a surface area of 10×3 cm^2. Therefore, normalization is done to ensure that the loads are represented per unit area, making it easier to compare the performance of different adhesives. The results of the original load measurements and the normalized load values for these key parameters are summarised in Table 2.2. This table provides the average values for each adhesive, considering all the tested samples.

Table 2.2: Results of lap shear test for all adhesive samples before and after the samples underwent thermal cycling. Ten thermal cycles were performed for each sample in a climatic chamber between +40 °C and -40 °C by keeping the sample at each extreme temperature for 1 hour. The load mentioned here is normalised w.r.t. area of the glued samples i.e., 5×5 cm^2.

Glue sample	**Type of Thermal Cycling (TC)**	**Load for 0.1 mm extension [N]**	**Normalised load for 0.1 mm extension [kPa]**	**Break-off load [N]**	**Normalised break-off load [kPa]**
Stycast 2850 FT	Before TC	29.29	11.71	1572.76	629.10
	After TC	25.22	10.08	1366.75	546.70
Dowsil SE4445	Before TC	8.87	3.54	413.89	165.56
	After TC	8.17	3.26	38.25	15.30
Bergquist EA1805	Before TC	16.81	6.72	1427.69	571.07
	After TC	20.41	8.16	1126.87	450.74

From the table, it becomes evident that the choice of adhesive material significantly affects bonding strength. Here are some key findings:

- Dowsil, a silicon-based composition, exhibits lower bonding strength due to its softer nature. This softness makes it less resilient in mechanical applications.
- Stycast and Bergquist demonstrate comparable break-off loads. These adhesives prove to be more robust choices for mechanical bonding.

Additionally, when considering the samples that underwent thermal cycling, a trend has been observed. The break-off load for thermally cycled samples are lower compared to the freshly bonded samples. This suggests that thermal stress influences the mechanical strength of adhesive bonds. However, even under the influence of thermal cycling, the performance of Stycast and Bergquist was comparable. On the other hand, Dowsil samples did not meet the mechanical strength criteria, as their bonds proved to be more vulnerable after exposure to thermal stress.

2.3.3 Results and outlook

Three adhesive candidates were tested to ensure optimal thermal and mechanical performance between the cooling shelves and the FEBs: Stycast 2850FT, Dowsil SE4445, and Bergquist EA1805. The results of these evaluations are summarised in Table 2.3, providing insights into their respective thermal stress analysis, lap shear test outcomes, and application procedures.

Table 2.3: Summary of the results of the different tests performed for the three candidate glues.

Glue samples	**Thermal Stress Analysis**	**Lap Shear test**	**Application Procedure**
Stycast **2850 FT**	No deterioration	Strong joint	Low viscosity **Easy capillary action**
Dowsil **SE4445**	No deterioration	Weakest joint	Medium viscosity **Easy capillary action**
Bergquist **EA1805**	No deterioration	Strong joint	High viscosity **Requires extra force for dispersion**

The lap shear test shows a significant difference in mechanical strength among the adhesives. Dowsil SE4445, despite showing no thermal deterioration similar to the others, exhibited the weakest joint strength, making it unsuitable for the mechanical requirements needed for the interface. Therefore, the choice narrows down to Stycast 2850FT and Bergquist EA1805, both demonstrating strong joint formation and no thermal deterioration.

Considering the adhesive application process is essential due to the interface specifications, as detailed in Section 2.2. A glue with medium to low viscosity is preferred for easy application, integral for ensuring full surface coverage without exerting excessive force that could damage the electronic components on the FEBs. Although all three adhesives were applied similarly, Bergquist EA1805's high viscosity presented challenges during the application phase, as it requires substantial force for dispersion.

The outcome of the glue samples after a 24-hour application (see Fig. 2.11) showed that Stycast 2850FT, with its low viscosity and ease of capillary action, emerged as the most suitable option. This choice aligns with the need for an adhesive that not only meets the thermal and mechanical performance criteria but also conforms to the application requirements for the TIM between the FEB and the cooling shelf. Further details regarding the adhesive application procedure and its implications on the assembly process will be discussed in the subsequent section.

Figure 2.11: The glue samples (left to right) Stycast 2850FT with 23 LV catalyst, Dowsil SE4445, and Bergquist EA1805, showing the surface coverage after the 24 hours of curing time.

Moreover, the effectiveness of Stycast 2850FT, especially when used together with the 23 LV catalyst is well-established,in the context of the LHCb VELO experiment for gluing sensors. The expected radiation fluence for the VELO sensors reaches 8×10^{15} $\mathrm{MeVn_{eq}/cm^2}$. This represents a factor of ten orders higher magnitude than that of the STS environment. Consequently, Stycast proves itself capable of withstanding the elevated radiation levels inherent to the STS application, as substantiated by its prior performance in the VELO experiment [80].

2.3.3.1 Thermal stress test with Stycast

With the selection of Stycast as the designated thermal interface material between the FEBs and the cooling shelf, the next step involves subjecting this interface to a series of rigorous thermal tests. These tests are designed to understand how Stycast behaves over time, particularly when subjected to multiple cycles of thermal stress.

The main parameters of thermal cycle testing include temperature limits, dwell time at both limits and change rate between the limits as shown in Fig. 2.12. The extent of temperature variation is important for intensifying the test conditions, the greater the difference between the limits, the higher will be the stress caused by them.

The dwell time defines the prolonged exposure at extreme temperatures that can impact the interface's long-term performance. Also, the rate of temperature change between the temperature extremes can induce thermal gradients among various components. The slower temperature transitions allow different materials within the FEBs and the interface to warm up or cool down at a uniform rate, reducing the potential for thermal stress. Therefore, by controlling the temperature limits, dwell times, and change rates, one simulates the challenging conditions that can be foreseen in the STS operating environment.

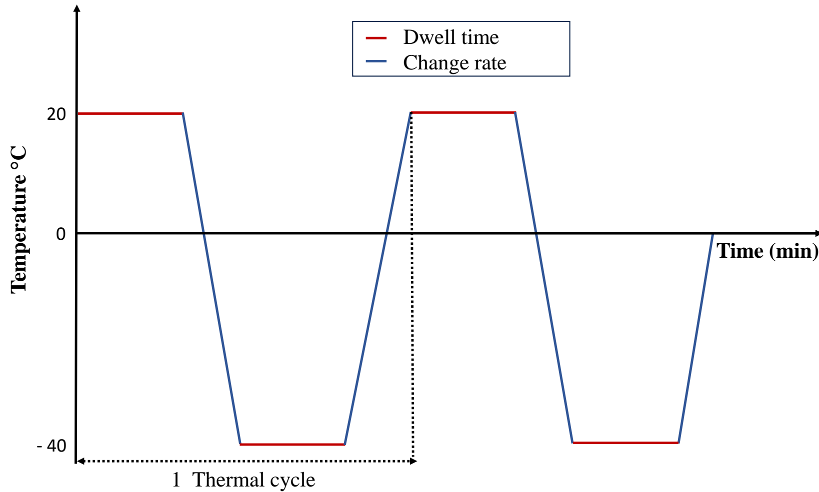

Figure 2.12: Sketch showing the important parameters for thermal cycling testing plotted between temperature and time.

Following the considerations described above, thermal cycling has been performed on a pair of thermal dummy FEBs glued to a cooling shelf using stycast. These FEBs underwent testing using the setup similar to that described in Section 2.3.1.1. However, unlike prolonged exposure, the dwell time was set to 20 minutes at each extreme temperature. This approach allowed sufficient time for FEBs to stabilize before the temperature was changed.

Throughout the thermal cycling process, the FEBs remained powered, and the transition times between extreme temperatures were automatically controlled without manual adjustments. This control was solely based on the power output of the Lauda chiller and the climatic chamber. A total of 50 thermal cycles were conducted, with extreme temperatures as +20 and -40 °C, to evaluate the interface's stress-handling capabilities within this temperature range.

The plots in Fig. 2.13 shows the results of thermal cycling tests for 2 FEBs glued to one cooling shelf. These tests were performed to assess the performance of the stycast under varying temperature conditions. The temperature differences between the LDO regulator and the cooling block, with a cooling block maintained at +20 °C and -30 °C, are represented as ΔT_{max-1} and ΔT_{max-2}, respectively.

The results obtained from these thermal cycling tests are quite promising. Throughout 50 cycles, only minimal temperature change has been observed within the range of 1-2 degrees. This stability in temperature performance indicates that Stycast as a thermal interface material can withstand temperature changes, and reduce thermal stress risks, ultimately extending the op-

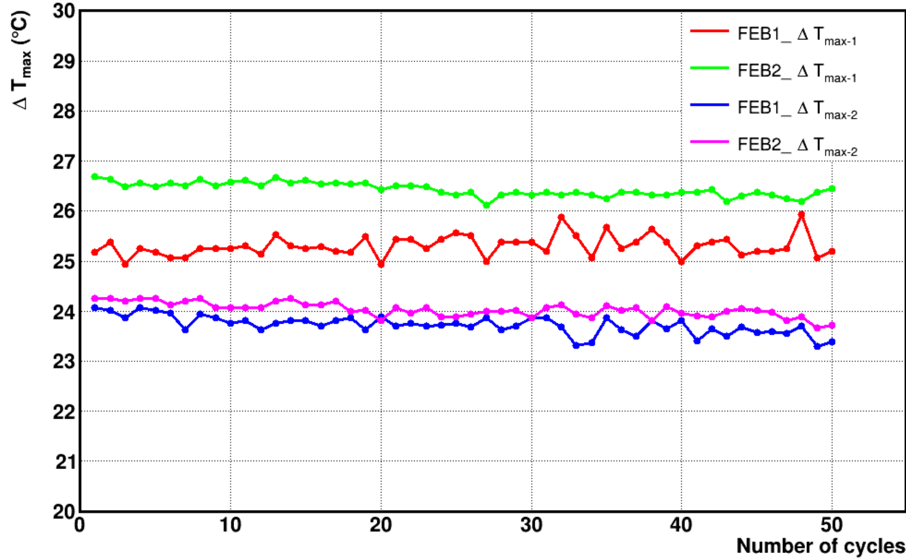

Figure 2.13: Thermal cycling plot to test the stycast interface at extreme temperature for the two thermal dummy FEBs glued to the cooling shelf. The image shows the temperature difference between the cooling block and LDOs at +20 °C (ΔT_{max-1}) and -30 °C (ΔT_{max-2}) for both the FEBs.

erational lifespan of the FEBs. Up to this point, the thermal interface has undergone rigorous testing but solely with thermal dummy FEBs. While the results have been promising, the next step involves the transition to the real FEBs. This allows to assess the interface's temperature control capabilities and its role in maintaining the functionality of the FEBs during their operational cycles. However, it is important to establish a well-defined assembly procedure for safely gluing the Stycast interface to the FEBs.

2.4 Characterisation of adhesive to be used as TIM

The gluing of two surfaces together while ensuring maximum coverage with a precisely defined thickness poses a significant challenge. Since the Stycast 2850 FT with 23 LV catalyst has been chosen as the promising candidate, a well-defined procedure needs to be defined. To use Stycast to glue the FEBs and the cooling shelf together with well-defined thickness, the gluing procedure requires careful attention to several key factors which are briefly described below:

- **Eliminating Bubbles:** It's important to mix the glue and catalyst in a way that it does not form any bubbles. Placing the mixture in a vacuum is one of the methods to avoid bubble formation.

- **Uniform Thickness:** Aiming for a glue layer thickness within 150 μm is important, ensuring it covers the entire surface with the glue.
- **Reproducibility:** Achieving a reproducible glue layer without excessive squeeze-out is important, which can be achieved using a specialized glue dispenser.
- **Thermal Conductivity and Viscosity:** The chosen glue should exhibit excellent thermal conductivity and low viscosity under the operational conditions of the STS.
- **Avoiding External Forces:** The gluing procedure should avoid the use of any additional pressure to ensure accuracy.
- **Proper Positioning:** Careful placement of the FEBs and cooling shelves is important, and achievable with a precisely designed tool.

All these parameters will be explained in detail in the next section, offering a comprehensive understanding of their significance in achieving a successful adhesive bonding process.

2.4.1 Optimisation of glue pattern

Covering large surfaces with glue is complex and requires some optimization of the glue pattern to be used. The fundamental objective in selecting a glue pattern is to ensure that, after capillary dispersion, the glue evenly covers the entire surface with minimal air bubbles while maintaining the required thickness. This process becomes more intricate as the size of the surface increases, especially when transitioning from small surfaces (less than 5 mm on each side) to larger ones [81]. Moreover, selecting an adhesive pattern is more straightforward for symmetrical shapes, such as squares but the challenge escalates with shapes, like rectangles, making the selection process more challenging [81].

Given that the surfaces of the FEB and cooling shelf are rectangular (10×3 cm^2), a common glue pattern employed is the "double Y" pattern [82]. In this pattern, two Y-shaped patterns are drawn, one on each side of the rectangular surface, as can be seen in Fig. 2.14.

The approach behind the double Y pattern is to ensure the coverage of the entire surface. The central line forms an elliptical shape, covering the central region of the surface, while the Y-shaped patterns at the ends of the rectangle ensure complete coverage of the edges [83]. Additionally, the angle between the glue lines can be adjusted to optimize the pattern's growth

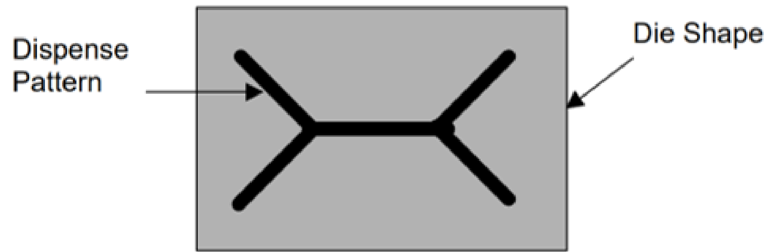

Figure 2.14: Double Y pattern is used often to cover rectangular surfaces, where die represents the surface to be covered, i.e., rectangle in this case.

rate in the horizontal direction. This approach balances adhesive distribution, ensuring that both the central and edge areas receive appropriate coverage.
To accomplish that there are certain key points to be taken into consideration which are mentioned as follows:

1. Calculate the length of the central line, with the dispense line's length closely matching the difference between the long and short side lengths of the die, i.e., for 10×3 cm^2 rectangular die, the length of the dispense line will be around 7 cm.

2. Distribute the remaining adhesive material's weight along the four lines, extending about two-thirds of the way from the center line towards the corners at a 45° angle from the center line, as can be seen in Fig. 2.14.

Following the steps mentioned above, a double Y pattern was applied using the stycast glue to determine if the pattern provided adequate coverage. It was initially tested on the transparent surface, using plexi glass sheets with the same dimensions as the FEBs, as can be seen in Fig. 2.15.

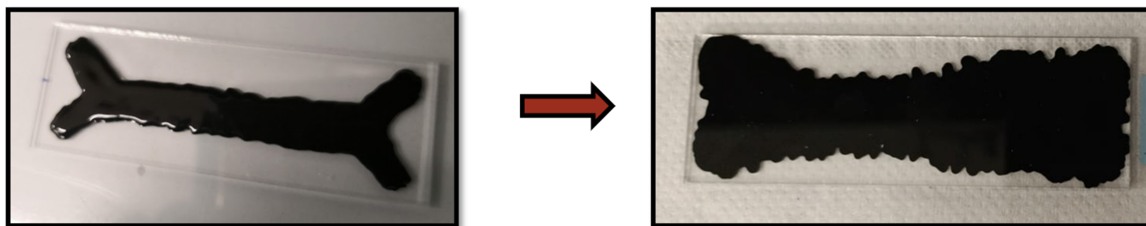

Figure 2.15: Double Y pattern pattern using Stycast was applied on a plexiglass sheet. (Left) Image of the glue when it was applied and the surface was covered with another plexiglass sheet. (Right) Image of the glue dispersion after 24 hours.

Figure 2.15 demonstrates that the double Y pattern alone did not fully optimize the coverage of the surface for the FEB. Hence, it is essential to comprehend how the adhesive pattern changes during the squeezing process. Although the adhesive effectively covered the inner region of the FEB, responsible for cooling ASICs and LDO regulators. There were areas in the middle and corners left uncovered, which could give rise to an edge effect. Therefore, it was required to customize the pattern in such a way that the maximum surface gets covered and there should not be any contact between the two surfaces to provide complete electric isolation between the two.

To address these issues, the adhesive pattern was customized by increasing the number of glue lines in the middle region while maintaining control over glue volume to achieve the desired thickness. Due to the presence of electronic components, no external force could be applied to the FEB, necessitating the need for even glue distribution through capillary action.

Along with the optimization of glue pattern, it was crucial to be careful with the thickness requirement of the TIM which is determined by the volume of glue required. With a target thickness of 150 μm, the total glue volume needed for a complete surface coverage was calculated as 0.45 ml (10 cm $\times$ 3 cm $\times$ 0.015 cm). The challenge lies in distributing this 0.45 ml of glue for maximum surface coverage without the application of additional force. After numerous iterations aimed at achieving the best possible surface coverage, the optimized pattern was found and it is shown in Fig. 2.16.

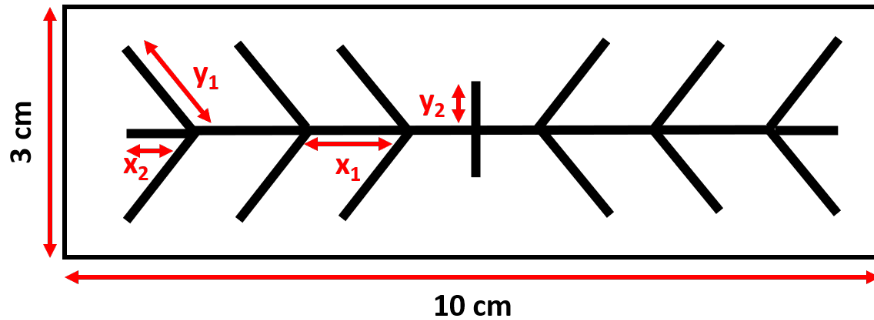

Figure 2.16: Customised double-y pattern designed to achieve complete surface adhesion, ensuring precise glue volume along each line. Specifically tailored to fit the dimensions of FEBs, the glue volume of 0.45 ml is distributed along the different lines shown in the pattern with the lengths of x_1 *= 15 mm,* x_2 *= 7.5 mm,* y_1 *= 13 mm,* y_2 *= 5 mm to ensure full coverage. Detailed explanations of this customization process and volume distribution strategy are available in the appendix A.1.*

The pattern has been cross-checked once again with transparent plexiglass sheets to observe the spread of glue over 24 hours. The spread of glue was observed and captured within different time intervals and has been shown in Fig. 2.17. There were 30 such samples prepared and it was observed that almost 60 % of the samples showed nearly full surface coverage as in Fig. 2.17 (d), whereas 30 % of samples were with the edges or the sides not fully covered (Fig. 2.17 (a)), and a remaining 10 % of samples were with trapped air bubbles (Fig. 2.17 (b)).

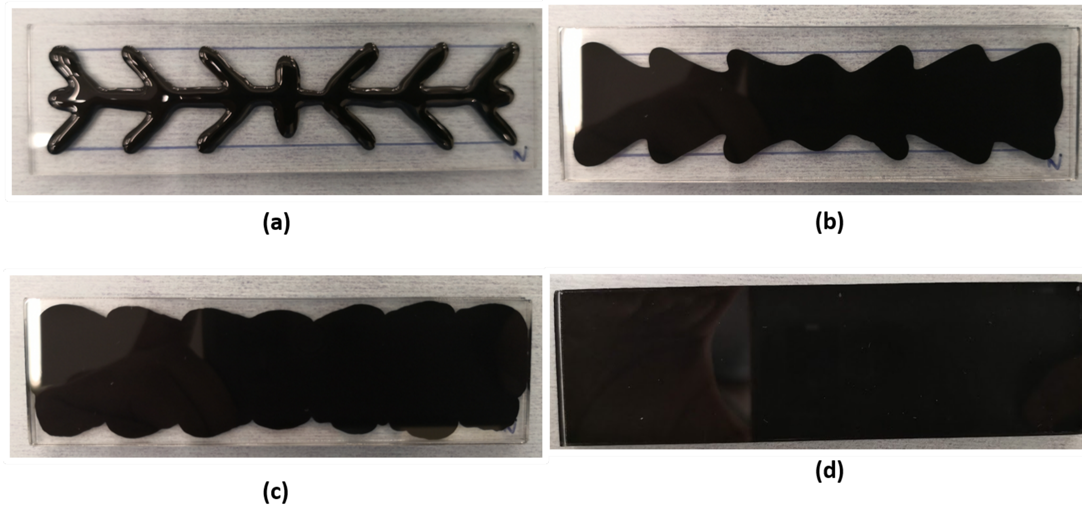

Figure 2.17: Illustrating the transformation of glue patterns over a 24-hours, with snapshots taken at different intervals: (a) immediately after application at 0 hours, (b) 6 hours post-application, (c) spread after 12 hours, and (d) the final spread after 24 hours. After the glue's application and the subsequent placement of plexiglass, the progression occurs naturally, without any external force. The evolution from the initial state through to the final observation demonstrates the glue's capillary action, highlighting a gradual increase in surface coverage.

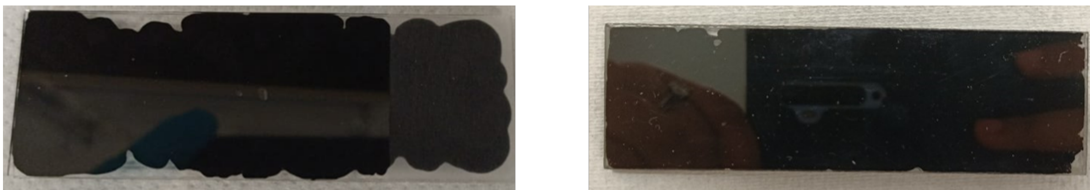

Figure 2.18: Left image shows the surface coverage, where many places are still not covered thoroughly, indicating issues with the accuracy of glue dispensing. The right image shows the presence of numerous air bubbles, which can occur during the manual mounting of the plexiglass sheet. This highlights the significant risk of mis-positioning the FEBs on the shelf, potentially resulting in trapped air.

The observations drawn from the above figure highlight the significance of both a glue dispenser and a gluing tool to achieve optimal results. While the customized pattern demonstrates satis-

factory performance, it is clear that further refinements are necessary. To address this problem, the Nordson 7017 glue dispenser [79] has been used as the next step. This dispenser provides precise control over the glue volume, ensuring an accurate amount for each line of the pattern. Additional details regarding the comprehensive glue distribution across the entire surface, as well as specific parameters for each line of glue dispensed, can be found in the Appendix A.1.

2.4.2 Gluing tool for the glue application

The previous section highlighted the risks of misalignment and air bubble entrapment while gluing two glass sheets, a problem that can also arise when attaching FEBs to the cooling shelves. Given that FEBs are already connected to the sensor via micro-cables, it is important to manage the risk of horizontal shifts during or after applying the glue. To address this, a specialized gluing tool has been designed, aimed at maintaining alignment and stability of the components during gluing. The gluing tool consists of two parts: one that holds the FEBs in place, ensuring they stay fixed during the curing process, and the other supports the cooling shelf to minimize movement and enable a structured approach to glue application. The cooling shelf's asymmetrical T-shape is leveraged to improve the setup's steadiness, as the wider side of the T shelf is fixed to the tool for stability.

In addition to positioning the components accurately, the tool is designed to ensure a gap of 150 μm between the FEB and the cooling shelf for the interface to be applied. This exact spacing is predefined by the counter-parts of the tool, holding the FEB and the shelf. To ensure the smooth movement of the shelf-holding part over the FEB surface once the glue is applied, gauge pins are used. This design ensures both precise alignment and ease of operation throughout the gluing process. To evaluate the tool's effectiveness in the gluing process, a series of tests were conducted with actual FEBs and cooling shelves, rather than using thermal dummies. To apply the glue pattern, a stencil has been designed to draw the pattern on the FEB surface followed by applying Stycast 2850 FT mixed with 23 LV catalyst using the glue dispenser. The sequential gluing process is illustrated in Fig. 2.19, demonstrating the gluing procedure. The gluing procedure has been defined in the Appendix A.1.

During the gluing procedure, it was determined that the glue would always be applied to the FEB's surface first, followed by the precise placement of the cooling shelf. The process of gluing both FEBs to the cooling shelf takes around two days, as one FEB will be glued at a time, and the curing period for the glue ranges from 18 to 24 hours. After the initial gluing of one side

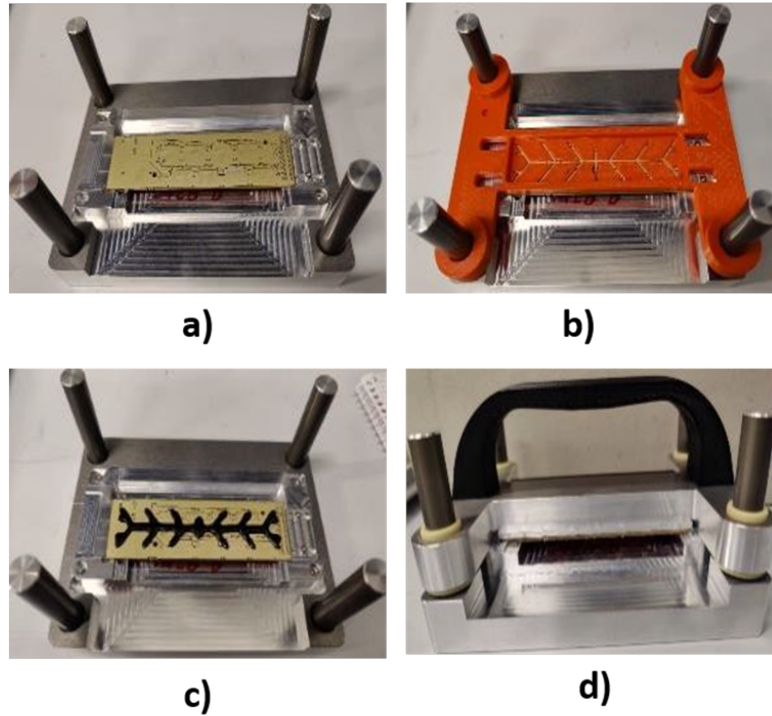

Figure 2.19: Procedure for gluing FEBs to a cooling shelf a) The FEB is positioned onto the gluing tool, depending on the type of FEB (A or B), the appropriate tool is chosen, b) To ensure that the glue pattern is as per the description, a stencil is used which helps in achieving accurate placement of the adhesive on the FEB surface, c) The glue is deposited onto the surface of the FEB using a glue dispenser aiming for an even layer of glue, d) The cooling shelf after fixing to the tool is smoothly slid down onto the surface of the FEB.

of the cooling shelf to a FEB, a similar procedure was applied to attach the other side of the cooling shelf to another FEB. The steps are illustrated in Fig. 2.20 and the detailed flowchart has been added in the appendix A.1.

2.4.3 IV measurement of the glued samples

On day 0 of STS operation, the modules will be operated at a bias voltage of 150 V, with ±75 V applied to each side [86]. However, during the electrical isolation testing of TIM, the sensors were not connected. There were three samples prepared using the tool to determine the electrical isolation capabilities of the components when the voltage is applied. The setup consisted of a Keithley power supply that allows to increase the potential difference, monitoring the leakage current. The samples were tested up to 500 V with a 50 V step increment. The results of the tested samples have been plotted in the form of a Current vs voltage graph, as

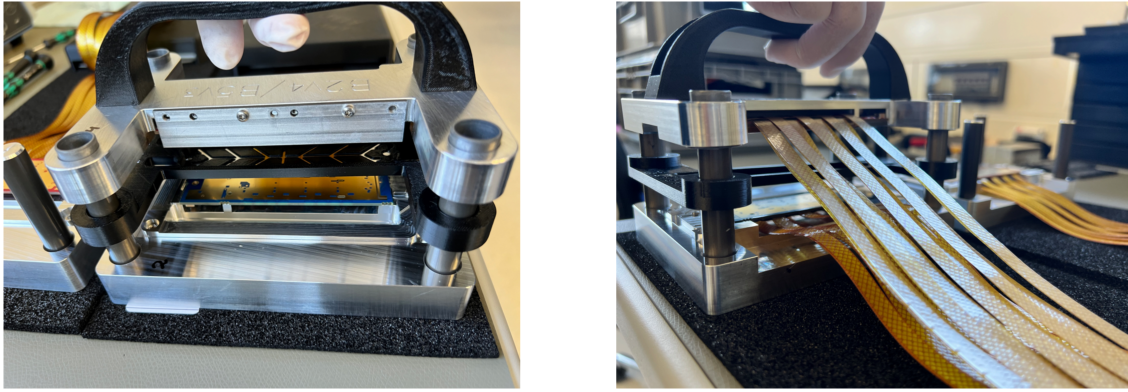

Figure 2.20: The image highlights the final step of the FEB to shelf gluing, showing the steps involved in the process showing, (left) Front view (Right) Back view. The base of the tool holds the FEB to be glued, and in the middle is a removable stencil used to draw the glue pattern. The top part of the tool holds a cooling shelf with the FEB glued to one side.

shown in Fig. 2.21. It illustrates how the current changes with an increase in the voltage applied to the samples.

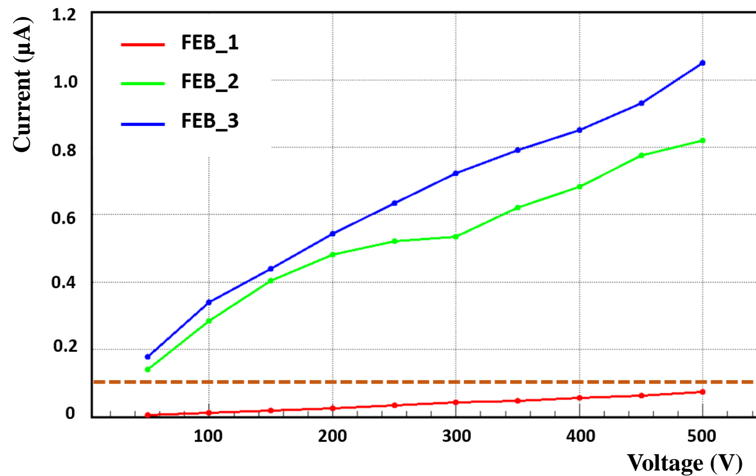

Figure 2.21: Current vs Voltage characteristics for samples prepared for testing Stycast 2850FT (23 LV) as TIM for the FEBs glued to cooling shelves. The dashed line indicates the threshold for acceptance and the sample referred to as FEB_2 *and* FEB_3 *shows a larger leakage current indicating the loss of electric isolation.*

It can be observed that in the first sample, the current remains consistently low, starting at less than 0.1 μA at 50 V and maintaining this level as the voltage increases. This result indicates that the sample exhibits a good electrical isolation, with minimal leakage current even at higher voltages. On the contrary, the other two samples show different behavior. The current starts at

0.1 μA at 50 V and gradually increases as the voltage is raised. By the time the voltage reaches 200 V, electric sparks are observed, indicating that the electrical isolation of these samples begins to break down at this point. The current continues to rise, reaching 1 μA at 500 V, which implies a significant loss of electrical isolation in these two samples. Therefore, it can be summarized that the gluing procedure developed so far is not completely satisfactory and needs to be optimized further.

2.4.4 Quality assurance of surfaces

Before pursuing further investigation, it was crucial to identify the cause of the failure. Despite all the precautions taken into consideration during the gluing parameters, including glue thickness, mixing, dispensing, and positioning, the results did not meet expectations. As a result, after the adhesive had fully cured, a thorough examination of the glued surfaces was performed, by carefully removing them to verify the extent of glue coverage. This revealed incomplete coverage on the FEB surfaces, raising the possibility that the problem might originate from the surfaces themselves rather than the adhesive application, as depicted in Fig. 2.22. Therefore, optical inspection was conducted on both the FEB and cooling shelf surfaces to assess their flatness.

Figure 2.22: Illustration of backplane of FEB, showing an incomplete surface coverage, despite using a well-defined glue application procedure. The encircled areas show the surfaces without glue when the FEB was detached from the shelf.

2.4.4.1 Inspection of the surface of the FEB

The primary objective of this investigation was to assess the non-flatness characteristics of the FEB surface. To accomplish this, the surface of one FEB was optically inspected. This approach involved optical inspection of both the front and back sides of the FEB, measuring various points across its thickness to determine the non-flatness of the surface. The data obtained from the

measurement helps to understand the extent to which the FEB surface deviates from being perfectly flat. The optically inspected FEB surfaces are plotted in Fig. 2.23. Given the known thickness of the FEB being 3 mm, the deviation from its nominal position was calculated based on optical inspections of both the top and bottom surfaces, as shown in Fig. 2.24. The plotted data shows that the surface of the FEB is not flat, with the deviation in non-flatness ranging from approximately 60 to 70 μm.

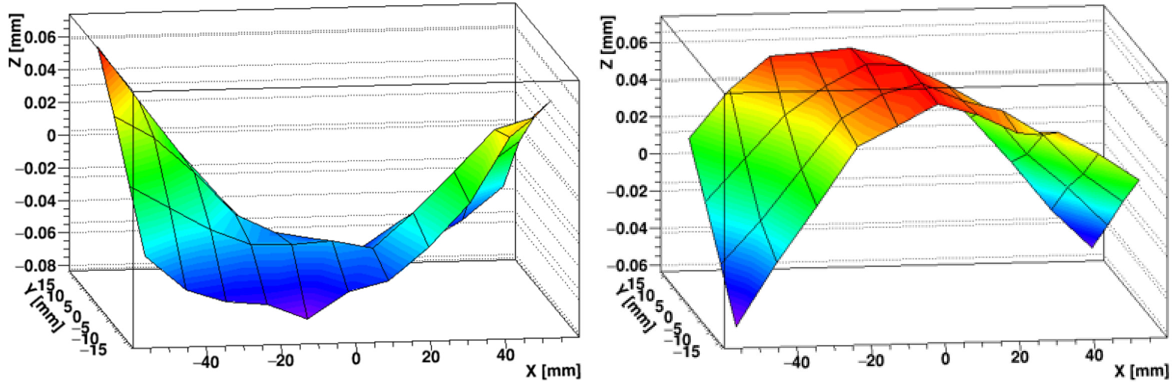

Figure 2.23: Optical inspection of FEB to measure the non-flatness in the surface of the FEB. On the left, the top surface of the FEB is shown as observed after the inspection, highlighting the surface irregularities. The right side of the image shows a view of the bottom surface, providing a complete analysis of the FEB's surface condition from both top and bottom perspectives, following the optical inspection.

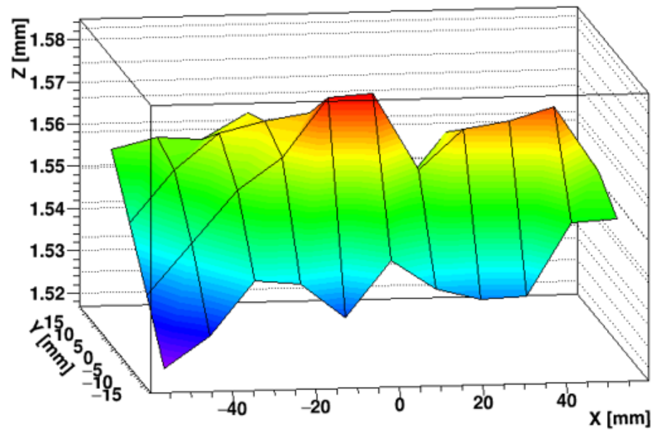

Figure 2.24: Deviation in non-flatness of the FEB surface from its nominal thickness of 3 mm.

2.4.4.2 Inspection of the surface of the cooling shelf

After identifying the non-flatness of the surface of FEB, it was important to examine the surface irregularities of the cooling shelf as well. Therefore, to investigate both the surfaces of the cooling shelf, optical inspection was performed as can be seen in Fig. 2.25. The cooling shelf has a nominal thickness of 2.7 mm, and the degree to which it deviates from its expected position has been graphically represented in Fig. 2.26. This resulting deviation is approximately 60 μm in the cooling shelves.

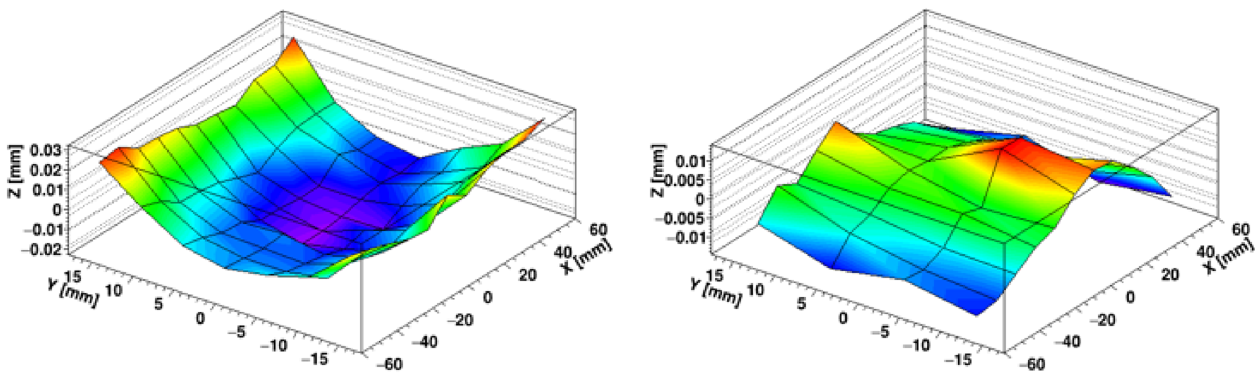

Figure 2.25: Optical inspection of the non-flatness of the surface of the cooling shelf where, the left image shows the top surface, and the right image shows the bottom surface.

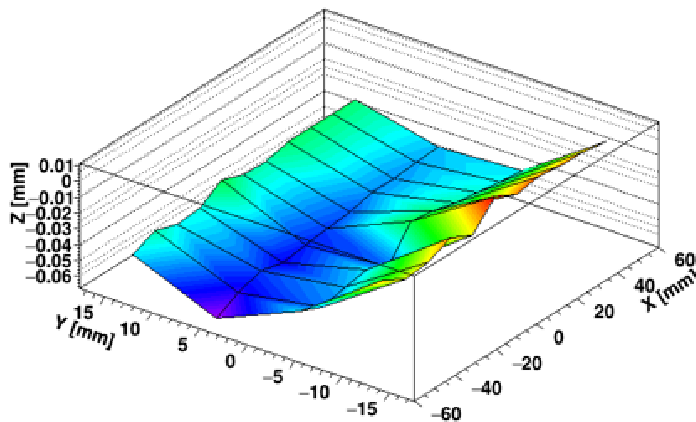

Figure 2.26: Deviation in non-flatness of the cooling shelf surface from its nominal thickness of 2.7 mm.

2.4.4.3 Results

Figure 2.27 illustrates the deviation in non-flatness of optically measured surfaces of the FEB and cooling shelf plotted together. It becomes evident from the plot that the non-flatness of these surfaces overlaps with the designated glue gap of 150 μm, making them unsuitable for effective gluing. The non-flatness exhibited by the FEBs and cooling shelf surfaces poses a critical challenge during the gluing process. As a result, this non-flatness could potentially contribute to short circuits between the two surfaces, which, in turn, can adversely impact the performance of the detector.

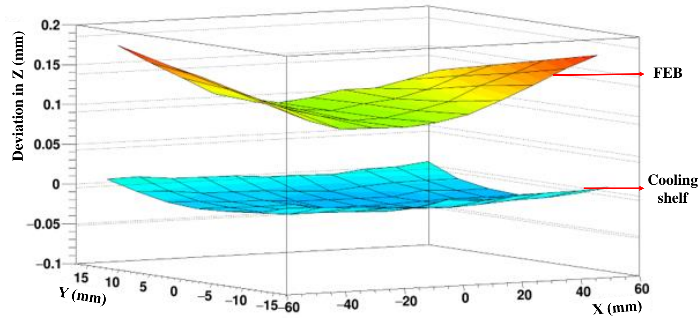

Figure 2.27: Deviation in the surface of FEB and cooling shelf from the nominal thickness. The non-flatness in the middle region of FEBs shows the possibility of having less glue, leading to unintended contact between the surfaces.

2.4.5 Possible solution for surface optimization

Given the critical boundary condition of a 150 μm gap between the two surfaces, options for adjustments were limited. Since the adhesive technique alone proved insufficient to achieve effective electrical insulation between the surfaces. This led to the evaluation of possible modifications to either the FEB, the cooling shelf, or both, to enhance electrical insulation while maintaining the cooling performance of the thermal interface. Two possible approaches were foreseen and were thoroughly tested. The procedure and findings of these tests are outlined in the following section.

2.4.5.1 Anodization process

To address the challenge posed by the non-flatness of the cooling shelf surface, a thorough inspection was conducted for 20 cooling shelves. The purpose was to precisely measure the extent at which each cooling shelf deviates from the nominal thickness of 2.7 mm. For the thickness measurement, a digital micro-meter with a resolution of 0.001 mm (and accuracy of ±0.002 mm) was used.

Nine points across the surface of each cooling shelf were measured with the micro-meter, as shown in Fig. 2.28, and the individual deviations from the nominal thickness were noted. Following the measurement of individual deviations, an average was calculated from these values, resulting in an overall deviation value for each shelf and has been plotted in Fig. 2.29, illustrating the range of thickness variations in the cooling shelves compared to the nominal thickness. These variations range from 58 μm to 71 μm with an average deviation of around 65 μm, aligning with the optically inspected value.

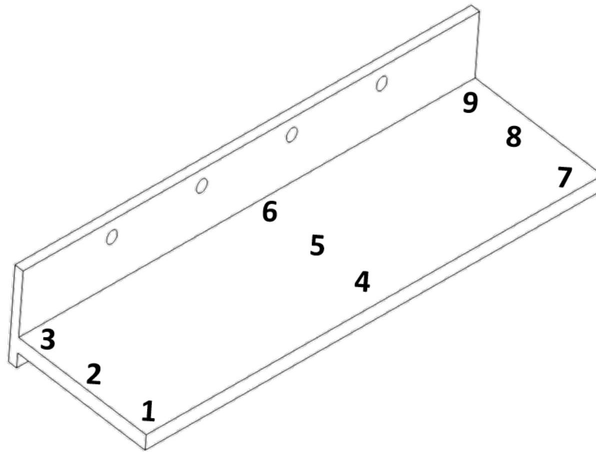

Figure 2.28: Drawing of one cooling shelf with the numbers marked show the different points measured for 20 shelves

Therefore, it becomes evident that the challenge posed by surface non-flatness can potentially contribute to electrical contact between these surfaces. As a result, a proposed solution involves the application of an additional thin oxide layer onto the aluminum surface, a process commonly referred to as anodization. The anodization process was selected as a viable option due to its ability to provide electrical insulation while offering additional advantages such as enhanced surface hardness, and corrosion resistance [84].

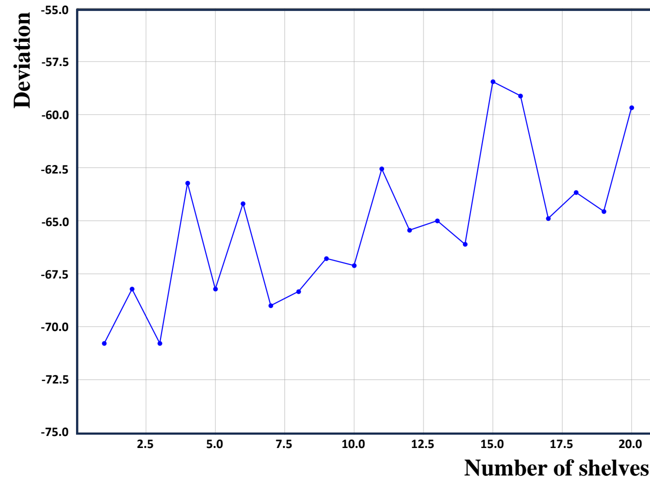

Figure 2.29: Mechanical inspection of 20 samples of cooling shelves.

The thickness of this extra layer of anodization is optimized to minimize its impact on the thermal conductivity of the interface. In our case, the thickness of the anodization layer was chosen to be 50 μm, where, approximately two-thirds of this thickness replaces the original aluminum thickness during the anodization process, as shown in Fig. 2.30.

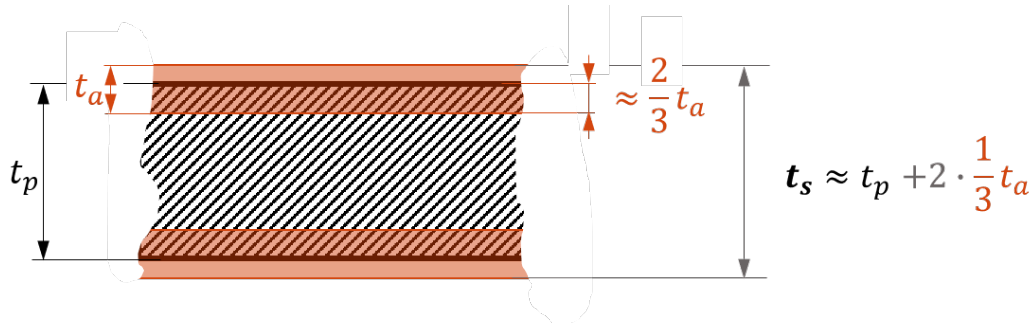

Figure 2.30: Thickness of the cooling shelf with anodization layer introduced into the thickness of the cooling shelf, where t_p *denotes to the original thickness of the cooling shelf (2.7 mm),* t_a *denotes the anodization layer (50 μm) and* t_s *denotes the final thickness of the cooling shelf after the anodization.*

To study the effects of anodization on the thermal path of a cooling shelf with two FEBs attached on both sides was simulated using the Finite Element Analysis (FEA) method. To perform the simulations, basic STS operating conditions were considered i.e.,

1. The temperature of the air was kept to -10 $^{\circ}$C.

2. Nominal power dissipation by ASICs and LDOs per FEB was considered i.e., 12 W.

3. Surface coverage of Stycast was taken as 95 % instead of 100 %, given the practical constraints posed by surface non-flatness.

When maintaining the cooling plate temperature at -28.2 °C (with the coolant at -40 °C), the hottest point on the FEBs reached -17.8 °C in the ideal scenario. Upon introducing anodization, this temperature increased to -17.1 °C.

The comparison results, summarised in Fig. 2.31, demonstrate that the introduction of a thin aluminum oxide coating through the anodization process does lead to a slight temperature increase of 0.7 °C at the hottest point on the FEBs. However, this slight thermal impact is offset by the considerable advantages it offers, including enhanced electrical insulation, increased resistance, improved hardness, and surface corrosion resistance. Therefore, it has been decided to apply anodization as an additional layer, providing a safety margin while significantly enhancing electrical insulation on the surfaces without compromising the cooling efficiency of the thermal interface.

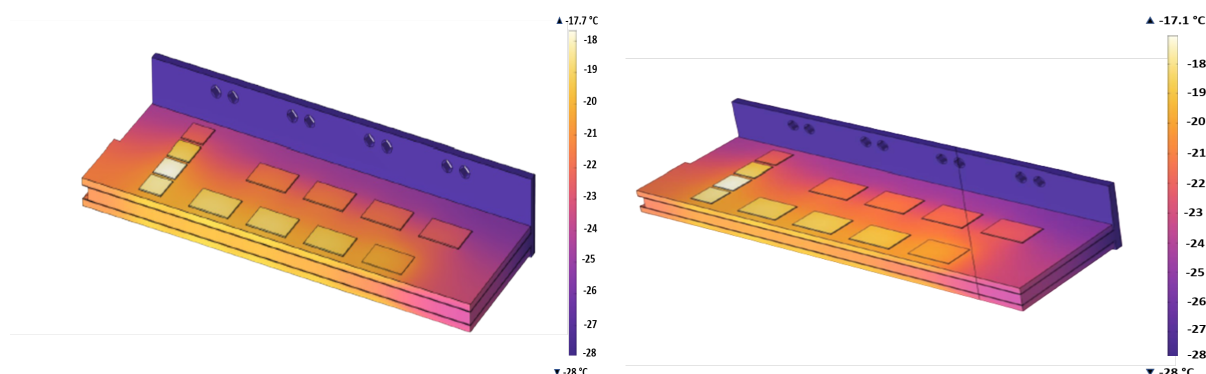

Figure 2.31: Thermal FEA simulations under nominal power dissipation showing the temperature distribution on the FEBs glued to the cooling shelf (left) and glued to the anodized cooling shelf (right).

2.4.5.2 Solder stop masking

The surface non-flatness of the PCB is a common issue encountered in various applications [87]. To overcome the challenge posed by the non-flatness of the FEB surface, a solution was required that did not require modifications to the existing design. Among the various electronic components comprising the FEB, the most critical were those in the middle region, i.e., ASICs and LDOs. These components require efficient cooling through the thermal interface to dissipate the heat they generate. Although the components at the edge may not generate substantial heat, it was still crucial to maintain the gap, preventing any undesired contact.

To ensure that each module is functional after the assembly and prevent any short circuits, a common approach is to use the solder mask on the surface of the [88] [89]. It acts as a protective layer that's about 25-30 μm thick, providing electrical insulation along the FEB's boundary. However, there may be a slight impact on thermal performance, but, the benefits of the solder mask, including good electrical isolation and safeguarding against contamination, generally outweigh any minor reduction in heat dissipation.

The aim was to incorporate the solder mask on FEB surface altering in the design, ensuring no electronic components were present on the top side of the designated solder mask area. A 2 mm wide frame of solder mask, approximately 30 μm thick, was planned. Additionally, to maintain surface symmetry, six strategically positioned points were integrated into the FEB design, as shown in Fig. 2.32. These points were placed carefully to avoid interfering with any electronic parts on the top of the FEB, thereby preserving their electrical connectivity.

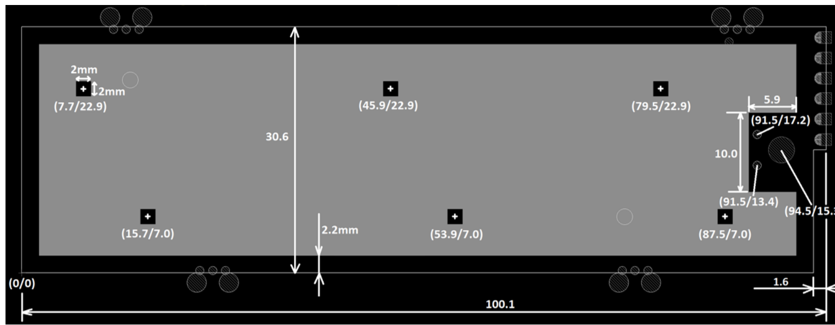

Figure 2.32: Position of solder stop mask on the bottom surface of the PCB (FEB8-2) with black frame and six single points. The solder mask used is 2 mm wide and the thickness of the solder mask and the single points was 35 μm.

Following the implementation of the solder mask to the FEB design, evaluation of its impact on temperature fluctuations became imperative. The thermal simulations were conducted by adding a solder mask to the FEBs along with anodized aluminum while keeping all other variables consistent across different scenarios. The results of the FEA simulation are explained in Fig. 2.33. The simulations revealed that the hottest point on the FEB corresponds to -16.8 °C, i.e., a slight elevation of 1 °C compared to the ideal case scenario. To ensure the maximum yield of functional modules, it was important to include these insulating layers. Therefore, by understanding the thermal behavior of the FEBs under different scenarios, the design of the FEBs and the cooling shelves were modified.

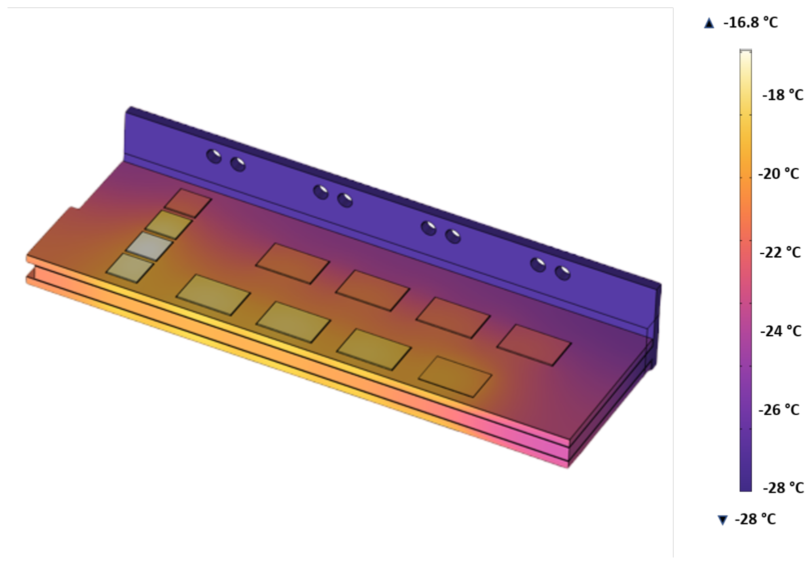

Figure 2.33: Thermal FEA simulations under nominal power dissipation showing the temperature distribution on the FEBs with solder mask glued to anodized cooling shelf.

2.4.6 Results of TIM characterization

Thermal simulations with different insulating layers demonstrate the impact of adding these layers on the cooling performance of the electronics. The objective was to ensure the complete functionality of modules following the gluing process while minimizing any adverse effects on the thermal performance. Consequently, the design of FEBs and cooling shelves was optimized, taking into account the non-flatness of both surfaces.

Figure 2.34, represents the final set of components in the last step of the module gluing process. To meet the specifications, modifications to the gluing tool design were required to ensure well-defined gaps and a proper fit for both the FEB and the cooling shelf. Additionally, it was essential to experimentally verify the electrical connectivity of FEBs and cooling shelves. To validate the procedure, electrical tests were performed on a set of samples. Initially, the FEBs with the solder stop were combined with anodized cooling shelves and clamped together (as illustrated in Fig. 2.35 (left). This setup allowed for the assessment of the insulating properties of the surfaces without an intermediate interface. The results from three such samples (Fig. 2.35 (right)) indicate that, at a voltage of 500 V, the observed current ranged from 0.15 to 0.30 μA, which is a significant improvement over the previous values.

After satisfactory results were obtained regarding the surface isolation, the test was conducted on a sample that closely resembled the final components including the thermal interface. In this case, the maximum current at 500 V was approximately 0.01 μA (see Fig. 2.36), further

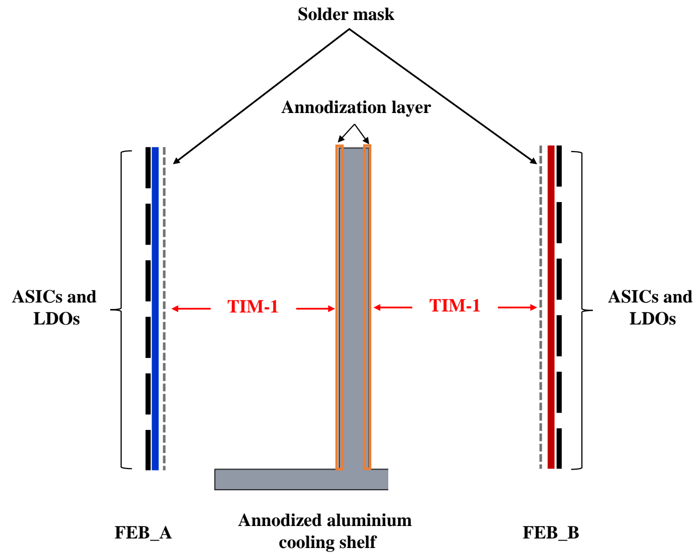

Figure 2.34: Sketch of the TIM gluing with an additional layer of anodization on the aluminum cooling shelf and solder mask on the surfaces of the FEBs.

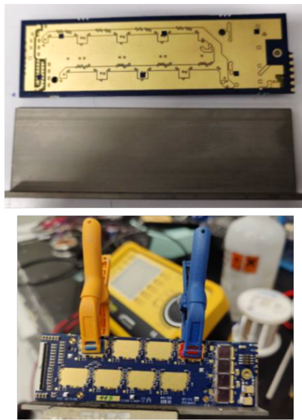

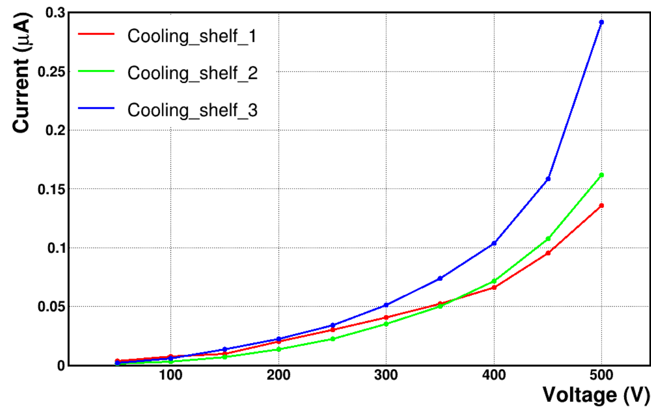

Figure 2.35: Top left image shows the FEB with the solder mask with an anodized cooling shelf. The bottom left image shows the FEB with the mask clamped to the anodized aluminum shelf, prepared for the testing. On the right is the graph that shows the Current vs Voltage variation for the clamped samples.

ensuring the low likelihood of direct contact between the two surfaces. Although there may be marginal impacts on thermal conductivity due to changes in the material properties of copper and aluminum, these results reassure that the risk of direct surface contact remains minimal.

Through these thermal simulations and carefully implementing the surface modifications, the use of Stycast as the TIM was optimized. This approach enabled efficient thermal management, even on non-flat surfaces, and brings us one step closer to achieving our ultimate goal: striking

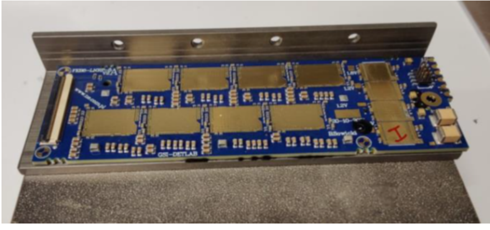

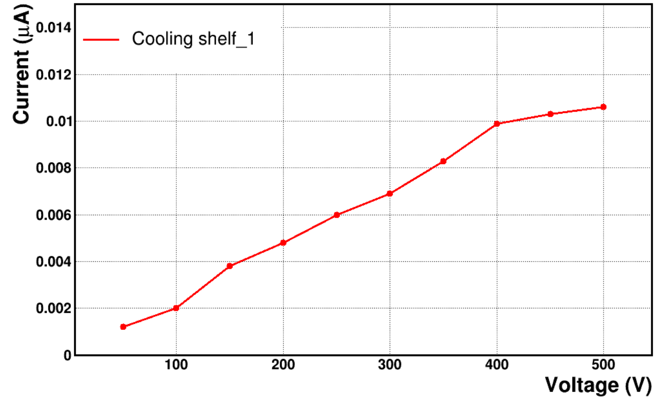

Figure 2.36: (Left) FEB with the solder mask glued to the anodized aluminum shelf, prepared for the testing. (Right) Graph showing Current vs Voltage variation for the glued samples.

the balance between electrical insulation and thermal efficiency, thereby ensuring the optimal performance of the modules.

In summary, to enhance the thermal performance and address the surface irregularities, there were two parallel activities ongoing. The primary focus was on optimizing the interface between the FEBs and cooling shelves. This optimization involved techniques such as anodization of the cooling shelves and the application of solder stops to the FEB surfaces. However, optimizing surface connections alone was not sufficient. Therefore, alongside the study of surface properties that have been summarised in this section, the thermal tests were conducted where FEBs were directly attached to the cooling shelves without the modified surfaces. This parallel investigation allows us to compare how these modifications affect performance compared to the unaltered surfaces, giving insights into their impact on thermal stability and overall functionality.

2.4.7 Failure scenario for TIM

Once the TIM material has been selected, it becomes essential to thoroughly test the interface under the operating conditions, which might lead to operational failure. Although boundary conditions are typically specified in data sheets, it is not always evident where and under what scenarios the interface might fail. Therefore, reliability and failure scenario tests were performed for the TIM.

Failure distributions are generally characterized by the probability distribution function (PDF) given by:

$$\mathrm{P_{failure}} = \int_0^{\mathrm{x}} \mathrm{f(x)\,dx} = \mathrm{F(x)} \tag{2.2}$$

where, f(x) is the probability density function and F(x) is the cumulative density function, defining the probability of failure before or after a certain time interval.

Among the various failure distributions used in data analysis, the Weibull distribution stands out for providing a flexible and versatile framework. The Weibull distribution is a probability distribution function (PDF) commonly used to model the lifetimes of materials and components, making it useful for predicting the performance and durability of TIMs. The PDF of the Weibull distribution is given by:

$$\mathrm{f(x)} = \frac{\beta}{\eta^{\beta}}\mathrm{x}^{\beta-1}\exp(-(\frac{\mathrm{x}-\mathrm{y}}{\eta})^{\beta}) \tag{2.3}$$

where, x is the variable representing time or life expectancy, $\beta > 0$ is the shape parameter, determining the distribution's shape, $\eta > 0$ is the scale parameter, influencing the spread or variability of the distribution, γ is the location parameter, which shifts the distribution horizontally.

The Weibull distribution exhibits three different shapes based on the value of β:

- If $\beta < 1$, the failure rate decreases over time, known as the "early-life" or "infant mortality" phase, where failures are more likely to occur early in the product's life.
- If $\beta = 1$, the failure rate remains constant, indicating a constant hazard rate during the "useful life" phase, where the product operates with a relatively constant failure rate.
- If $\beta > 1$, the failure rate increases over time, forming the characteristic "wear-out" phase. As the product ages, the likelihood of failure rises, and the curve takes on a bathtub-like shape as shown in Fig. 2.37.

To ensure the reliability of TIM, it's crucial to test them until they reach the wear-out stage and identify which conditions lead to the wear-out phase. This phase marks the point where failure rates increase over time, akin to the steep rise seen on the right side of a bathtub curve.

One effective approach to test the interface failure scenarios is to expose them to conditions more severe than normal. In most of the cases, extreme temperature gradients stand out as the leading cause of electronic system failures. Different studies suggest that approximately 55 % of electronic failures can be attributed to the impact of extreme temperatures, whether high or low, as well as temperature cycling, 20 % are related to the vibration and shock and 20 % are due to the humidity [85].

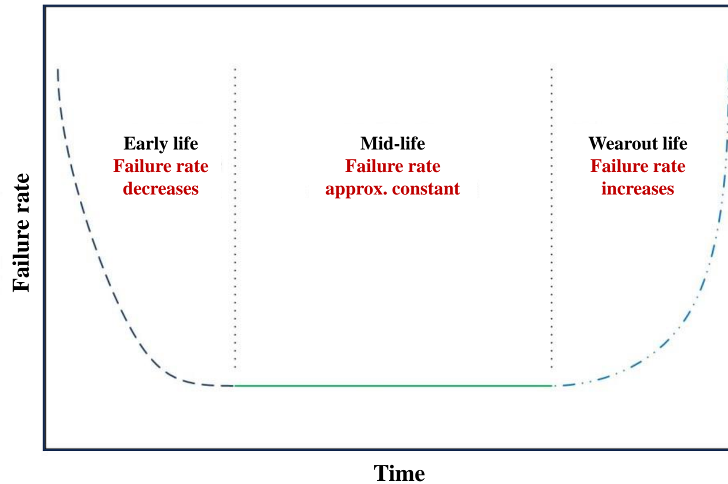

Figure 2.37: Bathtub curve is a graphical representation of the failure rate behavior of TIM over time, starting with an initial high failure rate due to early defects, followed by a period of stable, low failure rates during normal operation, and ending with an increased failure rate as the material degrades. This model helps predict the longevity and reliability of TIMs throughout their life-cycle.

As important as it is to test for the TIM material itself, it is equally important to test the interface together with the electronics or the components where it will be attached. These tests ensure that the interface efficiently dissipates heat from the electronics, maintaining functionality under both nominal and worst-case scenarios. As discussed in Section 2.3.3.1, Styast 2850 FT with 23 LV catalyst was tested as TIM under the worst-case scenario. However, in reality, the temperature will affect the TIM as well as the electronics. The thermal expansion properties of the TIM and the electronics differ, and if not accurately accounted for, this can lead to a CTE (coefficient of thermal expansion) mismatch. The different expansion rates of the TIM and the electronic components under varying temperatures can cause mechanical stress, leading to potential reliability issues. Therefore, the next section will describe a comprehensive test for the FEBs and the TIM, in which FEBs were glued to the cooling shelves following the gluing procedure.

2.5 Testing the thermal reliability of FEBs glued on cooling shelves

Considering that a significant proportion of electronic failures can be attributed to extreme thermal conditions, it becomes important to test the glued FEB samples under varying tem-

peratures. As part of the module assembly procedure, FEBs initially undergo comprehensive testing of all the components at room temperature. While this initial testing shows satisfactory performance at 20 °C, it does not accurately simulate the realistic operational conditions of the STS. To ensure robust module functionality, FEBs must be subjected to thermal cycling after being fixed to the cooling shelves.

Thermal reliability testing is essential due to the potential degradation of TIM which can reduce the thermal performance of the components. After applying TIM between FEBs and cooling shelves, they are thermally cycled to simulate potential failure scenarios. These tests include elevated temperature and humidity tests, high-temperature bake tests, temperature cycling tests, and power cycling tests. When FEBs undergo temperature changes after gluing, the mismatch in CTE of the different materials induces stresses along the TIM interface. Various materials expand at rates dictated by their CTE, which can result in deformation or misalignment within the assembly due to CTE mismatch. Therefore, thorough thermal reliability testing is essential to ensure the long-term performance and reliability of the modules.

To evaluate electronics reliability, the FEBs equipped with ASICs and LDOs, encapsulated with a protective glob-top layer were used. Fig. 2.38 provides a side view schematic of the FEB attached to the cooling shelf, highlighting the components prone to temperature variations. The CTE mismatch of these components can cause malfunctioning. The CTE of the components shown in Fig. 2.38 is summarised in Table 2.4. As can be seen from the table, the CTE of the glob-top materials and the conductive glue is significantly higher than that of PCB, silicon, and TIM.

The primary components that need to be tested under thermal cycling are the glues, bonds, and micro-electronics (LDO regulators and ASICs). An experimental setup similar to the one described in Section 2.3.1.1, was prepared for the thermal cycling tests. Each cooling shelf was affixed to a cooling block, connected to a Lauda chiller with precise temperature control, and housed within the climatic chamber. To replicate the conditions similar to STS, KRYO 51 coolant was used which can provide coolant temperature till -40 °C. To preclude icing during the cycling procedure, the chamber temperature was maintained consistently lower than that of the cooling plate.

To evaluate all FEB components and identify potential failures or thermally induced mechanical stress, 12 FEBs underwent thermal cycling. The study for finalizing the TIM and to test the components under the temperature variations was going in parallel. Therefore, initially, thermal

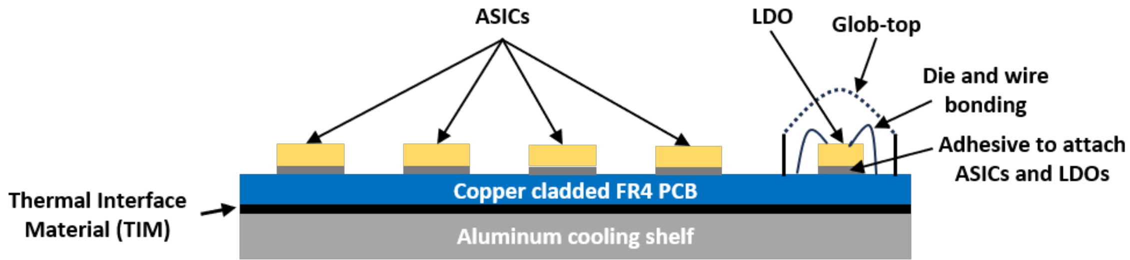

Figure 2.38: Schematic of the components to be thermally cycled, illustrating the FEB mounted on the cooling shelf with TIM. The sketch shows the front side view of the FEB, highlighting a single row of ASICs and a single LDO, with all the components on the LDO marked explicitly. Similar component labels for the ASICs are omitted for simplicity.

Table 2.4: Coefficient of Thermal Expansion (CTE) values and applications for various materials used in the assembly of FEBs.

S.No.	Material	Application	CTE $\alpha 2$ [μm/m/°C]]
1	DYMAX 9001-E-V3.5	Globtop candidate	180
2	DYMAX 9014	Globtop candidate	192
3	DYMAX 9008	Globtop candidate	230
4	EPO-TEK E4110	Adhesive to attach ASICs and LDOs	150
5	Silicon	ASICs and LDOs	2.6
6	FR4	FEB PCB	15
7	Stycast 2850 FT (23 LV)	TIM between FEB and Cooling shelf	39.4
8	Aluminium	Cooling shelf	23.1

cycling tests were performed using thermal pads as the TIM between FEBs and cooling shelves, and later on, the thermal pads were replaced with Stycast 280FT (with 23 LV catalyst). The thermal studies for both the TIMs are summarised in this section. Different versions of glob-top materials were also tested i.e., DYMAX 9001, DYMAX 9008 as filling and DYMAX 9001 as dam and DYMAX 9014. After each cycle, along with the electronics testing, FEBs were optically inspected under the microscope to identify any visible anomalies. The thermal cycling procedure itself was categorized into three distinct types: passive cycling, active cycling, and power cycling. Each of these processes is explained in detail in this section.

2.5.1 Passive cycle

The passive cycling tests for the FEBs were conducted by placing the powered-off FEBs inside a thermal chamber and exposing them to temperature cycles. During each cycle, the temperature was held constant for 20 minutes at extreme temperatures (i.e. -20 °C and +20 °C), as plotted in Fig. 2.39. After every 50 passive cycles, FEBs were optically inspected and a noise scan was performed to cross-check any deterioration in FEB's noise performance because of the thermal stresses and compared to the noise before thermal cycling. Additionally, the FEBs were tested under different temperature gradients (ΔT) during the passive cycling phases, varying the lower temperature limits to simulate the diverse thermal stresses they might encounter during the operation.

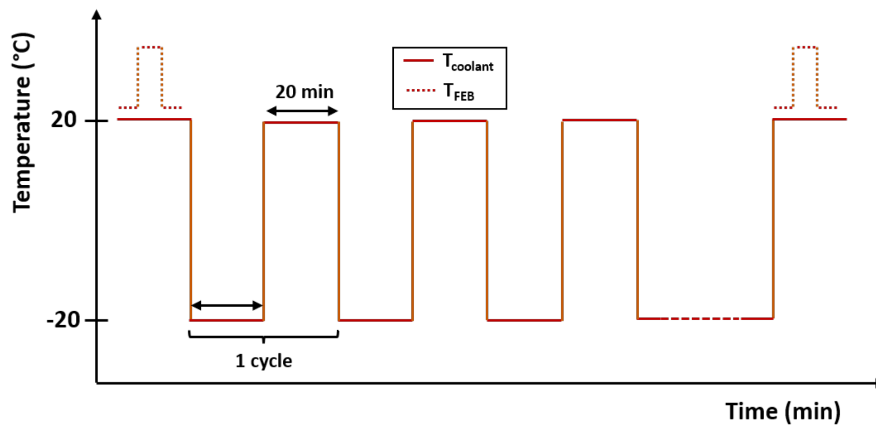

Figure 2.39: The schematic shows the Temperature versus Time plotted for passive cycling, setting -20 °C and +20 °C as the low and high-temperature extremes respectively. Each cycle indicates a rise to a high temperature and a fall to a lower one, with horizontal lines representing phases where the temperature is kept constant. The thick lines show the temperature of the coolant, while dotted lines denote the FEB's temperature, measured once before the cycling and subsequently after every 50 cycles. The height of the temperature rise is random and will depend on the object under thermal cycling.

Passive thermal cycling ensures that all components of a FEB can withstand the same temperature changes. Such a scenario could happen if all connected low-voltage channels are switched off, say, due to radiation exposure. Under such conditions, if the power is not swiftly restored, the FEBs can cool down to match the temperature of the cooling block within a matter of seconds. Hence, it becomes essential to assess whether the FEBs can endure such extreme temperature conditions, especially in low-temperature scenarios.

The results for all the tested FEBs have been summarised in Section 2.5.4. For all the FEBs tested with different temperature gradients, no deterioration in FEB performance was observed

after the passive cycling test. This implies that the FEBs are robust and retain their operational integrity even after being exposed to repeated thermal stresses.

2.5.2 Active cycle

During active cycling, the FEBs are operated in a powered-on state within a temperature-controlled chamber, subjecting them to a range of temperatures in a series of cycles between high and low extremes. This is shown in the schematic in Fig. 2.40 (a), where the temperature of both the FEBs and the coolant varies over time. This not only tests the endurance of the TIM but also monitors the integrity of connections like solder joints and the functional performance of ASICs and LDOs.

The significance of these tests can be extrapolated to the operating scenario of STS. This scenario replicates conditions that might occur in the STS during the cooling system failure. In such a scenario, even though the electronics power will be shut down immediately, it could still lead to an uncontrolled rise in the temperature of ASICs and LDOs. Also, the maintenance procedures may require powering down certain parts of the STS while others remain active, leading to a temperature gradient. The active cycling tests, therefore, serve as a proactive measure to evaluate how such temperature deviations might influence the FEB's behavior. The temperature profile of an ASIC during these tests is shown in Fig. 2.40 (b).

The plot shows temperature changes of the ASIC, Binder, and Lauda temperatures over a series of cycles, with the ASIC temperature demonstrating a consistent gradient of approximately 20 °C higher than the Lauda temperature. This temperature gradient is essential for establishing the operating thresholds within which the FEBs must reliably function. Further details regarding the tested FEBs and observed failures are summarised in Section 2.5.4. It was observed that most of the failures were observed in LDOs at lower temperatures. This observation highlights the importance of further investigating the behavior of LDOs under these thermal stress conditions.

During the cycling, to evaluate the impact of the TIM on the thermal conductivity of the FEBs and to identify hot spots on the FEBs, three DS18B20 temperature sensors were attached to the cooling shelf in different locations, as shown in Fig. 2.41 (a) and the variation of these temperature sensors along with coolant temperature is shown in Fig. 2.41 (b). The results can be summarised as follows:

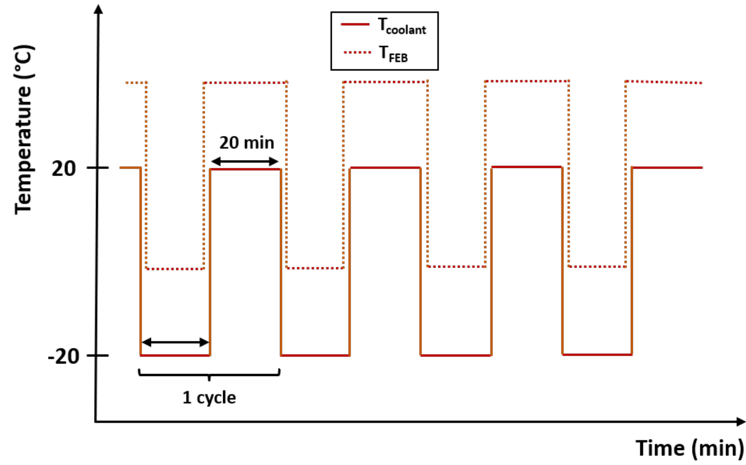

(a)

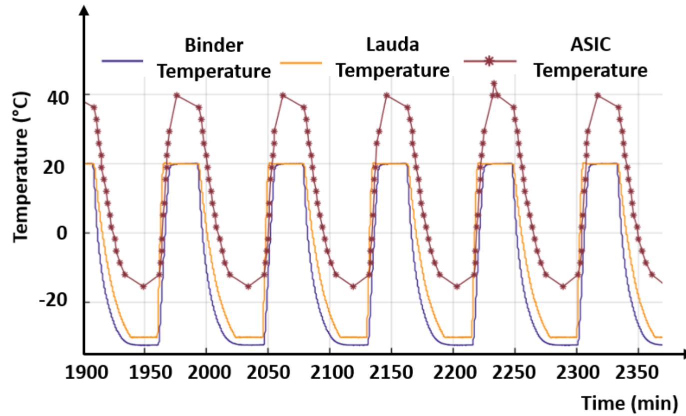

(b)

Figure 2.40: (a) The schematic shows the Temperature versus Time plotted for active cycling, setting -20 °C and +20 °C as the low and high-temperature extremes respectively. (b) Temperature profile for active cycling for a defined time interval, showing the change in the ASIC temperature with respect to the Lauda chiller and the climatic chamber.

- Temperature sensor 1, located on the side of the T-shelf near the power lines, recorded significantly lower temperatures due to its proximity to the cooling plate.
- Temperature sensor 2, positioned on top of the cooling shelf, closely monitoring the temperature of one of the ASICs.
- Temperature sensor 3, placed above the LDO regulators on the left side of the cooling shelf, recorded the highest temperature values, indicating localized heating.

These temperature sensors were placed on a single FEB during active cycling. The data collected from different active cycles demonstrated a constant temperature gradient, suggesting that the

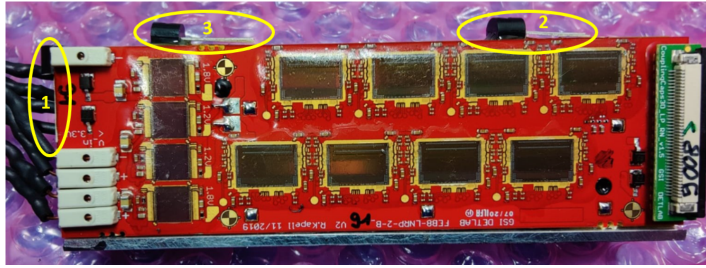

(a)

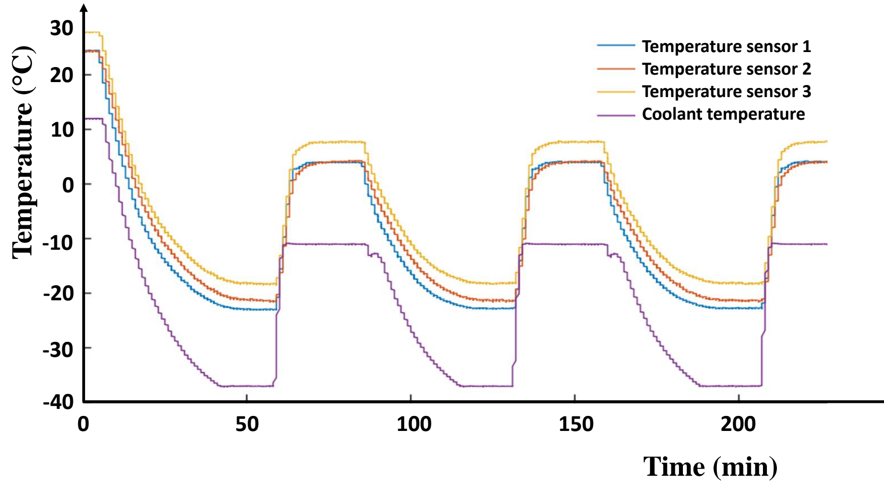

(b)

Figure 2.41: (a) Temperature sensors positioned on different locations on the cooling shelf, (b) Temperature profile during active cycling for a defined time interval, showing the variation of temperature monitored with sensors with respect to the Lauda chiller.

TIM effectively maintains thermal contact. While some failures were observed during active cycling, there was no indication that these failures resulted from the detachment of the FEBs from the cooling shelf during cycling. More details about the failure of FEBs during active cycling are summarised in Section 2.5.4.

2.5.3 Power cycling

Given that radiation damage is expected during detector operation, affecting not only the sensors but also the power electronics, it is essential to investigate the impact of radiation on the entire system. The FEE of the STS will be powered by about 140 low-voltage modules. These modules can be exposed to around 40 mGy/month, resulting in about 9 SEEs (Single event effect) per month per module. Consequently, each FEB must withstand 9 power cycles at low temperatures monthly, highlighting the importance of understanding radiation effects

on these electronics. An irradiation campaign conducted at GSI involved testing several low-voltage power modules with neutron radiation. The goal was to detect radiation-induced errors[1] in the power electronics. Assuming 2 months of operation per year over a 10-year lifespan, the electronics must withstand at least 180 power cycles [91].

In power cycling at a particular temperature (generally the lower temperature), the FEBs are subjected to active heating and cooling cycles by alternately switching the power supply on and off for a desired interval of time. These tests are mostly performed to trigger the wear-out mechanism of components in a shorter period. During detector operation, it is essential to maintain continuous cooling to stabilize the ambient temperature and dissipate the heat generated by the electronics. Therefore, there is a high possibility that the electronics will experience power cycling scenarios during both the operational and commissioning phases. Contrary to passive and active cycling, power cycling represents a more realistic scenario that places maximum stress on the electronics. In power cycling, the temperature difference is generated by turning the FEBs on and off for a desired interval of time, keeping the coolant temperature the same. This process is then repeated multiple times as shown in the schematic in Fig. 2.42.

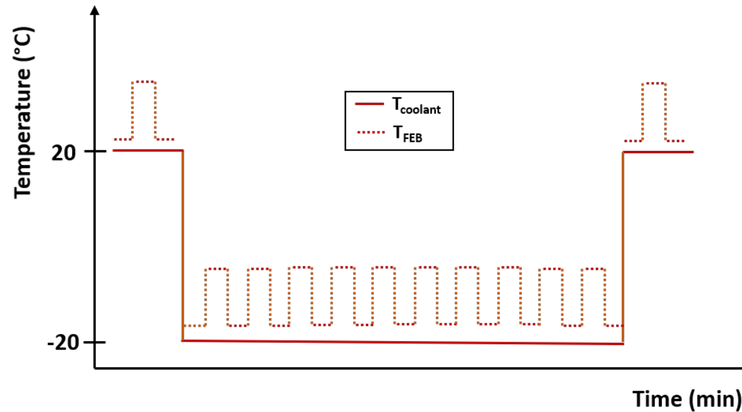

Figure 2.42: The schematic shows the Temperature versus Time plotted for power cycling, setting -20 °C and +20 °C as the low and high-temperature extremes respectively.

Before starting the power cycling, the FEBs are cooled to the specified lower temperature, such as -20 °C (as shown in Fig. 2.42), while keeping the FEB powered off. Once the stable temperature is reached, functionality tests are performed before switching on the electronics. During functional testing with the power off, the FEB remains at a lower temperature for 5 minutes. Subsequently, the FEB is powered on and tested again for functionality, where it stays

[1] A radiation-induced soft error is a temporary malfunction in the low-voltage power modules caused by neutron radiation altering the state of electronic components without causing permanent damage.

for 20 minutes, as shown in Fig. 2.43. This defines one power cycle and such a cycling process is repeated multiple times until any failure is observed. The results of the power cycling tests have been summarised in Section 2.5.4.

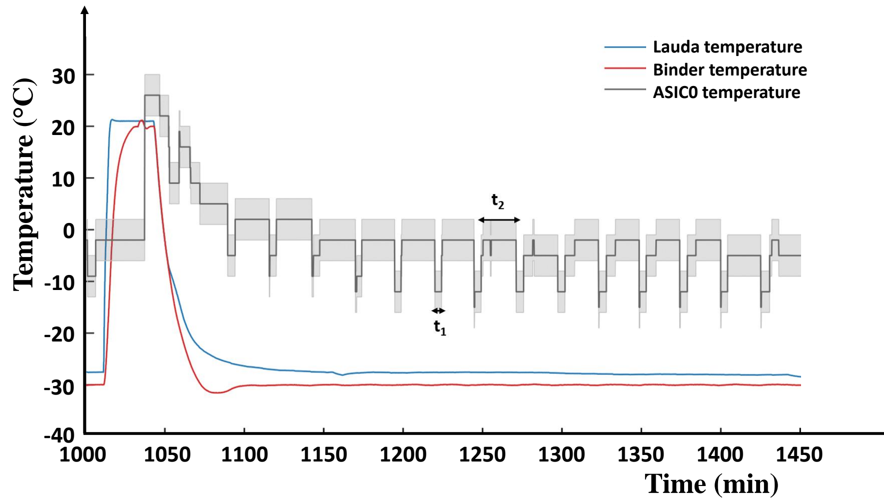

Figure 2.43: Temperature profile for a Power cycling for a defined time interval showing the change of ASIC temperature with respect to Lauda chiller and Binder climatic chamber. The time interval $t_1 = 5$ *minutes when the FEBs are powered off and* $t_2 = 20$ *minutes when the FEBs are powered on with the shaded area shadowed area showing the fluctuations in the temperature values.*

2.5.4 Results and conclusion

The primary objective of the thermal cycling tests was to explore various temperature scenarios that could potentially lead to electronic failures. To track the failures, certain parameters were considered, and FEBs irrespective of the type A or B, were considered as same from a mechanical point of view. All these tests were initially performed with the thermal pads as TIM between FEBs and cooling shelves and later on replaced with Stycast 2850 FT, with 23 LV catalyst. From the previous thermal cycling activities, there were certain components that can show failures during the thermal cycling includes TIM failure, glob top rip-off, ASIC or LDO failures.

12 FEBs were tested under different ΔT by varying the difference in extreme temperatures and the measurements were taken in two sets as shown in the flowchart in Fig. 2.44.

- **First set** of measurement included eight FEBs which are described below:
  - Four FEBs fixed to two cooling shelves using thermal pads and DYMAX 9001 as the glob-top material.

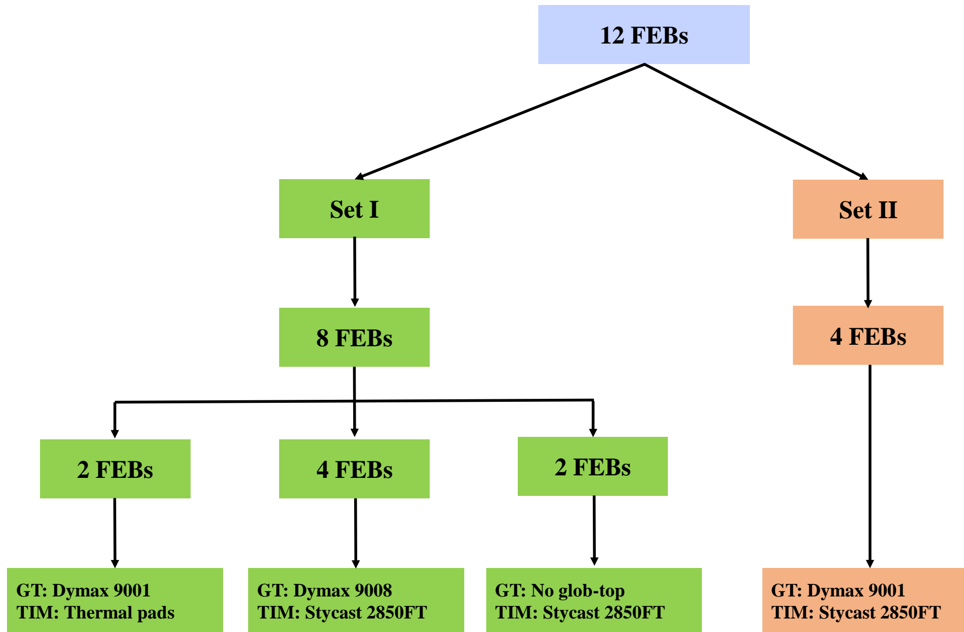

Figure 2.44: Flow chart showing the division of the FEBs into two sets of measurements, where GT refers to Glob-top material and TIM refers to the Thermal Interface material.

- Two FEBs fixed to one cooling shelf using Stycast 2850 FT as the TIM and Dymax 9008 as the glob-top. Since the viscosity of Dymax 9008 is low, therefore, Dymax 9008 was used as the fill for the glob-top material and Dymax 9001 was used as the dam to control the viscosity of the 9008.
- Two FEBs fixed to one cooling shelf using Stycast 2850 FT and without any ASICs and glob-top.

The measurements were taken in such a way that initially a temperature range was defined, followed by passive cycling. FEBs that survived passive cycling underwent functionality tests and optical inspections. After completing passive cycling, the same temperature range was used for active cycling. The FEBs that survived the active cycling were later on power cycled. Each cycling involved a set of 50 cycles and the results of the first set of measurements have been summarised in Table 2.5.

No deterioration in the FEBs was observed during passive cycling. Most temperature-related failures occur when the temperature goes below -30 °C. In these cases, LDOs were the main cause of malfunctioning. Also, it was observed that the FEBs without ASICs and no glob top on the LDOs did not show any malfunction.

Table 2.5: Summary of the Thermal cycling of the first set of measurements including eight FEBs

FEB S.No. and type	Glob-top material	TIM	Temperature range	Passive cycling	Active cycling	Power cycling	Failure scenarios
83 A	Dymax 9001	Thermal pads	-20 to +20 -30 to +20	50 50	50 43	50 (-20) -	No failure 1.2 V LDO failure
90 B	Dymax 9001	Thermal pads	-20 to +20 -30 to +20	50 50	50 50	50 (-20) 40 (-30)	No failure Both 1.2 V LDO and one 1.8 V LDO failure
89 B	Dymax 9001	Thermal pads	-30 to +20 -40 to +20	50 50	50 29	50 (-30) -	No failure 1.2 V LDO failure
89 A	Dymax 9001	Thermal pads	-30 to +20 -40 to +20	50 50	50 29	50 (-30) -	No failure
96 B	No ASIC No glob-top	Stycast 2850 FT	-10 to +20 -40 to +10 -30	- - -	50 50 -	- - 100	No failure
97 A	No ASIC No glob-top	Stycast 2850 FT	-10 to +20 -40 to +10 -30	- - -	50 50 -	- - 100	No failure
93 A	Fill: Dymax 9008 Dam: Dymax 9001	Stycast 2850 FT	-10 to +20 -40 to +10 -30	50 50 -	50 50 -	- - 100	No failure No failure No failure
91 B	Fill: Dymax 9008 Dam: Dymax 9001	Stycast 2850 FT	-10 to +20 -40 to +10 -30	50 50 -	50 50 -	- - 100	No failure No failure 1.8 V LDO failure

Table 2.6: Summary of the Thermal cycling of the second set of measurements including four FEBs

FEB S.No. and type	Glob-top material	TIM	Temperature range	Passive cycling	Active cycling	Power cycling	Failure scenarios
94 A	Dymax 9001	Stycast 2850 FT	-10 to +20 -40 to +10 -30	50 50 -	50 50 -	- - 200	No failure No failure 1.2 V LDO failure
94 B	Dymax 9001	Stycast 2850 FT	-10 to +20 -40 to +10 -30	50 50 -	50 50 -	- - 200	No failure
95 A	Dymax 9001	Stycast 2850 FT	-10 to +20 -40 to +10 -30	50 50 -	50 50 -	- - 300	No failure
95 B	Dymax 9001	Stycast 2850 FT	-10 to +20 -40 to +10 -30	50 50 -	50 50 -	- - 300	No failure No failure 1.2 V LDO

- **Second set** of measurements were conducted after gaining experience and learnings from the first measurements. Four more FEBs were taken using Dymax 9001 as the glob-top material for all the FEBs. The four FEBs were glued to two cooling shelves using Stycast 2850 FT as the chosen TIM. The main observable in this scenario was to check that at what low temperatures it is possible to go so that electronics can survive without showing any failures due to the thermal stress. The results of the second set of measurements have been summarised in Table 2.6.

  Table 2.6 indicates that no failures were observed during the passive or active cycling even at low temperatures till -30 °C. However, this set of measurements underwent a higher number of cycles, and most failures were observed during the power cycling, starting from 100 cycles. The failures were observed in the LDO operation as well as in several ASICs. The results have been shown in Fig. 2.45.

  The Fig. 2.45 (a), illustrates the onset of failure in the 1.2 V LDO at -30 °C, where the current starts to drop at t = 500 min, indicating increased circuit resistance. As soon as the temperature reaches 20 °C, the current returns to normal at t=1000 and t=2500 min. However, after t = 3000 minutes, the failure became irreversible, indicating complete LDO failure. This irreversible failure indicates that prolonged exposure to extremely cold temperatures can permanently damage the LDOs, leading to a loss of functionality.

  In Fig. 2.45 (b), the onset of ASIC malfunction in a FEB is demonstrated. A temperature drop of 15 °C, signifies an issue where the LDO fails to provide the nominal current to the ASIC. This indicates that the ASIC's performance is directly affected by the LDO's inability to maintain a stable current at lower temperatures.

  These electrical failures were also confirmed through optical inspections, providing visual evidence of the damage caused by temperature variations. In Fig. 2.46, the lifting of the glob-top surface at low temperatures creates an air bubble, which in turn causes the lifting of the LDO bonds. This damage explains the electrical malfunctions observed: the glob-top lifting disrupts the connection between the LDOs and ASICs, leading to increased resistance and eventual component failure.

In summary, two parallel studies were conducted to enhance the understanding of the thermal stress induced on the components of the FEB. The studies involved testing of a TIM material and examining glob-top material during the thermal cycling tests. The primary findings after the thermal cycling are as follows:

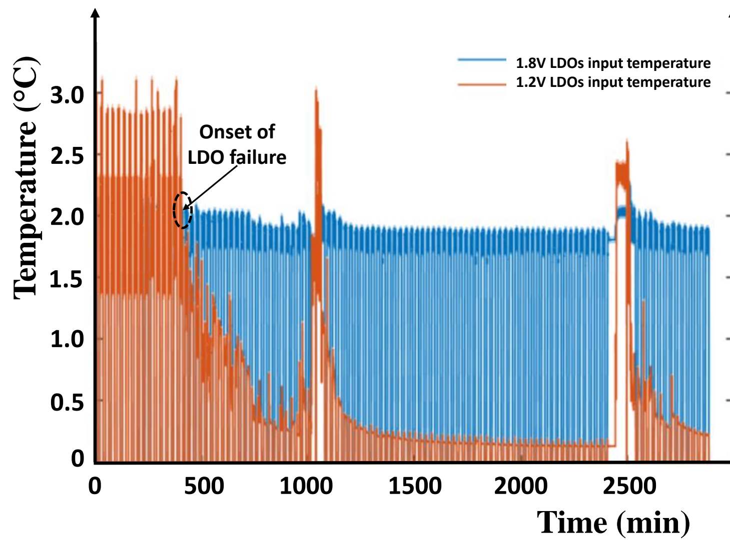

(a)

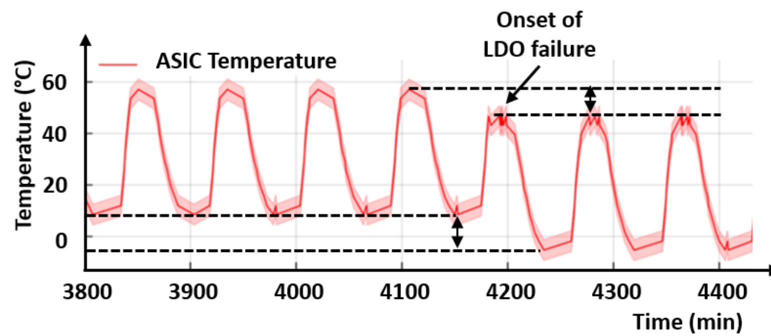

(b)

Figure 2.45: During the power cycling of FEBs at T= -30 °C, (a) Current consumed by 1.8V and 1.2V LDO regulators, (b) Temperature change in the chosen ASIC of one of the FEBs.

- **Power Cycling Failures:** The majority of failures occurred during power cycling at -30 °C, with failures predominantly becoming evident after an average of 100-120 cycles.

- **Material Selection:**

  - **Thermal Interface Material:** Stycast 2850FT was selected over thermal pads for its enhanced performance between the FEBs and the cooling shelf.

  - **Glob-top Material:** Dymax 9001 was chosen to be the right globtop material for ASICs and LDOs, due to its sustainability under thermal stress and easy handling.

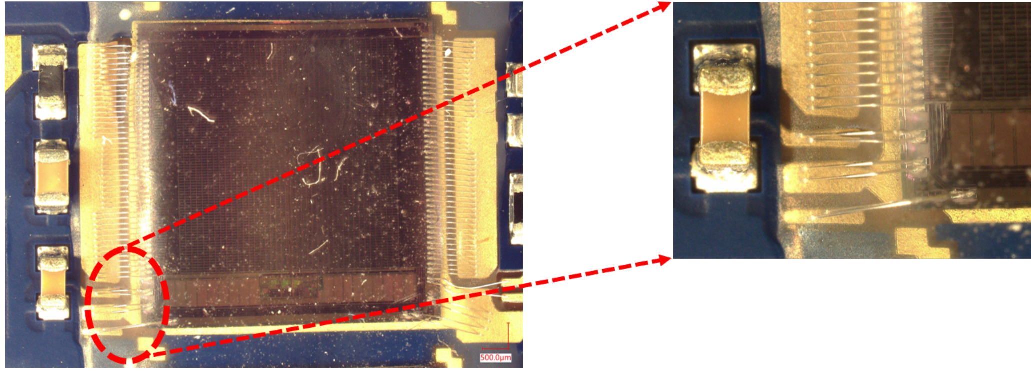

Figure 2.46: Zoomed-in image showing the air bubble between bonds of the LDO and the glob-top.

The main findings from this chapter include the choice of TIM and glob-top materials that can survive the operating as well as the worst-case scenario conditions of the STS. Since there have been no failures observed across all 12 FEBs concerning TIM, therefore, Stycast 2850 FT (23 LV catalyst) was finalized as the preferred TIM for the module production. Additionally, for the glob-top material, Dymax 9001 was favored over Dymax 9008 (with Dymax 9001 as the dam) due to its higher viscosity, which simplifies handling during module assembly.

After finalizing the TIM and glob-top materials, further failures were observed. It is important to highlight that the summarized thermal cycling tests were conducted with FEBs mounted on non-anodized cooling shelves and without solder masks. Further tests were conducted using anodized aluminum shelves and FEBs with solder masks, reflecting the finalized component choices.

The subsequent testing focused on determining safe operational temperatures for the electronics. Using the finalized components, four FEBs with solder masks were glued with Stycast 2850FT (23 LV catalyst) to two anodized cooling shelves. The setup was subjected to a revised cycling procedure, which was adapted from learnings gained during previous thermal cycling experiments.

The updated procedure, detailed in Fig. 2.47 [90], involved a combination of passive and power cycling, with ten power cycles within each thermal cycle at the lowest temperature. Consequently, 50 thermal cycles resulted in 500 power cycles, significantly higher than the expected operational number of around 200 [91]. This rigorous testing was designed to challenge the electronics under extreme conditions and ensure their reliability. Although simultaneous failure of all electronics is unlikely, subjecting the samples to a high number of cycles provides confidence and ensures stability.

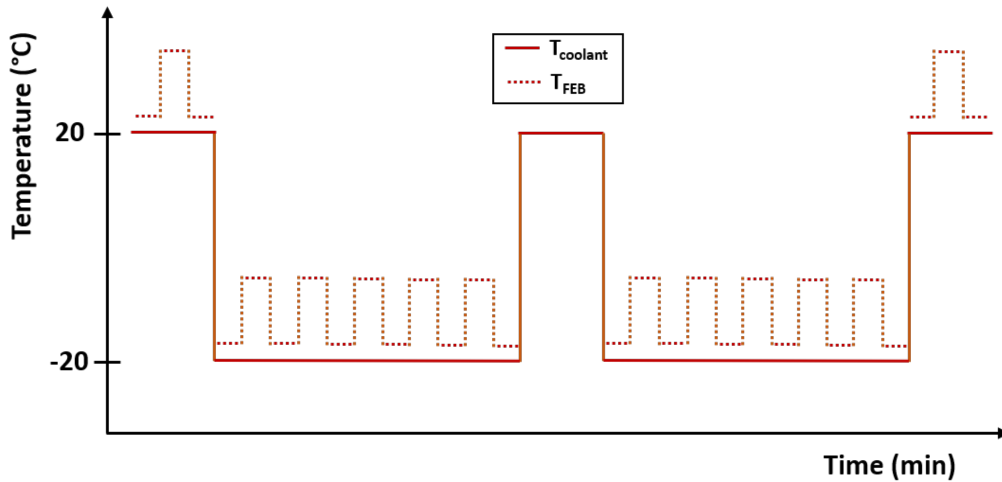

Figure 2.47: The schematic shows the Temperature versus Time plotted for updated power cycling, setting -20°C and +20°C as the low and high-temperature extremes respectively.

Given that the majority of previous failures were typically anticipated at or below -30 °C, it was decided to conduct testing at somewhat milder conditions. Therefore, 50 thermal cycles were performed at -20 °C and the results were promising. All four FEBs showed no signs of failure, confirming that the electronics are capable of operating reliably at this temperature. Similar measurements were performed for the same FEBs for -25 °C, where once again, no failures were observed. Therefore, this confirms that the electronics can reliably function at temperatures as low as -25 °C, with issues becoming apparent only at lower temperatures.

Chapter 3

Ladder Assembly for STS

3.1 Motivation for ladder assembly

Particle physics experiments rely heavily on detectors to explore and analyze the characteristics of particles generated during collisions or interactions. A key parameter to measure in these experiments is the momentum of particles. Precision in momentum measurement necessitates detectors to mitigate any sources of uncertainty or error that may compromise the accuracy of the measurement. This precision is compromised by any source of uncertainty, particularly the material within the detector through which particles must pass through. These materials include layers of detectors, support structures, shielding, and other components essential for the operation of the detector but can impact the measurement accuracy.

When charged particles interact with these materials, they may scatter, deviating from their intended paths due to interactions with atomic nuclei and electrons. This scattering is a primary source of uncertainty in momentum measurements and is heavily influenced by the thickness and composition of the material encountered. The extent of this scattering is quantitatively described by the Gluckstern formula, which connects the scattering angle to the particle's properties and the material's characteristics, given by the Equation [42]:

$$\theta_0 = \frac{13.6\mathrm{MeV}}{\beta.\mathrm{c.p}} \frac{\mathrm{z}}{\sqrt{\mathrm{x}/\mathrm{X}_0}} [1 + 0.038 \ \cdot \ \ln\frac{\mathrm{x}}{\mathrm{X}_0}] \tag{3.1}$$

where, θ_0 is the scattering angle, βc is the velocity of the charged particle relative to the speed of light, p is the momentum of the particle, x is the distance traversed and X_0 is the radiation length of the material.

According to Equation 3.1, the scattering angle is inversely proportional to the momentum of the particle for a given material thickness. This implies that high-momentum particles are less affected by scattering compared to low-momentum particles under similar conditions. Therefore, to enhance the momentum resolution, especially for the particles with lower energies, it is crucial to minimize the uncertainties caused by material-induced scattering. This is achieved by reducing the material budget of the detector design, thus enabling more precise measurements of particle momentum.

3.1.1 Specifications of STS ladder

The main component of STS is the silicon sensors, which serve as the detector for the charged particles. The use of silicon sensors enables precise spatial information crucial for reconstructing particle paths with high accuracy [44]. While the intrinsic resolution of the sensors is critical, equal importance is attributed to the design and the materials of the detector structure. Therefore, the choice of materials for constructing the detector components becomes important, especially for the components that will be placed in the detector's sensitive area.

To start with, a module when assembled, needs to be placed on a support structure where it can be positioned within the defined precision. This support structure, which holds the modules, including sensors and micro-cables, is referred to as "ladders" in STS. These ladders must ensure that sensors are maintained in their exact geometrical positions with high mechanical precision and stability, which is vital for the accurate measurement of particle trajectories. The design and material selection for the ladders are governed by several key specifications defined as below:

- **Low mass**: The weight of the STS ladders directly impacts the system's momentum resolution and overall efficiency. The primary advantage of low-mass materials is their ability to reduce multiple scattering of particles, minimizing angular deviations as they traverse the detector. According to the Gluckstern formula (Eq. 3.1), the scattering angle θ is influenced by several factors including the material thickness x and the radiation length X_0 of the material, given by Eq. 3.2 [45].

$$X_0 = \frac{716.4 \cdot A_N}{Z(Z+1) \cdot \ln\left(\frac{287}{\sqrt{Z}}\right) \cdot \rho} \text{ cm} \tag{3.2}$$

where X_0 is dependent on the material's atomic number (Z), mass number (A_N), and density (ρ) of the material.

Therefore, to minimize the material budget, the ladder material should be composed of lightweight material with a low atomic number to minimize the contribution to multiple scattering and acquire maximum resolution as needed.

- **Radiation tolerance**: When a charged particle passes through a silicon detector module, it generates both ionizing and non-ionizing energy losses, described by Total Ionising Dose (TID) and Non-Ionising Energy Loss (NIEL), respectively. Ionizing effects produce electron-hole pairs essential for signal processing, while non-ionizing damage impacts the material structure of the detectors, affecting both the bulk and surface layers. Such damage increases leakage currents and requires higher depletion voltages, which can escalate to thermal runaway, potentially causing detector failure.

  The STS ladders, which support the silicon sensors, are designed to maintain their structural integrity and functionality in a harsh radiation environment. They should be constructed from materials with high radiation hardness to withstand intense radiation without significant deterioration throughout detector's lifetime. This choice is essential to prevent degradation that could impair the detector's performance or structural integrity.

Considering the specifications outlined, it is important to make a balance between the detector's design requirements and the materials chosen. To enhance material efficiency, Carbon Fiber (CF) was chosen for constructing the STS ladders. CF is favored not only for its strength, lightweight, and durability but also for its low atomic numbers, resulting in a reduced x/X_0 ratio. A smaller x/X_0 ratio allows particles to pass the material with minimal distortion of their properties.

In Fig. 3.1, the material budget simulation for the last station of the STS is shown, based on the v22d geometry of the STS [43]. The plot includes all planned ladders to be used in the STS, along with perforated tubes, silicon sensors, and micro-cables. Notably, the cut-out for the beam pipe is excluded pending finalization. The maximum material budget achieved is $x/X_0 = 0.35$ % for the carbon fiber twist and 0.60 % for the knots on the tubes. The average material budget originating from the carbon fibers on the sensors stands at $x/X_0^{avg} = 0.047$ %.

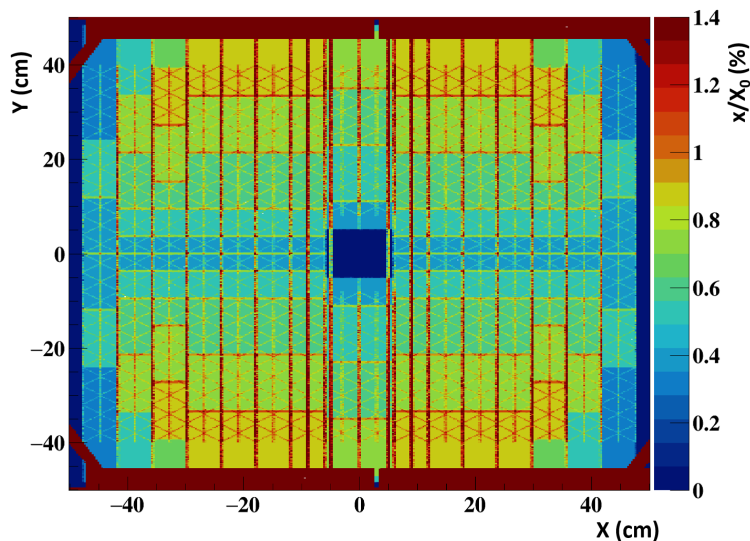

Figure 3.1: Material budget simulation for station 7 (last station) of STS.

3.1.2 Performance requirements of STS ladder

With the selection of Carbon Fiber as the designated material for STS ladders, it becomes imperative to outline the performance requirements to ensure optimal functionality. The precision and accuracy of particle detection rely significantly on the performance of the detector ladder. The following outlines the essential performance requirements for the STS ladder:

- **Ladder design optimization**: The ladder design is a crucial aspect, ensuring compatibility with module integration. The ladder serves as a support structure for multiple modules, each containing sensors and micro-cables. Given that each ladder will hold up to 10 modules, each weighing approximately 10 g (weight of the sensor and the cables), ladder stability is important to support the weight of these modules with minimum displacement. Excessive bending will lead to misalignment of sensors, resulting in inaccurate measurements.

  Also, the shape of the ladder must accommodate the mounting of sensors and modules effectively, i.e., the base of the ladder has to be wide enough to fit the micro cable stacks underneath. The manufacturing process must achieve precise dimensional accuracy, especially for the base width, with a tolerance of ± 200 μm. Therefore, ensuring optimal ladder design and stability is essential for maintaining structural integrity over time.

- **Position Accuracy**: Achieving precise sensor positioning better than ± 100 μm in transverse directions (xy) after installation of ladders in STS, so that software-based alignment procedures [47] can be applied. But to aim for the spatial resolution of STS, we can not rely only on the mechanical mounting precision alone. After the sensors (with micro-cables and FEBs) are mounted on the ladder, the ladder needs to be mounted with even higher precision to ensure that the overall system meets its position accuracy requirements. Therefore the CF part has to be mounted with its end-plates to the STS detector's C-frames with an accuracy one order of magnitude higher, i.e. 10 μm, better than the sensors' spatial resolution.

- **Vibration characteristics**: To ensure robust and reliable operation, detector ladders must exhibit a vibrational behavior characterized by eigenfrequencies that differ from the system frequencies. When an object's eigenfrequency coincides with the system's frequency[1], resonance can occur, leading to excessive and potentially disruptive vibrations. This section will be discussed in detail in the next chapter.

The performance requirements outlined for STS ladders, are covered in detail showcasing how its implementation directly influences the overall performance of the STS.

3.2 Design of carbon fiber ladder

After specifying the material choice for the STS ladder and understanding its performance requirements, the next crucial step is to optimize the ladder's design. The concept of the STS ladders has been adapted from the barrel geometry of the ALICE Inner Tracking System [48], with modifications for the STS ladder. Although the ladder's mechanical contribution to the material budget is minimal compared to sensors and micro-cables, specific changes are made to the shape, material, and production methods. In the ALICE ITS design, the side beams of the staves are constructed from folded carbon fiber prepreg material[2] [46], known for its strength

[1] System frequency refers to the inherent frequencies at which a system naturally oscillates during its operation. These frequencies are fundamental to the design and functioning of mechanical systems and are determined by various factors such as the system's physical configuration, material properties, and operational conditions.

[2] Prepreg materials consist of fibers, such as carbon fiber, that are already impregnated with a resin system, including a curing agent. This preparation allows for precise control over the resin content and fiber alignment, leading to materials with consistent quality and superior mechanical properties. It is ideal for applications requiring lightweight yet strong components, such as in aerospace or sports equipment manufacturing.

and lightweight properties. For the CBM-STS, an alternative approach has been explored using carbon fiber tubes with dimensions of 1.5 mm outer diameter and 0.7 mm inner diameter. This choice favors tubes over solid beams to facilitate fiber winding processes while eliminating sharp edges that could complicate manufacturing and integration.

The ladders are designed to maintain sufficient stiffness to prevent excess bending, ensuring they remain stable and rigid during the assembly and operational phases. The winding technique involves using a winding hub with a core and three detachable side pieces. Carbon fiber tubes are installed on the side pieces, and an endless fiber bundle is wound on the revolving hub, following a designed cell grid, as shown in Fig. 3.2.

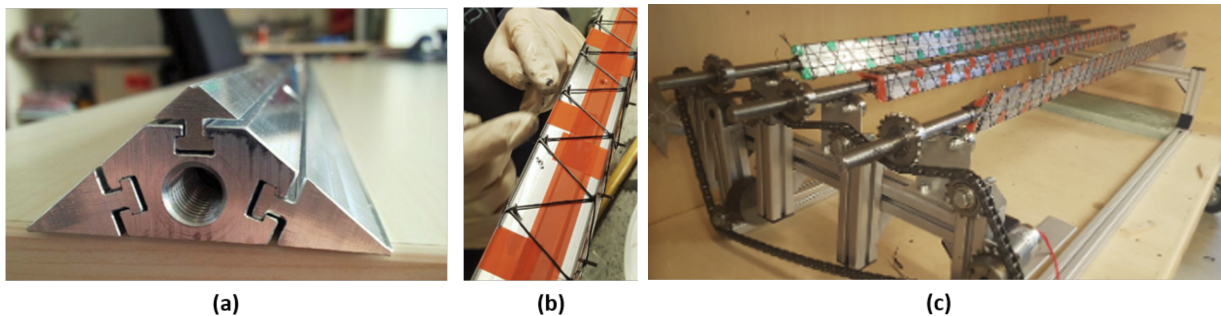

Figure 3.2: (a) Hub for winding fiber on carbon tubes – core with side pieces, (b) CF winding on hub (c) Rotation device for winding the cores.

Prototype ladders, prepared with a winding technique using CF material, were fabricated to be tested for stiffness and compatibility (see Fig. 3.3). Given that the maximum ladder length will be 970 mm, each initially prepared ladder will be 1200 mm in length and can subsequently be cut to the desired size, weighing approximately 14.8 g.

Due to the CBM forward geometry, modifications are made to the standard ladder's geometry to accommodate intersections with the beam pipe. Standard ladders with 27 variants are designed for various lengths, ranging from 480 to 970 mm, while central ladders, having 16 variants, will be manufactured for positions close to the beam pipe [49]. The goal is to create a sufficiently stiff ladder without introducing unnecessary passive material. The ladder variants, with and without central openings, are carefully designed, considering the positioning of sensors, as can be seen in Fig. 3.4.

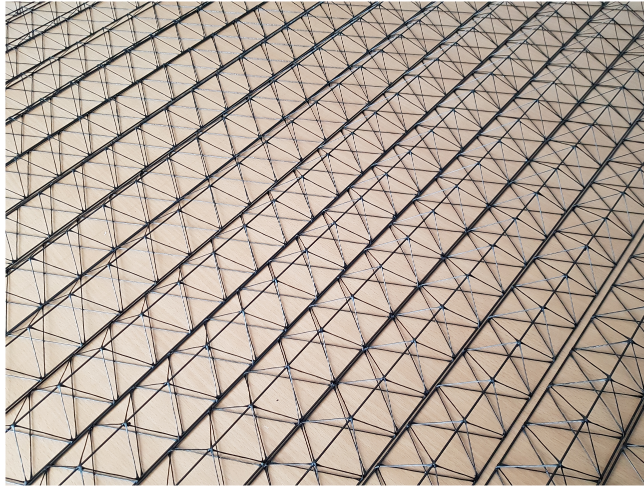

Figure 3.3: Prototypes of carbon fiber ladders after manufacturing.

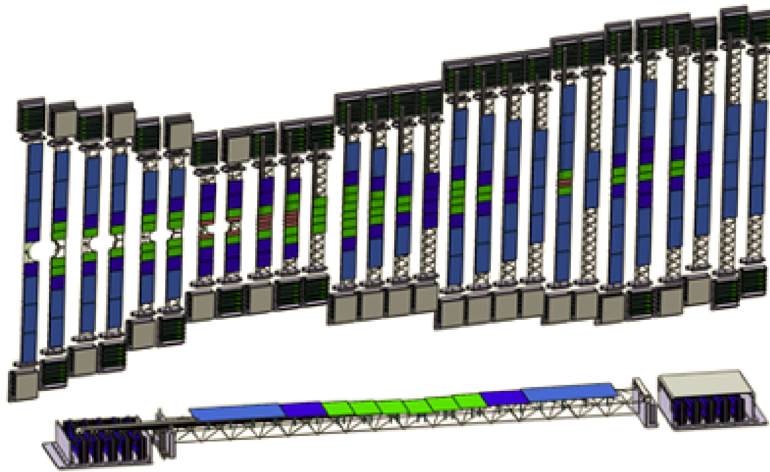

Figure 3.4: Computer-Aided Design (CAD) drawing of different ladder variants.

3.3 Quality assurance of bare ladders

To evaluate the structural integrity and stiffness of the bare ladders, a series of prototype ladders were manufactured. This included one standard ladder, and two central ladders with cut-out diameters of 104 mm and 83 mm, as shown in Fig. 3.5. The ladders were optically inspected to cross-check their mechanical stability, before the final production.

The central ladders, due to the presence of middle cut-outs, exhibit reduction in stiffness compared to the standard ladder, leading to significantly larger deformations under similar loads. This resulted in about twice the elongation for the central ladders compared to the standard ladder when subjected to a load equivalent to the weight of sensors and micro-cables, estimated at 110 grams for 10 modules. The ladders were placed on support structures and the load was

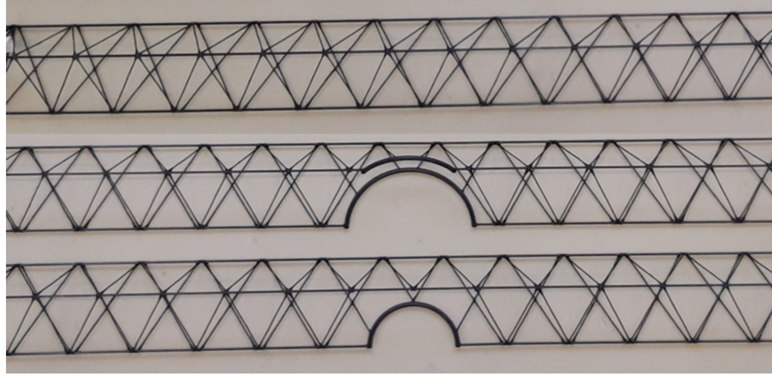

Figure 3.5: Prototype of different ladder types, including a standard ladder and two central ladders with different-sized openings in the middle for the beam pipe, to be tested optically for stiffness.

uniformly distributed along their length. Fig. 3.6, shows an example of a central ladder with an 83 mm diameter, and other two ladders also underwent similar inspection.

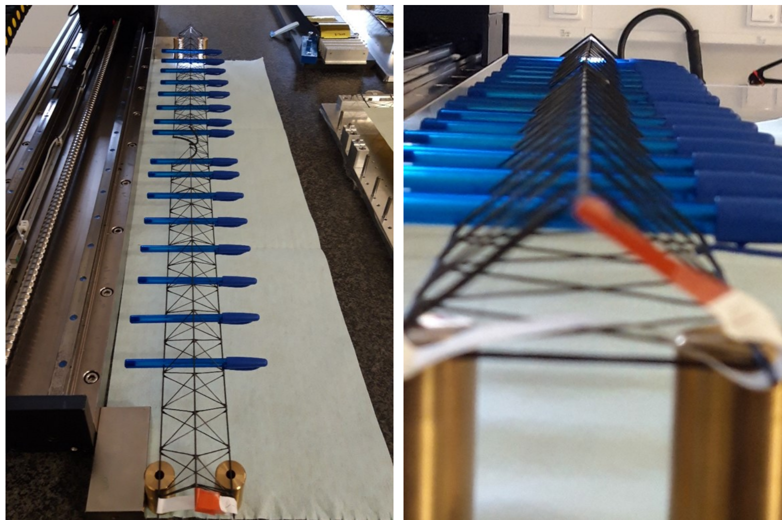

Figure 3.6: Central ladder fixed on support for optical inspection with a load equivalent to the weight of sensors and micro-cables.

The result of the optical inspection for one standard ladder and two central ladders has been plotted in Fig. 3.7, showing the deviations in the z and y axis from their nominal positions. It is essential to highlight that during these measurements, the ladders were not affixed but simply supported on blocks. Under the influence of the load equivalent to the combined weight of the sensors and cables, the central ladder with the larger cut-out (considered as the worst-case scenario) deviated by approximately 2.8 mm in the z-direction. The ladder with a smaller cut-out experiences a bending of 1.4 mm, while the standard ladder remains nearly flat with a bending of only 0.3 mm. This observed deviation is of paramount concern, as it signifies that the

central ladders, when loaded with modules, are already 2.8 mm away from the desired position resolution, emphasizing the need for improved structural rigidity in central ladder design (see Fig, 3.7 (top)).

The plot in Fig. 3.7 (bottom), shows the deviation in y-direction experienced by the ladder from its nominal position after it is loaded. The y-direction deviation is of particular concern, as any movement in the sensor position along the y-axis, resulting from the applied load, could interfere with particle tracking. It was observed that the standard ladder exhibits almost no deviation (0.007 mm), showcasing its robustness. Meanwhile, in the case of a smaller cut-out, the deviation is around 0.91 mm and a large cut-out deviates the maximum by 1.6 mm.

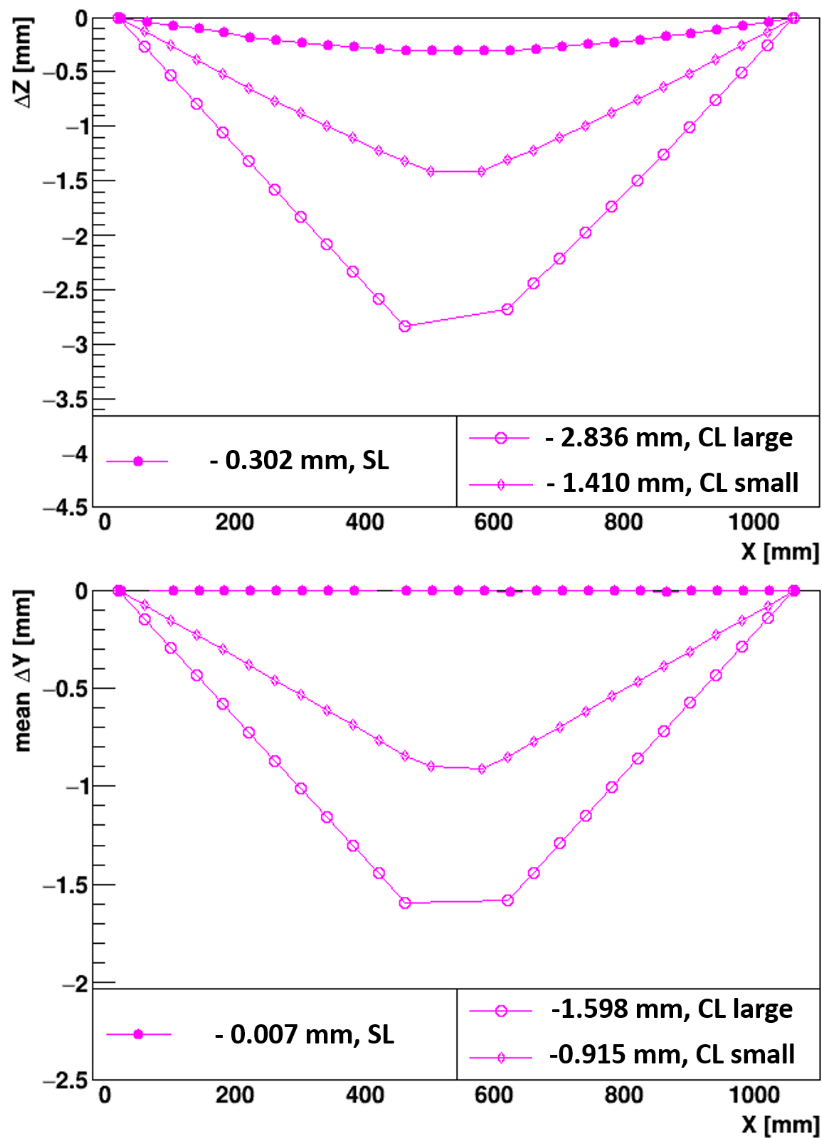

Figure 3.7: Plots showing the deviation in ladder structure under load in (a) z direction (b) y direction. SL denotes the standard ladder and CL represents the Central ladder with smaller and larger cut-outs .

These findings underscore the need for further enhancements in the design and assembly procedures of the central ladders to ensure they meet the required rigidity, especially in the z-direction. Apart from optimizing its design, measures should be taken to provide mechanical support during assembly, thereby alleviating sagging in the Z direction. In the case of y-direction, an assembly procedure involving the gluing of ladders to bearings prior to module mounting could help minimize deviations.

Moreover, it is noteworthy that although the ladder is initially assembled horizontally, it will ultimately be mounted vertically on the stations. To facilitate this transition without inducing additional forces during ladder installation on the detector frame, a dedicated transfer tool will be used. Detailed discussions of these procedural steps are provided in this chapter.

3.4 Components of Ladder Assembly

From the sensor production to the final assembly of ladders at the stations, it is important to establish a well-structured procedure. The initial phase includes the assembly of modules, starting from optical [50] and electrical [51] testing of sensors and progressing to the different steps, including the connecting of sensors via data cables to the FEBs, forming a complete module. This process has been developed, resulting in the preparation and testing (electrical) of several modules to test their noise performance [52].

However, the preparation of functional modules does not guarantee the particle tracking requirements for the STS. To enable the precise reconstruction of particle trajectories, it is essential to maintain the necessary mechanical precision in mounting a module on the ladder. Therefore, ensuring an assembly procedure is crucial when positioning sensors on the ladder. The ladder assembly procedure in STS comprises of different components that are described as follows:

- **Bare ladder**: The fundamental component of STS integration is the ladder structure. The ladder plays a crucial role as the primary support structure for holding the detector module in its precise location. This precision is paramount, as any deviation in module positioning can potentially introduce challenges to the efficiency of track reconstruction within the detector system. When the module positioning is compromised, the risk of errors in alignment software increases. To start with the ladder assembly, the ladder depending on its location in the STS geometry is chosen and cut into the right length.

- **Bearings** The ladder after cutting, needs to be aligned in a way that the three edges of the ladder from both ends can be fixed. To ensure the stability and structural integrity of the ladder, it is glued to the aluminum structures, referred to as "Bearings". There are two types of bearings used for ladder fixation: a fixed bearing and a floating bearing, each serving specific purposes. The bearings mentioned here are already the modified version of the bearings that will be used to assemble the ladders for the final STS.

  1. **Fixed bearing** The fixed bearing is designed to offer robust support to the ladder structure. It consists of essential components, including the bearing block, ballpin, compression spring, spacer sleeve, and cable clamp, as shown in Fig. 3.8 (left). The ballpin helps in accurately positioning the bearing block while preventing torque transmission from the screws.

     During installation, precision is maintained to ensure that the bearing is positioned perpendicular to the ladder's direction, as shown in Figure 3.8 (right) during ladder assembly. Additionally, the use of springs during fixation allows for a slight rotational flexibility around the ballpin in the z-axis. Therefore, a fixed bearing is characterized by five fixed degrees of freedom (DOF), including translational movement along the x, y, and z-axis, as well as rotational movement along the x and y axes, while allowing rotational freedom along the Z-axis.

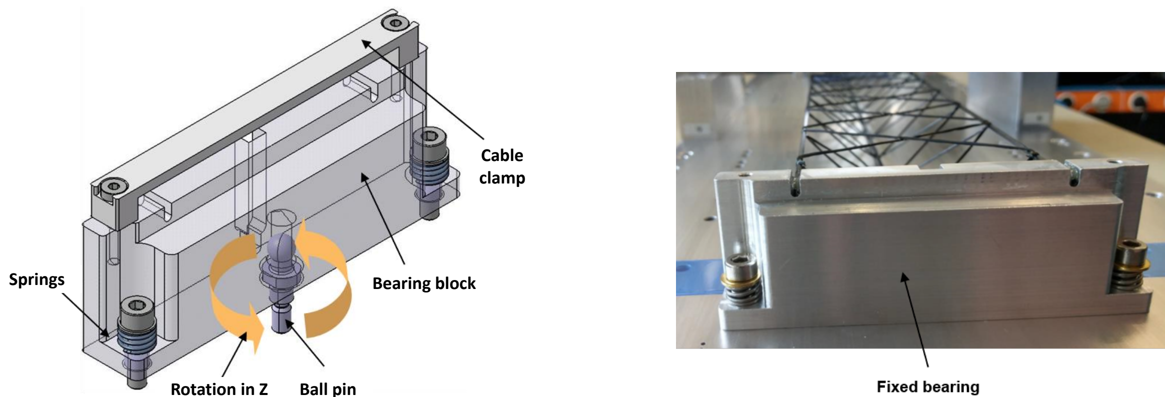

Figure 3.8: (Left) CAD drawing of the fixed bearing with all the components labeled, (Right) Fixed bearing holding the edges of the ladder from one side.

  2. **Floating (or loose) bearing**: The floating bearing introduces flexibility into the ladder's design, offering DOF in both translational and rotational aspects. This flexibility is achieved through components such as the bearing block, ball pin, clamps for securing the bearing block, and clamps for cable management (See Fig. 3.9) (left).

The term ”floating” signifies the allowance for subtle rotational adjustments around the ballpin. A floating bearing has 4 DOF fixed including translational x and z axis and rotational x and y axis, whereas translational y and rotational Z are kept loose. To accommodate for thermal contraction, a prescribed 0.8 mm gap is maintained between the bearing block and the clamp, ensuring structural stability.

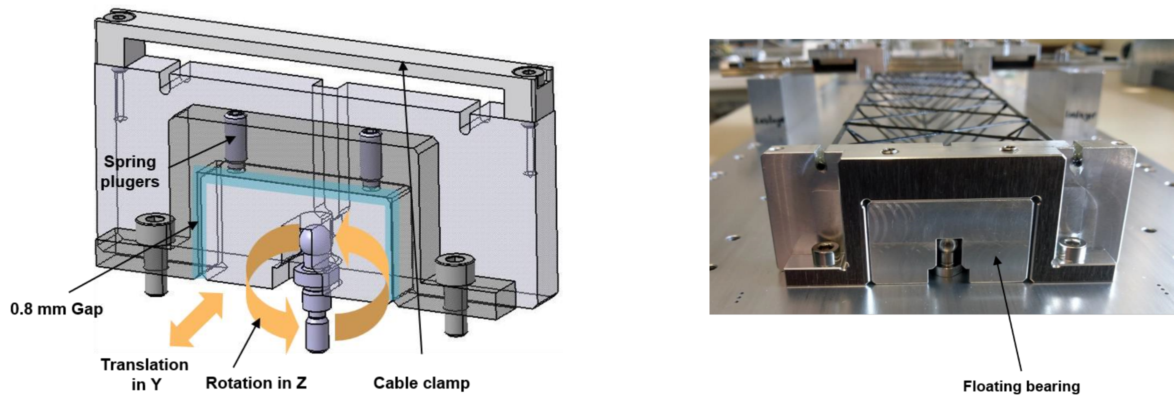

Figure 3.9: (Left) CAD drawing of the floating bearing with all the components labeled, (Right) Floating bearing holding the edges of the ladder from one side.

- **L-legs** To position the sensors on the ladder, direct gluing is not feasible due to the presence of micro-cables following each sensor. Hence a defined gap needs to be maintained between two sensors while positioning them on the ladder. Therefore, L-shaped glass fiber support structures, commonly referred to as “L-legs” (see Fig: 3.10), are used for this purpose.

  The L shape is selected so that the longer arm can be glued to the ladder, and the top shorter arm provides support to the sensor. However, due to the ladder’s winding technique, there’s a possibility that the region intended for gluing the L-leg may coincide with the winding knot, where two fiber bundles attach to the carbon tube. Therefore, to compensate for the enlargement of the CF ladder structure, the length of the shorter arm is chosen as 2.6 mm, while the longer arm is set at a length of 12 mm (see Fig: 3.10 right).

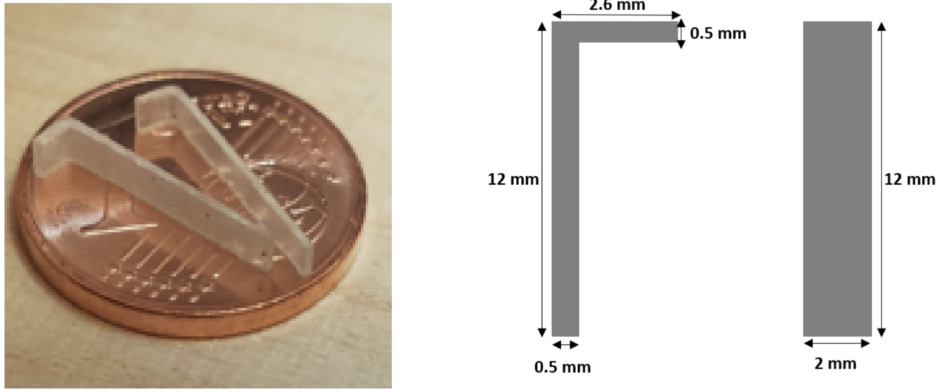

Figure 3.10: (left) Carbon-fiber L-shaped support structures used for the sensor mounting, referred to as "L-legs", (Right) Side and front view of the L-legs, including dimensional details.

3.5 Ladder Assembly procedure

The accuracy with which the modules will be mounted to construct the ladders needs to be cross-checked experimentally. After defining the boundary conditions, the assembly procedure should be developed to ensure that the mounting precision can be achieved. Hence, it is imperative to emphasize the significance of well-defined tools and structured assembly procedures.

A standardized assembly process serves two primary purposes. Firstly, it ensures uniformity and dependability in the construction of each ladder, as they are all built following the same procedure. The uniform construction of individual ladders significantly contributes to the precision and reliability of the entire system.

The advantages of a standardized assembly process go beyond individual ladders. To achieve mechanical precision, the assembly procedure should be designed with tools that minimize errors. Moreover, it should be sufficiently straightforward to be replicated consistently across a large number of ladders. Therefore, it is important to establish a ladder assembly procedure using appropriate tools and systematic steps. This section outlines all the necessary steps for assembling a ladder.

3.5.1 Ladder preparation and integration

The initial step in assembling the ladder for module mounting involves preparing the ladder itself. Depending on the length of the ladder to be assembled, a corresponding aluminum-based baseplate is designed. This baseplate has specific requirements, including predefined holes for

attaching bearings and positioning blocks. These features help guide the tools during module mounting.

Once the appropriate baseplate is selected, bearings are fixed onto it to define the correct positioning for the ladder. The ladder is then cut to the required length, given by the STS geometry. After the cutting, the edges of the ladder are attached to the bearing grooves on both sides using Araldite 2011 glue, as shown in Fig. 3.11. It is important to note that this adhesive needs approximately 24 hours to cure, following the instructions provided in the glue data sheet. During this curing period, the ladder is left undisturbed.

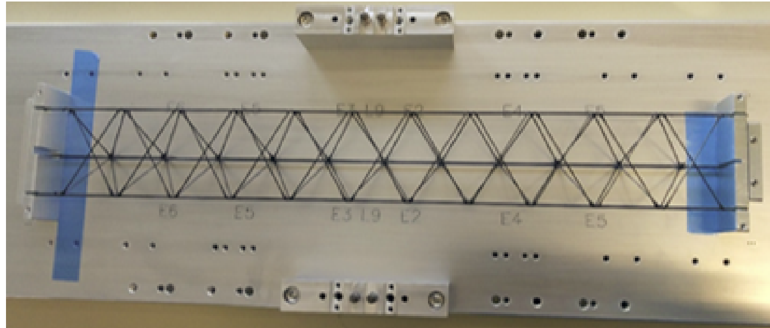

Figure 3.11: STS ladder, once cut into the required shape, is glued to both the bearings, with a fixed bearing positioned on the left and a floating bearing on the right side.

3.5.2 Mounting of L-legs on the ladder

The integration of L-legs onto the ladder structure is a critical step in the preparation of the sensor module. Once the ladder has been glued to the bearings, the subsequent phase involves attaching L-legs onto the ladder to allow the mounting of sensors. The distribution of these L-legs along the length of the sensor is determined based on its dimensions, aiming to minimize warping of the sensor surface.

Each sensor type is mounted on four legs, except for the 124 mm length sensor, which is supported by eight legs as shown in Fig. 3.12. The positioning of the first L-leg from the sensor edge for the 22 mm sensor is 8 mm, while for all other sensors, this distance is 15 mm from the sensor edge. The dimensions of the L-legs from the sensor edge on one side of the sensor have been summarised in the table 3.1.

Specialized aluminum blocks, referred to as positioning blocks, are used to position the L-legs accurately on the ladder. These blocks serve a dual purpose by providing support for L-leg

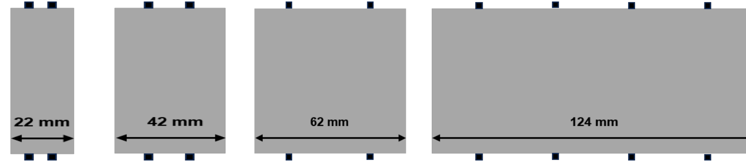

Figure 3.12: Sensor variants showing the positioning of L-legs from the sensor edge.

S.No.	Sensor size (mm)	Distance of first L-leg (mm)	Distance of second L-leg (mm)	Distance of third L-leg (mm)	Distance of forth L-leg (mm)
1	22	8	12	-	-
2	42	15	25	-	-
3	62	15	45	-	-
4	124	15	46	76	107

Table 3.1: Table summarising the distance of the L-legs from the edge of each sensor, only showing the one side of the ladder with L-legs, since the position on the other side of the ladder will be mirrored.

holding fixtures, which are mounted on a sliding rail, and maintaining a desired gap between sensors in the z-direction (see Fig. 1.14, left). The sensor pitch, defined as 1.5[3], allows the smooth passage of micro-cables through the gaps, minimizing any potential strain on the sensor surface caused by the cables.

The L-leg holding fixtures are designed to fix the L-legs on the fixture, which is fixed to the positioning block, ensuring the proper separation between the two legs. Once the L-legs are positioned on the fixture, they can be easily moved along a rail system. A specialized 3D-printed fixture is used to guide the accurate placement of glue for the l-legs (see Fig. 3.13 (left)). Araldite 2011 glue is applied following the fixture's markings, adhering the L-legs to the ladder at specified locations. After gluing, the L-leg holding fixtures are moved along the rail system to their designated positions and left undisturbed for 24 hours. This process allows for all the L-legs to be attached to the ladder simultaneously using multiple fixtures depending on sensor geometry, as shown in Fig. 3.13 (right).

After the completion of the gluing process for all L-legs, an additional step involves the optical inspection of the leg positions. This step is important to verify that none of the L-legs is situated at an elevated position that could impede the proper placement of sensors. In the case that any L-leg is identified as being positioned higher than expected, it is replaced with a new L-leg before proceeding with the mounting of modules.

[3]Sensor pitch is defined as the gap between two sensors i.e., 1.2 mm and sensor thickness of 0.3 mm.

Figure 3.13: (Left) L-leg fixture mounted on the rails, fixed to the positioning blocks, and (Right) L-legs glued onto the ladder after the curing of glue.

3.5.3 Positioning of sensors on the ladders

The subsequent step involves positioning the sensors on the ladder structure after the L-legs have been glued. Sensors are positioned on the ladder in a staggered arrangement, with the spacing in the Z-direction defined by the positioning blocks. To prevent any gaps that could interfere with the particle trajectories, an overlap of 4.6 mm is maintained between adjacent sensors in the X-Y projection. This overlap is defined during the assembly of the module on the ladder using a tool designed for the positioning.

The fixation of the module on the tool, shown in Fig. 3.14 (left), involves manual placement of the sensor at the right position, ensuring contact with the tool's corner before applying vacuum fixation. Also, the tools are cleaned before sensor placement to maintain a dirt-free assembly environment. Once fixed, the sensor positioning is verified under a microscope to eliminate any gaps between the tool edge and the sensor. Following sensor fixation, micro-cable un-entanglement is conducted to ensure cables lie flat, followed by fixation of the FEBs on the tool. The flat cables minimize interference between the individual cables, ensuring that signals from sensors remain clear and distinct. Also, the shielding layer covering the flat cables acts as a shield against external electromagnetic interference, preserving signal clarity.

In the early ladder assembly stages, FEBs were initially fixed with thermal pads, later replaced by thermally conducting glue (as also explained in Chapter 2). The gluing approach simplified cable entanglement issues during assembly since both the FEBs of a module are already glued to the cooling shelf. Upon correct positioning of all module components, glue is applied to the L-leg's top surface, before transporting the module to the ladder (see Fig. 3.14 (right)). CAF4 glue, chosen for its soft silicon composition, addresses thermal expansion concerns during STS operation.

The sensor holding tool is then flipped 180°, ensuring proper fitting into positioning blocks. Direct module placement onto the ladder is avoided to prevent any damage to the sensors.

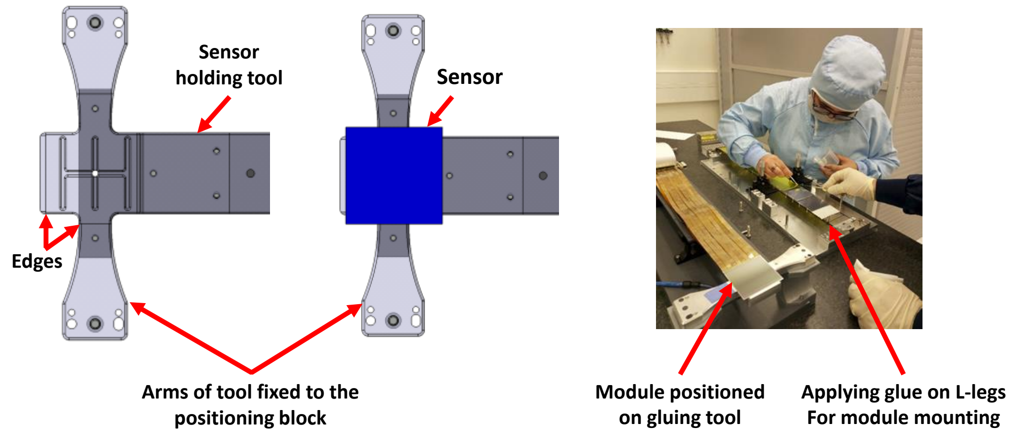

Figure 3.14: (Left) CAD drawing of the module holding tool where positioning of sensors (followed by micro-cables and FEBs) is defined by the edges of the tool. (Right) Image illustrating the two key steps: applying glue to the top L-leg surface and transferring the module from the holding tool to the ladder for final gluing.

Therefore, the arms of the sensor holder are carefully positioned onto the vertical stage and fixed into the positioning blocks, as shown in Fig. 3.15.

Sensors remain under vacuum suction for 24 hours to allow the glue to cure. This assembly approach is replicated for all the modules, allowing simultaneous assembly following the staggered geometry, starting from the middle of the ladder. While the assembly of one module on the ladder takes approximately 24 hours, the overall ladder assembly process, for an average ladder, takes around 7-8 days.

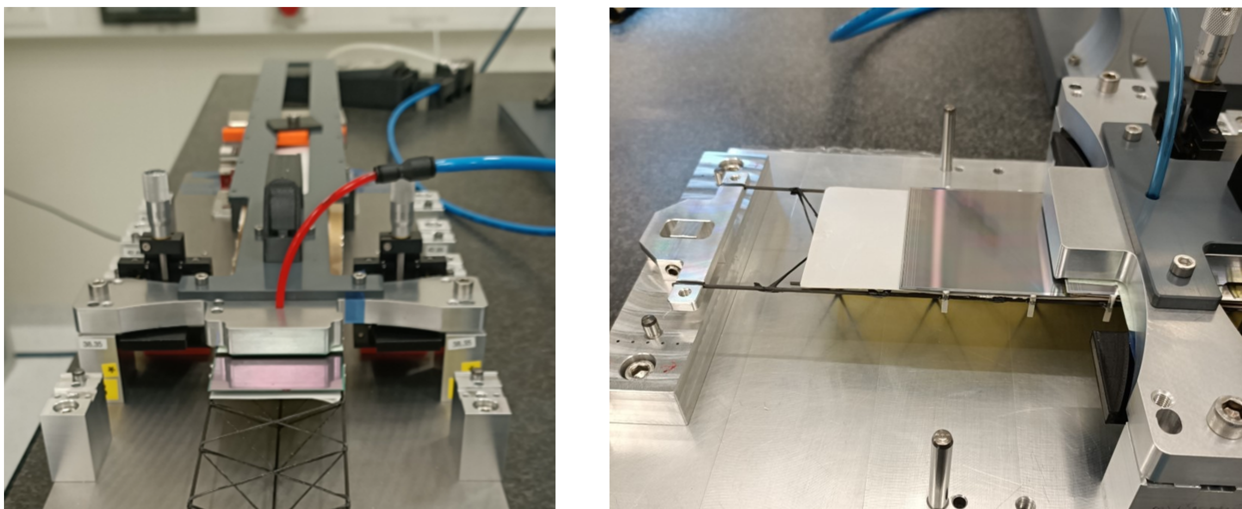

Figure 3.15: Module fixed under vacuum and mounted on the positioning blocks of the ladder holding baseplate: (Left) Front view and (Right) Side view.

3.5.4 Optical survey of silicon sensor positions

The assembly of silicon sensors on ladders is a critical step in constructing the detector system. This process involves a defined procedure and specialized tools, ensuring the precise positioning of sensors on ladders. Quality control and metrology play an important role in assessing and improving the assembly procedure. The objective is to maintain sensor positions within a deviation of no more than 100 μm from their nominal positions. Therefore, after the assembly of ladders, an optical survey is performed to determine the positions of silicon sensors in three dimensions. This step is essential for identifying any misalignment in sensor position and providing input for track-based alignment software, such as Millepede [55].

The measurement of sensors post-assembly necessitates the ladder's placement on a flat surface. A large granite table (see Fig. 3.16), measuring 1100 x 800 x 170 mm^3, equipped with a movable camera and X-Y motor bridges is used for contactless optical 3-D metrology. The overall precision, accounting for factors like correction of granite table flatness and long-term reproducibility, is better than 10 μm.

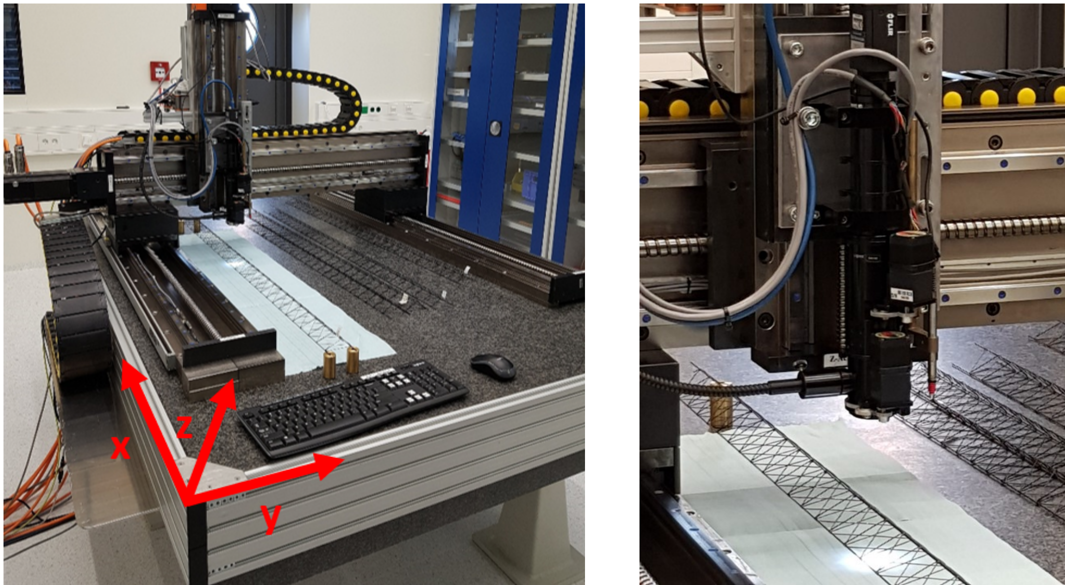

Figure 3.16: Image of the setup showing granite table with X, Y, and Z motor stages, used to measure the position of the sensors mounted on the ladder as well as the bending of the bare ladders under load.

During the optical inspection, alignment marks on silicon sensors, with predetermined XY coordinates, are identified using motor positions and pattern recognition techniques [56]. Each sensor has eight alignment marks, with only five being visible during inspection due to overlap between adjacent sensors (Fig. 3.17 - top).

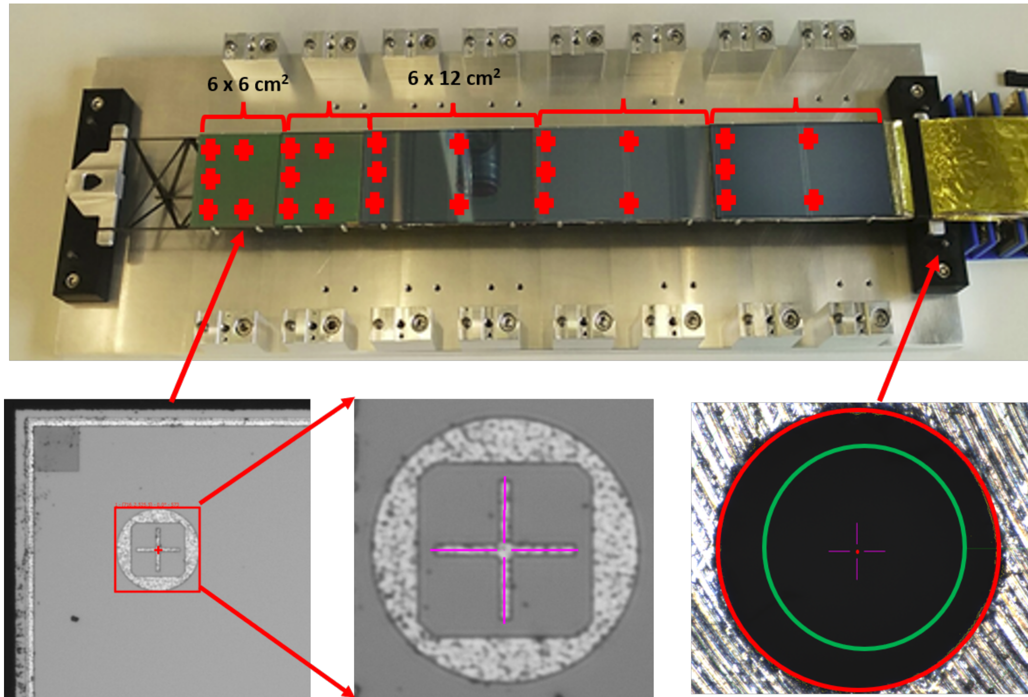

Figure 3.17: (top) Image of first half ladder assembled with non-functional modules. (Bottom left) Coarse image of the alignment mark on the sensor, (bottom middle) fine image of the alignment mark after auto-focusing, (bottom right) fine search of the blind spots as reference mark on the ladder bearing blocks mounted on the base-plate.

So, once the sensors are mounted on the ladder, to cross-check how good is the placement, the position of these alignment marks is inspected. However, a reference coordinate system must first be established for the baseplate holding the ladder, ensuring measurements in a fixed frame of reference. Notably, the alignment marks on the sensor are highly precise, and creating a mechanically consistent and automatically recognizable mark on the baseplate with the necessary micron-level precision is challenging. The opted solution is to have circular embossing of 1 mm diameter as the reference marks on the ladder bearing blocks mounted on the baseplate. Each ladder bearing block has 6 circular embossing, 3 on either side of the bearings, allowing to accurately locate the circle's center (see Fig. 3.17, bottom right). A circle is fit to many edge points which yields the center with sufficient precision. Having reference marks with sufficient precision, space points on the sensor's surface can be measured.

The 3-D position of sensors in the XY-plane is determined from the alignment marks through pattern recognition, together with appropriate calibration of motor positions. The positioning in Z -direction is obtained by analyzing image sharpness at different focus positions after calibration, using a Fast Fourier Transform (FFT). This approach ensures sharp focus on the

underlying surface and readjusts for the most focused image, enabling extraction of the object's height [57].

In this way, the sensor positioning in all three dimensions is calculated. The optical metrology has been performed for various standard ladders and also for one central ladder. The results after the optical survey of sensor positions after assembling on the ladders are presented in the next section. The optical assembly procedure will be performed for all 108 ladders to be assembled for the STS to have input for the track-based alignment software.

3.6 Evolution of ladder assembly procedure

3.6.1 Assembly of (prototype) half ladder

To test the ladder assembly process, a standard half ladder with five non-functional modules was assembled. The ladder assembled was half of a full-size ladder[4]. The purpose of assembling a half ladder was to gain experimental understanding and minimize the complexity of building a full ladder as this was the first ladder to be built. The half ladder consisted of two modules of dimensions 6 × 6 cm^2 followed by three modules of 6 × 12 cm^2.

During this assembly, there was a lot of learning involved, contributing to an improved understanding of the assembly procedures. Some adjustments were made based on these learnings, shaping the existing assembly process. Initially, while assembling this ladder, the gap between two sensors in the Z direction was kept at 1 mm and the design of the bearings was also different from the current configuration.

Following the assembly, the sensors underwent optical inspection [62] and the resulting surface view is shown in Fig. 3.18 (left). The image shows the scan of the sensor surface, highlighting the staggered geometry. The black dots on the sensors indicate the alignment marks, with different colors corresponding to the different sensors. It should be noted that the staggering of the sensor position in Z by 1 mm has been removed by software for better representation of the measured data (see Fig. 3.18 (right)).

From the inspection results, two key observations were made. Firstly, there was a slight warp in the sensor surfaces. Secondly, deviations in sensor positioning from the nominal position were evident. The sensor surfaces exhibited inclinations in the range of 100 - 200 μm in the

[4] It is to be noted that, during the integration of STS, the construction of half ladders will not be undertaken.

Z-direction. Among the five inspected sensors, three sensors were accurately positioned within a 100 μm range in the XY dimensions. The inspection results indicated that the current ladder assembly procedure is feasible. However, there exists a potential for further optimization to enhance precision.

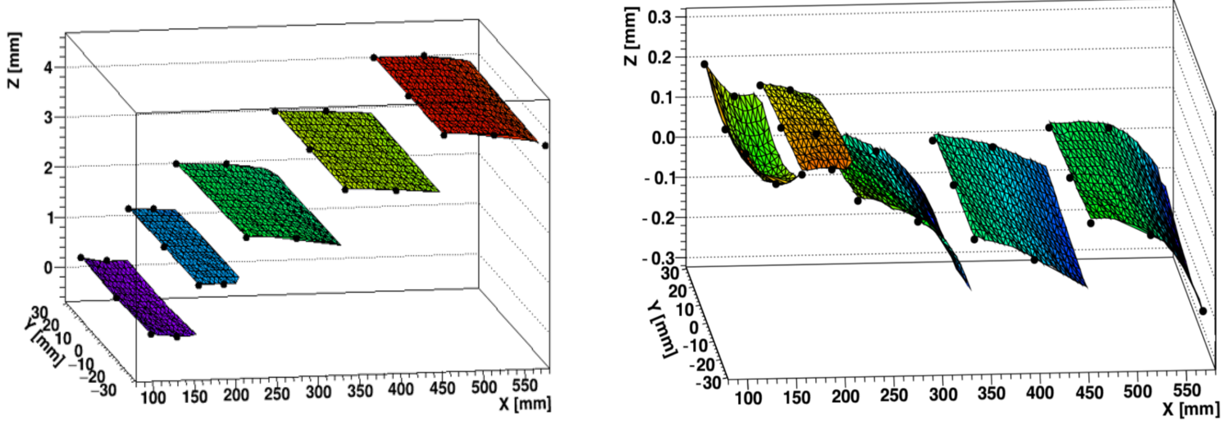

Figure 3.18: Optical inspection of sensor surface after assembly on half ladder, (left) showing the staggered geometry, (right) showing sensor scan after removing the sensor gap of 1 mm.

3.6.2 Functional standard ladder for mini-STS(mSTS)

The prototype ladder helped to gain experience with the ladder assembly procedure. However, since non-functional modules were used for the assembly of half ladder, it was not possible to test the functionality of the modules. Therefore, to refine the assembly procedures and test the functionality of the modules once assembled on the ladder, it was important to assemble a ladder with functional modules. Therefore, eleven modules—the first to be fully assembled, were prepared for laboratory testing. Later, these same modules were integrated into the ladder and used in the mSTS detector.

mSTS is part of the mini CBM (mCBM) project, a precursor of the CBM experiment at the existing accelerator facilities in GSI. The design requirements of mSTS placed specific constraints on module dimensions, resulting in objects featuring the largest sensors (6.2 cm and 12.4 cm), arranged on two tracking stations. The eleven modules (approximately 1% of STS modules) prepared were mounted on four ladders as part of the two tracking stations (see Fig. 3.19).

To assess the functionality of the modules, equivalent noise charge (ENC) measurements for all the channels were conducted both before and after assembly on the ladder. Symmetrical biasing

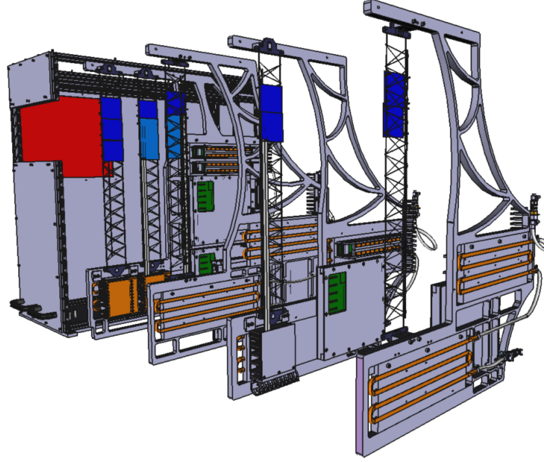

Figure 3.19: CAD drawing of the modules mounted on two stations of mSTS.

at ±75 V ensured full depletion of the sensor. The ENC calculations considered contributions from the sensor, micro-cables, and a factor of 25 e/pF, accounting for the measured ASIC noise dependence on the input capacitance (see eq. 3.3).

$$\text{ENC(e)} = [\underbrace{\text{L}_{\text{sensor}} \cdot 1.02\frac{\text{pF}}{\text{cm}}}_{\text{Sensor}} + \underbrace{\text{L}_{\text{cable}} \cdot 0.38\frac{\text{pF}}{\text{cm}}}_{\text{microcable}}] \cdot 25\frac{\text{e}}{\text{pF}} + \underbrace{350\text{e}}_{\text{ASIC}} \tag{3.3}$$

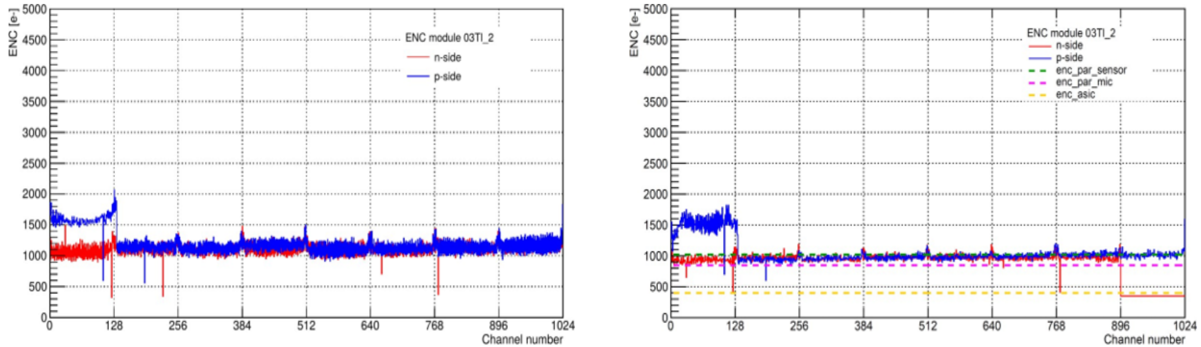

Figure 3.20: ENC plot for different channels of a module is plotted, (a) after the module was assembled, (b) after the module was mounted on the ladder.

The Fig. 3.20 (a) shows the ENC plot for a module (out of 11 modules) tested after being assembled and the Fig. 3.20 (b) shows the ENC plot for the measurement of the same module after being assembled on the ladder. The measured noise of around 1000e ENC aligns within a 6 % range, consistent with an estimation based on the total detector capacitance. In Fig. 3.20 (b), it can be observed that the different colors with the dotted lines represent the contribution

from the sensor, micro-cables, and ASIC. The red color represents the noise contribution from the n-side of the module and the blue color represents the p-side noise contribution.

From the comparison of both plots, it can be concluded that the noise in both cases is comparable. The fluctuations in noise are reduced when the module is assembled on the ladder. This observation indicates that proper stretching of the micro-cables on the ladder helps to reduce variations in the ENC, enhancing overall signal consistency.

Similarly, all eleven modules underwent testing before and after assembly on the ladder, and consistently similar results were observed. The assembly of modules for the mSTS ensured that the existing ladder assembly procedure did not adversely impact the performance of the modules. This outcome reinforces the reliability of the assembly process and ensures the functional integrity of the modules for their intended use in the detector.

3.6.3 Standard full ladder

The assembled ladders so far involved only a limited number of modules. While demonstrating optimal module performance, it became evident that the existing procedure, while demonstrating optimal module performance, required refinement to enhance mounting precision. Assembling a 4-ladder setup for mSTS provided experience with real sensors and micro-cables, particularly concerning the impact of micro-cable entanglement on noise levels. Additionally, issues were identified with the previous method of fixing FEBs to cooling shelves using the thermal pads, which resulted in the detachment of FEBs from two modules, following the vertical mounting of ladders on the C-frame.

To address these challenges and optimize the ladder integration procedure, lessons learned from the assembly of half ladders and mSTS ladders were considered. Subsequently, several changes were implemented, detailed as follows:

- **Change of bearings**: An essential parameter that underwent modification is the bearings. As shown in Fig. 3.21, the old bearings consisted of two parts, providing a higher degree of freedom leading to more flexible bearings. This led to a change in the design of the bearings. The idea behind the new bearings was to design them in such a way that they are fixed directly to the ladder base plate to provide more stability to the bearings and to compensate for the effect of mechanical stresses which can lead to a gradual shift in the ladder's position.

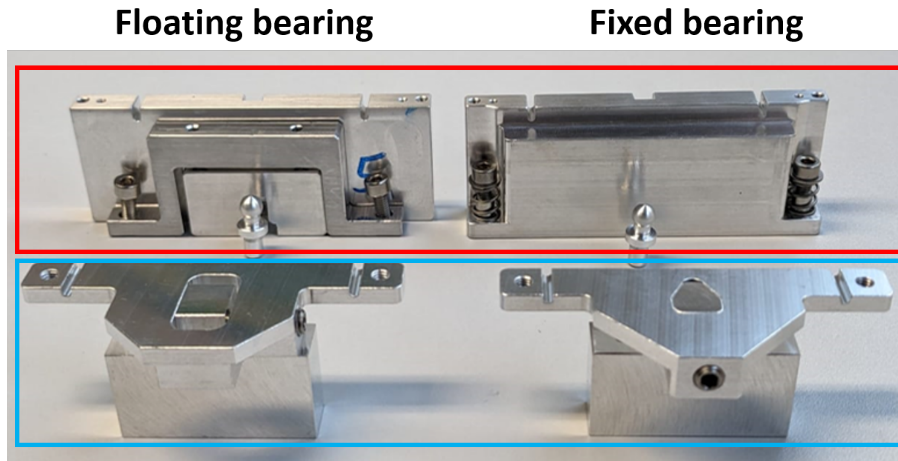

Figure 3.21: Image shows the fixed and floating bearing blocks used for mounting a ladder. The bearing blocks in the red box (top) represent the new design, featuring improvements in precision and stability. The bearing blocks in the blue box (bottom) show the older design, highlighting the structural differences between the two versions.

- **Optimization of sensor gap in Z direction**: During the assembly of mSTS ladders, it was realized that the initial gap of 1 mm between sensors in Z direction might not be sufficient. There was a concern that the micro-cable and the shielding layer might not have enough space to fit between the two sensors. Therefore, to address this, as per the STS geometry described in V21e [60], different overlapping parameters (see Fig. 3.22) were taken into consideration that has been summarised in the Table 3.2.

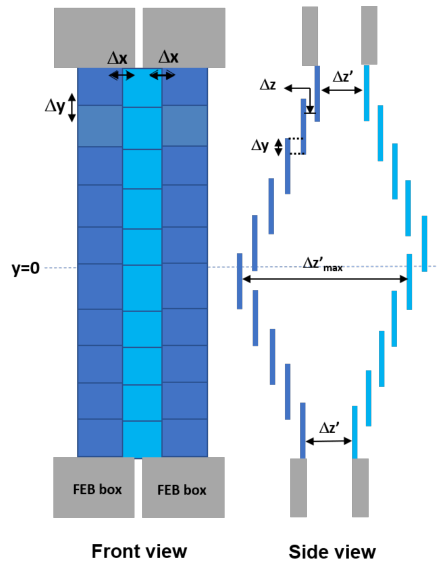

Figure 3.22: Image showing front and side view of two ladders showing the overlapping parameters between the two sensors on the same ladder as well as the sensors on different ladders.

S.No.	Parameters	Distance (mm)
1.	Horizontal width of the sensor	62
2.	Sensor thickness	0.32
3.	Sensor overlap on ladder, (Δy)	4.6
4.	Ladder overlap (maximum possible), (Δx)	2.5
5.	Sensor gap (pitch) on ladder, (Δz)	1.2
6.	Sensor distance at top (or bottom) of unit, ($\Delta z'$)	5.0
7.	Maximum sensor distance in unit, ($\Delta Z'_{max}$)	17.0

Table 3.2: Table summarises the parameters in x, y, z direction in two ladders as specified in the v22d geometry of STS.

Taking into consideration the distance defined in the geometry, it was possible to increase the gap between the two sensors in the z-direction to 1.2 mm (instead of 1 mm), without making any changes in the detector's geometry. This adjustment ensures that the sensors will be precisely positioned without having any physical collision. Insufficient spacing between the sensors can also cause electrical shorts and degrade the performance of the sensors. Also, defined spacing minimizes the risk of micro-cable entanglement and ensures uninterrupted data flow from the sensors.

- **Optical inspection of L-legs**: Based on the experience gained during ladder assembly, improvements have been made in placing sensors along the XY direction. However, the positioning in the Z direction still needed refinement, even after adjustments to the tool. Upon closer investigation of the assembly procedure, it was foreseen that the mismatch in the height of the L-legs significantly influences the placement of sensors along the z-axis.

  To address the challenges associated with positioning sensors along the z-axis, an additional step in the ladder assembly procedure has been introduced. Before mounting the module on the ladder, an optical inspection of the L-legs is performed. This inspection ensures that the L-legs are within specified tolerances and meet the required height criteria. If the L-legs fail to meet the desired specifications, adjustments or replacements are made to ensure that the sensors can be positioned at the right height. This additional

step, while adding complexity to the assembly process, is essential for guaranteeing the accuracy and precision of the modules on the ladder.

By making above mentioned amendments and optimizing the ladder assembly procedure accordingly, the efforts were made to improve the precision of sensor mounting. As an outcome, to assess the improved assembly procedure, a prototype ladder was assembled using 10 non-functional modules. These modules had sensors connected to non-functional micro-cables, and FEBs were not used to avoid complexity.

To achieve the sensor mounting precision within $\pm$ 100 μm, a re-defined assembly technique was tested on a full-size ladder with 10 non-functional modules. This ladder was not the longest (620 mm long) but could accommodate the maximum number of modules. The assembly involved gluing the ladder edges and arms, followed by L-legs, as shown in Fig. 3.23 (top). As an additional step, the optical inspection of L-leg positions was then performed, and the deviation from the nominal Z position along the length of the ladder is shown in Fig. 3.23 (bottom).

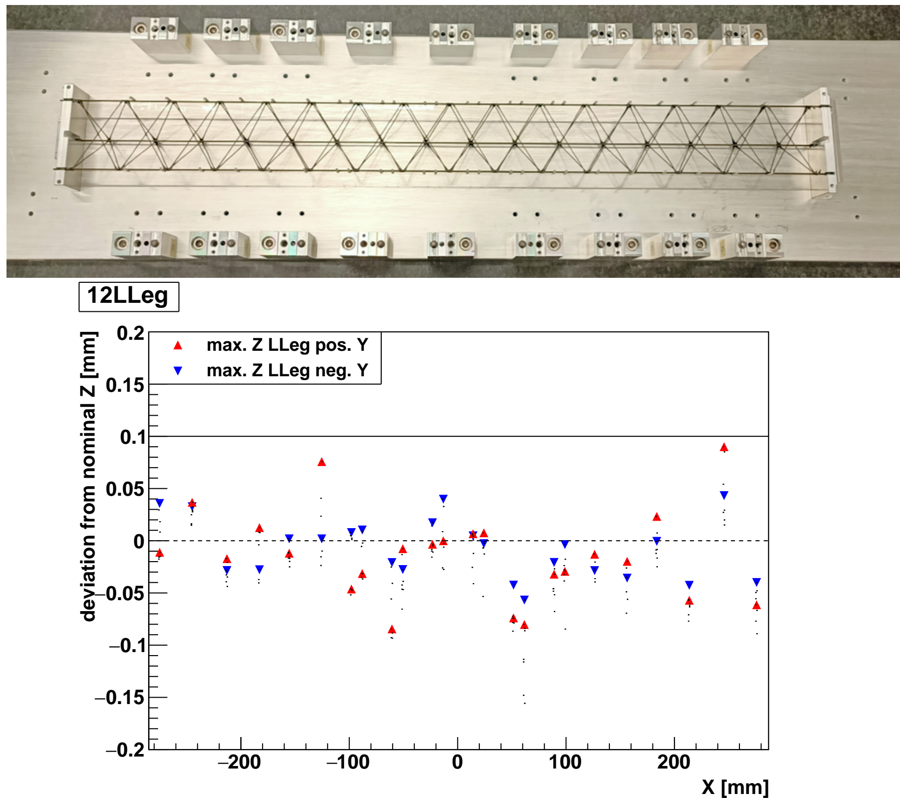

Figure 3.23: (Top) Image of the ladder assembled with the L-legs glued, (Bottom) Optical inspection of L-legs after gluing on the ladder where the dotted horizontal line defines the nominal position.

To achieve the targeted module mounting precision, it is essential to cross-check that every L-leg remains below this threshold, allowing space for the glue. If any L-leg exceeds this threshold,

it must be replaced with a new one. Four L-legs were initially replaced for this ladder until all met the required precision.

Optical inspection of L-legs is followed by the mounting of modules on the ladder. While the assembly procedure remained the same, the tools were reworked and tolerances were improved. Since this ladder was the first ladder to be assembled with 10 modules, an exploration of potential failure scenarios during assembly was undertaken. Therefore, an optical inspection of each module post-assembly was conducted. The image of the ladder after assembly is shown in Fig. 3.24 (top) and Fig. 3.24 (bottom) showing the optical inspection of the sensor surface along measurements of markers.

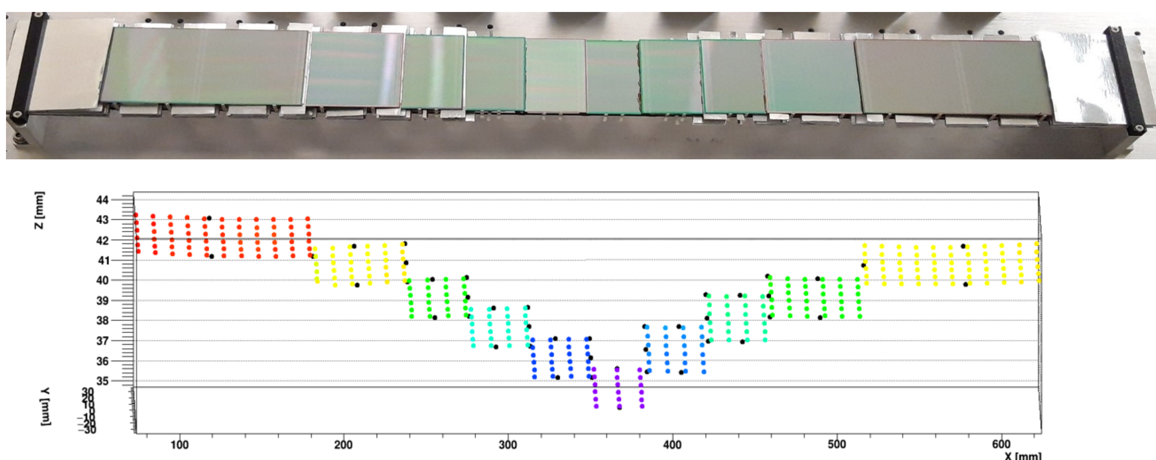

Figure 3.24: (Top) STS ladder assembled with 10 non-functional modules i.e., modules with sensors and micro-cables with the shielding without any FEBs, (Bottom) Optically inspected surface of sensors.

The Z-direction deviation for all sensors from their nominal positions indicated that all sensors were positioned within the $\pm$ 100 μm range, meeting the required precision for optimal particle tracking (see Fig. 3.25). Additionally, it was observed that, with increasing sensor sizes from the middle towards the end of the ladder, the sensor surfaces are not flat, displaying noticeable warp, even with correctly positioned L-legs. Investigation revealed that the tools holding the modules exhibited tolerances and lacked complete flatness, contributing to misalignment in sensor height, as shown in Fig. 3.25 (Right). This tool-related non-uniformity explains the observed non-planarity in the sensor surfaces.

Another identical ladder was prepared for additional assembly experience and vibration studies (Chapter 4). These two ladders have helped understand possible issues during assembly providing valuable insights for refining the assembly process. However, the existing assembly procedure is sufficient for preparing ladders for the final STS with minor tool adjustments.

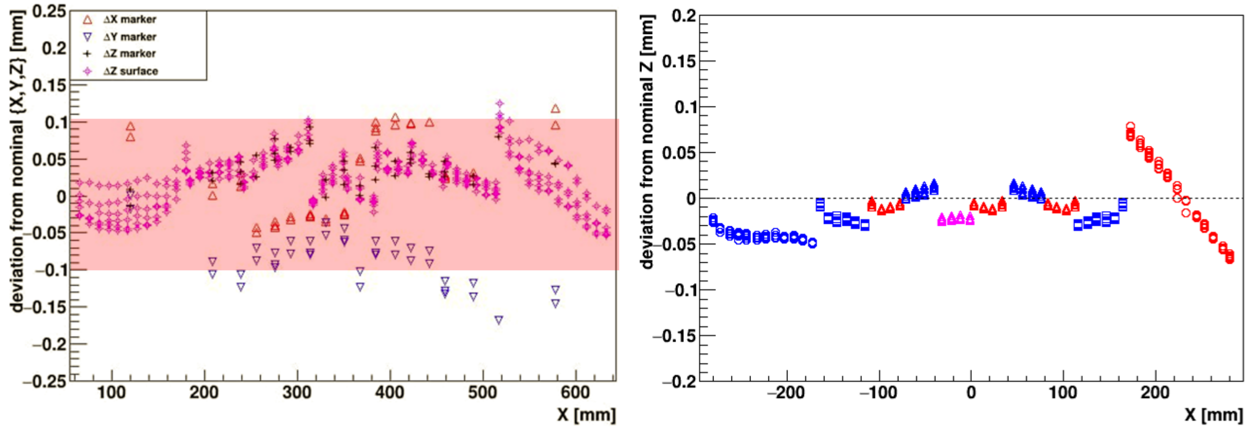

Figure 3.25: Deviation in Z from the nominal position, (Left) in the sensors mounted on the ladder, (Right) in the tools used to mount the modules on the ladder.

In preparation for the final STS, an optical inspection protocol will be implemented post-assembly for all the ladders. To ensure accessibility for detector alignment, the survey data for all assembled ladders will be systematically stored in a database. Optical inspection is planned to be performed for all the ladders, before their mounting on the C-frame, to get an estimate of how much can the effect be on the particle tracking.

3.6.4 Central ladder

Another type of ladder undergoing assembly is the central ladder which poses even greater challenges due to its structural characteristics. These ladders exhibit reduced stiffness and are more prone to sagging, particularly in the Z direction, compared to standard ladders. The primary factor contributing to sagging in central ladders is the cut-out in the middle for the beam pipe, making them less stiff, especially under the weight of the modules, as explained in section (sec 1.3).

To compensate for the sagging during the assembly in the Z-direction, gauge blocks are mounted underneath the ladder close to the cut-out section. Additionally, to counteract the tilting in the y-direction, a precautionary measure is implemented before gluing the bare ladder to the bearings. External support is provided to the cut-out section, ensuring correct centering of the ladder cut-out, as shown in Fig. 3.26. These measures are essential not only to counteract sagging during assembly but also to ensure the structural integrity of central ladders, recognizing their vulnerability to deformation under the load.

The central ladder used in this study is from one of the three prototype central ladders delivered

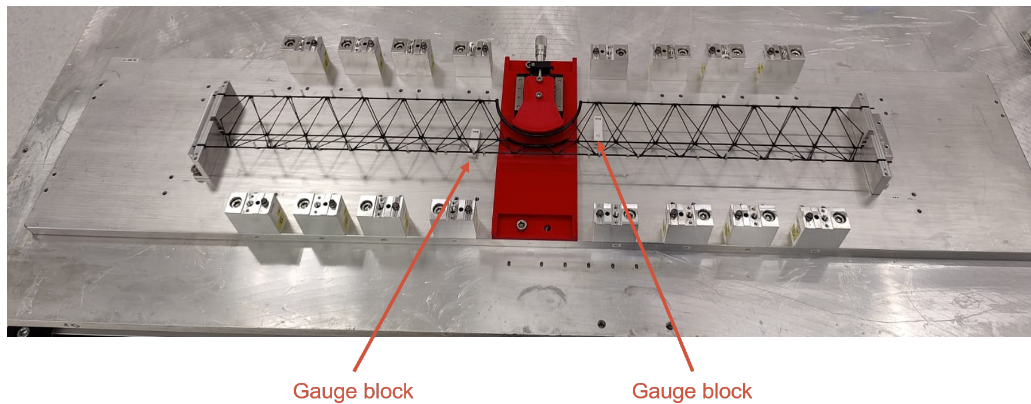

Figure 3.26: Assembly of a prototype of the central ladder using a specifically designed tool to support the cut out in the central ladder and gauge blocks to avoid sagging in the ladder during the assembly.

(as mentioned earlier in this chapter). While it is recognized that the ladder requires increased stiffness and studies are ongoing to achieve this improvement with minimal additional material. Despite these ongoing studies, the assembly of the central ladder proceeded to assess the worst-case scenario if it were to represent the final ladder version. The assembly of the central ladder followed a systematic procedure mirroring that of a standard ladder, including the additional gauge blocks and support for the ladder cut-out.

To enable a thorough comparison, the ladder was resized to match the length of the standard ladder (Ladder type 12, with a length of 620 mm). However, it was mounted with 8 modules instead of the standard 10 due to the cut-out in the middle. The purpose was to enable a comparative analysis of their assembly procedures. Subsequently, both ladders were later tested to measure the vibrations under the impact of airflow.

Before mounting the sensors, an optical inspection of the ladder was conducted after the gluing of L-legs, see Fig. 3.27. Notably, all the L-legs on either side of the ladder were observed to be below the required height, ensuring ample space for the adhesive.

Throughout the assembly of the central ladder, silicon wafers were used as substitutes for the actual STS silicon sensors, with a thickness approximately 30 % greater than the specified 320 μm due to the unavailability of the intended sensors. The modules on both sides were mounted in parallel and the assembled ladder is shown in Fig. 3.28 following the mounting of all modules on the ladder, an optical inspection was conducted as shown in Fig. 3.29.

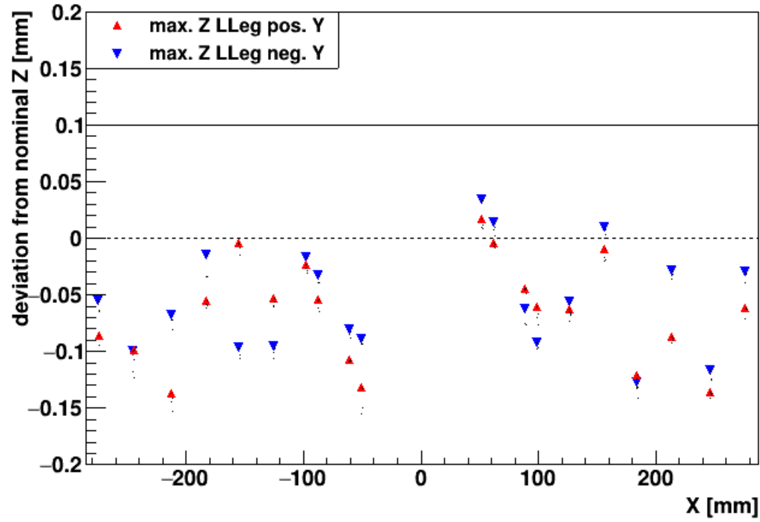

Figure 3.27: Optical inspection of the L-legs glued to the central ladder showing the deviation in Z from the nominal position.

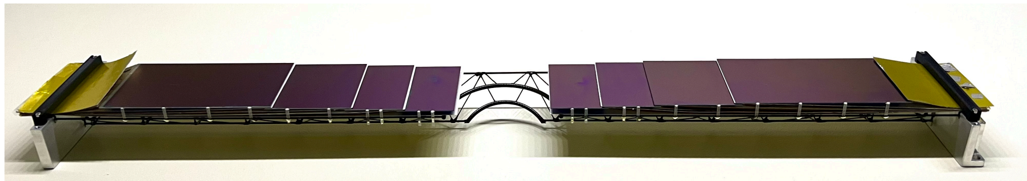

Figure 3.28: Image of the central ladder after the assembly of eight non-functional modules.

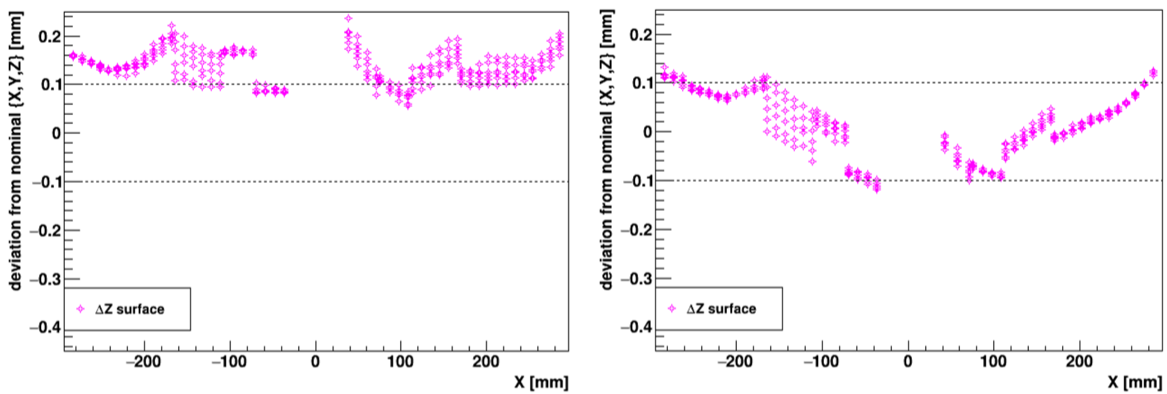

Figure 3.29: Image of optical inspection of central ladder after assembly, (left) with gauge blocks, (b) without gauge blocks underneath the ladder.

During the inspection of the central ladder, the sensor's additional thickness wasn't considered for the comparison. In the image shown in Fig. 3.29 (left), it is apparent that the sensors are mounted within a precision of approximately $\pm$ 100 μm. However, in this instance, the ladder still had gauge blocks underneath it. In the realistic scenario, after assembling the ladder, the

next step involves transporting it onto the C-frame, where it can no longer be supported by gauge blocks.

Therefore, the ladder was re-evaluated by removing the gauge blocks, as can be seen in Fig. 3.29 (right). The noticeable bend in the middle of the ladder shows the weakness of the ladder indicating the necessity for increased stiffness in the ladder design to prevent sagging. This also showcases the importance of having bearings where sagging is reduced by nearly 10 orders of magnitude when compared to the central ladder in Fig. 3.7, where the ladders were only supported on blocks.

Therefore, ensuring the structural integrity of the ladder is paramount because even slight deviations in its alignment can disrupt the precision required for particle tracking. Therefore, the assembly of the ladder gives an insight into the importance of the further optimization of the improved stiffness of the central ladder with a minimum material budget to be implemented.

Chapter 4

Vibration measurement

4.1 Introduction to the cooling concept

Throughout the operational lifetime of the detector, the silicon sensors in the STS are expected to endure a high-radiation environment, with a fluence reaching up to 10^{14} n_{eq}/cm^2, and an ionizing dose of approximately 11.4 KGy [32], particularly for the sensors located close to the beam pipe (see Fig. 4.1). This has been confirmed as a lower limit for the sensor operation throughout the different irradiation campaigns [92][93].

The high amount of radiation accumulated during the operation of the detector causes a significant amount of defects in the silicon lattice. These defects, characterized by deep energy levels within the forbidden gap, are the regions where the electrons can exist in an unoccupied space between the conduction band and the valence band and can act as recombination and generation centers. This leads to an increase in the detector's leakage current. Even after irradiation, the effects of these defects may persist, affecting the detector's performance, resulting in annealing, rise of sensor leakage current, and degradation of charge collection efficiency (CCE).

Cooling plays a vital role in the performance of STS and key factors affected by cooling are as follows:

1. **Leakage Current Reduction:** The rise in leakage current is directly associated with the radiation-induced defects in the silicon lattice. However, by implementing low-temperature operation, cooling effectively suppresses the movement of additional charges caused by these defects in the silicon lattice. This suppression mechanism restricts the leakage cur-

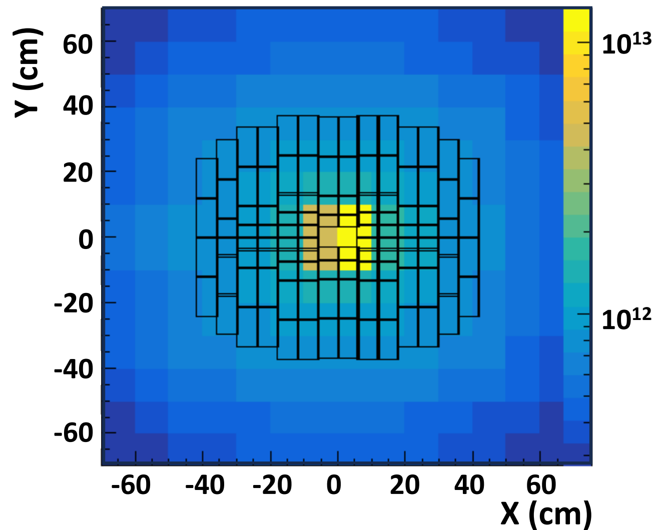

Figure 4.1: FLUKA Simulations of Non-Ionizing Energy Loss (NIEL) distribution for STS Station-8 positioned 100 cm downstream from the target, with overlaid layout of Silicon sensors highlighting most irradiated Sensors. Calculations are based on CBM's Hadron setup (11 AGeV Au+Au at 10 MHz) after 1 month of irradiation [94].

rent, leading to an improved sensor performance and reduced noise levels (see Eq. 4.1) [95].

$$\mathrm{I_{Leakage}} \propto \mathrm{T}^2_{\mathrm{Sensor}} \cdot \mathrm{e}^{-\frac{\mathrm{E_{gap}}}{2 \cdot \mathrm{T_{Sensor}} \cdot \mathrm{k_B}}} \tag{4.1}$$

2. **Charge Collection Efficiency (CCE) Enhancement:** To create a controlled operational environment through cooling in STS is important to enhance the sensor's ability to effectively capture the charge generated by ionizing particles. This helps to improve the sensor's capability to accurately capture the charges generated by ionizing particles, resulting in high-precision measurements of charged particles. On the contrary, inadequate cooling in high radiation dosage environments can result in a degradation of CCE. This deterioration can adversely impact the tracking performance of the detector, emphasizing the critical role of cooling in maintaining optimal CCE.

3. **Signal-to-Noise Ratio (S/N) optimization:** For the EOL operation of STS, it is crucial to optimize the S/N $\geq$ 10 to ensure the desired track reconstruction efficiency and momentum resolution [96]. Since there is a strong dependency of the S/N ratio and leakage current of the sensors cooling becomes an essential factor in noise reduction and S/N enhancement. By cooling down the sensors, the noise is minimized, resulting in an improved S/N ratio.

4. **Power dissipation management:** To maintain stable operating conditions, it is crucial to get an understanding of power dissipation scenarios. The front-end electronics alone dissipate around 40 kW. To overcome this dissipated power, it is imperative to implement appropriate cooling systems. By effectively absorbing excess heat, cooling measures ensure that the sensors operate within their specified temperature range, thereby facilitating accurate measurements of charged particles and maintaining the stability and reliability of the STS.

5. **Annealing:** After the high-radiation operation, two types of annealing processes are possible: short-term beneficial and reverse annealing. Short-term beneficial annealing occurs during the initial days of operation at room temperature, resulting in a reduction of radiation-induced defects within the silicon lattice and improved sensor performance. Conversely, reverse annealing becomes relevant during long-term detector operation when the full depletion voltage experiences an increase after reaching its minimum level. This voltage rise occurs due to the reactivation of defects, subsequently leading to degraded sensor performance. To mitigate the adverse effects of reverse annealing on the irradiated sensors, it becomes imperative to keep the STS at low temperatures all the time. By cooling the detector and maintaining it within a thermally controlled enclosure, reverse annealing can be effectively prevented.

To mitigate all the parameters mentioned above and for good detector performance, the sensors need to be cooled. The cooling is essential to reduce the leakage current and hence the power dissipation in silicon sensors. These parameters are influenced by the accumulated fluence and operating temperature, with a potential risk of thermal runaway[1], if left uncontrolled.

To meet the stringent requirements for momentum resolution ($\Delta p/p < 2$ %), the material budget is limited to 0.3 % - 2 % X_0 per tracking station. The STS has been designed so that only the silicon sensors are positioned within the detector's acceptance range. To minimize the overall material budget, the read-out electronics are placed outside this region.

The entire detector, including the electronics, is kept within a thermally controlled enclosure, maintained at a constant temperature of +10 °C at all times, even during shutdown periods, to prevent reverse annealing. As a result, two types of cooling systems will be used during the operation of the STS:

[1] Thermal runaway is a condition where increased temperature causes a device to generate more heat, preventing the effective removal of excess heat.

- Electronics cooling: To overcome the power generated by the electronics and cool them down at low temperatures, 3M^{TM} NOVEC^{TM} 649 is planned to be used.

- Sensor cooling: Since the innermost sensors that are close to beam pipe will be expecting high radiation, therefore, the additional heat generated by inner sensors is foreseen to be removed using forced gas cooling.

4.1.1 Electronics cooling

To neutralize 40kW of heat dissipated by the front-end electronics over a volume of 3.5 m^3 area, efficient cooling is required. To overcome this heat, FEB boxes are attached to aluminum cooling plates, which use 3M^{TM} NOVEC^{TM} 649 coolant and can reach temperatures as low as -40 °C. The FEB boxes provide an efficient thermal interface, facilitating the transfer of the power dissipated from the FEBs to the cooling plates. To understand how effective is the cooling, thermal simulations were performed and it has been seen that FEB power dissipation can be effectively neutralized, with the maximum temperature on the electronics reaching approximately -12.5 °C [100]. More details about the electronics functioning at this temperature range have been explained in detail in Sec. 2.5.

4.1.2 Sensor cooling

As shown in Fig. 4.1, the innermost sensors, positioned close to the beam-pipe i.e. $\Delta x = \Delta y \leq$ 10 cm, are subjected to the highest radiation dose producing up to 40 mW/cm^2 at +10 °C at EOL. It becomes crucial to effectively dissipate the resulting excess heat to prevent thermal runaway. To achieve this, active air cooling will be employed for the sensors in the high radiation zone, while the peripheral sensors in all the stations can be cooled through natural convection.

To ensure minimal impact on the detector geometry and material budget, a cooling element with low material content that fits within the detector acceptance is opted for. The concept of "Impinging Jets" will be used, where cold dry nitrogen is blown directly onto the sensors surface, particularly targeting the innermost sensors, to effectively remove the heat produced by them [101]. Impinging Jets offers the advantage of easy jet creation and precise targeting to a specific location, in this case, the sensor surface of STS, for efficient heat transfer. There are several ways

to use the concept of impinging jets such as pipe-shaped nozzles[2] or cylindrical nozzles[3] [102].

The addition of the perforated tubes introduces extra material to the detector's acceptance. These tubes will be fabricated from the carbon fiber by the ICM composites company [105] and result in a 0.68 % increase in the material budget locally. These tubes will be placed in front of the ladder on adjacent C-frames to blow the air directly onto the exposed sensor surface. Each station will have in total 2 perforated tubes on either side of the beam pipe per station as can be seen in Fig. 4.2.

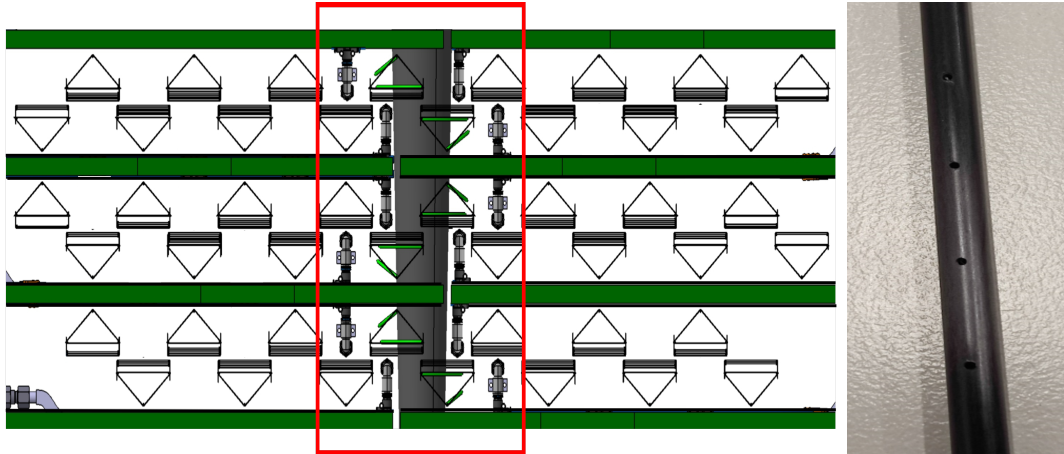

Figure 4.2: (a) Top view of the STS ladder assembled on the C-frame with perforated tubes mounted on adjacent C-frames, highlighted region shows the inner region where sensors need active cooling (b) CF perforated tube with the holes to blow the air.

The tube is designed with precisely positioned holes to allow the smooth injection of air. Simulations have been performed to optimize the size and distribution of these outlets for maximum efficiency. Each tube will have 16 equidistant holes, spaced 14 mm apart, ensuring uniform airflow. During the operation of STS, a controlled airflow will be directed from both the top and bottom of the perforated tube with an inner diameter of tube 3.5 mm and a thickness of 0.25 mm. A blockage is introduced at the mid-point of the tube to prevent asymmetric flow patterns and ensure balanced airflow.

To verify the uniformity of airflow from each hole and assess variations, the airflow velocity at each hole was experimentally tested using an anemometer[4] (testo 405i smart probe) positioned

[2] A pipe nozzle, typically an extension of a pipe, produces a stable and coherent jet flow, suitable for direct impingement applications.

[3] A cylindrical nozzle allows for customized flow characteristics, suitable for varied impinging jet requirements.

[4] An anemometer measures the air velocity, temperature, and volume flow in ventilation ducts and outlets, and transmits the data wirelessly to a mobile device for easy analysis and monitoring.

close to each hole. These measurements were carried out at two different flow rates: 30 L/min (15 L/min per 8 holes) and 40 L/min (20 L/min per 8 holes), as shown in Fig. 4.3. The plot indicates that at both flow rates, the airflow velocity from each hole is relatively consistent, with only minor variations. The inlet airflow measurements shown for both sets of measurements ensure that the flow from the top and bottom sections of the tube is well-balanced. This confirms the fine-tuning of the specifications of the holes in the perforated tube and can be used for the airflow measurements on the ladder. A detailed description of how the perforated tube will be used in STS is provided in Section 4.3.

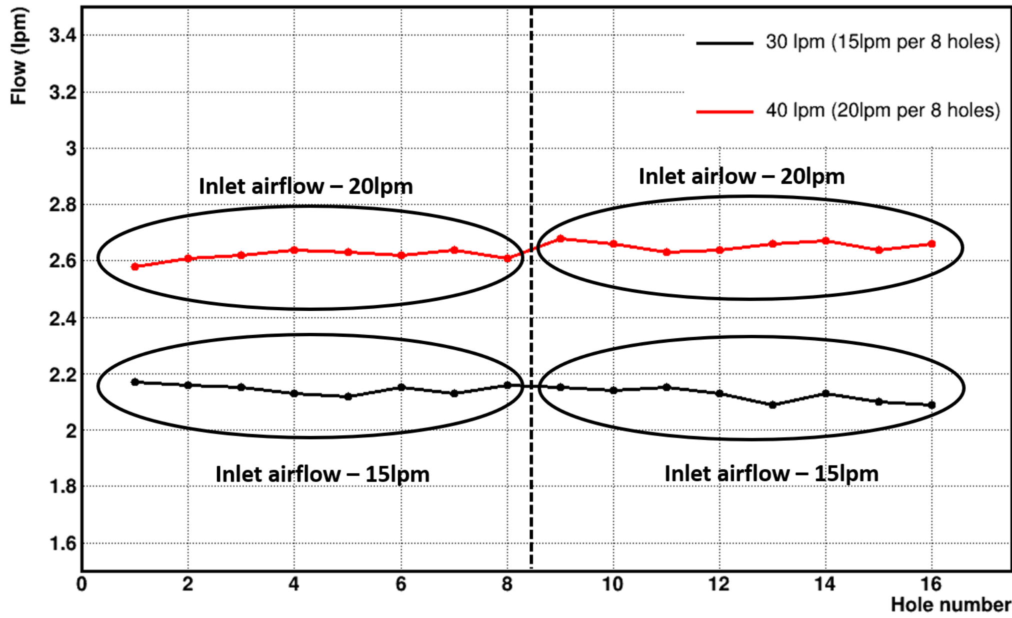

Figure 4.3: Measurement of airflow velocity across all the holes of perforated tubes at two different flow rates (measured in liter per minute), when air was blown from both ends of the tube. The black line represents the 30 L/min flow rate, while the red line represents the 40 L/min flow rate.

4.1.3 Consequence of air cooling on silicon sensors

Since active cooling using perforated tubes has been optimized for the innermost sensors, with 20 x 20 cm^2 area, it is important to determine the required airflow rate for sensor cooling. Therefore, the airflow distribution passing through the holes of the perforated tube was optimized to avoid thermal runaway. This has been tested experimentally using a thermal demonstrator and the results are illustrated in the plot shown in Fig. 4.4. The plot shows how the power density varies with the sensor temperature and the parabolic curve shows the heating power

variation with sensor temperature after 10 years and after EOL [110]. The different colors reflect the cooling power achievable with the given perforated tube geometry at various airflow rates ranging from 0 L/min to 40 L/min when the air inlet temperature is -10°C.

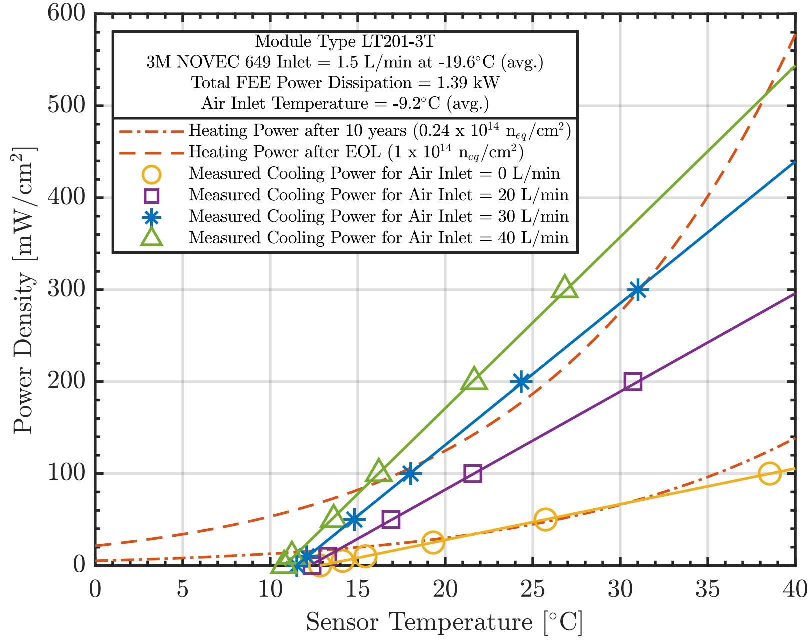

Figure 4.4: Thermal runaway plot showcasing the power density variation with sensor temperature for the two fluence scenarios, after 10 years and after EOL (Plot is taken from [100]).

The plot demonstrates that higher flow rates offer a larger margin from thermal runaway. By considering the optimal flow rate of 30 L/min passing through the perforated tube, sensors can still be operated at 10 °C having sufficient margin from thermal runaway. However, it should be noted that excessively high flow rates close to the sensors can result in unwanted vibrations, which may interfere with the tracking reconstruction software and consequently impact the detector's momentum resolution.

4.1.4 Impact of Vibrations on detector performance

To assess the impact of vibrations on the reconstruction software, simulations were performed on the inner region of central Au+Au collisions at 10 AGeV, an area expected to have a high event rate. To simulate the effects of vibrations, STS hit-producer [96] was used. By introducing controlled random shifts to hits associated with the sensors, the resulting shifts in module positions were calculated, providing an understanding of the impact of vibrations. However,

vibrations in the sensor modules can introduce ghost or fake hits[5], leading to misidentified tracks and potentially affecting the overall accuracy of the system.

Preliminary results indicate that larger vibrations (more than 10 μm) in the sensor modules significantly increase the occurrence of fake hits [97]. In the baseline scenario of central Au+Au collisions at 10 AGeV, there are typically about 22 ghost tracks per event with 397 Monte-Carlo points correctly reconstructed [98] [99]. The ghost probability is given by the equation:

$$\mathrm{P_{ghost}} = \frac{\mathrm{N_{ghost}}}{\mathrm{N_{total}}} \tag{4.2}$$

where, $\mathrm{N_{total}}$ is given by:

$$\mathrm{N_{total}} = \mathrm{N_{ghost}} + \mathrm{N_{reconstructed}} \tag{4.3}$$

Three scenarios were considered:

- **No vibrations:** This is considered a baseline scenario when there are no vibrations produced in the sensors. Without any vibrations, there are 22 ghost tracks per event, resulting in a ghost probability of 0.053 or 5.3 %. This scenario indicates that, even without vibrations, there is an inherent level of ghost hits present in the system.

- **Moderate vibrations:** In this scenario, moderate vibrations are introduced by causing displacement of about 1 μm in the XY direction (3.7 μm in Z) in the sensors. This results in 22.58 ghost tracks per event, resulting in a ghost probability of 0.054 or 5.4 %. This indicates that even the small vibrations cause a slight increase in the number of ghost hits, suggesting that the system is sensitive to minor disturbances.

- **Higher vibrations:** This scenario involves introducing higher vibrations by causing displacement of about 10 μm in the XY direction (37 μm in Z) in the sensors. These more significant vibrations lead to approximately 121.22 ghost tracks per even, resulting in a ghost probability of about 0.234 or 23.4 %. This signifies that higher levels of vibrations severely degrade the performance of the detector, leading to a high probability of ghost hits and misidentified tracks.

[5] A reconstructed track is considered a fake hit, if it does not correspond to any generated particle according to 70 % criterion.

These results highlight the importance of minimizing vibrations in the sensor modules to achieve accurate particle tracking. Even slight vibrations can introduce additional fake hits, while higher vibration levels can significantly degrade the system's performance. Based on these results, it is imperative to check for the magnitude of vibrations generated in the sensors after the airflow in the perforated tube. The experiment results will be further summarized in the upcoming sections.

4.2 Eigenfrequency measurement for STS ladder

To ensure the mechanical stability of silicon sensors after they are mounted on the ladders, a thorough investigation of the structural behavior is essential. The sensors must remain stable and maintain their precise positions throughout the detector's lifetime, which spans approximately 10 years, even under the influence of vibrations. However, this requires the verification of the stability performance under realistic loads.

These measurements under load are important for STS ladders because during the assembly, the ladders are loaded with the weight of the modules which comprises the weight of sensors and micro-cables ($\sim$ 10 - 12 g per module). In high-radiation areas, where sensors are exposed to direct airflow, thermal and mechanical stresses may cause deformation of the ladders, potentially affecting the alignment of the mounted sensors.

In the context of linear elastic systems, the degree of deformation in the ladder depends on various factors, including the magnitude and frequency of external forces such as airflow and environmental conditions, as well as the ladder's eigenfrequency. Resonance, a critical problem, may occur if the eigenfrequency of the ladder aligns closely with the frequency of the external forces, causing significant vibrations and potential structural or functional damage.

To investigate the dynamic behavior of any system, generally, a 1-D harmonic oscillator is used. In the case of STS ladders, it can be approximated as a 1-D system that oscillates around its equilibrium position due to the elastic deformation of structural points, providing a clear picture of the ladder's dynamic behavior under realistic loads.

The displacement u(t) of the mass from its equilibrium position in such systems is governed by simple harmonic motion, described by the equation:

$$\mathrm{m}\frac{\mathrm{d}^2\mathrm{u(t)}}{\mathrm{dt}^2} + \mathrm{c}\frac{\mathrm{du(t)}}{\mathrm{dt}} + \mathrm{ku(t)} = \mathrm{F(t)} \tag{4.4}$$

where m is the mass of the system, c is the damping coefficient indicating energy loss per oscillation cycle, k is the stiffness of the system, u(t) is the displacement from the equilibrium position, and F(t) represents the time-dependent external force. [103].

For an undamped system (where c=0 and F(t)=0), the displacement simplifies to:

$$u(t) = A\cos(\omega_n t + \phi) \tag{4.5}$$

where, A is the amplitude of oscillation equivalent to the maximum deformation δ_{max} [6], ϕ is the phase angle at t=0, and $\omega_n = \sqrt{\frac{k}{m}}$ is the natural frequency (eigenfrequency) of the system.

The natural frequency, ω_n, represents the frequency at which the system will oscillate when no external forces are acting on it, and it is directly related to the stiffness (k) and mass (m) of the system. A higher natural frequency indicates a stiffer system with a faster oscillation rate, while a lower natural frequency suggests a more flexible system with a slower oscillation rate.

For the system integration, understanding the eigenfrequency $\omega_n$is essential to prevent resonances [7]. Hence, determining the eigenfrequency of the STS ladder and ensuring it does not match any resonant frequencies, is important for safety and functionality.

The relationship between the maximum deformation (δ_{max}) and eigenfrequency (ω_n) is given by:

$$\delta_{max} = \sqrt{\frac{2E}{m\omega_n^2}} \tag{4.6}$$

where E is the total energy of the system.

The Equation 4.6 highlights that the maximum deformation is influenced by the system's energy, mass, and eigenfrequency. This relationship allows us to predict how deformations will occur under realistic load conditions. Therefore, studying these dynamics is essential to design stable STS ladders, ensuring their long-term operation without succumbing to vibrational damages.

[6] In the Eq.4.5, the amplitude A is equivalent to maximum deformation δ_{max}, because it represents the maximum extent of the system's deviation from its equilibrium position, occurring at the peak displacement. Therefore, the displacement in Eq.4.5 can be expressed as: $u(t) = \delta_{max}\cos(\omega_n t + \phi)$.

[7] Resonance is a phenomenon where the system's natural frequency aligns with vibrational frequencies from external sources, potentially causing structural failures.

4.2.1 Experimental set-up description

To measure the eigenfrequency of STS ladders, two ladders were subjected to comprehensive testing as part of the EU project AIDA2020 [107], conducted at the University of Oxford, Great Britain. The university's facility offered a setup, that can be used for the STS ladders, allowing accurate measurements of structural deformations. These deformations were measured non-intrusively using capacitive sensors, and the data was acquired at different frequencies, facilitating spectral analysis of the structure's dynamic response up to several hundred Hz.

The University of Oxford possesses a specialized vibration test stand, originally developed for LHC (Large Hadron Collider) experiments and tracking detector research, which was made available for use by interested research groups [108]. This test stand employs a specially designed shaker table, optimized for minimal vibration interference in typical static environments commonly encountered in particle physics experiments. The shaker table was driven by a 10" speaker, and precise monitoring of vibrations was achieved through the utilization of MEMS-based accelerometers (ADXL 325) boasting an acceleration noise density of 250 μg / $\sqrt{\text{Hz}}$, where g refers to acceleration due to gravity (1g = 9.8 m/s^2).

The principal objective of using the shaker table was to conduct a thorough analysis of the ladder's eigenfrequency. This allowed for subsequent measurements of a similar ladder under airflow conditions, enabling a cross-validation process to ascertain any potential impact of airflow on the ladder's eigenfrequency.

To ensure comprehensive investigations, two identical ladders were prepared with the same assembly procedure. One ladder was subjected to eigenfrequency testing on the shaker table, while the other was tested under airflow conditions to determine if the eigenfrequency was excited. Additionally, considering the inherent weight of the modules themselves, it was imperative to evaluate the damping effect in the ladder due to the module's weight. Therefore, an additional ladder was dispatched to Oxford, which was solely glued into the bearings providing a comparative assessment of the results with the ladder after mounting the modules as can be seen in Fig. 4.5.

Two accelerometers, referred to as left and right accelerometers, are placed on both ends of the shaker table. Typically, the noise level for accelerometers in the unexcited regions is as low as 10^{-4} g. Before performing any measurements with the ladder on the shaker table, spectra for both accelerometers were obtained to identify the inherent vibrational characteristics of the table. The results are shown in the graph shown in Fig. 4.6. The graph depicts the peak

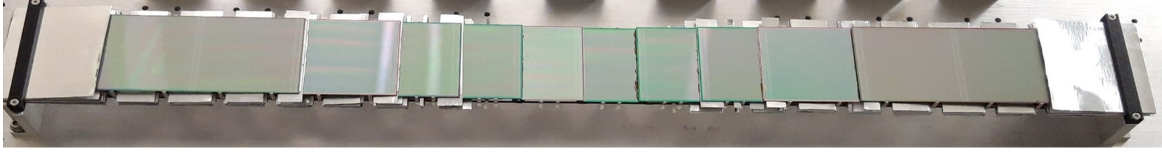

Figure 4.5: Image of STS ladder assembled with 10 non-operational modules prepared for the eigenfrequency tests and analysis at the University of Oxford.

acceleration plotted against the frequency in the x, y, and z directions. From the accelerometer spectra, it can be observed that the rocking mode[8] of the table is around 42 Hz and any excitation during the ladder scan around this frequency range can be neglected since that is solely coming from the table.

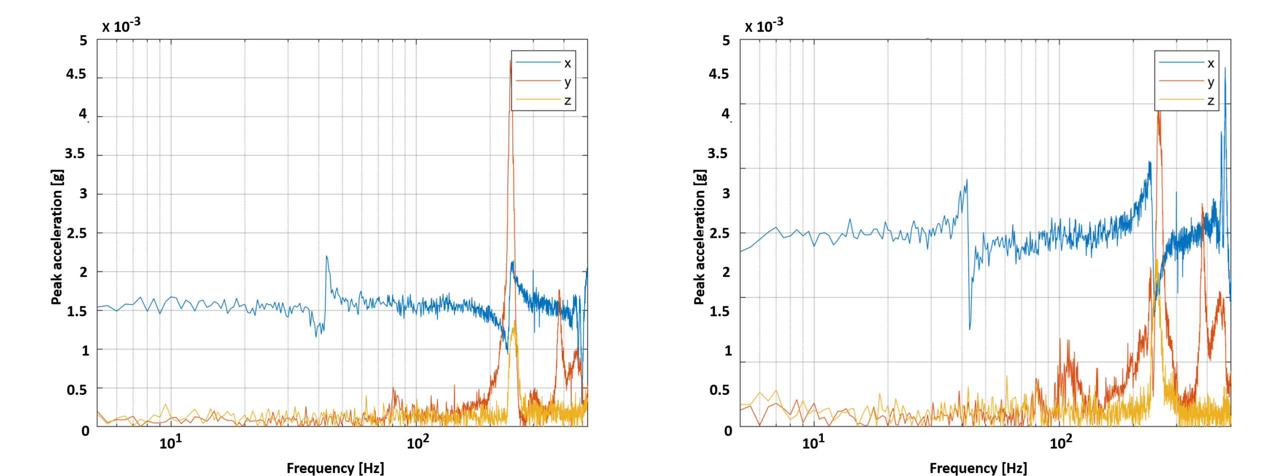

Figure 4.6: Plots showing the data from the accelerometers placed at the left and right end of the shaker table. Both the accelerometers show the rocking mode at 42 Hz.

To enable precise displacement measurements of the object mounted on the shaker table, capacitive sensors were used for good sensitivity in the presence of conductive and reflecting surfaces like silicon. Four capacitive sensors were used to measure the displacement in the ladder. Two sensors were fixed close to the supported end of the ladder, i.e., the ladder bearings, to measure the displacement in the table due to the accelerometers. The other two sensors were positioned at distances of 330 mm and 510 mm from the fixed bearing of the ladder, respectively, to scan the displacement in the ladder, as illustrated in Fig. 4.7.

[8]The rocking mode refers to the natural vibrational frequency at which the shaker table itself tends to oscillate.

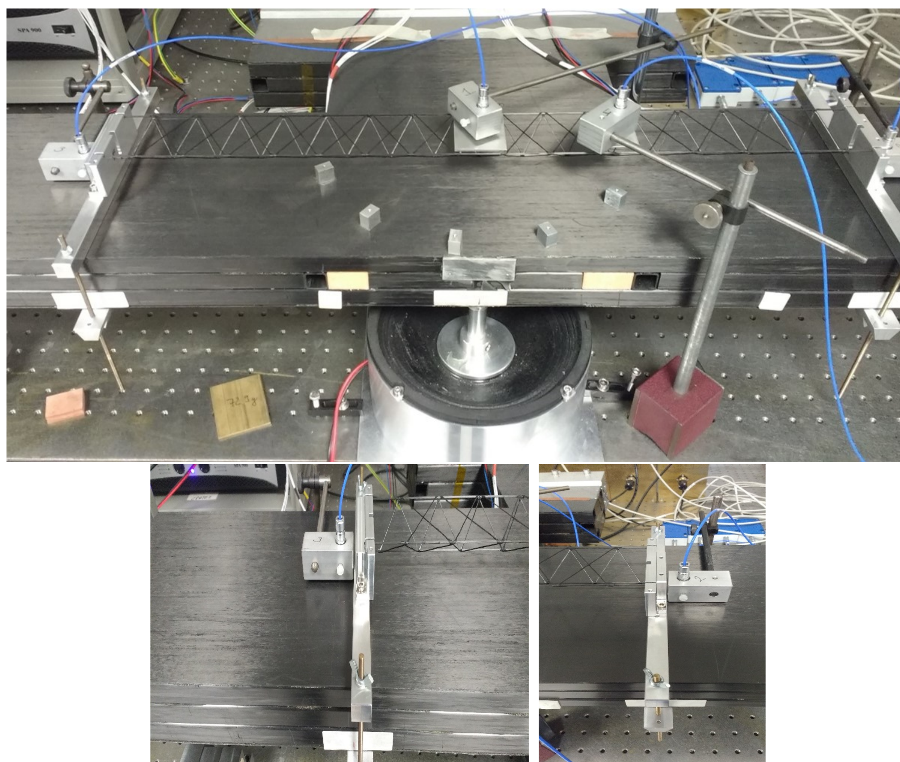

Figure 4.7: Top image: Bare ladder mounted on the shaker table with 4 capacitive sensors, bottom left: capacitive sensor positioned close to fixed bearing, bottom right: capacitive sensor positioned close to floating bearing.

4.2.2 Displacement measurement using capacitive sensor

The data obtained from the capacitive sensors consists of approximately 250 samples recorded at a sampling frequency of 2 kHz. To extract the displacement amplitudes relevant to the ladder's performance, i.e., from the middle sensors, and to negate the influence of the shaker table, the spectra from both the table sensors were averaged and systematically subtracted from the middle sensor measurements. The resultant spectrum is shown in Fig. 4.8.

From the graph it can be seen that both middle sensors exhibit high noise levels and resonances, making it challenging to accurately predict the frequency modes. To enhance the stability of the lightweight ladder (around 10-12 g per 1 m length), and to attenuate extra noise, small weights were added to the ladder's surface. Specifically, two aluminum sheets, each measuring 60 x 60 mm^2 were mounted underneath the capacitive sensors on the ladder, as shown in Fig. 4.9. These sheets' dimensions align with those of one of the STS sensors, ensuring that the modification closely mimics operational conditions. This addition resulted in the significant improvement of the resonance peaks, providing insights into the eigenfrequency of the ladder. The subtraction of

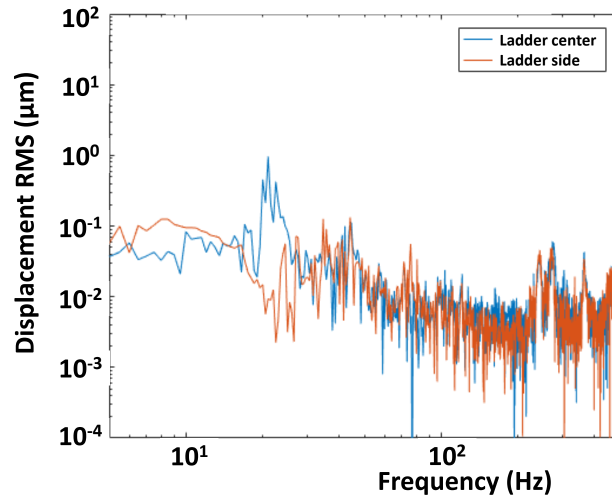

Figure 4.8: The RMS vs frequency plot of middle sensor's spectrum after subtracting the table measurements.

averaged measurements from both accelerometers reveals the first eigenfrequency of the ladder at approximately 42 Hz, with a subsequent eigenfrequency observed at 114 Hz.

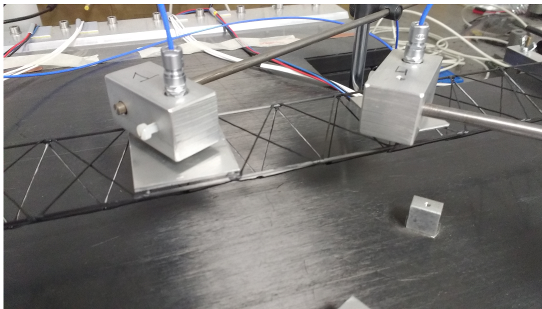

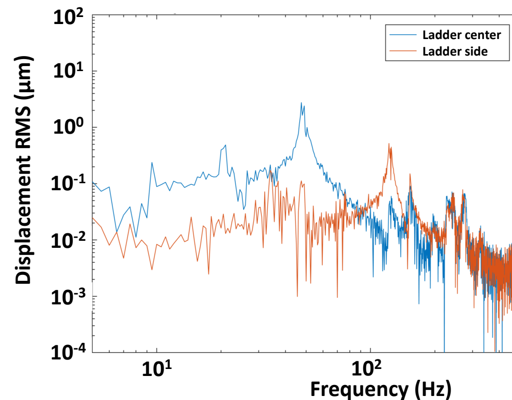

Figure 4.9: (Left) Closer view of the ladder with weights mounted underneath capacitive sensors, (Right) Frequency vs RMS plot showing the spectra for both the middle sensors after the subtraction of measurements from the table.

After becoming acquainted with the eigenfrequency values of the bare ladder, the subsequent investigation involved monitoring potential shifts in the resonant peaks when the ladder was equipped with sensors and cables. The measurement procedure was similar to the previous setup, with the assembled ladder replacing the bare ladder and mounted on the shaker table, as depicted in Fig. 4.10. Unfortunately, due to a malfunction in one sensor, only a single capacitive sensor was used to scan the displacement at the middle of the ladder during this measurement.

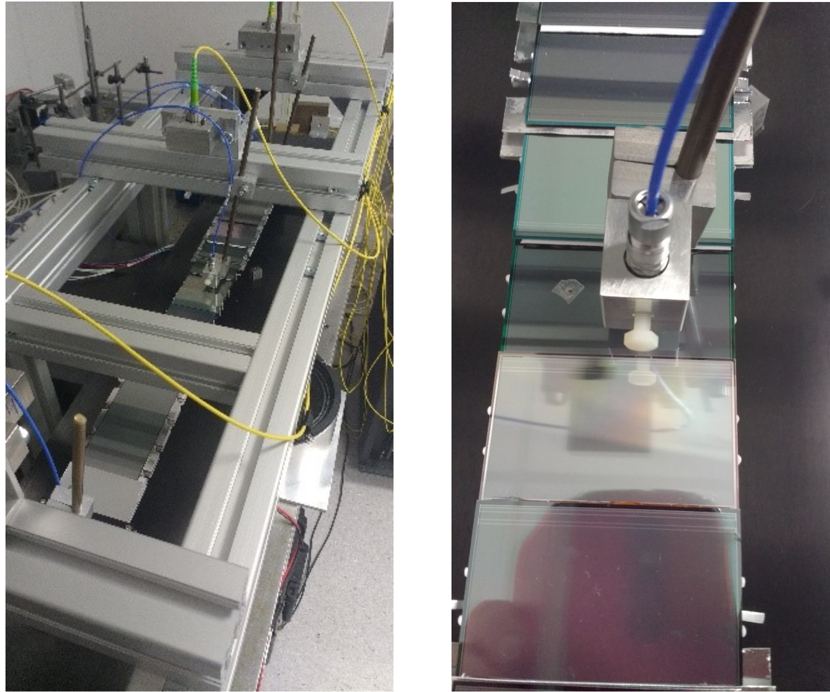

Figure 4.10: (Left) Top view of the fully assembled ladder mounted on the shaker table, (Right) closer view of the capacitive sensor mounted close to the surface of silicon.

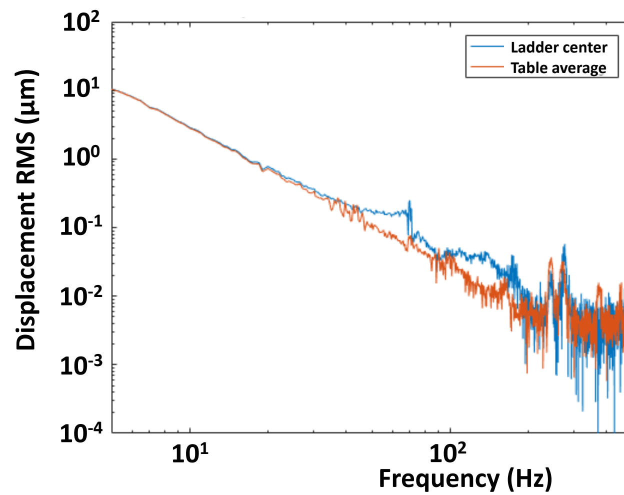

Figure 4.11: Frequency vs RMS plot showing the spectra for a fully assembled ladder with the middle sensors as well as the averaged measurements from the table.

The displacement data shown in Fig. 4.11, represents the averaged displacement data obtained from both the table sensors and the middle sensor for the ladder assembled with modules. In the figure, a pronounced peak at 67 Hz is visible which is indicative of the ladder's first eigenfrequency. This shows a notable shift when compared to the bare ladder's eigenfrequency. The observed shift in the eigenfrequency can be attributed to the impact of the added mass

and the alterations in the ladder's stiffness due to the presence of the sensors and micro cables. As the modules are mounted onto the ladder, they contribute to an increase in their overall mass, and their distribution along the ladder affects their stiffness properties. Consequently, the ladder's natural frequency of vibration, i.e., the first eigenfrequency, is modified as a result of these changes.

For the comparison to the behavior of a simple 1D oscillator, the experimental data has been processed to remove the influence of the shaker table by subtracting its displacement from the ladder's data. Following the data refinement, a sine wave fitting is applied based on the excitation frequency, which confirms the ladder's primary eigenfrequency, as shown in Fig. 4.12.

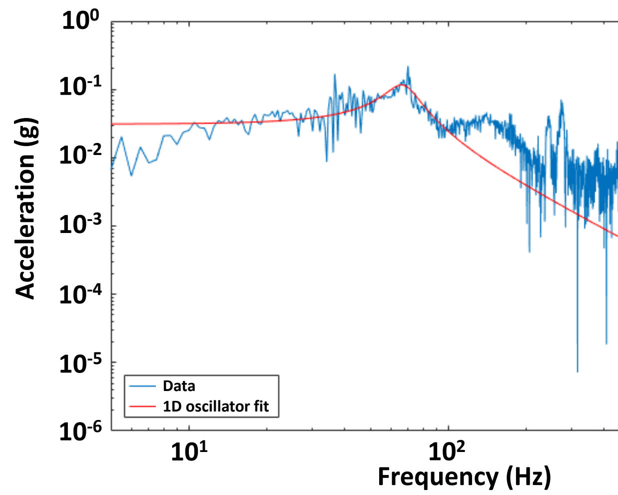

Figure 4.12: Table subtracted displacement data with 1D oscillator fit for capacitive sensor system for the dummy ladder.

Therefore, it can be concluded that the initial eigenfrequency mode identified to be approximately 67 Hz, aligns with the expected response of a simple 1D oscillator. To further investigate the influence of external factors on the ladder's eigenfrequency, it is essential to conduct experimental tests to ascertain if airflow has any impact on the eigenfrequency of the assembled ladder.

4.3 Vibration measurement under air flow

After conducting the analysis at Oxford, the subsequent step involved examining whether the flow of air would excite this eigenfrequency. To perform this investigation, the setup was prepared at the GSI laboratory, using an identical assembled ladder to the one sent to Oxford.

This allowed for a comparison of results with the Oxford analysis and enabled the measurement of the amplitude of vibrations induced by the airflow.

During the measurement of the ladder's eigenfrequency on the shaker table, it was positioned horizontally. It is worth noting that, as outlined in Section 3.6, all modules will be mounted on the ladder when it is placed horizontally on a granite table. However, when the STS is operational, the ladders will be mounted vertically inside the STS box. Hence, it becomes crucial to investigate if this change in orientation might introduce any damping factor. Therefore, a testing procedure was optimized to evaluate the impact of airflow on the ladder and sensor vibrations.

4.3.1 Experimental set-up description

For precise vibration measurements, it's essential to establish a stable environment that mitigates the impact of vibrations from the surroundings. To achieve this, a single ladder was chosen as the test subject. To ensure stability, an aluminum base plate was used which is mounted onto an optical bench with vibration isolators to minimize the floor vibrations [109]. The ladder itself was mounted onto the base plate, while a perforated tube was attached to facilitate the airflow for sensor cooling (see Fig. 4.13).

It is crucial to position the tube correctly with the holes facing the surface of the sensor to provide sufficient cooling. For standard ladders (excluding the central ones), the tube is positioned 12.5 mm away from the innermost sensor [111]. However, for the central ladder, due to the beam-pipe opening resulting in the absence of the middle two sensors, the tube will be placed 10.5 mm away from the central sensor.

To accurately measure the volumetric flow of gas while maintaining a relatively constant pressure drop, FLK 2216 Acrylic variable area flow meters were used. The flow meters were connected to the perforated tube with Swagelok fittings, ensuring an airtight connection. The connection between the two was established via a tube with an inner diameter of 4 mm.

The ideal air flow rate for sensor cooling through the tube is approximately 30 L/min, and the FLK 2216 flow meters allowed us to measure flow rates ranging from 0 L/min to 20 L/min in each flow meter, resulting in a maximum flow of 40 L/min passing through the tube. Therefore set-up has been prepared to measure the ladder under the airflow, with a specific focus on quantifying the displacement occurring on the sensor surface due to the airflow.

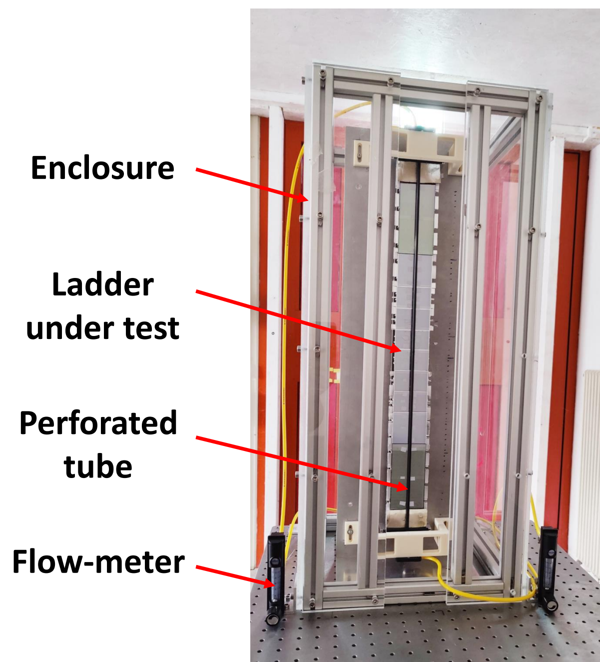

Figure 4.13: Setup to measure the vibrations on the ladder which is fixed to the optical bench, where two flow meters are connected to both ends of the perforated tube.

4.3.2 Approach to measure sensor vibration

Several techniques can be used to measure vibrations, depending on the type and frequency of the vibration, and the accuracy and precision required for the measurement. Generally, these measurements are divided into two main types:

- **Contact measurements:** These measurements involve direct contact between the measurement sensor and the object to be tested. In this method, a sensor is directly attached to the surface of a vibrating object to measure the displacement. The sensor can be in the form of an accelerometer, velocity, or displacement transducer. The primary advantage of contact measurements is that they provide accurate and precise data on the vibrating object. However, the disadvantage is that they may alter the natural vibration behavior of the object due to added mass from the sensor. Also, the process of attaching the sensor can be time-consuming and may require access to the vibrating part, which could be challenging in certain cases.

- **Non-contact measurements:** These measurement methods offer an alternative approach, which does not require any direct contact with the surface of a vibrating object. They use remote sensing techniques to capture the data of the vibrating object. This

method is particularly beneficial when contact measurements are not possible or when contact with the object could alter its behavior or damage the sensor. Common examples of non-contact vibration measurement techniques include Laser-based sensors like Laser Doppler Vibrometer (LDV), capacitive sensors, etc. The main advantage of performing non-contact measurements is that the natural vibration characteristics of the object can be preserved since there is no physical attachment. Also, the non-intrusive nature makes it suitable for delicate or sensitive objects. However, the disadvantage of these measurement devices is that they can be more challenging to set up. Also, the accuracy and precision of non-contact measurements might be lower compared to contact measurements, especially for very small displacements or high-frequency vibrations. In the case of ultra-light structures like CF ladders in STS, it becomes necessary to have non-contact measurements because of the sensitive surface of sensors (320 μm thickness) glued onto the ladders. Therefore, LDV has been used to measure the vibrations in sensors.

4.3.2.1 Vibration measurements using LDV

Vibration measurement using a Laser Doppler Vibrometer (LDV) uses the Doppler effect to accurately measure the movements of objects, including their velocity and vibratory motions. When the target's velocity remains relatively stable over a defined time frame, the technique is known as Laser Doppler Velocimetry. However, if the target is vibrating, the technique used to capture vibration information is referred to as Laser Doppler Vibrometry. These two techniques require different configurations, as illustrated in Fig. 4.14. Laser Doppler Velocimetry systems typically send two light beams from the same laser source to the moving target within the same region using the external interference method, whereas, Vibrometry uses a single beam that interacts with the target and measures the internal interference of the reflected signal with a reference beam.

Since the ladder under vibration will experience a certain level of vibrations due to airflow, therefore, the use of a laser Doppler vibrometer was preferred. LDV provides a convenient way to perform non-contact measurements of vibrating objects and various types of LDVs, such as single point, scanning, and 3D LDVs, serve different purposes. The fundamental operation involves an interferometer that detects frequency shifts caused by the motion of the object along the laser beam's path. These shifts are minute compared to the laser's high frequency, but through the process of interference, they are converted into measurable intensity fluctuations [112]. This

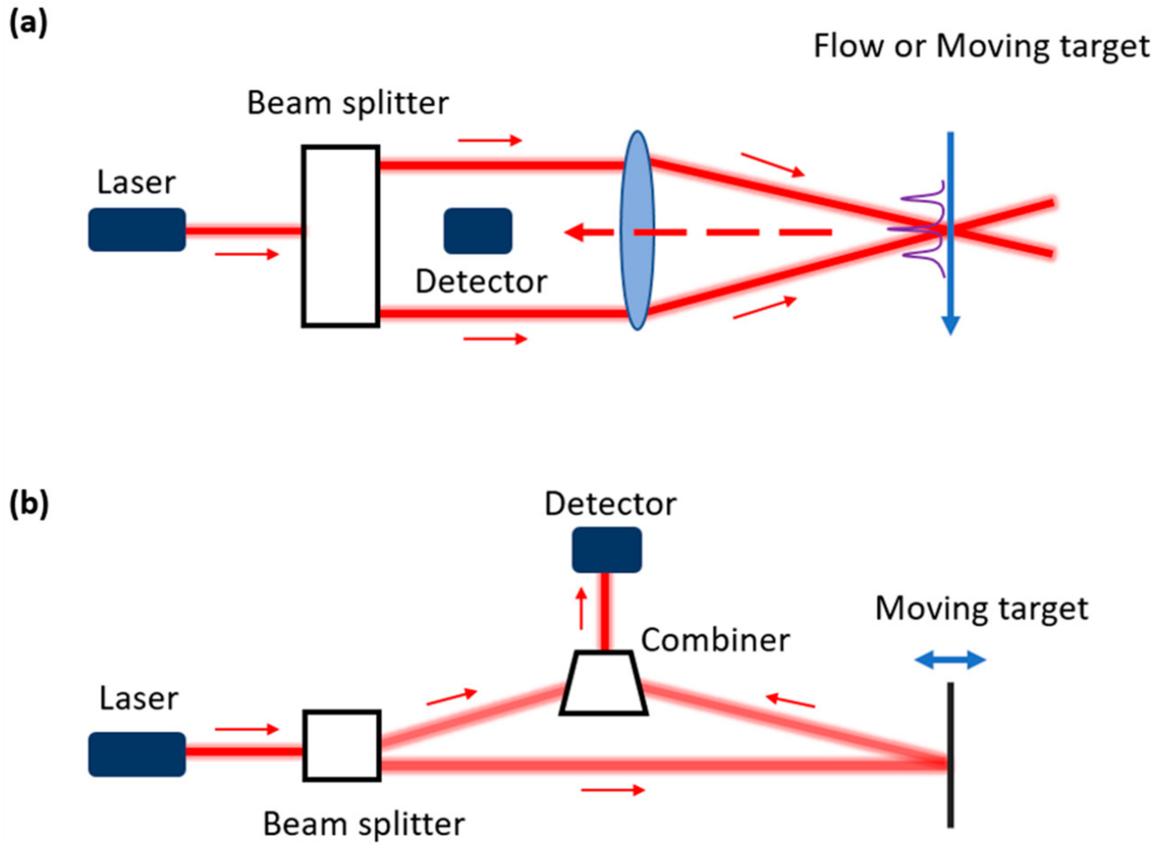

Figure 4.14: Laser Doppler velocimetry (top) and laser Doppler vibrometer (bottom) [114].

conversion is expressed mathematically by the interferometer Equation 4.7 [113]

$$I_{tot} = I_1 + I_2 + 2\sqrt{I_1 I_2 \cos\frac{[2\pi(r_1 - r_2)]}{\lambda}} \tag{4.7}$$

where, I_1 and I_2 are the intensities of the two coherent light beams, r_1 and r_2 are their respective path lengths, and λ is the wavelength of the laser light.

The laser vibrometer uses a Helium-Neon laser emitting a beam with a frequency of 4.74 x 10^{14} Hz and a wavelength of 633 nm. In the schematic shown in Fig. 4.15, this laser beam is first divided by a beam splitter (BS1) into a measurement beam, which will interact with the vibrating ladder, and a reference beam that remains unaffected by the ladder's movement. The measurement beam travels through a second beam splitter (BS2), after which it is finely focused by a lens onto the ladder, the object of our measurement.

When the ladder experiences vibration parallel to the laser beam, it causes a change in the frequency of the reflected light due to the Doppler effect. This phenomenon, called the Doppler frequency shift, is illustrated by f_d and is directly proportional to the velocity of the ladder's

surface (v_s) and the wavelength of the laser (λ), described by the equation:

$$f_d \propto 2v_s\lambda. \tag{4.8}$$

After reflecting from the ladder, the scattered light travels back through BS2 to Beam Splitter 3 (BS3), where it merges with the reference beam, which has been frequency-shifted by a Bragg cell to act as a stable point of comparison. This convergence of the measurement and reference beams creates an interference pattern, which is transmitted to the photo-detector. The role of the photo-detector is to convert the variations in light intensity, caused by the interference of the two beams, into an electrical signal, generating an interference pattern between the measurement and reference beams.

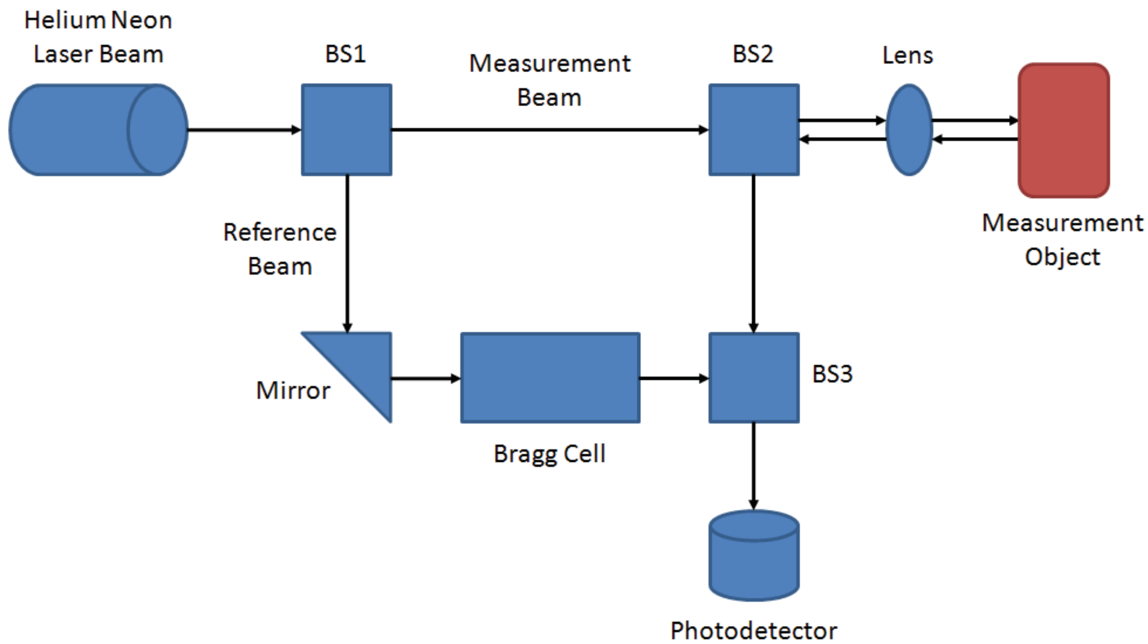

Figure 4.15: Schematic of laser Doppler vibrometer [114].

4.3.2.2 Measurement procedure and analysis

To measure the amplitude of out-of-plane vibration, it is important to optimize the measurement procedure using LDV. To accomplish this, precise and accurate measurements were carried out using a scanning LDV from Polytec (ref), which allowed for a comprehensive scanning of the entire surface. Typically an LDV system includes:

- **Laser head**[9] generates the laser beam used for the measurement. The laser head emits a coherent and focused laser beam that is directed toward the target surface [118]. The laser beam interacts with the vibrating surface and provides information about the object's velocity.

- **Vibrometer controller**[10] is responsible for controlling the LDV system and processing the signals generated by the photodetector. It typically includes a decoder that converts the high-frequency Doppler signal into a lower-frequency value that can be more easily analyzed and displayed. The vibrometer controller may also include various settings and adjustments to optimize the LDV measurement process [115] [116].

- **Junction head**[11] connects the laser head and the vibrometer controller. It typically includes fiber optic cables and signal conditioning electronics to ensure reliable and high-quality data transfer between the laser head and the vibrometer controller. The junction head ensures precise alignment of the optical elements to maintain the coherence and accuracy of the LDV measurements [117].

4.3.3 Optimization of the setup

Before performing measurements with the vibrometer, it is necessary to optimize the setup for accurate results. One of the key points in this case is how far or close the laser sensor should be kept from the sensor surface to achieve maximum laser focus while minimizing fluctuations. Several factors can influence signal fluctuations, including vibrometer calibration, laser beam alignment with the object, environmental stability, surface roughness, and the distance between the object and LDV. To address these concerns, enclosing the ladder set up on the optical bench and determining the optimal distance between the sensor surface and laser head have been crucial steps taken to minimize potential errors. Maintaining a stable signal level is crucial to achieve a higher signal-to-noise ratio (SNR) for more reliable data, with the optimal standoff distance closer to the visibility maxima where the signal level is at its maximum.

[9] Sensor head used is OFV-525

[10] Vibrometer controller used is OFV-5000

[11] Junction box used is VIB-E-400

The optimal standoff distance is given by the equation:

$$D = 234 + (n.l), \tag{4.9}$$

where D is the optimal standoff distance, n = 0, 1, 2, ...
l is visibility maxima = 204 mm.

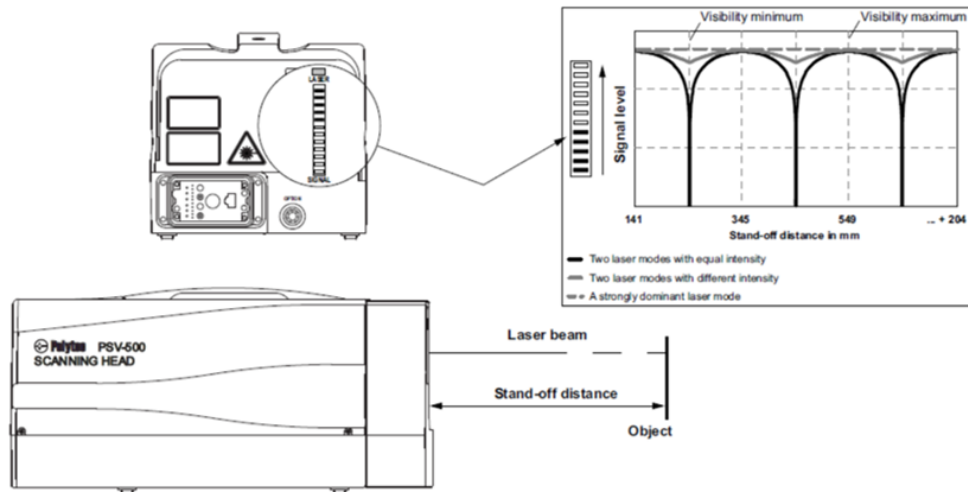

Figure 4.16: Measuring the stand-off distance between the laser and the object [119].

The dependence of signal level on the standoff distance can be observed in Fig. 4.16, where the signal level remains consistently high at the visibility maxima. The visibility maxima for OFV 525 lasers is approximately 642 mm, as per the values mentioned in the manual after optimization [119]. Hence, the ladder is positioned at a distance of 640 mm from the laser head. Figure 4.17 provides a detailed description of the ladder to be tested under the airflow.

4.3.4 Measurement of vibration signal and analysis technique

Once the mechanical setup was completed, the next step involved performing vibration measurements using an LDV. The data was acquired using VibSoft, a specialized software that streamlines data acquisition, signal processing, and analysis by allowing the installation of a data acquisition board in the computer [119, 120]. This software is designed to simplify and streamline data analysis, making it easier to interpret complex vibration signals. For the measurements, the ladder was positioned at a distance of 642 mm from the laser sensor head and interfaced with the vibrometer controller and a junction box. The measurement process in-

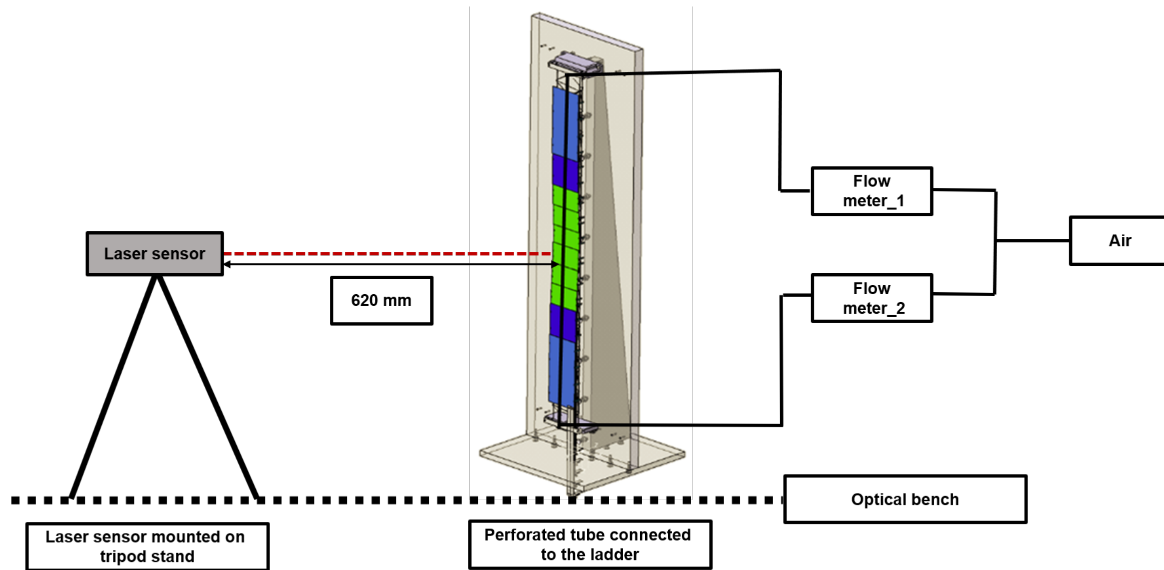

Figure 4.17: Set-up assembled for air-flow measurement with laser head of LDV focused on the silicon sensor. On the left side laser head is mounted on a tripod stand and affixed to the optical bench kept at an optimal stand-off distance from the sensor to be scanned. The right side of the image focuses on the ladder setup where the ladder is connected to the perforated tube which is then connected to the flow meters on both sides for the airflow to pass through.

volved selecting appropriate settings within VibSoft, initiating data capture, and storing the vibration data in a format suitable for analysis.

To analyze vibration signals, the transformation of vibration signals from their time domain into the frequency domain is important. This is achieved through Power Spectral Density (PSD) analysis, with Welch's method standing out as an effective technique. This method divides the signal into overlapping sections or windows applying the Fast Fourier Transform (FFT) to each section and then averaging the resulting power spectra. This averaging effectively reduces the impact of noise and provides a smoother estimate of the PSD. It also allows for adjusting the size and overlap of the sections, which helps in achieving an optimal balance between frequency resolution and noise reduction.

The PSD estimate (S(f)) for a given frequency (f) using Welch's method is given by:

$$\mathrm{S(f)} = \frac{1}{\mathrm{NK}} \sum_{\mathrm{k=1}}^{\mathrm{K}} |\mathrm{X_k(f)}|^2, \tag{4.10}$$

where K represents the total number of overlapping segments (windows), N is the length of each segment (number of data points in each window), and $\mathrm{X_k(f)}$ denotes the Discrete Fourier Transform (DFT) of the $\mathrm{k^{th}}$ segment at frequency f [122].

Welch's method balances the trade-off between frequency resolution and noise reduction by adjusting the window type, overlap percentage, and number of FFT points. These parameters are essential for achieving a reliable PSD estimate [121]. The selection of a window type significantly influences the accuracy of frequency estimation. The Hanning window, shown in Fig. 4.18, is particularly suited to random signals like vibrations, as it effectively reduces spectral leakage during FFT transformation. This window, when multiplied with the signal, attenuates the signal at the start and end, resulting in a smoothed, tapered signal with a more precise frequency spectrum determination.

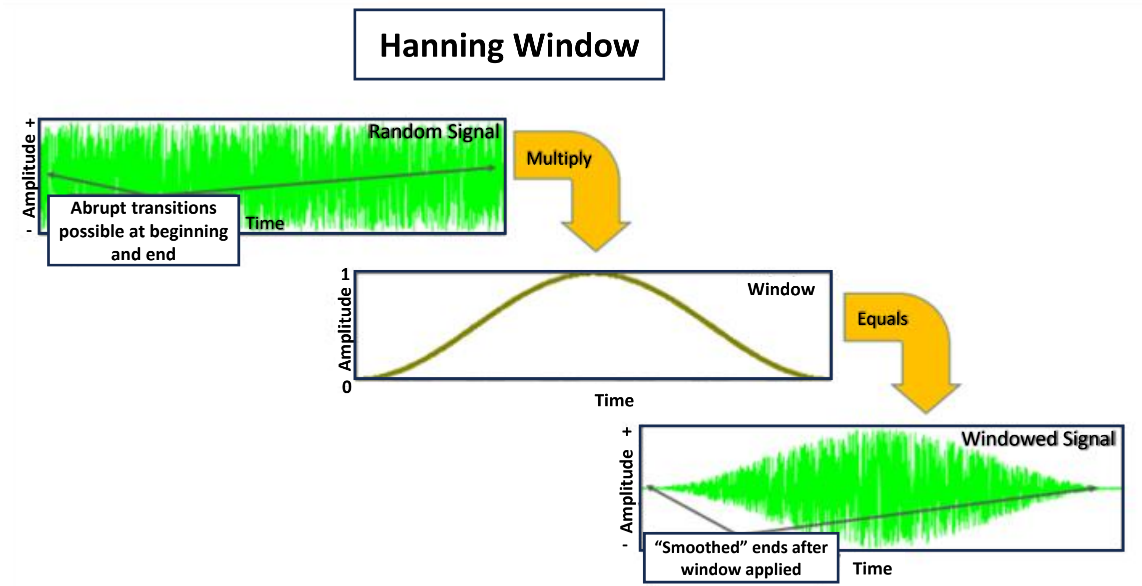

Figure 4.18: Upper left: Random data, Bottom: Hanning window, Bottom right: Resultant spectra after Hanning window applied.

The Hanning window application is graphically depicted in Fig. 4.18. The top graph shows the raw signal with potential abrupt transitions at the start and the end. The middle graph displays the Hanning window itself, and the bottom graph demonstrates show the signal is smoothed out after the window application. This windowing technique, along with the chosen degree of overlap, not only improves the PSD curve but also maintains the original signal's frequency characteristics, thus improving the accuracy of our vibration analysis. For the measurements in this study, the Hanning window with 66% overlap was chosen after careful consideration of the spectra. Detailed parameters for data acquisition and analysis are provided in the appendix.

4.4 Experimental Findings: Airflow Measurement Using Perforated Tube

After preparing the experimental setup and familiarizing with the data acquisition software, the final step is to conduct the measurements. The experimental setup in the laboratory, as shown in Fig. 4.19, features the laser sensor focusing on the silicon sensor surface, kept at a distance of 640 mm. The maximum signal level in the laser head implies that a stable signal can be expected. However, the reflective nature of the silicon surface poses a challenge in achieving maximum focus, as the laser was oriented at different angles to measure various positions on the sensors. To improve the signal-to-noise ratio, particularly for low-frequency measurements, reflective tape was applied to the ladder's surfaces to be measured, to enhance the focus as a common approach in LDV applications [123, 124].

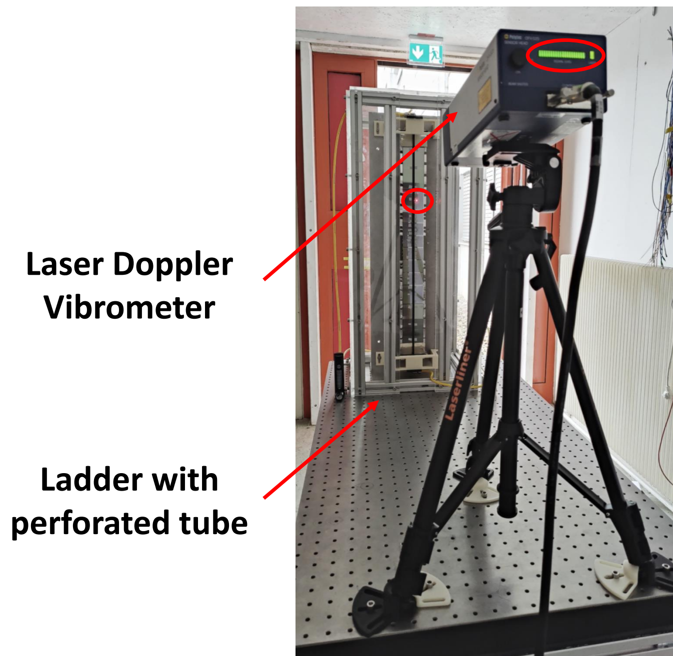

Figure 4.19: Laser doppler vibrometer and Ladder with perforated tube mounted on the optical bench. The encircled region on the ladder shows the point on the sensor focused by the laser, while the marked area on the LDV represents the point of maximum focus, ensuring accurate vibration measurements.

Simulations have indicated that vibration amplitudes must remain below 1 μm for the functionality of track-based alignment software. To verify this, airflow-induced vibrations were measured at 20, 30, and 40 L/min. However, these measurements include the contribution of background vibrations along with the flow-induced vibrations. Therefore, the limitation of having only one vibrometer introduced the complexity of separating these two components.

To separate the background noise from the flow measurements, a two-step approach was taken: initial readings were taken with the airflow activated, followed by a second set with the airflow switched off, without altering the setup. This second set of measurements provided the background data, which was subsequently subtracted from the initial readings. This process allows to measure the amplitude of vibration at a particular flow rate without the impact of the background.

It was expected that the highest level of vibrations would occur in the vicinity of the perforated tube. As such, the amplitude of out-of-plane vibrations[12] was measured at various points along both sides of the perforated tube, regardless of the size of the sensor. Fig. 4.20 (left) illustrates a schematic of a 6×6 cm^2 sensor with the selected measurement points to capture the effects of vibrations near both layers of L-legs and in the middle of the sensor between the L-legs where vibrations were expected to be prominent. The measured points were averaged to obtain an overall assessment of vibrations across the entire sensor surface, as shown in Fig. 4.20 (right).

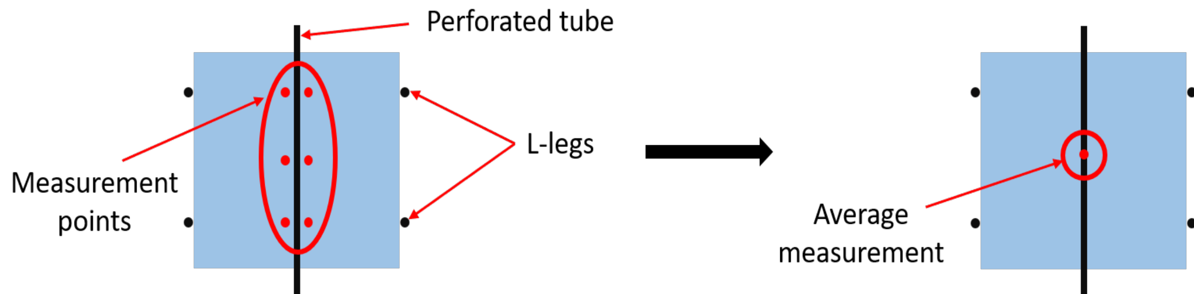

Figure 4.20: (a) Schematic illustrating the positioning of different measurement points on 6×6 cm^2 *sensor surface (b) Averaging of measured points to obtain an overall assessment of vibrations across the entire sensor surface.*

For each sensor point, a sequence of 10 measurements was conducted, after focusing the laser on the sensor. The initial reading, taken in the absence of airflow, served as a baseline. The flow rates were subsequently varied to obtain a set of measurements at each specified rate. The goal was to obtain two measurements per-flow rate to enhance reliability through averaging.

However, considering that each measurement took approximately 64 seconds to complete, it was essential to maintain consistency in the measurements. To achieve this, a measurement approach was adopted, which involved gradually increasing the flow rate from zero to 40 L/min and back to zero, as illustrated in Fig. 4.21 (left). This way, two measurements were obtained at each flow rate for every point on the sensor, and three measurements were taken for the

[12]"Out-of-plane vibration" refers to motion that occurs perpendicular to a reference plane or surface

background (no flow) condition. These measurements were later averaged, enabling a more comprehensive assessment of the airflow effects on the sensor (Fig. 4.21 (b)).

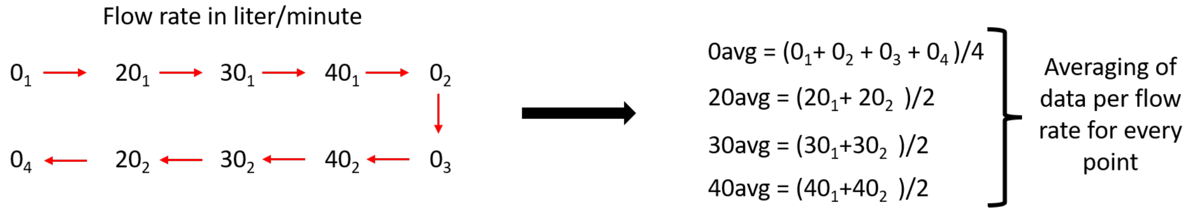

Figure 4.21: Air flow measurement procedure for each point on the sensor.

The flow measurements served two important purposes: firstly, to identify the sensors most vulnerable to airflow-induced vibrations, and secondly, to determine the amplitude of these vibrations, ensuring the track alignment software functions optimally within acceptable vibration limits. To evaluate the effect of airflow on ladder stability, PSD spectra were measured for both standard and central ladders, focusing on inner sensors that require active air cooling. The PSD spectra for both ladder types were analyzed and their vibration amplitudes were compared.

4.4.1 Standard ladder

The PSD measurements taken at the points specified in the Fig. 4.20, was measured for each sensor on the ladder under different air flow rates. The PSD spectra for the innermost sensor are shown in Fig. 4.22 (left), with each color representing different airflow rates through the perforated tube. From the plot, it can be observed that multiple peaks are excited because of the airflow. The first peak appears at approximately 7.5 $\pm$ Δf Hz, followed by another peak at approximately 22.5 Hz. However, it can be noticed that these peaks are also visible in measurements taken without airflow, indicating that they are likely due to external environmental noise rather than eigenfrequencies of the sensor.

The subsequent peak that is excited due to airflow is expected to correspond to the first eigenfrequency of the sensor. When compared with measurements conducted in Oxford, it can be inferred that the first eigenfrequency of an assembled ladder (at 67 Hz) is not being excited, indicating that the ladder structure remains stable and airflow does not significantly influence the vibrational behavior of the ladder.

Taking a closer look at the PSD spectra in Fig. 4.22, it was observed that the frequencies below 1 Hz, exhibit a more pronounced impact on the PSD spectra, which could be attributed to external

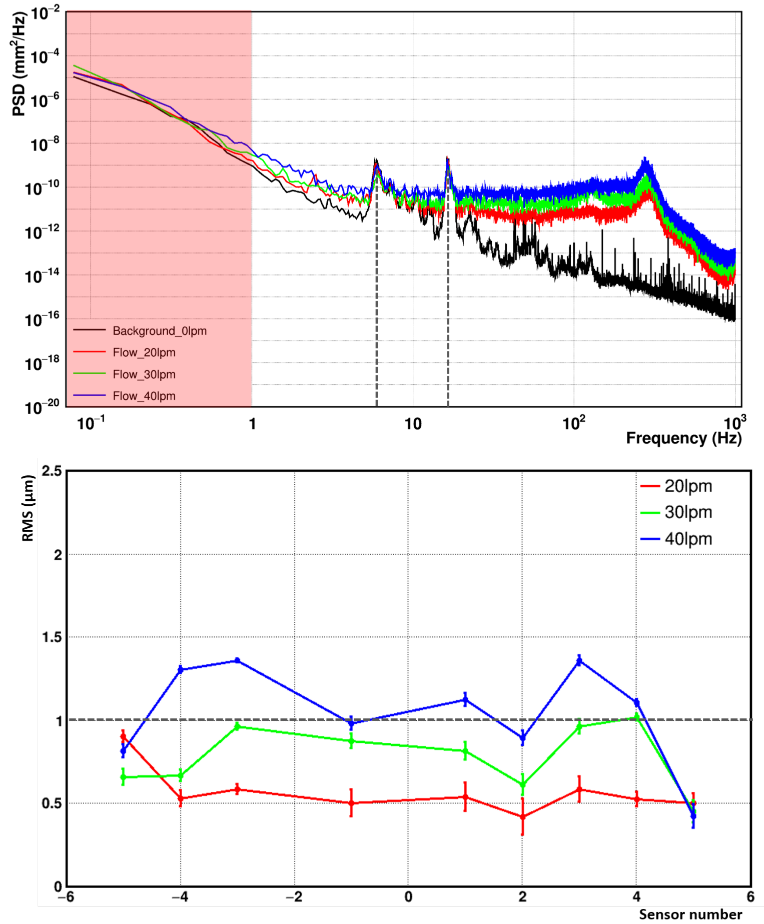

Figure 4.22: (Top) Frequency vs PSD spectra of one of the points on the innermost sensor, with each flow-rate shown by a different color. The vertical dotted lines highlight the excitation of peaks at frequencies of 7.5 and 22.5 Hz, because of the airflow. The shaded region on the left side of the plot shows the frequency range that has been excluded from the analysis due to the background noise. (Bottom) The plot shows the vibration amplitude (RMS) for each sensor on the ladder with the red, green, and blue colors corresponding to airflow rates of 20, 30, and 40 L/min, respectively. The horizontal dotted line shows the baseline limit for the maximum vibration amplitude so that track-based alignment software can work properly.

background effects or seismic noise. This observation is consistent with measurements taken without airflow, suggesting that the observed vibrations may not be solely due to airflow-induced effects. Therefore, to account for this, a soft frequency cut was applied during the calculation of vibration amplitudes, excluding frequencies below 1 Hz. This approach of applying a soft frequency cut below 1-2 Hz is commonly used in calculations for vibration analysis to minimize the impact of external factors [125].

To calculate the amplitude of vibration in the sensors, the RMS was calculated from the PSD spectra. The RMS value, which represents the amplitude of vibrations induced by airflow on the sensors, was obtained by integrating the PSD over the frequency range of interest i.e., $f_1 = 1$ Hz to $f_2 = 1000$ Hz and then obtaining the square root of this integrated value, resulting in the RMS value for each spectrum.

$$\mathrm{RMS} = \sqrt{\int_{\mathrm{f}_1}^{\mathrm{f}_2} \mathrm{PSD(f)}\,\mathrm{df}} \tag{4.11}$$

The RMS values, indicative of the vibration amplitude, were plotted as a function of different airflow rates for each sensor, as shown in Fig. 4.22 (bottom). From the plot, a trend can be observed where higher flow rates correspond to greater RMS values, indicating rise in induced vibrations. The more pronounced vibrations are observed in central sensors, particularly sensor numbers +3 and -3 because the holes of the perforated tube are closest to these sensors.

Therefore, it can be summarised from the plot that to mitigate the impact of airflow on the ladder vibration, the optimal flow rate of 30 L/min is appropriate. The plot indicates that at this flow rate, the maximum amplitude of out-of-plane vibrations is estimated to be around 1 μm (less than 3.7 μm). This indicates that vibrations in the sensors will not adversely affect the particle tracking, and the reconstruction software can be used without any detrimental effects induced by the airflow. Also, for the required cooling of STS, the flow rate of 30 L/min has been tested in a thermal demonstrator experiment and was found to be sufficient to cool down the innermost sensors [111].

The experimental data presented in Fig. 4.22 shows the measurements taken by switching airflow on and off, which does not fully represent the realistic operating conditions of the STS. During the operation of the STS, the detector will be continuously subjected to cold airflow. To verify this scenario, a worst-case scenario test was performed, wherein the ladder setup was exposed to continuous airflow of 40 L/min (exceeding the optimal airflow). The measurements were conducted for the critical sensors, i.e., sensor 3 and sensor -3. A total of 14 measurements were taken at different time intervals for 3 days, and the PSD spectra were plotted for both sensors. Fig. 4.23 shows the spectra of the first and last measurements taken for both sensors under continuous airflow.

Using the same measurement approach as described earlier in the schematic in Fig. 4.21, further measurements were conducted with and without the airflow. RMS values were calculated from the PSD spectra for the frequency range of 1 Hz to 1000 Hz and were plotted for the different

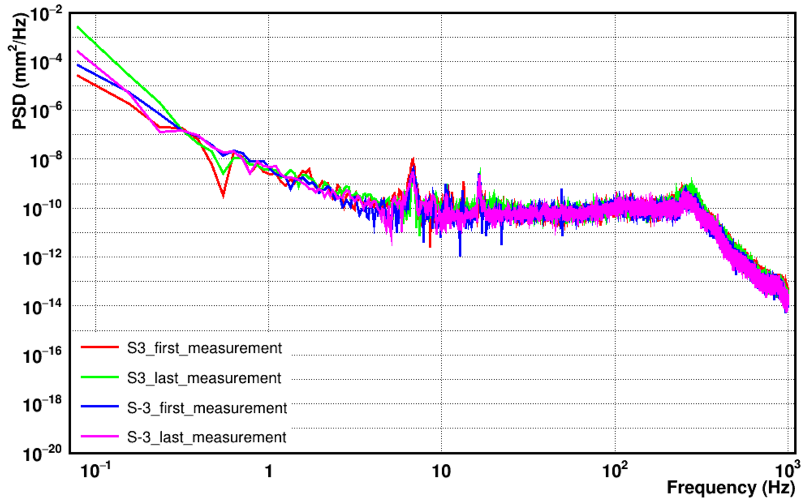

Figure 4.23: Frequency vs PSD spectra for the most critical sensors (S3 and S-3) under a continuous airflow of 40 L/min.

measurements of both sensors (See Fig. 4.24). The plots show that the RMS values for both sensors ranged between 1 μm to 2 μm. It can be noted that the error bars in the plots are relatively large due to less number of measurement points. Thus, it can be concluded that operating the inner sensors of the STS with a flow rate of 30 L/min will produce minimal vibrations leading to negligible impact on particle tracking precision.

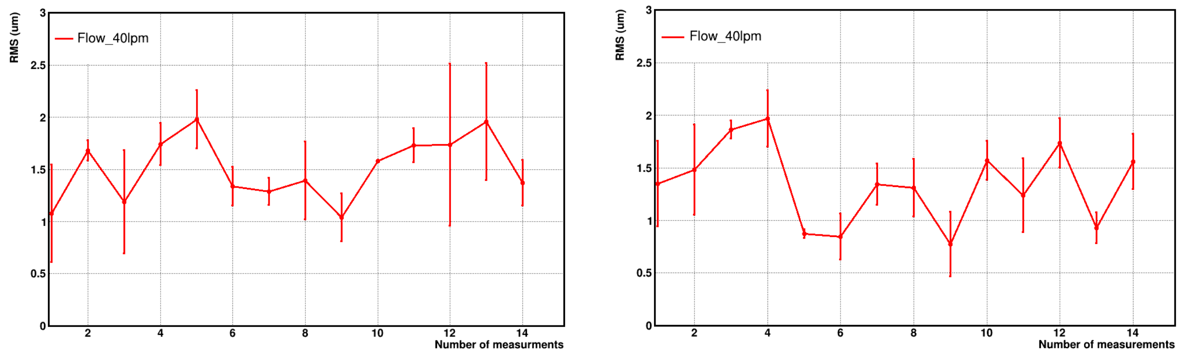

Figure 4.24: Position vs RMS plot for long-term tests for (a) sensor 3 (b) sensor -3.

4.4.2 Central ladder

The central ladder, once assembled, underwent testing to measure the vibrations caused by airflow on the sensors. In standard ladders, the perforated tube is positioned in the middle of the ladder whereas in the case of the central ladder, due to the presence of a beam pipe, the perforated tube is shifted by 2 mm, making the sensor surface on one side (closer to the tube)

more vulnerable to vibrations (see Fig. 4.25). The measurements were performed following a similar procedure as explained in the previous section. The RMS values were calculated for different airflow after subtracting the background and results are summarised in the Fig. 4.26.

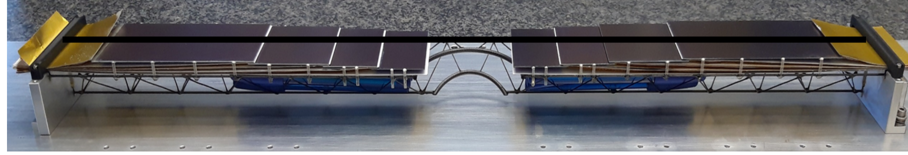

Figure 4.25: Image showing the central ladder with the shift in the perforated tube.

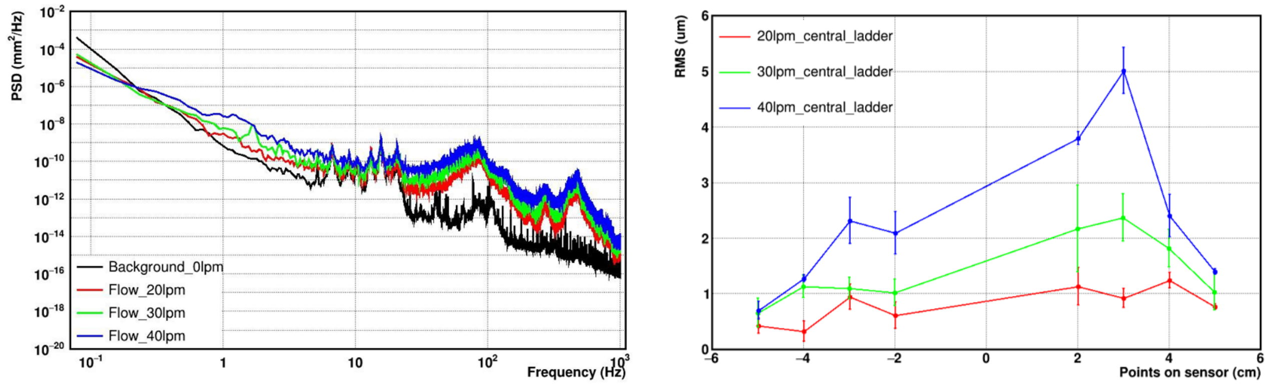

Figure 4.26: (Left) Frequency vs PSD spectra for different airflow on one of the points on the innermost sensor on the central ladder. (Right) Plot showing sensor numbers on the x-axis and their corresponding RMS values on the y-axis for all sensors on the central ladder.

The plot indicates that positioning the perforated tube closer to the sensors (rather than in the middle of the ladder) as well as the stiffness of the central ladder, leads to increased vibrations in the sensors. Despite the ladder being relatively less stiff, the amplitude of vibration for the airflow rate of 30 L/min is around 2 μm, which is considered acceptable and not very detrimental to particle tracking. However, these results are preliminary, as the structure of the central ladder is not yet finalized and the thickness of silicon wafers used was different from normal sensors. Nevertheless, these measurements provide an initial understanding of handling the central ladder and familiarize oneself with the expected vibration amplitudes. The ongoing simulations for a stiffer ladder version with improved reinforcement will be conducted, and the entire procedure will be repeated to obtain the final results.

Chapter 5

Summary

The central component of the Silicon Tracking System of the CBM experiment is the detector module which consists of a double sided silicon micro-strip sensor connected to two Front-End Boards (FEBs) via signal transmission micro-cables. This thesis investigates several key aspects necessary for the optimal performance of the modules, focusing primarily on thermal management, structural integrity and vibration stability.

As part of this thesis, the thermal performance of the detector module components, particularly the FEBs located outside the detector's acceptance region, was thoroughly investigated. The study explores the requirements for thermal interface materials (TIMs) between the FEBs and the cooling shelf to facilitate efficient heat dissipation. A thorough survey of thermally conductive adhesives was conducted, evaluating their thermal and mechanical properties through various tests. Stycast 2850FT with 23 LV catalyst was chosen as the most suitable TIM. The optimal adhesive application techniques and solutions for surface optimization were also developed to ensure reliable thermal performance. To verify the efficiency of the FEBs after TIM application, a series of thermal reliability tests were conducted, including passive, active, and power cycling tests. The results demonstrated that the FEBs remain intact down to - 25°C, beyond which the LDOs and ASICs begin to fail. These conclusions are based on tests conducted on 12 FEBs, revealing various failure modes, including mismatch in thermal expansion coefficient between the different materials and bond breakages at extremely low temperatures. These findings establish the necessary boundary conditions for the FEBs operation till the end of STS lifetime, aligning with the cooling requirements to prevent thermal runaway conditions.

Following the electrical and optical testing, the modules undergo quality inspection and are

assembled onto ultra-light carbon fiber ladders. These ladders act as support structure that defines the precise positioning of the sensor modules after the assembly. In this work, efforts have been taken towards the development of an assembly procedure that ensures easy handling and precise mounting of the modules, with deviations from its nominal position not exceeding $\pm 100\mu$m. The design, assembly processes, and quality assurance measures for these ladders are thoroughly described to maintain the structural integrity and precision. The evolution of ladder assembly methods is documented, from prototype half-ladders to fully functional standard ladders. The research also includes the investigation and procedure development for central ladder assembly, despite their current design lacks the required stiffness and requires re-design for the improved structural integrity. The ladder assembly procedure has been finalized, and series production for the STS modules and the ladders has commenced using the established procedures. So far, 24 % of the total production of modules and three ladders (out of 106) have been assembled.

To test for the structural integrity of the ladder after assembly, the impact of air cooling on sensor stability was evaluated. Sensors near the beam pipe, exposed to high radiation doses, require additional cooling achieved through direct airflow from a perforated tube. This air flow can induce vibrations in the sensors, leading to misalignment in the track reconstruction software. The study outlines experimental setups for measuring the eigenfrequency and vibration of the ladders. At the University of Oxford, a shaker table setup was used to measure the eigenfrequency of both a bare ladder glued to the bearings and an assembled ladder with sensors. Vibration analysis under air flow conditions was performed at GSI on a similar assembled ladder to compare the results with the ladder sent to the Oxford. The first eigenfrequency of a fully assembled ladder was found to be around 67 Hz, which was not excited under airflow conditions, ensuring ladder stability. Additionally, air flow at 30 L/min resulted in maximum sensor surface vibrations of approximately 1 μm, fulfilling the accuracy requirements of track-based alignment software for particle track reconstruction. Along with the standard ladder, vibrations under airflow were also measured for a prototype central ladder. Due to cut-outs in the middle, central ladders have reduced stiffness, making them more susceptible to air-induced vibrations. These measurements are performed only to get an understanding of the magnitude of vibration which was found to be around 3 μm for a ladder with cut-out of 104 mm. This magnitude of vibration is likely to change once the design of the cut out is finalised and will also depend on the cut out length.

In summary, this thesis contributes to the optimization of silicon detector modules in the STS

of CBM experiment, improving their thermal management, structural integration after assembly, and vibration stability. The conducted research determined that electronic failures in the FEBs occur below - 25°C. As higher radiation doses over time may require operating at lower temperatures, those scenarios were examined to understand potential failure modes. The ladder assembly procedure has been refined to minimize sensor misalignment, ensuring precision with each assembled ladder undergoing optical inspection. The results obtained from assembling ladders has led to the series production of standard ladders for the STS, with minor modifications anticipated for central ladders. Additionally, an optimal airflow rate of 30 L/min has been established to maintain the stability for the sensors across the beampipe, ensuring minimal vibration impact.

Appendix

A.1 Gluing procedure for FEB to the cooling shelf

After the selection of TIM, a procedure has been developed to apply the glue between FEB and cooling shelf surface using the gluing tool. The gluing technique is done in certain steps which are defined as follows:

1. The first step is the preparation of the tool to fix the bottom surface of the FEB, depending on the type of FEB to be glued first (both types have minor modifications in their holding surfaces). The tool is designed in such a way that there are space holders which provides support to the FEB surface without touching any components on the FEB as highlighted in the Fig. A.1.1 (a) and (b).

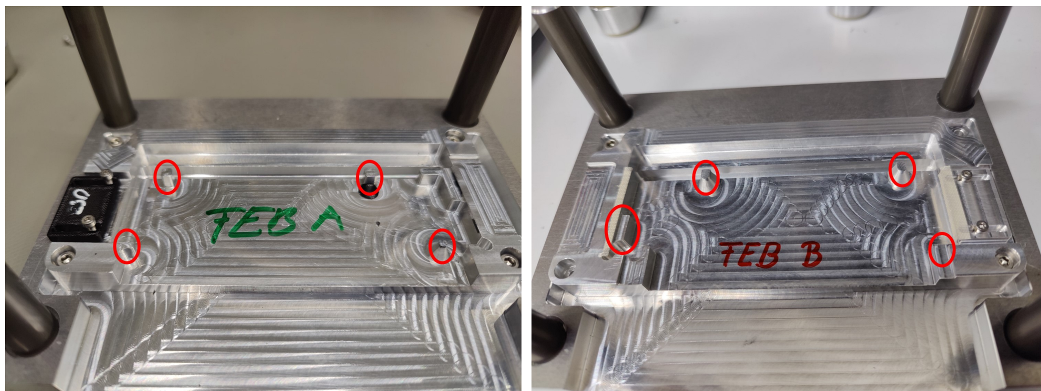

Figure A.1.1: Preparation of the tool depending on the type of FEB used (A/B). The encircled regions highlights the areas that will provide support to the FEB surface.

2. In the next step, FEB is fixed to the tool where it is important to ensure that FEB is screwed at the right position such that there is no movement of the FEB afterwards (Fig. A.1.2 (a)).

3. Once the FEB is positioned accurately, the surface of the FEB should be cleaned properly with ethanol to ensure that there are no dust particles on it.

4. Before applying the glue onto the surface, it is important to know the position where glue needs to be applied. Therefore, a stencil is used to draw the glue pattern which has been customized to get the maximum surface coverage of the FEB. The stencil is used only to draw the pattern and is removed before gluing as shown in Fig. A.1.2 (b).

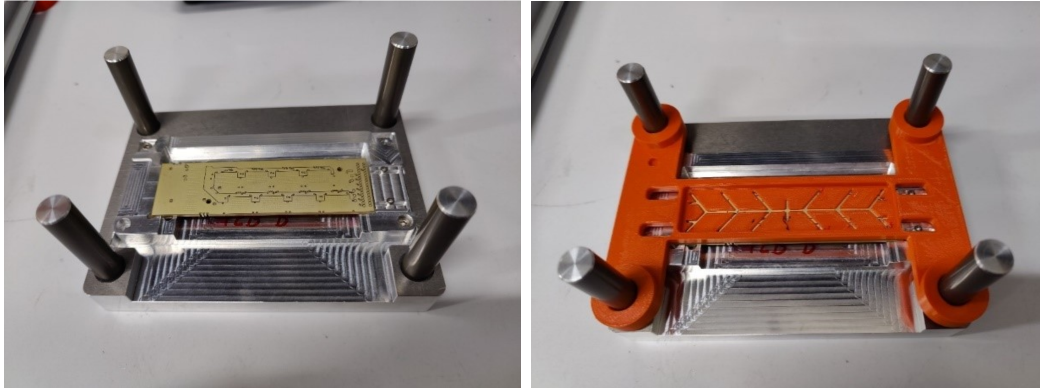

Figure A.1.2: (a) Fixation of FEB on the tool at the right position; (b) Stencil to draw the glue pattern.

5. Next step is the preparation of the glue. Stycast 2850 FT is a two-component glue where the black colored resin is mixed thoroughly before using. After the mixing, the resin is weighed into a container and 23 LV catalyst is then added to it. The mixing ratio of resin to catalyst by weight is 100:7.5 as mentioned in the data sheet. After weighing, the resin and catalyst are mixed thoroughly to get the right viscosity of the glue. During the mixing, there is a high possibility of air bubbles being trapped. To minimize the amount of trapped air during the mixing, the glue mixture is then kept in a vacuum chamber for about 5 to 6 minutes to get rid of the trapped air.

6. The glue is then transferred into a syringe and then applied on the FEB surface using a glue dispenser (Fig. A.1.3 (a)). The glue dispenser used is a specialized one which allows good control over the volume and has the possibility to use different programs to define the glue volumes [79]. For our pattern, we use four different programs with defined glue volume for each program.

7. In the next step, glue is applied to the FEB surface following the pattern drawn with the stencil using the dispenser as shown in Fig. A.1.3 (b).

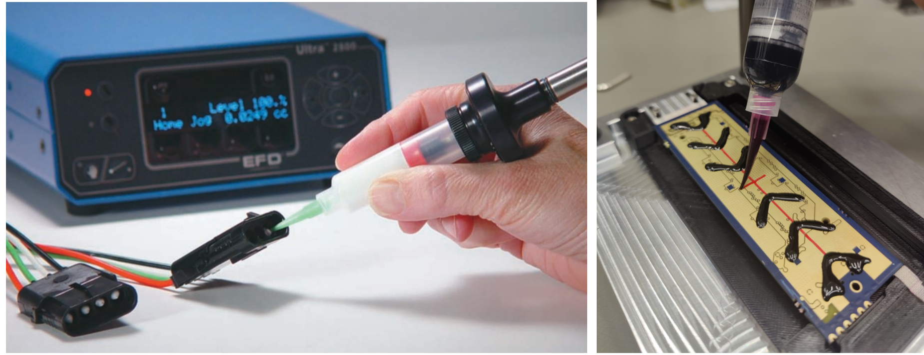

Figure A.1.3: (a) Glue dispenser to control glue volume; (b) Glue pattern using the dispenser.

8. Once the glue is applied, cooling shelf is fixed to the counter part of the tool with the screws (see Fig. A.1.4 (a)) and slowly slides down to the bottom of the tool where both surfaces of the tool touch each other (see Fig. A.1.4 (b)). The tool is designed in such a way that the thickness of the glue is pre-defined using the tool by having a constant gap of 150 μm between FEB and cooling shelf.

Figure A.1.4: (a) Fixation of cooling shelf with the screws; (b) Sliding down of screwed shelf on the FEB for gluing.

9. The setup is left untouched for about 24 hours for the glue to be cured at room temperature, followed by disassembling of the tool the next day.

10. The next step is to change the bottom surface of the tool for the assembly of the other FEB, and the same sequence of steps are followed for the gluing as can be seen in the Fig. A.1.5.

11. The setup is again left untouched for the next 24 hours before the FEBs are ready for the final testing.

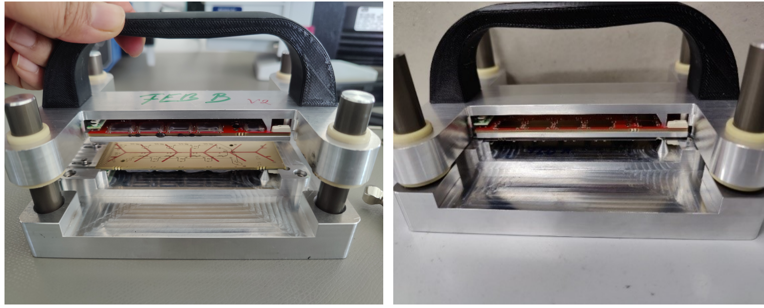

Figure A.1.5: Image showing (a) FEB A glued to one side of the cooling shelf and FEB B is attached to the bottom tool for gluing on the opposite side of the cooling shelf; (b) FEB B glued to the other side of the cooling shelf.

This procedure tells that gluing of both FEBs to cooling shelf in a module will take nearly two days, which goes well with the throughput of module production. Also, considering the glue working time, it is possible to glue more than one FEB within 45 minutes of glue working time, therefore, four tools have been prepared which allows to increase the yield of module production, as in four modules can be glued simultaneously in two days.

The steps above are demonstrated with only the FEBs without the microcables and sensors for the easiness of the procedure. But the same procedure is adopted while gluing the FEBs after the assembly of the module. Handling of the micro-cables was taken into the consideration and the nearly 1/3rd of the modules for the series production has been produced and the same gluing procedure with minor add ons has been implemented as precautions.

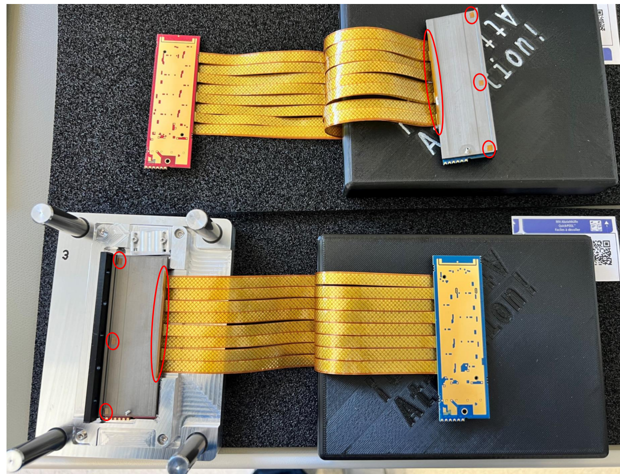

Figure A.1.6: Image shows the module handling and fixation into the gluing tool for the gluing process. The encircled areas are the kapton sheets that are applied at the edges to ensure that there is atleast a minimum gap of $120\ \mu m$ (thickness of the kapton sheet).

Table 1: Volume distribution parameters for the glue pattern

S.No.	Pattern length (in mm)	Amount of glue volume (in mL)
1	$y_1 = 13$	0.0162
2	$y_2 = 5$	0.0125
3	$x_2 = 7.5$	0.01
4	$x_1 = 15$	0.0374

A.1.1 Calculations for the glue pattern

Depending on the requirements of the glue pattern to get a maximum surface coverage, the pattern has been defined for 10 cm × 3 cm FEB surface (see Fig. A.1.7). To acquire a glue thickness of 150 μm, the total amount of volume required was 0.45 ml (10 cm × 3 cm × 0.015 cm). The glue needs to be evenly distributed across the pattern to maximise coverage, especially in the inner regions of the FEB.

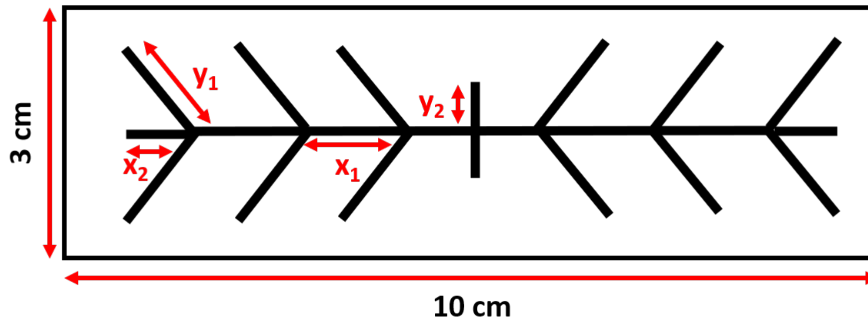

Figure A.1.7: Customised double-y pattern designed to fit the dimensions of FEBs. The glue volume of 0.45 mL is distributed along the different lines shown in the pattern to ensure full coverage.

To accomplish this, the glue pattern is divided into four different lengths and the glue volume is distributed amongst the pattern depending on the lengths. These four volumes are then programmed into the glue dispenser for the precise glue distribution. This distribution strategy ensures that the glue spreads uniformly, providing the necessary adhesion and coverage. The specifics of the volume distribution and corresponding parameters for the glue dispenser are summarized in the Table 1.

A.2 Acquisition of data using Laser Doppler Vibrometer

To establish different parameters for data acquisition, the Acquisition settings (A/D) are used. This allows the users to set various parameters, such as sampling rate, number of samples, signal range, window type and many more. The choice of the appropriate acquisition settings significantly impacts the accuracy and precision of the acquired data. The details about the parameters used for the measurements are summarized in the table.

Table 2: Summary of parameters used for data acquisition

Parameter Type	**Setting**	**Value**
General settings	Measurement mode	FFT
	Averaging	5 times (Magnitude)
Channel settings	Channel	Vibrometer, Reference 1
	Active	Yes
	Direction	+Z
	Range	10 V
	Coupling	DC
	Quantity	Velocity 20 mm/s/V Displacement 3.2 μm/V
Filter settings	Filter type	No filter
Frequency settings	Bandwidth	1 KHz
	Frequency range	0 - 1 KHz
	FFT lines	12800
	Overlap	66 %
Window settings	Window function	Hanning
Vibrometer settings	Velocity	VD-09-S 20 mm/s/V
	Displacement	DD-900-S 3.2 μm/V
	Overrun	Return to zero
	Filters	Off

References

[1] A. D. Falco (NA60+), "The Physics program of the NA60+ experiment at the CERN SPS," presented at CPOD2021. Available online: https://indico.cern.ch/event/985460/adf$_c$pod.pdf

[2] T. Ablyazimov, A. Abuhoza, R. P. Adak, et al. *Challenges in QCD matter physics – The scientific programme of the Compressed Baryonic Matter experiment at FAIR, The European Physical Journal A*, vol. 53, no. 3, 2017, DOI: http://dx.doi.org/10.1140/epja/i2017-12248-y

[3] G. Baym, T. Hatsuda, and T. Takatsuka, *From hadrons to quarks in neutron stars: A review,Reports on Progress in Physics*, vol. 81, Feb. 2018, https://iopscience.iop.org/article/10.1088/1361-6633/aaae14

[4] R. Bellwied, *Hadron formation in the deconfined matter at RHIC and LHC,* PoS BORMIO (2012), 045, DOI: 10.22323/1.160.0045.

[5] E. V. Shuryak, *What RHIC experiments and theory tell us about properties of quark-gluon plasma?,* Nucl. Phys. A 750 (2005), 64-83, DOI: 10.1016/j.nuclphysa.2004.10.022.

[6] K. Yagi, T. Hatsuda, and Y. Miake, *Quark-Gluon Plasma: From Big Bang to Little Bang,* Cambridge University Press, 2005. ISBN: 978-0521553022.

[7] A. Bazavov et al., *Chiral crossover in QCD at zero and non-zero chemical potentials,* Phys. Lett. B, vol. 795, pp. 15–21, 2019, DOI: 10.1016/j.physletb.2019.05.013.

[8] M. A. Stephanov, *QCD Phase Diagram and the Critical Point,* Prog. Theor. Phys. Suppl. **153** (2004), 139-156, DOI: 10.1143/PTPS.153.139

[9] L. Adamczyk *et al. Bulk Properties of the Medium Produced in Relativistic Heavy-Ion Collisions from the Beam Energy Scan Program,* Phys. Rev. C 96, no. 4, 044904 (2017), DOI: 10.1103/PhysRevC.96.044904

[10] D. Tlusty, *The RHIC Beam Energy Scan Phase II: Physics and Upgrades,* arXiv:1810.04767 [nucl-ex]: https://arxiv.org/abs/1810.04767.

[11] András László, *The NA61/SHINE Experiment at the CERN SPS,* Nucl. Phys. A 830.1 (2009): 559c–562c. Quark Matter 2009, DOI: 10.1016/j.nuclphysa.2009.09.047.

[12] D. Blaschke et al., *Topical issue on exploring strongly interacting matter at high densities - NICA white paper,* Eur. Phys. J. A 52, 267 (2016), DOI: 10.1140/epja/i2016-16267-x

[13] T. Galatyuk, *Future facilities for high μ_B physics, Nucl. Phys. A*, vol. 982, pp. 163–169, 2019, DOI: 10.1016/j.nuclphysa.2018.11.025.

[14] F. Gao and J. M. Pawlowski,*QCD phase structure from functional methods,* Phys. Rev. D **102**, no.3, 034027 (2020), DOI: 10.1103/PhysRevD.102.034027.

[15] H. Kolanoski and N. Wermes, *Particle Detectors: Fundamentals and Applications*, 1st edition, Oxford University Press, 2020, ISBN: 978-0-19-885836-2, https://global.oup.com/academic/product/particle-detectors-9780198858362.

[16] Spieler, Helmuth, *Semiconductor Detector Systems*, Oxford University Press, 2005. ISBN 9780198527848, DOI: https://doi.org/10.1093/acprof:oso/9780198527848.001.0001.

[17] D. Bortoletto, *How and why silicon sensors are becoming more and more intelligent?,* DOI: 10.1088/1748-0221/10/08/C08016.

[18] Alison, John, *The Road to Discovery: Detector Alignment, Electron Identification, Particle Misidentification, WW Physics, and the Discovery of the Higgs Boson*, CERN Thesis, 2012, https://cds.cern.ch/record/1536507

[19] I. Panasenko, *Development of Electrical Quality Assurance Procedures and Methods for the Silicon Tracking System of the CBM Experiment*, PhD thesis, Eberhard Karls University of Tuebingen, March 2023, https://indico.gsi.de/event/17214/contributions/70781/.

[20] C. Lippmann, *Particle identification,* Nuclear Instruments and Methods in Physics Research Section A, vol. 666, pp. 148–172, 2012. DOI: 10.1016/j.nima.2011.03.009

[21] L. Arnold, *The STAR silicon strip detector (SSD),* Nucl. Instrum. Meth. A **499** (2003), 652–658, doi:10.1016/S0168-9002(02)01963-0.

[22] W. Poonsawat *et al.*, *Stave module design and development of the new ALICE Inner Tracking System, JINST* **14** (2019) no.05, P05003. DOI: 10.1088/1748-0221/14/05/P05003.

[23] P. Martinengo, *The New Inner Tracking System of the ALICE Experiment,* presented at Quark Matter 2017, DOI: 10.1016/j.nuclphysa.2017.05.069.

[24] Mandic, I. (2023). *Design and construction of the ATLAS ITk Strip Detector*. CERN. Available online: https://cds.cern.ch/record/2884800

[25] T. Ablyazimov *et al.*, *Challenges in QCD matter physics – The scientific programme of the Compressed Baryonic Matter experiment at FAIR, Eur. Phys. J. A* **53** (2017) no.3, 60, DOI: 10.1140/epja/i2017-12248-y.

[26] B. Friman *et al.*, *The CBM Physics Book*, ISBN: 978-3-642-13292-6, https://www.cbm.gsi.de/physics/book.html.

[27] M. Teklishyn *et al.*, *From 3D to 5D tracking: SMX ASIC-based Double-Sided Micro-Strip detectors for comprehensive space, time, and energy measurements,* DOI: 10.1088/1748-0221/19/07/C07002.

[28] J. de Cuveland, D. Emschermann, *et al. Technical Design report for the online systems of the CBM experiment*, Available online: https://repository.gsi.de/record/340597

[29] Private communication with Patrick Dahm

[30] A. Rost *et al.*, *Design of Beam Monitors and T0-Counters for CBM*, CBM Progress Report 2020, pp. 141. GSI, Darmstadt, 2021, Available online: https://repository.gsi.de/record/237432

[31] P. Klaus *et al.*, *Status of the vertex detector program of the CBM experiment at FAIR, Nuclear Instruments and Methods in Physics Research Section A: Accelerators, Spectrometers, Detectors and Associated Equipment* **936** (2019), 705-706. Available online: https://doi.org/10.1016/j.nima.2018.09.092.

[32] J. M. Heuser *et al.*, *Technical Design Report for the CBM Silicon Tracking System (STS)*, GSI, Darmstadt, 2013. Available online: https://repository.gsi.de/record/54798.

[33] A. Malakhov *et al.*, *Technical Design Report for the CBM Superconducting Dipole Magnet*, GSI, Darmstadt, 2013. Available online: http://repository.gsi.de/record/109025.

[34] S. Chattopadhyay, *et al.*, *Technical Design Report for the CBM : Muon Chambers (MuCh)*, GSI, Darmstadt, 2015. Available online: https://repository.gsi.de/record/161297.

[35] C. Höhne, *et al.*, *Technical Design Report for the CBM : Ring Imaging Cherenkov Detector (RICH)*, GSI, Darmstadt, 2013. Available online: https://repository.gsi.de/record/65526

[36] C. Blume, *et al.*, *Technical Design Report for the CBM : Transition Radiation Detector (TRD)*, GSI, Darmstadt, 2018. Available online: https://repository.gsi.de/record/217478

[37] N. Herrmann, *et al.*, *Technical Design Report for the CBM : Time Of Flight (TOF)*, GSI, Darmstadt, 2014. Available online: https://repository.gsi.de/record/109024

[38] F. Guber and I. Selyuzhenkov, *et al.*, *Technical Design Report for the CBM :Projectile Spectator Detector (PSD)*, GSI, Darmstadt, 2015. Available online: https://repository.gsi.de/record/109059

[39] H. R. Schmidt, *The silicon tracking system of the CBM experiment at FAIR, Nucl. Instrum. Meth. A* **936** (2019), 630-633. DOI: 10.1016/j.nima.2018.09.094.

[40] Private communication with Oleg vasylyev.

[41] O. Bertini, *Quality grading and position mapping of the STS silicon sensors, CBM Progress Report 2021*, p. 23. Available online: https://repository.gsi.de/record/246663.

[42] R. L. Gluckstern, *Uncertainties in Track Momentum and Direction, Due to Multiple Scattering and Measurement Errors*, *Nuclear Instruments and Methods*, vol. 21, pp. 47-56, 1963. DOI: 10.1016/0029-554X(63)90347-1.

[43] Private communication with Mehul Shiroya.

[44] Hans-Günther Moser, *Silicon detector systems in high energy physics*, DOI: 10.1016/j.ppnp.2008.12.002.

[45] Manuel Gómez Marzoa, *Innovative Low-Mass Cooling Systems for the ALICE ITS Upgrade Detector at CERN*, Ph.D. thesis, CERN, 2016. Available online: CERN-THESIS-2016.pdf

[46] M.Sokolowski, *Process of Preparing and Laying Carbon Prepregs*, *Transactions on Aerospace Research*, vol. 2017, no. 1, pp. 27-34, Mar. 2017. DOI: 10.2478/tar-2017-0003.

[47] S. Das, *Misalignment effects on track reconstruction for CBM-STS*, in *CBM Progress Report 2016*, GSI, Darmstadt, 2016. Available online: CBM Progress Report 2016.pdf

[48] G. Dellacasa *ALICE technical design report of the inner tracking system (ITS), CERN-LHCC-99-12*.

[49] J. Heuser *et al.*, *A full-size prototype of the STS beam pipe: design improvement, fabrication*, *CBM Progress Report 2022*, Darmstadt: GSI, 2023. Available online: CBM Progress Report 2022.pdf

[50] M. Shiroya, *Optical Inspection of Micro-strips Silicon Sensors for the Compressed Baryonic Matter Experiment at FAIR*, Masters dissertation 2021, Goethe U., Frankfurt (main), 2021. Available online: M. Shiroya, Masters dissertation 2021.pdf

[51] I. Panasenko *Development of Electrical Quality Assurance Procedures and Methods for the Silicon Tracking System of the CBM Experiment*, Ph.D. dissertation, University of Tübingen, 2023. Available online: I. Panasenko, Ph.D. dissertation 2023.pdf

[52] O. Rodríguez *Characterization and commissioning of the front-end electronics of the Silicon Tracking System of the CBM experiment*, Ph.D. dissertation, Goethe U., Frankfurt (main), 2023. Available online: O. Rodríguez, Ph.D. dissertation 2023.pdf

[53] The FAIR GSI accelerator facility. Available online: `https://www.gsi.de/en/research/accelerators/fair/the_machine`

[54] CAF4 Datasheet. Available online: Datasheet for the CAF4

[55] V. Blobel, C. Kleinwort, *A New Method for the High-Precision Alignment of Track Detectors*. Available online: `https://arxiv.org/abs/hep-ex/0208021`

[56] F. Y. Shih, *Image Processing and Pattern Recognition: Fundamentals and Techniques*. ISBN: 978-0-470-40461-4. Available online: https://www.wiley.com/en-us

[57] E. Lavrik, U.Frankenfeld, S.Mehta, *et al.*, *High-Precision Contactless Optical 3D-Metrology of Silicon Sensors*. DOI: j.nima.2019.04.039

[58] D. Ramírez, A. Toia, *Performance of the mSTS detector during the mCBM beam campaign 2021*, CBM Progress Report 2021, GSI Darmstadt, 2022, p. 239. Available online: CBM Progress Report 2022.pdf

[59] A. Rodríguez Rodríguez, *Functional characterization of modules for the Silicon Tracking System of the CBM experiment*, vol. 1041, 2023. DOI: j.nima.2023.168813

[60] M. Shiroya, *Update on the simulation geometry for the Silicon Tracking System,* CBM Progress Report 2021, GSI Darmstadt, 2022, p. 59. [Online]. Available online: https://repository.gsi.de/record/336786.

[61] J. Heuser *et al.*, *Production Readiness Review for the STS Carbon Fiber Ladders*, Technical Note CBM-TN-19006, GSI, 2019. Available online: https://repository.gsi.de/record/22198

[62] E. Lavrik, et al., *Development of quality assurance procedures and methods for the CBM Silicon Tracking System*, PhD thesis, Eberhard Karls University of Tuebingen, November 2017, https://cbm-wiki.gsi.de/bin/view/Public/Thesis2017.

[63] S. Das *et al.*, *Track Based Alignment Procedure for CBM-STS Using Millepede II*, CBM Progress Report 2017, GSI Darmstadt, 2017. Available online: https://repository.gsi.de/record/209729

[64] *Datasheet for Kryo 51*. Available online: https://www.lauda.de/en/kryo-51.

[65] S. Dinesh Ram, *et al.*, *Fatigue strength of copper and mild steel single lap joints bonded with epoxy-alumina nano composite adhesive*, Journal of Physics: Conference Series **1248** (2024) 012091.

[66] P. Gorbounov, *et al.*, *NOVEC Fluids Qualification Report*, Technical Report CERN-ACC-2017-0001, CERN, Geneva, 2017. Available online: https://cds.cern.ch/record/2288320

[67] C. Simons *et al.*, *The assembly of the STS-sensor-modules at GSI*, CBM-TN-18005. Available online: Technical note 2018.pdf.

[68] S. Sequeira Tavares *et al.*, *Aluminum Alloy Production for the Reinforcement of the CMS Conductor*. DOI: 10.1109/TASC.2002.1018435.

[69] Henrik Forsback *et al.*, *Reliability of Thermal Interface Materials for Power Semiconductor Devices*, Masters thesis, Aalto University School of Electrical Engineering. Available online: https://core.ac.uk/80723497.pdf.

[70] *Silicone gel interface material*. Available online: https://de.rs-online.com/GCS-060-S.

[71] S. de Capua *et al.*, *Shear and Thermal Testing of Adhesives for VELO Upgrade,* LHCb-PUB-2016-026, CERN, 2016. Available online: https://cds.cern.ch/record/2229009.pdf.

[72] M. Chertok *et al.*, *Thermal and tensile strength testing of thermally-conductive adhesives and carbon foam,*. DOI: https://dx.doi.org/10.1088.

[73] *Data-sheet for the adhesive Stycast 2850 FT with 23LV catalyst.* Available online: https://next.henkel-adhesives.com/LOCTITE-STYCAST-2850FT-CAT-23LV.pdf.

[74] *Data-sheet for the adhesive Dowsil SE 4445.* Available online: https://www.ellsworth.com//dow-se-4445-cv-thermally-conductive-gel.

[75] *Data-sheet for the adhesive Bergquisit EA1805.* Available online: https://eu.mouser.com/Bergquist.

[76] *Data-sheet for the climatic chamber, Binder MK-56* , Available online: https://www.binder-world.com/mk-56.

[77] James J. Licari, Dale W. Swanson *Adhesives Technology for Electronic Applications Materials, Processing, Reliability- William*, ISBN: 9781437778892.

[78] *Data-sheet for Instron machine.* Available online: https://www.instron.com//manuals/5940.pdf.

[79] Volumendosiergerät Ultimus™ IV, Technical Data Sheet, Available online: https://www.weidinger.eu/ultimusiv.pdf.

[80] LHCb collaboration, *LHCb VELO Upgrade Technical Design Report, CERN, Geneve, Switzerland, 2013.* Available online: https://cds.cern.ch/LHCB-TDR-013.pdf.

[81] Michael D. Capili, *Optimization of Dispensing Parameter to Speed up the Die Attach Throughput.* DOI: https://dx.doi.org/10.9734/JERR/2020/v18i117201.

[82] Mark Lee *et al.*, *The squeezing process of complex epoxy patterns in the die-attaching of large IC-chip.* DOI: https://dx.doi.org/10.1109/EMAP.2006.4430590.

[83] Alan Lewis and Alec Babiarz, *Conductive Adhesive Dispensing Process Considerations*, Asymtek, Nordson Electronic Business Group. Available online: https://citeseerx.ist.psu.edu/.

[84] J.Lee *et al.*, *Thermal conductivity of anodized aluminum oxide layer: The effect of electrolyte and temperature* DOI: https://doi.org/10.1016/j.matchemphys.2013.05.058.

[85] H.S. Chung *et al.*, *Reliability of power electronic converter systems* Available online: ISBN: 978-1-84919-902-5, DOI: https://doi.org/10.1109/MIE.2016.2590783

[86] A.Rodriguez *The CBM Silicon Tracking System front-end electronics : from bare ASIC to detector characterization, commissioning and performance*, PhD. dissertation, Goethe u.Frankfurt (main), 2020. Available online: http://publikationen.ub.uni-frankfurt.de.

[87] Q.P. Minh *et al.*, *Milling Microwave Printed Circuit Boards With Inconsistent Flatness With Safety Function* http://www.ijstr.org/Milling-Microwave-Printed-Circuit-Boards.pdf.

[88] *Solder Mask Handbook*, IPC-HDBK-840, Developed by the Solder Mask Handbook Task Group (5-33d) of the Cleaning and Coating Committee (5-30) of IPC. Available online: https://www.ipc.org/TOC/IPC-HDBK-840.pdf.

[89] S. Kramer, *Thermal Capabilities of Solder Masks and Other Coating Materials – How High Can We Go*. Available online: https://smtnet.com/library/solder-mask-thermal-capabilities.pdf.

[90] Private communication with Lady Maryann Collazo Sanchez and Maksym Teklishyn.

[91] M. Bajdel, *Development of the detector control system and instrumentation for the Silicon Tracking System in the Compressed Baryonic Matter experiment*, PhD. dissertation, Goethe u.Frankfurt (main), 2023. Available online: https://publikationen.ub.uni-frankfurt.de/marcel+bajdel/docId/74602.

[92] P. Larionov *Systematic irradiation studies and Quality Assurance of silicon strip sensors for the CBM Silicon Tracking System*, PhD. dissertation, Goethe u.Frankfurt (main), 2016. Available online: https://cbm-wiki.gsi.de/Thesis2016.

[93] I. Momot *Characterization and radiation hardness studies of the silicon microstrip sensors for the CBM experiment*, PhD. dissertation, Goethe u.Frankfurt (main), 2019. Available online: https://publikationen.ub.uni-frankfurt.de/docId/52021.

[94] O. Bertini *et al.*, *Basic electrical inspection of silicon microstrip sensors for the STS*, CBM Progress Report, 2020, p. 16, GSI Darmstadt. Available online: https://repository.gsi.de/record/237432.

[95] A. Chilingarov *Temperature dependence of the current generated in Si bulk.* Journal of Instrumentation, 8(10):P10003, Oct 2013. DOI: https://doi.org/10.1088/1748-0221/8/10/P10003.

[96] H.Malygina, *Hit reconstruction for the Silicon Tracking System of the CBM experiment*, PhD. dissertation, Goethe u.Frankfurt (main), 2018. Available online: https://publikationen.ub.uni-frankfurt.de/docId/46401.

[97] Private communication with Iouri Vassiliev.

[98] V. Akishian and I.Kisel, *Parallel 4-Dimensional Cellular Automaton Track Finder for the CBM Experiment*. DOI: https://doi.org/10.1088/1742-6596/762/1/012047.

[99] I.Kisel and S. Gorbunov, *Event Reconstruction in the CBM Experiment. Nuclear Instruments and Methods in Physics Research Section A: Accelerators, Spectrometers, Detectors and Associated Equipment*, vol. 566, no. 1, pp. 85-88, 2006. DOI: https://doi.org/10.1016/j.nima.2006.05.040.

[100] Private communication with K.Agarwal.

[101] V. Tesař *et al.*, *Vortex Rings and Jets: Recent Developments in Near-Field Dynamics*, Daniel T. H. New and Simon C. M. Yu. (Eds.), Singapore: Springer Singapore, 2015, pp. 191–231. DOI: https://doi.org/10.1007/978-981-287-396-5_6.

[102] N. Zuckerman, *et al.*, *Jet Impingement Heat Transfer: Physics, Correlations, and Numerical Modeling* in *Advances in Heat Transfer*, G. A. Greene, J. P. Hartnett, A. Bar-Cohen, and Y. I. Cho (Eds.), Elsevier, vol. 39, pp. 565-631, 2006. DOI: https://doi.org/10.1016/S0065-2717(06)39006-5.

[103] M. A. Wahab, *Dynamics and Vibration : An introduction*, 1st ed., John Wiley & Sons, 2008. ISBN: 978-0-470-72300-5.

[104] Theory manual for polytec scanning vibrometer, PSV theory, 41088-Man-Vib-PSV-Theorie-0515-11. Available online: https://pearl-hifi.com/Polytec Software Manuals/PSV 400 Theory.pdf.

[105] ICM Composites GmbH, "Company website,". Available online: `https://icm-composites.de/`. [Accessed: 13-Aug-2024].

[106] M. Singla, *The Silicon Tracking System of the CBM experiment at FAIR- Development of microstrip sensors and signal transmission lines for a low-mass, low-noise system*, PhD. dissertation, Goethe u.Frankfurt (main), 2014. Available online: http://publikationen.ub.uni-frankfurt.de/msingla-thesis.pdf. [Accessed: 13-Aug-2024].

[107] Advanced European Infrastructures for Detectors (AIDA) at Accelerators, EU Horizon 2020 Grant Agreement no. 654168. Available online: https://aida2020.web.cern.ch.

[108] A. Nomerotski *et al.* [PLUME], *PLUME collaboration: Ultra-light ladders for linear collider vertex detector*, Nucl. Instrum. Meth. A **650** (2011), 208-212. DOI: https://doi.org/10.1016/j.nima.2010.12.083.

[109] Newport Corporation, *The Need for Vibration Isolated Rigid Support Structures*. Available online: https://www.newport.com/the-need-for-vibration-isolated-rigid-support-structures. [Accessed: 25-Jan-2024].

[110] J. Thaufelder *et al.*, *First Results from the STS Thermal Demonstrator with Pilot Cooling Plants*, Technical note 2023, GSI Darmstadt. Available online: https://indico.gsi.de/event/18698/.

[111] K.Agarwal thesis in the preparation titled "Thermal management of the Silicon Tracking System of the CBM-FAIR experiment".

[112] Rothberg, S.J *et al.*, *An international review of laser Doppler vibrometry: Making light work of vibration measurement*, *Optics and Lasers in Engineering*, vol. 99, pp. 11-22, 2017. DOI: https://doi.org/10.1016/j.optlaseng.2016.10.023.

[113] G. F. Alfrey, *The laser doppler technique*, *Physics Bulletin*, vol. 31. DOI: https://dx.doi.org/10.1088/0031-9112/31/9/045.

[114] Carmen L. McKnight, *VIBRATORY RESPONSE OF DRY HUMAN SKULLS*, M.A.Sc., Dalhousie University, Halifax, Nova Scotia, March 2012. Available online: https://dalspace.library.dal.ca/McKnight_Carmen_MASc.

[115] User manual for ploytec laser doppler vibrometer with OFV 5000 controller. Available online: https://www.scribd.com/document/539352229/Polytec-Vibrometer-Controller-OFV-5000.

[116] Product Brochure for Polytec OFV-5000 Modular Vibrometer, Non-Contact Vibration Measurement. Available online: https://www.polytecstore.fr/documents/ofv-5000.pdf.

[117] Data sheet for Polytec Junction box VIB-E-400, Non contact measurements. Available online: https://www.acoutronic.se/pdf/vibration/Polytec Datasheet VDD.pdf.

[118] Data sheet for Polytec Laser sensor head OFV-525, Non contact measurements. Available online: https://www.acoutronic.se/pdf/vibration/Polytec Datasheet OFV-525.pdf.

[119] Manual for the Vibsoft software from Polytec company. Available online: https://www.polytec.com/de/vibrometrie/produkte/software/vibsoft.

[120] Data sheet for the Vibsoft data acquisition software. Available online: https://www.polytecstore.fr/vibsoft.pdf.

[121] Narayan P Subramaniyam, *Factors that Impact Power Spectral Density Estimation*, Sapiens lab 2018. Available online: https://sapienlabs.org/lab-talk/factors-that-impact-power-spectrum-density-estimation.

[122] Otis M. Solomon, Jr., *PSD Computations Using Welch's Method*, SAND91-1533, UC-706, Unlimited Release, Printed December 1991. https://www.osti.gov/servlets/purl/5688766.

[123] Mostafa Hasanian *et al.*, *Assessment of Reflective Tapes on the Accuracy of Displacement Measurement in Laser Doppler-vibrometry*, *AIP Conference Proceedings*, vol. 1806, pp. 050006, Feb. 2017. DOI: https://doi.org/10.1063/1.4974600.

[124] K. Agusanto *et al.*, *Effect of oblique retroreflection from a vibrating mirror on laser Doppler shift*, textitAppl. Opt., vol. 58, no. 9, pp. 2277–2283, Mar. 2019. Optica Publishing Group. DOI:https://doi.org/10.1364/AO.58.002277.

[125] Bruel and Kjaer *et al.*,*Measuring Vibration*, Technical Documentation BR 0094, 1998. Available online: https://www.bksv.com/media/doc/br0094.pdf.

List of Figures

1.1 Schematic of the phase diagram of strongly interacting matter, in the Temperature and Baryon chemical potential region [1]. 2

1.2 Comparison of interaction rate as a function of center-of-mass energy for the existing and planned heavy-ion experiments [13, 2]. 4

1.3 Increase in the number of read-out channels with the change in the area of the strip in silicon for different experiments has been shown. The different experiments are shown with circle and CBM experiment, focus of the thesis has been shown with star (Figure is taken from [19]). 5

1.4 Schematic diagrams showing the support structures for different detector systems. (a) shows the staves in inner and outer barrel of ALICE ITS, [22] [23] (b) details the stave design of ATLAS ITk [24], (c) outlines the ladder configuration of STAR SSD, [21] and (d) presents the integration of silicon sensors on the carbon fiber ladder for CBM STS. 8

1.5 Overview of the FAIR experiment facility [53], where blue and red lines shows the existing and planned facilities. SIS100 will provide beam to the CBM experiment. 9

1.6 The experimental setup of CBM experiment at FAIR [29], with STS and MVD located inside the dipole magnet. 10

1.7 (a) STS tracking stations with C-frames equipped with the cooling plate are shown. (b) Conceptual design of STS with silicon sensors (in blue, green, and red color) mounted on the ladders, assembled on the mechanical C-frames. The Front-End Electronics is located outside the periphery of the detector [40]. . . . 12

1.8 (a) Variants of Silicon sensors with width of sensor equals 6.2 cm and length varies from 2.2 cm, 4.2 cm, 6.2 cm and 12.4 cm distributed over the stations. (b) STS module after connecting to its components. The module afterwards is covered with the shielding layer and the FEBs are glued to the cooling shelves. . 13

1.9 Illustration of the conceptual design for the C-frame, which shows four mounted ladders in the front. On the right side of the C-frame, the read-out and power electronics are integrated, allowing for efficient signal processing and power distribution. A perforated tube, running along the entire length of the central ladders, is positioned to channel cold air directly onto the sensor surfaces. 14

2.1 Image of an STS module (top) before and (bottom) after connecting the shielding layers of the microcables ([59]). 18

2.2 (Left) Image of FEB8_A (Blue) and FEB8_B (red) that connects the p-side and n-side of the sensor, (Right) Image of an asymmetric T-shaped cooling shelf, having length equal to that of FEBs. 19

2.3 Sketch showing the spacing between two FEBs (shown in blue and red), where the gap is filled with the cooling shelf and TIM. 22

2.4 Thermal dummy FEBs with DS-18 temperature sensors glued on the copper meanders. Three sensors have been positioned: two to monitor the temperature of individual ASIC rows, and the third to measure the temperature of the LDO regulators. FEBs were glued to the cooling shelf with different glue candidates (Dow-corning in this image) and finally mounted on to a cooling plate. 26

2.5 Plot showing single thermal cycle from +40 °C to -15 °C for one thermal dummy FEB where different colors represent the temperature variation in ASICs, LDOs with respect to the cooling block. 27

2.6 Plot showing the variation of temperature with 25 cycles for different glues. . . . 27

2.7 Wettability of adhesives with respect to contact angle [77]. 29

2.8 Side view of the sample for lap shear test: Aluminum and copper with overlapping region covered by different adhesives aiming for a thickness of 0.015 cm. . . 29

2.9 Front-view of Instron 5940 testing machine to perform the lap shear test. At the bottom grip, the aluminum sheet is clamped and the copper sheet is fixed on the top grip which is pulled at 180° until the surfaces are separated or maximum limit of the software is reached. 30

2.10 Graph representing a single stycast sample before the thermal cycling, showing load plotted against the sample extension. 31

2.11 The glue samples (left to right) Stycast 2850FT with 23 LV catalyst, Dowsil SE4445, and Bergquist EA1805, showing the surface coverage after the 24 hours of curing time. 34

2.12 Sketch showing the important parameters for thermal cycling testing plotted between temperature and time. 35

2.13 Thermal cycling plot to test the stycast interface at extreme temperature for the two thermal dummy FEBs glued to the cooling shelf. The image shows the temperature difference between the cooling block and LDOs at +20 °C (ΔT_{max-1}) and -30 °C (ΔT_{max-2}) for both the FEBs. 36

2.14 Double Y pattern is used often to cover rectangular surfaces, where die represents the surface to be covered, i.e., rectangle in this case. 38

2.15 Double Y pattern pattern using Stycast was applied on a plexiglass sheet. (Left) Image of the glue when it was applied and the surface was covered with another plexiglass sheet. (Right) Image of the glue dispersion after 24 hours. 38

2.16 Customised double-y pattern designed to achieve complete surface adhesion, ensuring precise glue volume along each line. Specifically tailored to fit the dimensions of FEBs, the glue volume of 0.45 ml is distributed along the different lines shown in the pattern with the lengths of $x_1 = 15$ mm, $x_2 = 7.5$ mm, $y_1 = 13$ mm, $y_2 = 5$ mm to ensure full coverage. Detailed explanations of this customization process and volume distribution strategy are available in the appendix A.1. . . . 39

2.17 Illustrating the transformation of glue patterns over a 24-hours, with snapshots taken at different intervals: (a) immediately after application at 0 hours, (b) 6 hours post-application, (c) spread after 12 hours, and (d) the final spread after 24 hours. After the glue's application and the subsequent placement of plexiglass, the progression occurs naturally, without any external force. The evolution from the initial state through to the final observation demonstrates the glue's capillary action, highlighting a gradual increase in surface coverage. 40

2.18 Left image shows the surface coverage, where many places are still not covered thoroughly, indicating issues with the accuracy of glue dispensing. The right image shows the presence of numerous air bubbles, which can occur during the manual mounting of the plexiglass sheet. This highlights the significant risk of mis-positioning the FEBs on the shelf, potentially resulting in trapped air. . . . 40

2.19 Procedure for gluing FEBs to a cooling shelf a) The FEB is positioned onto the gluing tool, depending on the type of FEB (A or B), the appropriate tool is chosen, b) To ensure that the glue pattern is as per the description, a stencil is used which helps in achieving accurate placement of the adhesive on the FEB surface, c) The glue is deposited onto the surface of the FEB using a glue dispenser aiming for an even layer of glue, d) The cooling shelf after fixing to the tool is smoothly slid down onto the surface of the FEB. 42

2.20 The image highlights the final step of the FEB to shelf gluing, showing the steps involved in the process showing, (left) Front view (Right) Back view. The base of the tool holds the FEB to be glued, and in the middle is a removable stencil used to draw the glue pattern. The top part of the tool holds a cooling shelf with the FEB glued to one side. 43

2.21 Current vs Voltage characteristics for samples prepared for testing Stycast 2850FT (23 LV) as TIM for the FEBs glued to cooling shelves. The dashed line indicates the threshold for acceptance and the sample referred to as FEB_2 and FEB_3 shows a larger leakage current indicating the loss of electric isolation. 43

2.22 Illustration of backplane of FEB, showing an incomplete surface coverage, despite using a well-defined glue application procedure. The encircled areas show the surfaces without glue when the FEB was detached from the shelf. 44

2.23 Optical inspection of FEB to measure the non-flatness in the surface of the FEB. On the left, the top surface of the FEB is shown as observed after the inspection, highlighting the surface irregularities. The right side of the image shows a view of the bottom surface, providing a complete analysis of the FEB's surface condition from both top and bottom perspectives, following the optical inspection. 45

2.24 Deviation in non-flatness of the FEB surface from its nominal thickness of 3 mm. 45

2.25 Optical inspection of the non-flatness of the surface of the cooling shelf where, the left image shows the top surface, and the right image shows the bottom surface. 46

2.26 Deviation in non-flatness of the cooling shelf surface from its nominal thickness of 2.7 mm. 46

2.27 Deviation in the surface of FEB and cooling shelf from the nominal thickness. The non-flatness in the middle region of FEBs shows the possibility of having less glue, leading to unintended contact between the surfaces. 47

2.28 Drawing of one cooling shelf with the numbers marked show the different points measured for 20 shelves 48

2.29 Mechanical inspection of 20 samples of cooling shelves. 49

2.30 Thickness of the cooling shelf with anodization layer introduced into the thickness of the cooling shelf, where t_p denotes to the original thickness of the cooling shelf (2.7 mm), t_a denotes the anodization layer (50 μm) and t_s denotes the final thickness of the cooling shelf after the anodization. 49

2.31 Thermal FEA simulations under nominal power dissipation showing the temperature distribution on the FEBs glued to the cooling shelf (left) and glued to the anodized cooling shelf (right). 50

2.32 Position of solder stop mask on the bottom surface of the PCB (FEB8-2) with black frame and six single points. The solder mask used is 2 mm wide and the thickness of the solder mask and the single points was 35 μm. 51

2.33 Thermal FEA simulations under nominal power dissipation showing the temperature distribution on the FEBs with solder mask glued to anodized cooling shelf. 52

2.34 Sketch of the TIM gluing with an additional layer of anodization on the aluminum cooling shelf and solder mask on the surfaces of the FEBs. 53

2.35 Top left image shows the FEB with the solder mask with an anodized cooling shelf. The bottom left image shows the FEB with the mask clamped to the anodized aluminum shelf, prepared for the testing. On the right is the graph that shows the Current vs Voltage variation for the clamped samples. 53

2.36 (Left) FEB with the solder mask glued to the anodized aluminum shelf, prepared for the testing. (Right) Graph showing Current vs Voltage variation for the glued samples. 54

2.37 Bathtub curve is a graphical representation of the failure rate behavior of TIM over time, starting with an initial high failure rate due to early defects, followed by a period of stable, low failure rates during normal operation, and ending with an increased failure rate as the material degrades. This model helps predict the longevity and reliability of TIMs throughout their life-cycle. 56

2.38 Schematic of the components to be thermally cycled, illustrating the FEB mounted on the cooling shelf with TIM. The sketch shows the front side view of the FEB, highlighting a single row of ASICs and a single LDO, with all the components on the LDO marked explicitly. Similar component labels for the ASICs are omitted for simplicity. 58

2.39 The schematic shows the Temperature versus Time plotted for passive cycling, setting -20 °C and +20 °C as the low and high-temperature extremes respectively. Each cycle indicates a rise to a high temperature and a fall to a lower one, with horizontal lines representing phases where the temperature is kept constant. The thick lines show the temperature of the coolant, while dotted lines denote the FEB's temperature, measured once before the cycling and subsequently after every 50 cycles. The height of the temperature rise is random and will depend on the object under thermal cycling. 59

2.40 (a) The schematic shows the Temperature versus Time plotted for active cycling, setting -20 °C and +20 °C as the low and high-temperature extremes respectively. (b) Temperature profile for active cycling for a defined time interval, showing the change in the ASIC temperature with respect to the Lauda chiller and the climatic chamber. 61

2.41 (a) Temperature sensors positioned on different locations on the cooling shelf, (b) Temperature profile during active cycling for a defined time interval, showing the variation of temperature monitored with sensors with respect to the Lauda chiller. 62

2.42 The schematic shows the Temperature versus Time plotted for power cycling, setting -20 °C and +20 °C as the low and high-temperature extremes respectively. 63

2.43 Temperature profile for a Power cycling for a defined time interval showing the change of ASIC temperature with respect to Lauda chiller and Binder climatic chamber. The time interval t_1= 5 minutes when the FEBs are powered off and t_2= 20 minutes when the FEBs are powered on with the shaded area shadowed area showing the fluctuations in the temperature values. 64

2.44 Flow chart showing the division of the FEBs into two sets of measurements, where GT refers to Glob-top material and TIM refers to the Thermal Interface material. 65

2.45 During the power cycling of FEBs at T= -30 °C, (a) Current consumed by 1.8V and 1.2V LDO regulators, (b) Temperature change in the chosen ASIC of one of the FEBs. 68

2.46 Zoomed-in image showing the air bubble between bonds of the LDO and the glob-top. 69

2.47 The schematic shows the Temperature versus Time plotted for updated power cycling, setting -20°C and +20°C as the low and high-temperature extremes respectively. 70

3.1 Material budget simulation for station 7 (last station) of STS. 74

3.2 (a) Hub for winding fiber on carbon tubes – core with side pieces, (b) CF winding on hub (c) Rotation device for winding the cores. 76

3.3 Prototypes of carbon fiber ladders after manufacturing. 77

3.4 Computer-Aided Design (CAD) drawing of different ladder variants. 77

3.5 Prototype of different ladder types, including a standard ladder and two central ladders with different-sized openings in the middle for the beam pipe, to be tested optically for stiffness. 78

3.6 Central ladder fixed on support for optical inspection with a load equivalent to the weight of sensors and micro-cables. 78

3.7 Plots showing the deviation in ladder structure under load in (a) z direction (b) y direction. SL denotes the standard ladder and CL represents the Central ladder with smaller and larger cut-outs 79

3.8 (Left) CAD drawing of the fixed bearing with all the components labeled, (Right) Fixed bearing holding the edges of the ladder from one side. 81

3.9 (Left) CAD drawing of the floating bearing with all the components labeled, (Right) Floating bearing holding the edges of the ladder from one side. 82

3.10 (left) Carbon-fiber L-shaped support structures used for the sensor mounting, referred to as "L-legs", (Right) Side and front view of the L-legs, including dimensional details. 83

3.11 STS ladder, once cut into the required shape, is glued to both the bearings, with a fixed bearing positioned on the left and a floating bearing on the right side. . . 84

3.12 Sensor variants showing the positioning of L-legs from the sensor edge. 85

3.13 (Left) L-leg fixture mounted on the rails, fixed to the positioning blocks, and (Right) L-legs glued onto the ladder after the curing of glue. 86

3.14 (Left) CAD drawing of the module holding tool where positioning of sensors (followed by micro-cables and FEBs) is defined by the edges of the tool. (Right) Image illustrating the two key steps: applying glue to the top L-leg surface and transferring the module from the holding tool to the ladder for final gluing. . . . 87

3.15 Module fixed under vacuum and mounted on the positioning blocks of the ladder holding baseplate: (Left) Front view and (Right) Side view. 87

3.16 Image of the setup showing granite table with X, Y, and Z motor stages, used to measure the position of the sensors mounted on the ladder as well as the bending of the bare ladders under load. 88

3.17 (top) Image of first half ladder assembled with non-functional modules. (Bottom left) Coarse image of the alignment mark on the sensor, (bottom middle) fine image of the alignment mark after auto-focusing, (bottom right) fine search of the blind spots as reference mark on the ladder bearing blocks mounted on the base-plate. 89

3.18 Optical inspection of sensor surface after assembly on half ladder, (left) showing the staggered geometry, (right) showing sensor scan after removing the sensor gap of 1 mm. 91

3.19 CAD drawing of the modules mounted on two stations of mSTS. 92

3.20 ENC plot for different channels of a module is plotted, (a) after the module was assembled, (b) after the module was mounted on the ladder. 92

3.21 Image shows the fixed and floating bearing blocks used for mounting a ladder. The bearing blocks in the red box (top) represent the new design, featuring improvements in precision and stability. The bearing blocks in the blue box (bottom) show the older design, highlighting the structural differences between the two versions. 94

3.22 Image showing front and side view of two ladders showing the overlapping parameters between the two sensors on the same ladder as well as the sensors on different ladders. 94

3.23 (Top) Image of the ladder assembled with the L-legs glued, (Bottom) Optical inspection of L-legs after gluing on the ladder where the dotted horizontal line defines the nominal position. 96

3.24 (Top) STS ladder assembled with 10 non-functional modules i.e., modules with sensors and micro-cables with the shielding without any FEBs, (Bottom) Optically inspected surface of sensors. 97

3.25 Deviation in Z from the nominal position, (Left) in the sensors mounted on the ladder, (Right) in the tools used to mount the modules on the ladder. 98

3.26 Assembly of a prototype of the central ladder using a specifically designed tool to support the cut out in the central ladder and gauge blocks to avoid sagging in the ladder during the assembly. 99

3.27 Optical inspection of the L-legs glued to the central ladder showing the deviation in Z from the nominal position. 100

3.28 Image of the central ladder after the assembly of eight non-functional modules. . 100

3.29 Image of optical inspection of central ladder after assembly, (left) with gauge blocks, (b) without gauge blocks underneath the ladder. 100

4.1 FLUKA Simulations of Non-Ionizing Energy Loss (NIEL) distribution for STS Station-8 positioned 100 cm downstream from the target, with overlaid layout of Silicon sensors highlighting most irradiated Sensors. Calculations are based on CBM's Hadron setup (11 AGeV Au+Au at 10 MHz) after 1 month of irradiation [94]. 103

4.2 (a) Top view of the STS ladder assembled on the C-frame with perforated tubes mounted on adjacent C-frames, highlighted region shows the inner region where sensors need active cooling (b) CF perforated tube with the holes to blow the air. 106

4.3 Measurement of airflow velocity across all the holes of perforated tubes at two different flow rates (measured in liter per minute), when air was blown from both ends of the tube. The black line represents the 30 L/min flow rate, while the red line represents the 40 L/min flow rate. 107

4.4 Thermal runaway plot showcasing the power density variation with sensor temperature for the two fluence scenarios, after 10 years and after EOL (Plot is taken from [100]). 108

4.5 Image of STS ladder assembled with 10 non-operational modules prepared for the eigenfrequency tests and analysis at the University of Oxford. 113

4.6 Plots showing the data from the accelerometers placed at the left and right end of the shaker table. Both the accelerometers show the rocking mode at 42 Hz. . 113

4.7 Top image: Bare ladder mounted on the shaker table with 4 capacitive sensors, bottom left: capacitive sensor positioned close to fixed bearing, bottom right: capacitive sensor positioned close to floating bearing. 114

4.8 The RMS vs frequency plot of middle sensor's spectrum after subtracting the table measurements. 115

4.9 (Left) Closer view of the ladder with weights mounted underneath capacitive sensors, (Right) Frequency vs RMS plot showing the spectra for both the middle sensors after the subtraction of measurements from the table. 115

4.10 (Left) Top view of the fully assembled ladder mounted on the shaker table, (Right) closer view of the capacitive sensor mounted close to the surface of silicon. 116

4.11 Frequency vs RMS plot showing the spectra for a fully assembled ladder with the middle sensors as well as the averaged measurements from the table. 116

4.12 Table subtracted displacement data with 1D oscillator fit for capacitive sensor system for the dummy ladder. 117

4.13 Setup to measure the vibrations on the ladder which is fixed to the optical bench, where two flow meters are connected to both ends of the perforated tube. 119

4.14 Laser Doppler velocimetry (top) and laser Doppler vibrometer (bottom) [114]. . 121

4.15 Schematic of laser Doppler vibrometer [114]. 122

4.16 Measuring the stand-off distance between the laser and the object [119]. 124

4.17 Set-up assembled for air-flow measurement with laser head of LDV focused on the silicon sensor. On the left side laser head is mounted on a tripod stand and affixed to the optical bench kept at an optimal stand-off distance from the sensor to be scanned. The right side of the image focuses on the ladder setup where the ladder is connected to the perforated tube which is then connected to the flow meters on both sides for the airflow to pass through. 125

4.18 Upper left: Random data, Bottom: Hanning window, Bottom right: Resultant spectra after Hanning window applied. 126

4.19 Laser doppler vibrometer and Ladder with perforated tube mounted on the optical bench. The encircled region on the ladder shows the point on the sensor focused by the laser, while the marked area on the LDV represents the point of maximum focus, ensuring accurate vibration measurements. 127

4.20 (a) Schematic illustrating the positioning of different measurement points on 6×6 cm^2 sensor surface (b) Averaging of measured points to obtain an overall assessment of vibrations across the entire sensor surface. 128

4.21 Air flow measurement procedure for each point on the sensor. 129

4.22 (Top) Frequency vs PSD spectra of one of the points on the innermost sensor, with each flow-rate shown by a different color. The vertical dotted lines highlight the excitation of peaks at frequencies of 7.5 and 22.5 Hz, because of the airflow. The shaded region on the left side of the plot shows the frequency range that has been excluded from the analysis due to the background noise. (Bottom) The plot shows the vibration amplitude (RMS) for each sensor on the ladder with the red, green, and blue colors corresponding to airflow rates of 20, 30, and 40 L/min, respectively. The horizontal dotted line shows the baseline limit for the maximum vibration amplitude so that track-based alignment software can work properly. 130

4.23 Frequency vs PSD spectra for the most critical sensors (S3 and S-3) under a continuous airflow of 40 L/min. 132

4.24 Position vs RMS plot for long-term tests for (a) sensor 3 (b) sensor -3. 132

4.25 Image showing the central ladder with the shift in the perforated tube. 133

4.26 (Left) Frequency vs PSD spectra for different airflow on one of the points on the innermost sensor on the central ladder. (Right) Plot showing sensor numbers on the x-axis and their corresponding RMS values on the y-axis for all sensors on the central ladder. 133

A.1.1 Preparation of the tool depending on the type of FEB used (A/B). The encircled regions highlights the areas that will provide support to the FEB surface. 137

A.1.2 (a) Fixation of FEB on the tool at the right position; (b) Stencil to draw the glue pattern. 138

A.1.3 (a) Glue dispenser to control glue volume; (b) Glue pattern using the dispenser. 139

A.1.4 (a) Fixation of cooling shelf with the screws; (b) Sliding down of screwed shelf on the FEB for gluing. 139

A.1.5 Image showing (a) FEB A glued to one side of the cooling shelf and FEB B is attached to the bottom tool for gluing on the opposite side of the cooling shelf; (b) FEB B glued to the other side of the cooling shelf. 140

A.1.6 Image shows the module handling and fixation into the gluing tool for the gluing process. The encircled areas are the kapton sheets that are applied at the edges to ensure that there is atleast a minimum gap of 120 μm (thickness of the kapton sheet). 140

A.1.7 Customised double-y pattern designed to fit the dimensions of FEBs. The glue volume of 0.45 mL is distributed along the different lines shown in the pattern to ensure full coverage. 141

List of Tables

2.1 Summary of the important properties of the selected adhesives. 24

2.2 Results of lap shear test for all adhesive samples before and after the samples underwent thermal cycling. Ten thermal cycles were performed for each sample in a climatic chamber between +40 °C and -40 °C by keeping the sample at each extreme temperature for 1 hour. The load mentioned here is normalised w.r.t. area of the glued samples i.e., 5×5 cm^2. 32

2.3 Summary of the results of the different tests performed for the three candidate glues. 33

2.4 Coefficient of Thermal Expansion (CTE) values and applications for various materials used in the assembly of FEBs. 58

2.5 Summary of the Thermal cycling of the first set of measurements including eight FEBs 66

2.6 Summary of the Thermal cycling of the second set of measurements including four FEBs 66

3.1 Table summarising the distance of the L-legs from the edge of each sensor, only showing the one side of the ladder with L-legs, since the position on the other side of the ladder will be mirrored. 85

3.2 Table summarises the parameters in x, y, z direction in two ladders as specified in the v22d geometry of STS. 95

1 Volume distribution parameters for the glue pattern 141

2 Summary of parameters used for data acquisition 142

Acknowledgment

This work would not have been possible without the guidance, support, and encouragement of the many individuals I encountered throughout this journey. First and foremost, I extend my deepest gratitude to my supervisor, Prof. Dr. Hans Rudolf Schmidt, for providing me with the opportunity to pursue my PhD research and for his unwavering support throughout the entire process. His insightful feedback and continuous encouragement were invaluable in keeping me motivated and broadening my knowledge.

I would also like to express my sincere thanks to my co-supervisor, Dr. Ulrich Frankenfeld, who provided me with such a delightful environment to work with. From the initial challenges with the first baby ladder to the successful production of a fully assembled ladder, his strength and mentorship have been invaluable. I am deeply grateful to both of my supervisors for their support, especially during moments of doubt, and for their invaluable feedback The success of my thesis is dedicated to their guidance and the hard work that I learned from them. I am thankful to them for proofreading the dissertation and giving me feedback for the betterment.

I am thankful to Dr. Christian J. Schmidt, who has been a mentor throughout this research journey. His support and the many insightful discussions were crucial to the progress of my work. I would like to express my deep gratitude to Dr. Johann Heuser, Prof. Dr. Alberica Toia, and Dr. Jorg Lehnert for their constructive feedback, suggestions, and willingness to engage in discussions whenever needed. I owe my deepest gratitude to Annette Zimbelius for helping me with all the paperwork and taking care of my never-ending stationery requirements.

I am thankful to Dr. Georg Viehhauser for allowing me to help me with a major part of my thesis. His support, especially during the covid times has been immensely helpful for my work to go on. I enjoyed having discussions with him.

I am sincerely grateful to Dr. Georg Viehhauser for his support, particularly during the challenging COVID-19 period, which enabled me to progress with a major part of my thesis. I truly enjoyed our discussions and his guidance throughout this time.

Special thanks to Prof. Dr. Tapan K Nayak and Prof. Dr. Subhasis Chattopadhyay for giving me the opportunity to undertake my master's thesis under their supervision, which opened the door to the world of research and detector development. I am also grateful to Dr. Loveleen Kaur Brar for encouraging me to take the risk of pursuing research in my chosen field during my master's, a decision that has led me to where I am today.

As an experimental physicist, I had the privilege of working closely with engineers whose technical expertise and collaboration were important. I would like to thank Oleg, Jenz, and Patrick for their assistance. A special note of gratitude goes to Carmen and Robert who were always there to help me whenever it was needed. I can not thank Frederike enough, with whom I spent a considerable amount of time in the lab. Thank you for being there to listen to my ideas and help me implement them with your expertise, as well as for accommodating my working hours.

I have been fortunate to work alongside colleagues who eventually became friends. I would like to thank Anton, Maksym, Adrian and Osnan for introducing me to the STS lab and supporting me from the very beginning. I learned so much from you, whether it was soldering, testing modules, dealing with problems in the lab, or spending hours finding the scissors. Evgenia, your presence in the group was a blessing, which helped me professionally as well as personally. Marcel, I have spent a lot of time working with you and it has always been a nice time with full of discussions, be it inside GSI or outside. Merve, you have been my favorite coffee partner, and our coffee breaks often led to solutions for many problems.

I would also like to thank Olga, Hanna, Evgeny, Iroslav, Shahid, and Elena. It was a pleasure to work with all of you. This journey would be incomplete without my dear Cuban friends. Thank you, Lady, Dario, and Dairon, for reminding me how to stay young at heart and for keeping me sane, especially during the intense thesis writing phase.

A special mention goes to my Indian friends who have always been there to uplift my spirits. Kshitij, I am deeply thankful for your unwavering support over the years, from drafting research proposals to navigating the challenges of lab work, to hosting Indian parties, to never-ending walks discussing life. Mehul, our journey from heated debates to eagerly seeking each other's advice has been remarkable. I can't thank you two enough for being there.

This journey would not have been the same without my amazing friends. Ragan, thank you for always being just a call away, even when I was not expressing much. Kanika, your sisterly love and support have always made me feel special. Meetika, my adopted sibling, you helped me survive the final, demanding phase of thesis writing. You will always be my favorite dine-in buddy and cheerleader. Shubham, from meeting each other randomly to being a dear friend, thank you for being there. Omvir, thank you for cheering me up every time with the amazing food. Shreya, thank you for the shopping sprees that provided much-needed breaks. I am thankful to Ajit and Sayak for the motivating video calls and endless laughter.

I would like to thank Arindam, Rajesh, Vivek for being my guardians during this journey. To Shaista, Sudhir, Narender, Arzoo, Anurag, Reema, Khwaish, Priyanka, Shri and Twinkal — thank you for your friendship and support at various stages of this journey. Special thanks to Vibhuti, Rajni, Monika, and Sachin, who have stood by me for years, long before this journey began.

Finally, I owe my deepest gratitude to my family, my grandfather, Harnam Das Mehta, and my parents, Sunil Mehta and Neelam Mehta, for their unwavering faith in me and their constant support. My little brother Harshit, your encouragement has been a source of strength. My sister Shruti and brother-in-law Himanshu, thank you for being my human diary and support system. I also want to thank my nephew Vyom for our long-distance calls that always brought a smile to my face.